

AMPS CO-CHANNEL INTERFERENCE REJECTION TECHNIQUES AND THEIR IMPACT ON SYSTEM CAPACITY

By

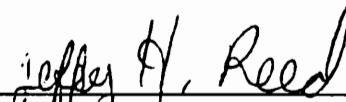
Rong He


Dissertation submitted to the Faculty of the
Virginia Polytechnic Institute and State University
in partial fulfillment of the requirements for the degree of
DOCTOR OF PHILOSOPHY


in

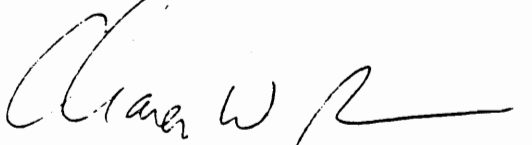
Electrical Engineering

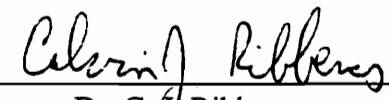
APPROVED


Dr. J. H. Reed, Chairman


Dr. B. D. Woerner


Dr. T. S. Rappaport


Dr. C. W. Bostian


Dr. C. J. Ribbens

July, 1996

Blacksburg, Virginia

Key words: AMPS, Adaptive Filtering, Cyclostationarity, Cellular Capacity, Interference Rejection, Wireless Communications

c.2

LD
5655
V856
1996
H4
c.2

AMPS CO-CHANNEL INTERFERENCE REJECTION TECHNIQUES AND THEIR IMPACT ON SYSTEM CAPACITY

By

Rong He

Dr. Jeffrey H. Reed, Chairman

Bradley Department of Electrical Engineering

Abstract

With the rapid and ubiquitous deployment of mobile communications in recent years, co-channel interference has become a critical problem because of its impact on system capacity and quality of service. The conventional approach to minimizing interference is through better cell planning and design. Digital Signal Processing (DSP) based interference rejection techniques provide an alternative approach to minimize interference and improve system capacity.

Single channel adaptive interference rejection techniques have long been used for enhancing digitally modulated signals. However these techniques are not well suited for analog mobile phone system (AMPS) and narrowband AMPS (NAMPS) signals because of the large spectral overlap of the signals of interest with interfering signals and because of the lack of a well defined signal structure that can be used to separate the signals.

Our research has created novel interference rejection techniques based on time-dependent filtering which exploit spectral correlation characteristics exhibited by AMPS and NAMPS signals. A mathematical analysis of the cyclostationary features of AMPS and NAMPS signals is presented to help explain and analyze these techniques. Their performance is investigated using both simulated and digitized data. The impact of these new techniques on AMPS system capacity is also studied. The adaptive algorithms and structures are refined to be robust in various channel environments and to be computationally efficient.

Acknowledgments

I am greatly indebted to my advisor, Dr. Jeffrey H. Reed, for providing insight and guidance in writing this dissertation. I am grateful to his role in the development of my research, thinking and writing skills during the years working with him.

I would like to express my gratitude to my committee members, Dr. Brian D. Woerner, Dr. Ted S. Rappaport, Dr. Charles W. Bostian and Dr. Carvin J. Ribbens, for carefully reviewing my dissertation and providing valuable suggestions.

I have had a great opportunity in studying for my Ph.D degree at the MPRG laboratory where I received enormous help from faculty, staff and students. I thank Paul Petrus, Mat Welborn, Khawar Khan, Nitin Mangalvedhe, Francis Dominique, Kevin Saldanha, Raqib Mostafa, Tom Biedka, Volker Aue, Nevena Zecevic, Mike Buehrer, Rick Cameron, and many others, for their help and suggestions. I also thank Prab Koushik for supporting my heavy computational demands. I would like to thank Jeff Laster and Steve Nicoloso, and especially Dr. Ivan Howitt, for their careful reading of my dissertation and their useful technical writing suggestions.

I would like to thank ARGOSystems, SAIC Inc., Motorola Inc., the Center for Wireless Telecommunications and the MPRG industry affiliates of their financial support for this work.

I wish to thank my family for their constant encouragement and support during my graduate school study.

Finally, I would like to convey my heart-felt thanks to Jason, for his patience, immeasurable support and understanding during the whole time.

Table of Contents

Chapter 1

Introduction to the Research	1
1.1 Problem Statement.....	1
1.2 Significant Contributions of this Research	2
1.3 Overview of the Research.....	4

Chapter 2

Literature Review of AMPS Interference Rejection Techniques	6
--	----------

Chapter 3

Second Order Cyclostationarity	16
3.1 Introduction	16
3.2 Second Order Cyclostationarity (Wide Sense Cyclostationarity)	18
3.3 Applications of Cyclostationarity	29

Chapter 4

Cyclostationarity of AMPS Signals	33
4.1 AMPS Background.....	33
4.2 Cyclostationarity of AMPS Signal	35
4.3 Cyclic Feature for AMPS Signals in Different Channels.....	40

Chapter 5

Optimal and Adaptive Time-Dependent Filtering	64
5.1 Introduction	64
5.2 Optimal Time-Dependent Filtering	66
5.3 Configuring the Adaptive Time-Dependent Filtering for Enhancing AMPS Signals	84
5.4 Simulation Study	87
5.4.1 Assumptions.....	87
5.4.2 Experimental Procedure.....	88
5.4.3 Results.....	89
5.4.4 Convergence and Computation Complexity	101
5.5 Refinements of TDAF Algorithms and Structures	104
5.5.1 Refinements of the Algorithms	104

5.5.2 Refinements of the Structures	109
---	-----

Chapter 6

Time-dependent Adaptive Filtering Techniques for NAMPS Co-channel Interference Rejection120

6.1 Introduction	120
6.2 Cyclostationarity of NAMPS Signal	121
6.3 Filter Implementation	124
6.4 Simulation Results	125
6.5 Summary and Future Work	128

Chapter 7

Statistical Analysis of Channel Interference and Capacity Improvement When Using Interference Rejection Techniques.....139

7.1 Adjacent Channel Interference	140
7.2 Co-channel Interference	146
7.2.1 Fading Only Environment.....	151
7.2.2 Fading and Lognormal Shadowing Environment	154
7.3 Percentage of <i>CIR</i> Coverage at a Receiver.....	156
7.3.1 Percentage of Average <i>CIR</i> Coverage at a Mobile Station.....	160
7.3.2 Percentage of Average <i>CIR</i> Coverage at a Base Station.....	163
7.4 Effect of Power Control on the Average <i>CIR</i> Coverage	171
7.4.1 Effect of Power Control on the Average <i>CIR</i> Coverage at a Mobile Station.....	172
7.4.2 Effect of Power Control on the Average <i>CIR</i> Coverage at a Base Station.....	176
7.5 System Capacity Improvement.....	179

Chapter 8

Future Work.....185

8.1 Performance of a TDAF with Multiple Co-channel Interfering Sources ..	185
8.2 Analysis of the Sensitivity to the SAT Frequency Bias	185
8.3 Co-channel Interference Mitigation Using Spectral Correlation Detection Techniques and Switched Diversity	185
8.4 Adjacent Channel Interference Rejection Using DSP Techniques	186

8.5 DSP Hardware for Real Time Implementation of the TDAF..... 186

8.6 Extended Analysis of System Capacity to Sectorized Antennas..... 186

Chapter 9

Conclusions and Summary.....187

References..... 189

List of Figures

Fig. 2.1	Block diagram of cross-coupled PLL receiver	7
Fig. 2.2	ALE structure.....	8
Fig. 2.3	Parasitic phase estimator.....	11
Fig. 2.4	Basic block diagram of geometric subtraction.....	11
Fig. 2.5	An open-loop (Baghdady) interference suppressor using an adaptive notch filter	13
Fig. 2.6	Block diagram of the Stojanovic and Dukic FM demodulator	14
Fig. 3.1	(a) Power spectral density (PSD) of a lowpass signal. (b) PSD of an AM signal (c) PSD of a squared lowpass signal. (d) PSD of a squared AM signal	24
Fig. 3.2	Magnitude of the spectral correlation density function for an AM signal	27
Fig. 3.3	One channel-pair of a spectral correlation analyzer	28
Fig. 4.1	Seven cell reuse concept	34
Fig. 4.2	Conventional spectrum of AMPS signal with SAT	39
Fig. 4.3	Contour of spectrum correlation density function $S_x^\alpha(f)$ for AMPS signal with a SAT.....	39
Fig. 4.4	AMPS signal generator	40
Fig. 4.5	Magnitude of the cyclic autocorrelation coefficients for AMPS signal with noise	44
Fig. 4.6	Magnitude of the cyclic autocorrelation coefficients for SOI and SNOI ($\alpha=kf_{sat}$)	44
Fig. 4.7	Flat fading generation using baseband Doppler filter.....	48
Fig. 4.8	Comparison of $\Gamma(\tau)$ using different measuring methods	52
Fig. 4.9	Comparison of the envelop autocorrelation using theoretical results and simulated data	55
Fig. 4.10	Autocorrelation function of the faded complex signal for flat fading channel.....	61
Fig. 4.11	Autocorrelation function of the faded complex signals for frequency selective fading channel.....	61
Fig. 4.12	Fourier transform of $\Gamma(\tau, \alpha)/ H_0 ^2$ for flat fading channel	62
Fig. 4.13	Fourier transform of $\Gamma(\tau, \alpha)/ H_0 ^2$ for frequency selective fading channel	62
Fig. 4.14	Comparison of the cyclic autocorrelation function for undistorted and faded AMPS signals	63
Fig. 5.1	The TSR TDAF.....	65
Fig. 5.2	The FRESH filter	67
Fig. 5.3	The circular FSR TDAF.....	67
Fig. 5.4	a Filter response $G_0(f)$ of optimal time-dependent filter..... b Filter response $G_1(f)$ of optimal time-dependent filter	77
Fig. 5.5	Output CIR of the TDAF and TIAF processed signal for interference-only and noisy channels.....	79
Fig. 5.6	Output CIR of the TDAF processed signal of flat fading case for different Doppler frequencies.....	82
Fig. 5.7	Output CIR of the TDAF assuming frequency-selective fading and various	

	channel delay spread, Doppler frequency is 30Hz	83
Fig. 5.8	Output <i>CIR</i> of the TDAF assuming frequency-selective fading and various channel delay spread, Doppler frequency is 60Hz	83
Fig. 5.9	Block diagram of the spectral correlation predictor (SCP).....	85
Fig. 5.10	Block diagram of a receiver using two-stage TDAF	87
Fig. 5.11	Block diagram for AMPS quadrature demodulator.....	88
Fig. 5.12	Output <i>CIRs</i> after the SCP for different carrier separations, $CNR=25\text{dB}$	95
Fig. 5.13	<i>MSE</i> of the demodulated voice signals after the SCP for different	95
Fig. 5.14	<i>MSE</i> of the demodulated SAT after the SCP for different carrier separations, $CNR=25\text{dB}$	96
Fig. 5.15	Output <i>CIRs</i> after the SCP for different Doppler frequencies, $CNR=25\text{dB}$..	96
Fig. 5.16	<i>MSE</i> of the demodulated voice signals after the SCP for different carrier separations, $CNR=25\text{dB}$	97
Fig. 5.17	<i>MSE</i> of the demodulated SAT after the SCP for different Doppler frequencies, $CNR=25\text{dB}$	97
Fig. 5.18	Comparison of <i>CIR</i> improvement for simulated and digitized signal, $f_d=30\text{Hz}$, carrier separation is 0Hz and CNR is 25dB	98
Fig. 5.19	<i>CIR</i> Comparison of the theoretical and blind TDAF for the AMPS FM signals, carrier separation=400Hz, $CNR=25\text{dB}$	98
Fig. 5.20	Demodulated voice signal for $CIR=-3\text{dB}$ and $CNR=25\text{dB}$, no fading.....	100
Fig. 5.21	Demodulated voice signal for $CIR=0\text{dB}$ and $CNR=25\text{dB}$, high Doppler frequency.....	100
Fig. 5.22	Filtered <i>MSEs</i> of the TDAF processed signals for different input <i>CIRs</i> , carrier separation is 0Hz and CNR is 25dB.....	102
Fig. 5.23	Filtered <i>MSEs</i> of the TDAF processed signals for different input <i>CIRs</i> , $f_d=30\text{Hz}$. Carrier separation is 0Hz and CNR is 25dB	103
Fig. 5.24	Filtered <i>MSEs</i> of the TDAF processed signals for different input <i>CIRs</i> , $f_d=30\text{Hz}$. Carrier separation is 0Hz and CNR is 25dB	103
Fig. 5.25	The CMA/TDAF structure.....	110
Fig. 5.26	Hybrid structure of CMA and Griffith's algorithm	110
Fig. 5.27	Output <i>CIRs</i> of the SCP and the hybrid CMA and Griffith's algorithm, $CNR=25\text{dB}$	112
Fig. 5.28	Comparison of the demodulated voice signals for different output branches using hybrid CMA and Griffith's algorithm	114
Fig. 5.29	Smoothed <i>MSEs</i> of the hybrid CMA and Griffith's algorithm processed signals for different input <i>CIRs</i> . Carrier separation is 0Hz and CNR is 25dB.....	115
Fig. 5.30	Smoothed magnitude of the hybrid CMA and Griffith's algorithm processed signals. Carrier separation is 0Hz and CNR is 25dB	115
Fig. 5.31	Output <i>CIRs</i> of the SCP and the hybrid CMA and Griffith's algorithm, $f_d=30\text{Hz}$, $CNR=25\text{dB}$	116
Fig. 5.32	<i>MSE</i> of the demodulated voice signals after the SCP and the hybrid CMA and Griffith's algorithm, $f_d=30\text{Hz}$, $CNR=25\text{dB}$	116
Fig. 5.33	Comparison of the demodulated voice signals using SCP and hybrid CMA and	

	Griffith's algorithm.....	117
Fig. 5.34	Output <i>CIRs</i> of the SCP and the hybrid CMA and Griffith's algorithm, $f_d=60\text{Hz}$, $\text{CNR}=25\text{dB}$	118
Fig. 5.35	<i>MSE</i> of the demodulated voice signals after the SCP and the hybrid CMA and Griffith's algorithm, $f_d=60\text{Hz}$, $\text{CNR}=25\text{dB}$	118
Fig. 5.36	Comparison of the demodulated voice signals using SCP and hybrid CMA and Griffith's algorithm.....	119
Fig. 6.1	The TSAF (or TSR) TDAF.....	125
Fig. 6.2	NAMPS signal generator	126
Fig. 6.3	<i>CINR</i> and <i>CDF</i> of segmented <i>CINR</i> for the corrupted NAMPS FM signal, $\text{CIR}=12\text{dB}$	129
Fig. 6.4	<i>CINR</i> and <i>CDF</i> of segmented <i>CINR</i> for the TDAF filtered NAMPS FM signal, $\text{CIR}=12\text{dB}$	130
Fig. 6.5	Demodulated voice signal without using the TDAF, and the corresponding segmented <i>SINR</i> and <i>CDF</i> , $\text{CIR}=12\text{dB}$	131
Fig. 6.6	Demodulated voice signal with the TDAF, and the corresponding segmented <i>SINR</i> and <i>CDF</i> , $\text{CIR}=12\text{dB}$	132
Fig. 6.7	<i>CDF</i> Comparison for segmented <i>CINR</i> and <i>SINR</i> with and without the TDAF, $\text{CIR}=12\text{dB}$	133
Fig. 6.8	<i>CINR</i> and <i>CDF</i> of segmented <i>CINR</i> for the corrupted NAMPS FM signal, $\text{CIR}=15\text{dB}$	134
Fig. 6.9	<i>CINR</i> and <i>CDF</i> of segmented <i>CINR</i> for the TDAF filtered NAMPS FM signal, $\text{CIR}=15\text{dB}$	135
Fig. 6.10	Demodulated voice signal without the TDAF, and the corresponding segmented <i>SINR</i> and <i>CDF</i> , $\text{CIR}=15\text{dB}$	136
Fig. 6.11	Demodulated voice signal with the TDAF, and the corresponding segmented <i>SINR</i> and <i>CDF</i> , $\text{CIR}=15\text{dB}$	137
Fig. 6.12	<i>CDF</i> Comparison for segmented <i>CINR</i> and segmented <i>SINR</i> with and without the TDAF, $\text{CIR}=15\text{dB}$	138
Fig. 7.1	a Adjacent channel interference for a mobile at a joint corner	142
Fig. 7.2	Probability of one adjacent interferer	145
Fig. 7.3	Probability of two adjacent interferers.....	145
Fig. 7.4	Carrier to interference ratio for different frequency reuse patterns with equal interfering distances	149
Fig. 7.5	Probability of n_c active interfering signals as a function of single channel blocking probability p	153
Fig. 7.6	Total probability of co-channel interference (Rayleigh only environment) of a seven-cell frequency reuse pattern as a function of blocking rate and <i>CIR</i> . Note there is little dependency on blocking rate.	154
Fig. 7.7	Comparison of the total probability of co-channel interference as a function of <i>CIR</i> for the Rayleigh only environment and Rayleigh lognormal shadowing environment assuming a seven-cell frequency reuse pattern1.....	57
Fig. 7.8	Worst case $p(\text{CIR} > \text{CIR}_0)$ for different frequency reuse patterns, $n=3.6$ and	

	$\sigma=8\text{dB}$, assuming single interference source	160
Fig. 7.9	Illustration of the co-channel interference for a mobile station.....	161
Fig. 7.10	<i>CIR</i> coverage comparison between a mobile station located at the worst location ($r_s=R$, and $l=D-R$) and the average value over the whole cell, $N=7$	164
Fig. 7.11	<i>CIR</i> coverage comparison between a mobile station located at the worst location ($r_s=R$, and $l=D-R$) and the average value over the whole cell, $N=3$	164
Fig. 7.12	Illustration of co-channel interference for a base station.....	165
Fig. 7.13	Probability density function $p_{pdf}(l)$ for $N=7$	169
Fig. 7.14	Probability density function $p_{pdf}(l)$ for $N=3$	169
Fig. 7.15	<i>CIR</i> coverage comparison between a base station located at the worst location ($r_s=R$, and $l=D-R$) and the average value over the whole cell, $N=7$	170
Fig. 7.16	<i>CIR</i> coverage comparison between a base station located at the worst location ($r_s=R$, and $l=D-R$) and the average value over the whole cell, $N=3$	170
Fig. 7.17	Average <i>CIR</i> coverage comparison at a base station and at a mobile station for different frequency reuse patterns.....	171
Fig. 7.18	Illustration of the co-channel interference for a mobile station with power control.....	172
Fig. 7.19	Comparison of the <i>CIR</i> coverage for a mobile station with and without power-controlled base stations, $N=3, 7$	176
Fig. 7.20	Comparison of the <i>CIR</i> coverage for a base station with and without power controlled mobile stations, $N=3, 7$	179
Fig. 7.21	Analytical <i>CIR</i> coverage at a mobile station by using the conventional receiver and the receiver incorporating a time-dependent filter. Flat fading channel models from Chapter 5, Section 5.2 are assumed, $N=7$	183
Fig. 7.22	Analytical <i>CIR</i> coverage at a mobile station by using the conventional receiver and the receiver incorporating a time-dependent filter. Flat fading channel models from Chapter 5, Section 5.2 are assumed, $N=3$	183
Fig. 7.23	Analytical <i>CIR</i> coverage at a base station by using the conventional receiver and the receiver incorporating a time-dependent filter. Frequency selective fading channel models from Chapter 5, Section 5.2 are assumed, $N=7$	184
Fig. 7.24	Analytical <i>CIR</i> coverage at a base station by using the conventional receiver and the receiver incorporating a time-dependent filter. Frequency selective fading channel models from Chapter 5, Section 5.2 are assumed, $N=3$	184

List of Tables

Table 5.1	Circular RLS Algorithm [Hay91]	86
Table 5.2	<i>CIR</i> , <i>MSE</i> improvement of the voice signals and the SAT provided by a two-stage TDAF	91
Table 5.3	Comparison of computational complexities of LMS and RLS algorithms ...	102
Table 5.4	Griffith's like LMS algorithm for the TDAF	107

Chapter 1. Introduction to the Research

1.1 Problem Statement

Cellular phone services and personal communication services have grown rapidly in recent years. With limited spectrum available for transmitting mobile phone signals, increasing system capacity has become a primary objective for many mobile phone companies. Interference, in fact, is the key problem limiting system capacity. Different modulation techniques have been developed to obtain more system capacity. For the current advanced mobile phone system (AMPS), which uses frequency division multiple access (FDMA), all users share different frequency slots. The radio frequencies (RF) for one region are reused in a non-adjacent region to avoid interference. For time division multiple access (TDMA) systems, all users occupy different time slots within a frame. For code division multiple access (CDMA) systems, each user is assigned a different spreading code which can be transmitted in the same band. Although the new technologies like CDMA and TDMA promise more capacity than AMPS, the cost to implement these new technologies is currently very high. These technologies may never fully supersede AMPS because of the need for backward capability and AMPS is the only standard deployed nation-wide. Unfortunately, AMPS is only $1/3$ to $1/20$ as spectrally efficient as these new modulation formats and will continue to be a hindrance in improving system capacity for the cellular service providers.

Cell splitting is the typical solution to obtain increased system capacity from AMPS in a region. However, creating a new cell is a costly proposition, requiring surveying the area, acquiring property, constructing cellular facilities, and reconfiguring the cellular network to handle the new cell. This approach is expensive since each new cell site can cost from \$500,000 to \$1,000,000. An alternative to the new transmission technologies and to cell splitting is to use interference rejection techniques to increase the system capacity. We expect this approach to provide a more economical solution for improving AMPS system

capacity and signal quality.

The goal of this research is to develop practical robust interference rejection techniques for AMPS and to show the impact on system capacity. Adaptive antenna arrays can effectively reduce channel interference, but this is still an expensive solution and difficult to implement. Single channel interference rejection techniques are much less costly. However, until recently these techniques have not been very effective, primarily because of lack of signal structure which can be used to discriminate the interference. In this research, one of the common features for many digital and analog communication signals, cyclostationarity or equivalently spectral correlation, has been successfully applied to discriminate signals. New interference rejection techniques have been developed that exploit the cyclostationary features of AMPS signals. The new interference rejection techniques could, through upgrading the current base station or mobile station receiver, offer the needed extra capacity without creating an expensive new cell and can work without modifying the AMPS standard. These techniques increase system capacity and provide a significant improvement in voice quality. This capability could provide a unique marketing feature for a cellular phone manufacturer in an extremely competitive business.

Military applications for interference rejection are also numerous. The most obvious applications are in mitigating the effects of intentional jamming and providing improved reconnaissance capability. The military has always been interested in single channel techniques for interference rejection because they are generally cheaper, less complex, smaller in size, and more suited to rugged military applications than multi-channel techniques.

1.2 Significant Contributions of this Research

The cyclostationary characteristics of an AMPS signal are first analyzed in this research. Theoretical analysis and measurement of the cyclic features of the AMPS signal are investigated and these features provide the key in creating the interference rejection algorithms. The cyclostationarity of the AMPS signal is exploited by using a linear frequency-shifted

(FRESH) filter, a class of time-dependent filters. By exploiting the cyclic features, the base station receiver can reject co-channel interference caused by frequency reuse. The new techniques developed in this research are flexible and robust and are also easy to implement in real systems. They do not need prior information, such as a training signal. The techniques increase the carrier to interference ratio (*CIR*) dramatically, and thereby improve the system capacity. Our results show that by using these novel interference rejection techniques, the seven-cell reuse pattern of the current AMPS system can be replaced by the three-cell reuse pattern, effectively doubling system capacity and reducing the probability of dropped calls.

In particular, the following specific significant original contributions have been made.

- The spectral correlation characteristics of AMPS signals are analyzed for different channels impairments. The characteristics of NAMPS signals are also derived. The analysis has broad applications in the fields of interference rejection, signal detection, signal classification, adaptive array processing and geolocation.
- The theoretical performance of the optimal time-dependent filter is derived for various channel impairments, including: co-channel interference, fading and noise. This analysis has been experimentally verified through extensive simulations.
- Five new adaptive filtering algorithms have been developed for AMPS and for NAMPS co-channel interference rejection. Four new blind adaptation techniques have been created for adapting the time-dependent filters. These techniques are robust to mobile channel impairments and some are computationally attractive for implementation at a mobile unit.
- The impact of interference on cellular system performance has been analyzed by computing the probability of co-channel interference for fading channels and for fading channels with lognormal shadowing. From this analysis, the probability of cell coverage above a particular *CIR* is determined for both a mobile station and a base station.
- The impact of the new interference rejection algorithms on cell coverage is computed.

It is shown that capacity is approximately doubled by using the interference rejection techniques to reduce the frequency reuse factor.

1.3 Overview of the Research

Below is a summary of the chapters composing this dissertation.

Chapter 2: Literature Review of AMPS Interference Rejection Techniques

Different single channel interference cancellation techniques are surveyed that are applicable to AMPS. The basic ideas behind these techniques are documented, noting their respective advantages and disadvantages.

Chapter 3: Second Order of Cyclostationarity

Cyclostationarity is a characteristic of most digital and analog modulated signals. An overview of the theory of cyclostationarity is presented. Along the same lines, the spectral correlation characteristic inherent to cyclostationary signals is reviewed and documented in this dissertation.

Chapter 4: Cyclostationarity of AMPS Signals

This chapter establishes the mathematical framework for analyzing the time-dependent interference rejection techniques. A general FM signal does not exhibit cyclostationarity. However an AMPS signal with a supervisory audio tone (SAT) exhibits cyclostationarity. This cyclostationary feature of AMPS with a SAT is derived and is verified by measurements. Effects of practical channels on this feature, such as noise, co-channel interference and fading, are theoretically computed and verified by simulations.

Chapter 5: Optimal and Adaptive Time-dependent Filters

A cyclostationary signal that exhibits spectral correlation characteristics can be used by a time-varying filter whose periodicities correspond to the cyclic frequencies of the desired

signal. Time-dependent optimal filters are designed to take advantage of the cyclostationary properties. The theoretical performance of this optimal filter in different radio channels is presented in this dissertation. Performance analysis and improvement measurements include the improvement of *CIRs*, demodulated voice waveforms and SAT mean squared error (*MSE*) of the AMPS signals.

Radio channels change dynamically and thus a practical filter for interference rejection must be adaptive. To make the time-dependent adaptive filter (TDAF) effective in less than ideal environments, various adaptive algorithms are developed. These TDAFs are robust in realistic channels and have low computational complexity.

Chapter 6: Time-dependent Adaptive Filtering Techniques for NAMPS Co-channel Interference Rejection

In this chapter, it is shown theoretically that the AMPS and the NAMPS signals have similar spectral redundancy characteristics. The TDAFs developed for AMPS signals are modified and applied to NAMPS signals. Simulations show that the interference rejection performance gains for NAMPS are comparable to those obtained with AMPS.

Chapter 7: Statistical Analysis of Channel Interference and Capacity Improvement Provided When Using Interference Rejection Techniques

Statistical properties of both adjacent channel and co-channel interference are discussed in this chapter. Given the improvement in signal quality provided by interference rejection techniques, it is possible to determine their impact on system capacity. The reduction in co-channel and adjacent channel interference is shown to produce a significant increase in system capacity considering both the base station and mobile station perspectives.

Chapter 2. Literature Review of AMPS Interference Rejection Techniques

In the past decade, considerable work on interference rejection for digitally modulated signals has been done. This interference rejection research can be divided into two categories, spread spectrum techniques and non-spread spectrum techniques [LR94]. However, little research has been focused on interference rejection for analog modulated signals. The reasons behind this lack of research are: a) analog communication systems are being phased out because of system capacity needs and limitations of service that can be supported; b) interference rejection is more difficult for analog modulated signals because of their lack of structure. This makes co-channel interference mitigation a more difficult problem for AMPS signals, especially using single channel interference suppression techniques. Previous interference rejection techniques that are applicable to AMPS signals can be classified as follows.

1) Cross-Coupled Phase Locked Loop (CCPLL)

Cassara and Schachter [CSS80] designed the cross-coupled PLL for single channel interference rejection in 1980. In Fig. 2.1, the novel detector consists of two phase-locked loop demodulators inter-connected in such a manner as to permit one PLL to lock onto and track the strongest received signal, while the other loop tracks and demodulates the weaker signal. The demodulator has two separate outputs, namely the outputs of each PLL, and thus possesses the capability of demodulating both signals even though they are co-channel signals. The demodulator is conceived using parameter estimation theory based upon maximum a posteriori (MAP) estimation techniques [SCS77]. Such optimization procedures led to a receiver structure which estimates (in the MAP sense) the phase of a FM signal when corrupted by a co-channel FM interferer plus additive white Gaussian noise. This technique was also studied by Martin [Mar84]. Other improvements using adaptive processing to help the PLL track both the stronger and the weaker signals were also developed based on this model [BCD84].

2) Extended Kalman Filtering

Due to the nonlinearity in the measurement equation in a PLL, an extended Kalman filter is used [Bra92]. The resulting system is composed of two interconnected second order PLLs, each of them tracking one of the two FM signals. The derived estimator was different compared to the previous CCPLL in the area in which maximum *a posteriori* estimation techniques and adaptive filter theory were combined to derive the CCPLL. The new system has variable loop gains, a different amplitude estimator structure, and an interconnection between the internal states of the PLLs. The Kalman filter is capable of producing accurate phase estimates in situations where CCPLL behavior is chaotic [Bra92]. However, this is traded off by greater computational costs than the CCPLL.

3) Adaptive Linear Enhancer (ALE)

David [DSE83] developed an adaptive structure which enables the detection and enhancement of narrow-band signals which are corrupted by broad band noise. A parallel configuration of second-order IIR adaptive filters is utilized, thus allowing detection of multiple signals [Dav84]. The IIR structure has an inherent advantage over the all-zero FIR filter

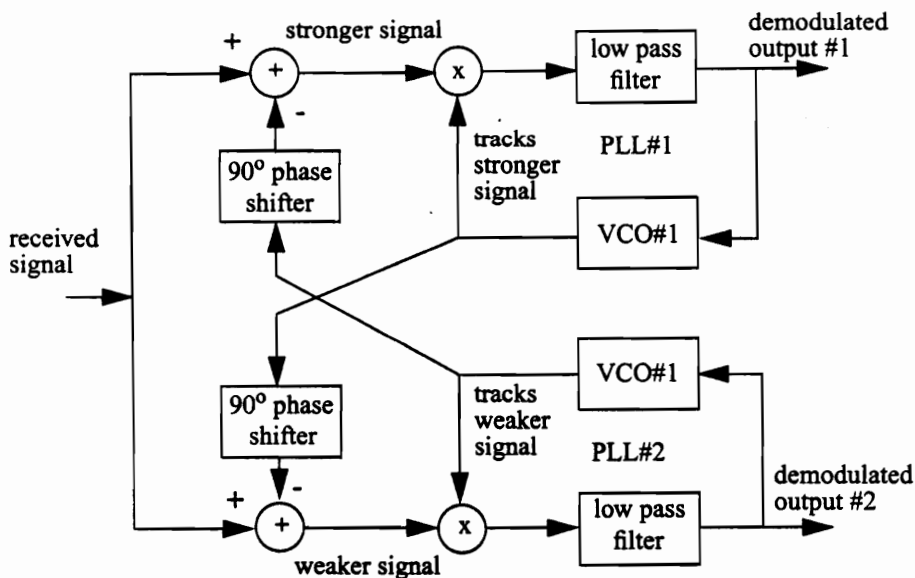


Fig. 2.1 Block diagram of cross-coupled PLL receiver

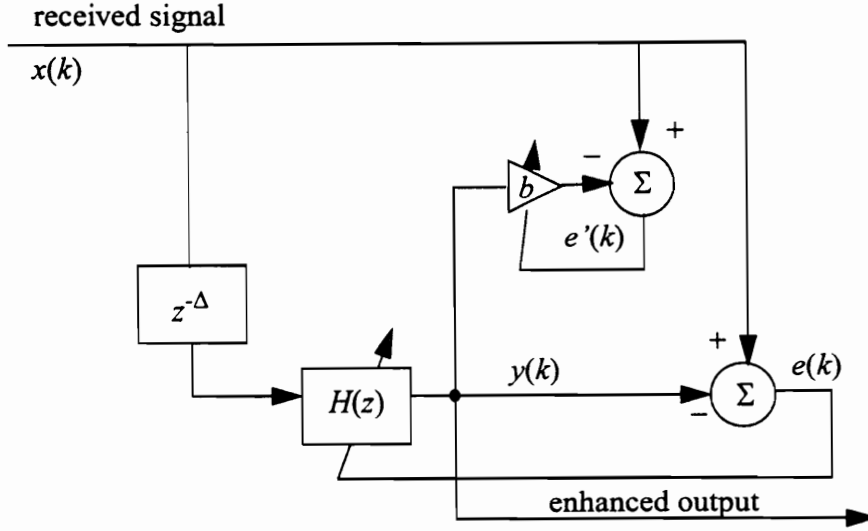


Fig. 2.2 ALE structure

due to the fact that linear enhancement is an application which requires a high Q resonant filter. The transfer function of a single IIR filter shown in Fig. 2.2 is

$$H(z) = \frac{(1-r^2)(a-z^{-1})}{1-(1+r^2)az^{-1}+r^2z^{-2}}, \quad (2.1)$$

where r determines the pole radius and a specifies a normalized angular frequency according to the relationship $\Theta = \cos^{-1}(a)$. This transfer function has zero phase shift and a peak gain of unity at frequency Θ . The pole radius determines the bandwidth of the filter. However, there are two major difficulties related to the utilization of IIR adaptive algorithms: stability maintenance during the adaptive process and convergence characteristics on a non-quadratic and potentially multi-modal performance surface.

4) IIR Adaptive Filter Bank

Martin [MP93] examined the performance of the IIR adaptive filter bank. This con-

strained adaptive IIR filter consists of a cascade of biquadratic notch sections and is used to track multiple sinusoids. The structure can be used to isolate individual sinusoids. The transient response is approximately independent of the number of sinusoids and their power levels. The IIR structure is very computationally efficient for the enhancement of sinusoids, especially when the sinusoidal frequency is much less than the sampling frequency. It is especially useful for the detection and isolation of multiple sinusoids. It can also be used to analyze the spectrum of short data streams with high resolution. An adaptive IIR filter can also be designed to track the various FM signals. The idea is that a narrowband adaptive IIR filter has the resolution to separate closely spaced narrowband signals, observed over a short time interval. The adaptive IIR filter can be configured in an adaptive linear-enhancer mode, and is constructed from cascading adaptive second order notch filters. The advantage of this arrangement is that multiple interfering signals can be canceled by multiple IIR filters and stability is easily assured by constraining the pole radius to be less than unity for each second order filter. The algorithm is simple and requires few computations. Convergence is obtained using a simple LMS algorithm typically within 200 or 300 data points.

These three algorithms have limitations when the frequency of the desired signal and the interfering signal are very close, which is the case usually observed for co-channel AMPS signals.

5) Geometric Subtraction

Bar Ness [Bar88] suggested a method for interference suppression and signal separation of angle modulated signals. The method is designed particularly for co-channel interference suppression. The main idea is to use amplitude variations of the composite signal (the strong plus weak signals) to estimate the parasitic phase distortion introduced by the interference. Consider the received signal as a summation of two signals:

$$S_1 = A_1 \sin \Phi_1(t) \quad (2.2a)$$

and

$$S_2 = A_2 \sin \Phi_2(t), \quad (2.2b)$$

where A_1 and A_2 are the constant amplitudes of the interference and the desired signal, respectively. The angle modulation functions are given by

$$\Phi_1(t) = \omega_1 t + \phi_1(t) \quad (2.3a)$$

$$\Phi_2(t) = \omega_2 t + \phi_2(t). \quad (2.3b)$$

where $\phi_1(t)$ and $\phi_2(t)$ are the phase information of S_1 and S_2 . The composite signal is given by

$$S(t) = A_2 \left[1 + \left(\frac{A_1}{A_2} \right)^2 + 2 \left(\frac{A_1}{A_2} \right) \cos \Phi(t) \right]^{\frac{1}{2}} \sin [\Phi_2(t) + \varphi_p(t)] \quad , \quad (2.4)$$

where $\Phi(t) = \Phi_1(t) - \Phi_2(t) = (\omega_1 - \omega_2)t + \phi_1(t) - \phi_2(t)$. The parasitic phase $\varphi_p(t)$ is computed by

$$\varphi_p(t) = \text{atan} \left[\frac{\frac{A_1}{A_2} \sin \Phi(t)}{1 + \frac{A_1}{A_2} \cos \Phi(t)} \right]. \quad (2.5)$$

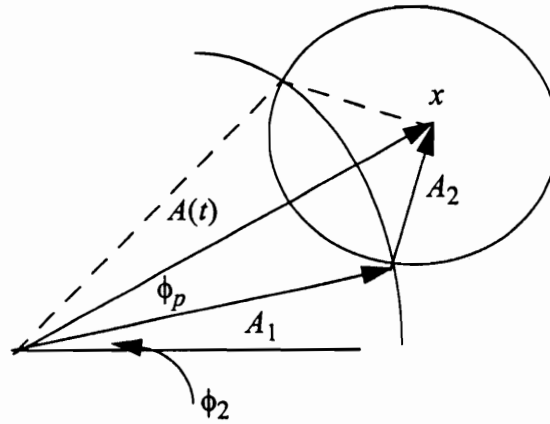


Fig. 2.3 Parasitic phase estimator

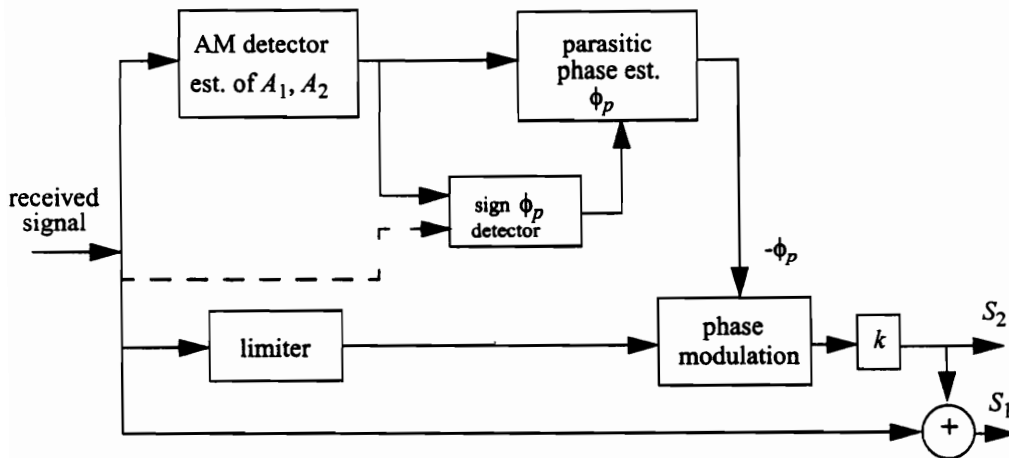


Fig. 2.4 Basic block diagram of geometric subtraction interference suppression method

The parasitic phase $\phi_p(t)$ can be eliminated if $\Phi(t)$ is properly estimated from the amplitude detector. This estimate can be utilized to cancel out the distortion at the composite signal and obtain the desired (strong) signal's angle information. The weak signal is then obtained by suitable subtraction from the composite signal after limiting, thus resulting in the separation of the two signals. The geometric relationship of the two signals and the block diagram of the geometric subtraction method are shown in Fig. 2.3 and Fig. 2.4, respectively. An adaptive method can also be applied to improve the estimates and results in a better cancellation of interference [Bar89].

This is a straight forward technique which uses the angle relationship of two FM signals. In our early stage of the research, this method was implemented. Results show that noise tends to make the estimation of the amplitude less precise, yielding in an inaccurate estimate for the parasitic phase. The phase estimate may be dominated by the noise, not by the FM signal. The amplitudes of signal of interest (SOI) and signal not of interest (SNOI) can be estimated effectively for a very low noise level by observing the minimum and maximum values. The noise problem limits its practicality for real channels. For a high level noise and a fading environment, more sophisticated estimation procedures are needed.

6) Adaptive Notch Filter

Rich and Cassara refined and extended the adaptive tracking notch filter which was first proposed by Baghdady [RBC94]. This notch filter is useful for suppressing co-channel FM and CW signals and allows a simple, practical realization of very high Q adaptive notch filters using either analog or digital technology. The block diagram of this filter is depicted in Fig. 2.5. When the instantaneous frequency of the stronger interfering FM carrier signal is known precisely, it can be eliminated. Placing an additional adaptive notch filter in front of the stronger interfering signal improves the estimate of this signal.

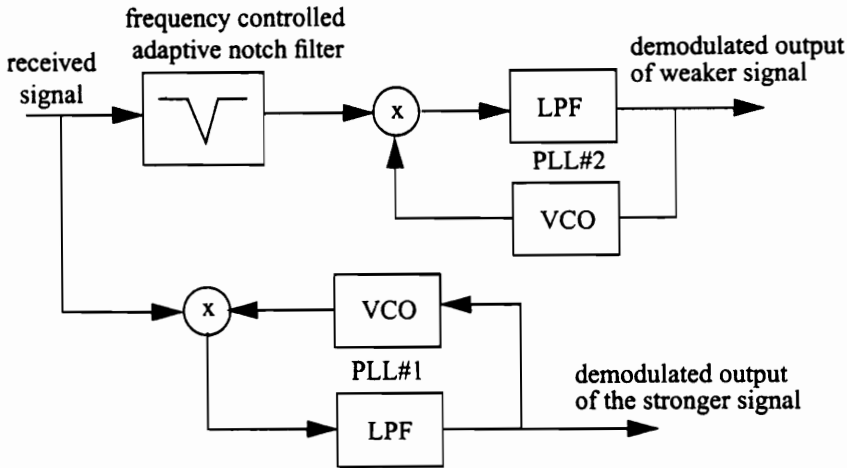


Fig. 2.5 An open-loop (Baghdady) interference suppressor using an adaptive notch filter

7) Robust Limiter-Discriminator Demodulation

The response of a conventional FM discriminator in the presence of noise and co-channel interference was investigated by Mizuno and Shimbo [MS94]. Stojanovic and Dukic [SDS81] improved the performance of a conventional FM limiter-discriminator for co-channel interference. The principle behind this demodulator is simple. An ideal FM signal has a constant envelope, while the envelope of a desired FM signal corrupted by interference varies randomly with time. Consider the demodulator in Fig. 2.6, some information about the interference phase can be obtained by detecting the square of this envelope. This signal and the signal from the output of the conventional limiter-discriminator are jointly processed and optimized to minimize the baseband interference noise. This optimization process involves matching the two weighting networks $H_1(j\omega)$ and $H_2(j\omega)$ based on knowledge of the statistics of the desired and interfering signals.

8) Neural Network

Howitt, Reed, and Hsia [HRVH93] surveyed recent developments in applying neural nets for equalization and interference rejection. The ability of neural networks to reject inter-

ference can be viewed from different perspectives:

- The neural network creates non-linear decision boundaries between signal states.
- The neural network provides a means of implementing non-linear filters for mitigating non-Gaussian interference.
- The neural network identifies and corrects specific error patterns.

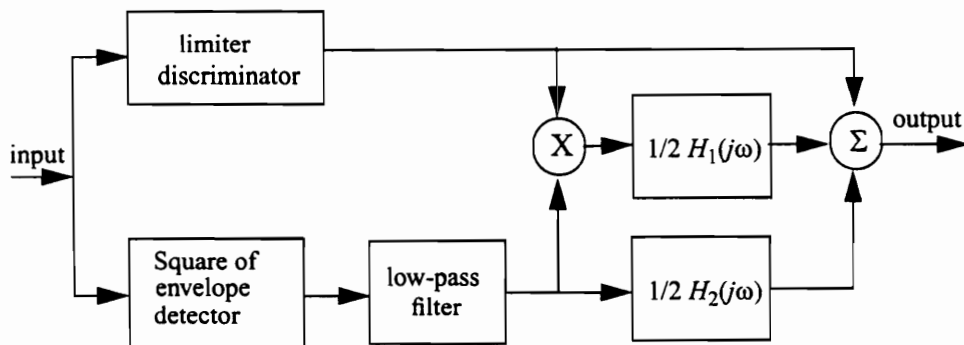


Fig. 2.6 Block diagram of the Stojanovic and Dukic FM demodulator with interference immunity

Generally, back-propagation and radial basis functions are the two methods which are implemented. Radial basis function neural nets provide an effective means of interpolating the desired signal phase from observations of the corrupted phase. Radial basis functions are natural for this application since the phase trajectory tends to be circular.

The application of backpropagation to FM interference rejection is currently being investigated and so far the results are promising [Kha96]. Remarkable interference rejection has been obtained for digital modulated signals, like QAM signals [XB92]. Chen and Mulgrew [CM92] show results of applying the adaptive radial basis function neural net to interference rejection and equalization. The algorithm converges remarkably fast compared even to traditional equalization algorithms. Merits of the neural network over conventional linear filtering and equalization include better rejection of non-Gaussian noise

and interference, and more robust and better compensation of non-linear distortion. On the negative side, with present neural net equalization techniques, there is no guarantee of reaching an optimal solution and the convergence rate can be very slow.

9) Constant Modulus Algorithm (CMA)

Interference and channel distortion will alter the envelope of a constant modulus (envelope) signal. The CMA works by adapting a filter to restore the constant envelope, thereby rejecting the interference and suppressing channel distortion [TA83]. The interference rejection capability is also addressed in literature [Fer85] [KUL92]. The adaptive algorithm distinguishes between target signal and interference on the basis of signal amplitude and envelope shape, given that the envelope of the target signal is approximately known or measurable. A major problem with the CMA is that interference can “capture” the adaptive algorithm resulting in interference enhancement. A spectrum whitening algorithm to initialize the filter weights prior to switching to the CMA is described by Gooch and Daelenbach [GD89] for preventing interference capture. The method requires no knowledge of the received interference scenario and it allows notching of one or more interferers.

Previous tests for AMPS signals using this algorithm show that a simple CMA can not effectively extract the desired signal by only recovering the constant envelope. Too much spectral overlap between the interference and the desired signal prevents the time-invariant filter from recovering the desired signal. However, our research shows that a CMA algorithm can be applied with time-dependent filtering to successfully reject the interference.

Chapter 3. Second Order Cyclostationarity

3.1 Introduction

A signal is a cyclostationary signal of order n if and only if the time fluctuation in n spectral bands with center frequencies that sum to certain discrete nonzero values are statistically dependent in the sense that their joint n th-order moment (the infinite time average of their product in which each factor is shifted in frequency to have a center frequency of zero) is nonzero [Gar94]. In contrast, for many stationary signals, only those bands whose center frequencies sum to zero can exhibit statistical dependency [Gar94]. Cyclostationary waveforms are persistent random waveforms with statistical parameters that vary periodically with time. This topic has been studied since the late 1950s. The term “cyclostationarity” was introduced first by Bennett in 1958 [Bro87] to describe random processes possessing periodic time-variant mean and autocorrelation functions. Recently, there has been extensive research on this topic and this is reflected in the increase in the number of published papers from one per year in 1955 to about twenty five presently [Gar94]. A growing number of research groups, journal editors and program directors at funding agencies have shown real interest in the last five years. Many important contributions to the theory of cyclostationarity have been made by Gardner’s research lab in University of California, Davis and also by many other isolated developments in the last twenty years. This work has emphasized cyclostationary modeling of common communication signals, series representations of cyclostationary random processes, and solutions to the minimum mean-square error linear filtering problem. The concept of cyclostationarity is applicable not only to communications, but also to other fields like climatic variability and econometrics [Bor87]. Cyclostationary properties provide extra information about a signal that can be applied to numerous applications.

Most man-made signals exhibit time periodicity. A time average approach gives rise to a spectral correlation interpretation of cyclostationary characteristics of signals. Erratic

behavior can be removed to reveal underlying nonrandom properties of the time series by forming an appropriate time average of a random quantity of interest. This approach enables generation of spectral lines from the signal by putting it through a non-linear transformation (quadratic transformation). It also explains the fundamental link between the spectral line generation property and the statistical property of spectral correlation. Some signals that can be appropriately modeled as cyclostationary come from the response of a linear or nonlinear system with some periodically varying parameters to a stationary random excitation. Specific examples include:

- stationary random modulation of the amplitudes, phase or frequency of a sinusoidal wave,
- stationary random modulation of the amplitude, width, or positions of pulses in a pulse train,
- periodically varying Doppler shift in a stationary random wave, and
- periodic sampling, multiplexing or coding of stationary random data.

By exploiting the inherent spectral redundancy associated with spectral correlation, various signal processing tasks can be performed, such as: signal detection, weak signal extraction, synchronization and timing recovery, crosstalk interference and noise cancellation, periodically time-variant system identification, and spread spectrum signal despreading. In this chapter we review some of the fundamental mathematical principles used to analyze cyclostationary signals. These mathematical principles are used to design and analyze the proposed interference rejection techniques based on time-dependent filtering.

Linear periodically time-variant system representation or associated optimal filtering issues are discussed by Gardner [Gar93]. The theory and method of cyclic Wiener filtering are generalized from stationary signal filtering by Gardner [Gar93]. The cyclic filters are polyperiodic time-variant linear filters which incorporate frequency-shifting operations as well as the usual frequency-dependent amplitude-weighting and phase-shifting

operations. These frequency-shift filters can separate signals that overlap in frequency as well as in time. Gardner and Reed's research shows that the minimum mean-square-error (MSE) performance of these filters is a function of number of frequency shifts used. It is evaluated for several digital modulated signals with different interference scenarios [Gar93] [RH90]. The spectral redundancy inherent in excess bandwidth can be used effectively to improve system performance. Recent work by Gardner has led to novel FRESH filtering structures that can be blindly adapted using least square (LS), recursive least square (RLS) and least mean square (LMS) algorithms [Gar91]. This involves a prior knowledge of only the modulation types and the values of carrier frequencies or baud rates, without the use of decision, direction, modulus restoral, or demodulation/remodulation methods, all of which exhibit threshold effects. The spectral self-coherence restoral (SCORE) method has been analyzed by Agee and Shell [ASW90]. A property exhibited by most communication signals is that they are correlated with frequency-shifted and possibly conjugated versions of themselves for certain discrete values of frequency shifts. Agee and Shell refer to this property as spectral self-coherence or spectral conjugated self-coherence. It is commonly induced by periodic mixing, or multiplexing operations at the transmitter. Different variations of SCORE algorithms including the basic SCORE algorithm, least square SCORE, cross-SCORE and auto-SCORE have been developed by Agee and Shell [SA88].

3.2 Second Order Cyclostationarity (Wide Sense Cyclostationarity)

The second order theory of a discrete-time stochastic process $x(t)$ deals with the probability space autocorrelation function

$$R_x\left(t - \frac{\tau}{2}, t + \frac{\tau}{2}\right) = E\left[x\left(t - \frac{\tau}{2}\right)x^*\left(t + \frac{\tau}{2}\right)\right], \quad (3.1)$$

where E denotes the expectation in a time average sense as explained in Eq. (3.4) and $*$ the conjugate operation.

For a polycyclostationary (PCS) process $x(t)$, the autocorrelation function is polyperiodic in t for each τ . This means the signal exhibits multiple cyclic frequencies. The associated Fourier series expansion for this function is [Gar94]

$$R_x\left(t - \frac{\tau}{2}, t + \frac{\tau}{2}\right) = \sum_{\{\alpha\}} R_x^\alpha(\tau) e^{j2\pi\alpha t} , \quad (3.2)$$

where $\{\alpha\}$ includes all values of α in the principal domain $(-1/2, 1/2]$. and $R_x^\alpha(\tau)$ is the Fourier coefficient of the additive sine-wave component with frequency α contained in the delay-product signal $R_x(\tau)$. $R_x^\alpha(\tau)$ can be expressed as

$$R_x^\alpha(\tau) = E\left[x\left(t - \frac{\tau}{2}\right)x^*\left(t + \frac{\tau}{2}\right)e^{-j2\pi\alpha t}\right] \quad (3.3)$$

or for a limit cyclic autocorrelation function [Che89]

$$R_x^\alpha(\tau) = \lim_{T \rightarrow \infty} \frac{1}{T} \int_{-\frac{T}{2}}^{\frac{T}{2}} x\left(t - \frac{\tau}{2}\right)x^*\left(t + \frac{\tau}{2}\right)e^{-j2\pi\alpha t} dt . \quad (3.4)$$

$R_x^\alpha(\tau)$ is the definition of analog second order cyclic autocorrelation function, and is related to the polyperiodic correlation function $R_x(\tau)$ as

$$R_x^\alpha(\tau) = E\left[R_x\left(t - \frac{\tau}{2}, t + \frac{\tau}{2}\right)e^{-j2\pi\alpha t}\right] . \quad (3.5)$$

However, for discrete-time signals, delays equal to half the time shift τ are not allowed.

Nevertheless, since [Gar94] shows that

$$E[x(t)x(t-\tau)e^{-j2\pi\alpha t}] = R_x^\alpha(\tau)e^{-j\pi\alpha\tau}, \quad (3.6)$$

the second order cyclic autocorrelation for discrete-time signals can be defined as follows in order to maintain the strongest analogy between the continuous- and discrete-time representations,

$$\tilde{R}_x^\alpha(\tau) = E[x(t)x^*(t-\tau)e^{-j2\pi\alpha t}], \quad (3.7)$$

or for a limit cyclic autocorrelation function [Che89]

$$\tilde{R}_x^\alpha(kT_0) = \lim_{N \rightarrow \infty} \frac{1}{2N+1} \sum_{n=-N}^N x(nT_0)x^*(nT_0+kT_0)e^{-j2\pi\alpha nT_0}, \quad (3.8)$$

where T_0 is the Fourier coefficient period, and k is an integer number.

The conventional autocorrelation function of $x(t)$ is

$$\tilde{R}_x(\tau) = E[x(t)x^*(t-\tau)]. \quad (3.9)$$

Comparing Eq. (3.9) to Eq. (3.7), it is clear that the cyclic autocorrelation at $\alpha=0$ is the conventional autocorrelation. Similarly, the cyclic cross-correlation for $x(t)$ and $y(t)$ are defined as

$$\tilde{R}_{xy}^\alpha(\tau) = E[x(t)y^*(t-\tau)e^{-j2\pi\alpha t}]. \quad (3.10)$$

The cyclic feature of a signal can also be developed in frequency domain in parallel with the time domain. A power spectrum density of $x(t)$ is the Fourier transform of its autocorrelation function. Similarly, the cyclic spectrum density of $x(t)$ is the Fourier transform of its cyclic autocorrelation function,

$$S_x^\alpha(f) = \int_{-\infty}^{+\infty} R_x^\alpha(\tau) e^{-j2\pi f\tau} d\tau . \quad (3.11)$$

For discrete time signal, the integral can be replaced by a summation,

$$\tilde{S}_x^\alpha(f) = \sum_{k=-\infty}^{+\infty} \tilde{R}_x^\alpha(kT_0) e^{-j2\pi f k T_0} . \quad (3.12)$$

For $x(t)$ real, $R_x^\alpha(\tau)$ has even symmetry in τ and $S_x^\alpha(f)$ has even symmetry in f . When $\alpha=0$, we know that the conventional autocorrelation function has the property

$$R_x(0) \geq R_x(\tau) . \quad (3.13)$$

This property can be generalized, for $\alpha \neq 0$, to $R_x(0) \geq R_x^\alpha(\tau)$.

Alternatively, we may characterize second-order periodicity in terms of spectral correlation. Consider the time-variant finite-time complex spectrum of $x(t)$ [Che89],

$$X_T(t, f) = \int_{t-\frac{T}{2}}^{t+\frac{T}{2}} x(u) e^{-j2\pi f u} du , \quad (3.14)$$

which is a measure of local frequency content of $x(t)$ in the interval $[t-T/2, t+T/2]$ with spectral resolution width $1/T$. The complex spectrum $X_T(t, f)$ is then shifted in frequency from f to $f+\alpha/2$ and $f-\alpha/2$, and the temporal correlation of the two shifted complex spectra is given by [Che89]

$$CS_{xT}^{\alpha}(t, f) = \frac{1}{\Delta t} \int_{t-\frac{\Delta t}{2}}^{t+\frac{\Delta t}{2}} \frac{1}{T} X_T\left(s, f - \frac{\alpha}{2}\right) X_T^*\left(s, f + \frac{\alpha}{2}\right) ds . \quad (3.15)$$

Then substituting Eq. (3.14) into Eq. (3.15) and letting $\Delta t \rightarrow \infty$ to remove all randomness, the spectral cross correlation becomes [Che89]

$$\lim_{\Delta t \rightarrow \infty} CS_{xT}^{\alpha}(t, f)_{\Delta t} = \int_{-\frac{T}{2}}^{\frac{T}{2}} R_x^{\alpha}(\tau) \left[1 - \frac{\tau}{T}\right] e^{-j2\pi f\tau} d\tau . \quad (3.16)$$

Finally letting $T \rightarrow \infty$ to obtain unlimited spectral resolution results in [Che89]

$$\lim_{T \rightarrow \infty} \lim_{\Delta t \rightarrow \infty} CS_{xT}^{\alpha}(t, f)_{\Delta t} = S_x^{\alpha}(f). \quad (3.17)$$

Observe from Eq. (3.17) that the cyclic spectrum defined by Eq. (3.11) can be obtained by first measuring the correlation of two spectral components at frequencies $f+\alpha/2$ and $f-\alpha/2$ and then idealizing the correlation by letting $\Delta t \rightarrow \infty$ and $T \rightarrow \infty$. Consequently the cyclic spectrum is called the spectral correlation function.

For an example, let $a(t)$ be a real random low pass signal with the PSD $S_a(f)$ shown in Fig.

3.1(a), which contains no spectral lines. If $a(t)$ is used to modulate the amplitude of a sine wave, an AM signal can be formed as

$$x(t) = a(t)\cos(2\pi f_0 t) , \quad (3.18)$$

whose PSD $S_x(f)$ is given by

$$S_x(f) = \frac{1}{4}S_a(f + f_0) + \frac{1}{4}S_a(f - f_0) , \quad (3.19)$$

as shown in Fig. 3.1(b).

Although the PSD is centered about $f = \pm f_0$, there is no spectral line at $\pm f_0$. The reason for this is that, as shown in Fig. 3.1(b), there is no spectral line in $S_x(f)$ at $f=0$. This means that the DC component is zero, since the strength of any spectral line at $f=0$ is the DC power of the signal $a(t)$.

If this AM signal is passed through a quadratic transform, taking its square, we obtain

$$y(t) = x^2(t) = \frac{1}{2}[a^2(t) + a^2(t)\cos(4\pi f_0 t)] . \quad (3.20)$$

Since $a^2(t)$ is nonnegative, its DC value must be positive. Consequently, the PSD of $x^2(t)$ is

$$S_y(f) = \frac{1}{4}\left[S_{a^2}(f) + \frac{1}{4}S_{a^2}(f + 2f_0) + \frac{1}{4}S_{a^2}(f - 2f_0)\right] . \quad (3.21)$$

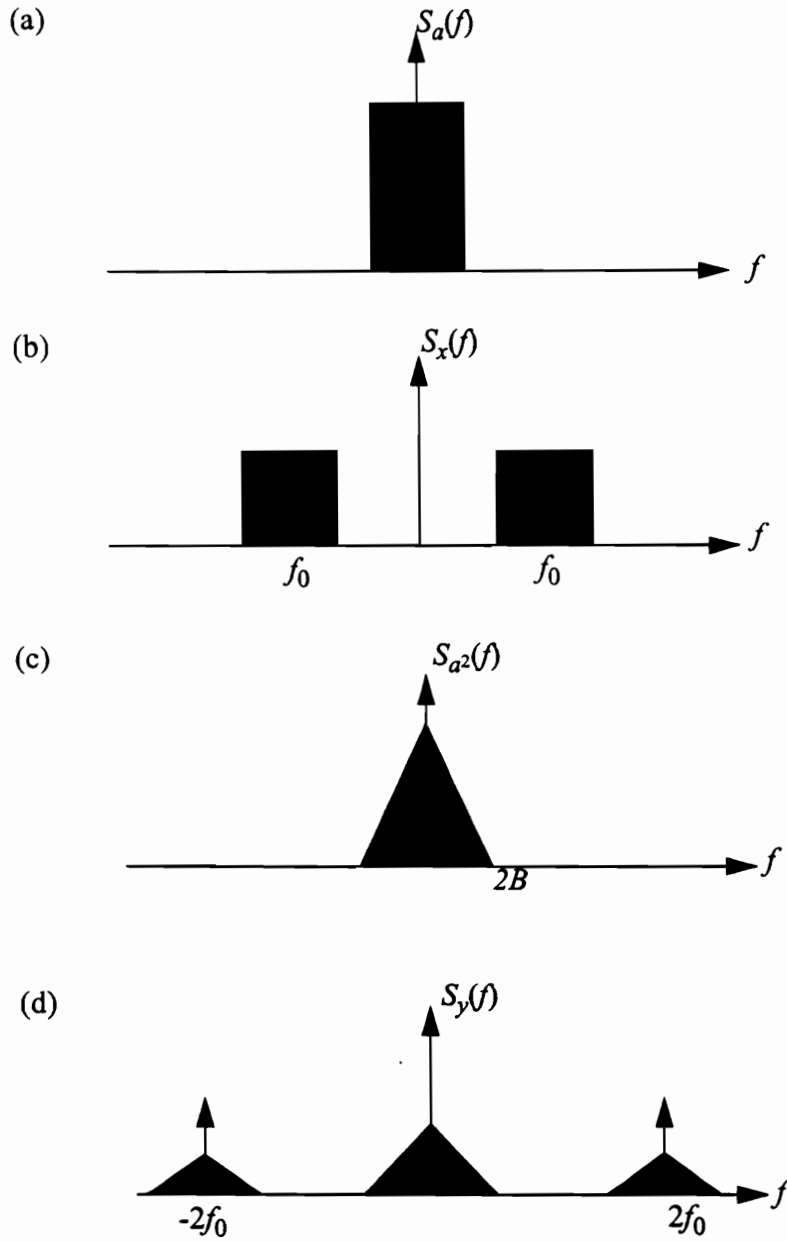


Fig. 3.1 (a) Power spectral density (PSD) of a lowpass signal. (b) PSD of an AM signal (c) PSD of a squared lowpass signal. (d) PSD of a squared AM signal.

It contains a spectral lines at $f=0$, as shown in Fig. 3.1(d) as well as at $f = \pm f_0$. Thus by passing $x(t)$ through a quadratic transformation we have converted the hidden periodicity resulting from the sine-wave factor $\cos(2\pi f_0 t)$ in Eq. (3.20) into a first-order periodicity with associated spectral lines.

If $a(t)$ is a real random stationary signal with zero mean, then

$$E[a(t)] = 0 \quad (3.22)$$

and

$$E[a(t)a^*(t-\tau)] \neq 0 \quad (3.23)$$

$$E[a(t)a^*(t-\tau)e^{-j2\pi\alpha t}] \neq 0, \text{ for all } \alpha \neq 0. \quad (3.24)$$

Eq. (3.22) guarantees that

$$E[a(t)e^{-j2\pi\alpha t}] \equiv 0, \text{ for all } \alpha \neq 0. \quad (3.25)$$

Consider the AM signal $x(t)$, because $a(t)$ contains no finite-strength additive sine-wave components, therefore $x(t)$ contains no finite-strength additive sine-wave components. This means that its power spectral density contains no spectral lines. However, the quadratic form $y(t)$ does contains finite-strength additive sine-wave components with frequencies $\alpha = \pm 2f_0$. These two frequencies are the only non-zero cyclic frequencies. The spectrum consists of only the two cyclic frequencies $\alpha = \pm 2f_0$. and the degenerate cyclic frequency $\alpha=0$ [Gar94].

According to the definition of $R_x^\alpha(\tau)$ in Eq. (3.3), the cyclic autocorrelation of $x(t)$ is

$$R_x^\alpha(\tau) = \begin{cases} \frac{1}{4}R_a(\tau) & \text{for } \alpha = \pm 2f_0 \\ \frac{1}{2}R_a(\tau)\cos(2\pi f_0\tau) & \text{for } \alpha = 0 \\ 0 & \text{otherwise} \end{cases} \quad (3.26)$$

The spectral correlation density function (SCD) for $x(t)$ can be computed from Eq. (3.11), which is the Fourier transform of $R_x^\alpha(\tau)$,

$$S_x^\alpha(f) = \begin{cases} \frac{1}{4}S_a(f) & \text{for } \alpha = \pm 2f_0 \\ \frac{1}{4}S_a(f+f_0) + \frac{1}{4}S_a(f-f_0) & \text{for } \alpha = 0 \\ 0 & \text{otherwise} \end{cases} \quad (3.27)$$

The magnitude of this SCD is depicted in Fig. 3.2 as the height of a surface above the bifrequency plane with coordinates f and α . For purposes of illustration, $a(t)$ is assumed to have an arbitrary low pass PSD for this graph. Observe that although the argument f of the SCD is continuous, as it is always for a random signal, the argument α is discrete, since it represents the harmonic frequencies of periodicities underlying the random time-series. The SCD can be measured by simply passing the signal of interest through two narrow-band bandpass filters with center frequencies at $\alpha+f/2$ and $\alpha-f/2$, and then measure the average power of the correlation between the outputs of the filters. By incorporating many filters whose center frequencies are separated by the bandwidth of the filters, we can partition any spectral band of interest into a set of contiguous narrow disjoint bands. Generally, we simply pass both of the frequency translates $u(t)$ and $v(t)$ of $x(t)$ through a set of bandpass filters, centered at f , and then measure the temporal correlation of the filtered signal to obtain

$$S_y^\alpha(f) = \lim_{B \rightarrow 0} \frac{1}{B} E[(h_B^f(t) \otimes u(t))(h_B^f(t) \otimes v(t))^*] \quad , \quad (3.28)$$

where \otimes denotes convolution.

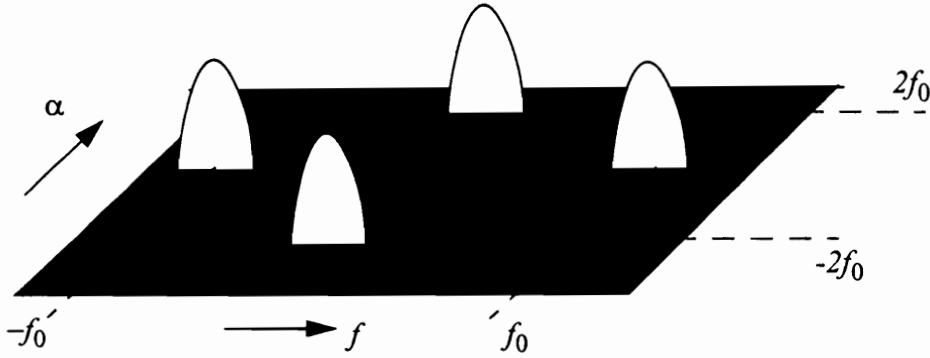


Fig. 3.2 Magnitude of the spectral correlation density function for an AM signal

The process is shown in Fig. 3.3. This yields the spectral correlation density between $u(t)$ and $v(t)$ at frequency f , which is identical to the spectral density of correlation of $x(t)$ at frequencies $f+\alpha/2$ and $f-\alpha/2$. Different measurement techniques for the SCD are developed which are more computationally efficient [Gar86] [RBL91] [BL93].

From the preceding definitions and analysis, cyclostationary signals have a very important property of spectral correlation, which can be utilized to build an optimal linear periodic time-varying filter.

Consider this time-variant filter with impulse response $h(t)$. The Fourier expansion of $h(t)$ is

$$h(t, \tau) = \sum_{n=-\infty}^{+\infty} g_n(\tau) e^{j2\pi\alpha_n t}, \quad (3.29)$$

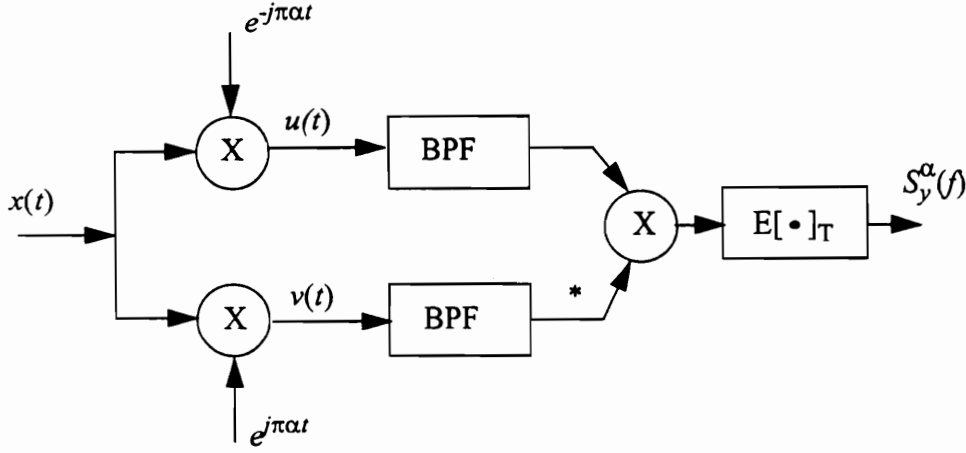


Fig. 3.3 One channel-pair of a spectral correlation analyzer (or a cyclic spectrum analyzer) for measuring the spectral correlation density (or cyclic spectral density).

and so its Fourier transform is [Che89]

$$H(t, f) = \int_{-\infty}^{+\infty} h(t, \tau) e^{-j2\pi f\tau} d\tau = \sum_{n=-\infty}^{+\infty} G_n\left(f + \frac{\alpha_n}{2}\right) e^{j2\pi\alpha_n t}, \quad (3.30)$$

where

$$g_n(\tau) = \int_{-\infty}^{\infty} h(t, \tau) e^{-j2\pi\alpha_n t} dt, \quad (3.31)$$

the corresponding Fourier transform of $g_n(\tau)$ is

$$G_n(t, f) = \int_{-\infty}^{+\infty} g_n(\tau) e^{-j2\pi f\tau} d\tau. \quad (3.32)$$

The output $y(t)$ is the linear convolution of input vector $x(t)$ and the filter impulse response,

$$y(t) = \int_{-\infty}^{+\infty} h(t, u)x(u)du \quad , \quad (3.33)$$

then the following cyclic autocorrelation of $y(t)$ is obtained

$$R_y^\alpha(\tau) = h(t, \tau) \otimes R_x^\alpha(\tau) \otimes h(t, -\tau) \quad . \quad (3.34)$$

By substituting Eq. (3.29) into Eq. (3.34), the cyclic spectrum of $y(t)$ can be found [Gar94]

$$S_y^\alpha(f) = \sum_{n=-\infty}^{+\infty} \sum_{m=-\infty}^{+\infty} G_n\left(f + \frac{\alpha}{2}\right) G_m^*\left(f - \frac{\alpha}{2}\right) S_x^{\alpha - \beta_n + \gamma_m}\left(f - \frac{(\beta_n + \gamma_m)}{2}\right), \quad (3.35)$$

where β_n and γ_m are subsets of the cyclic frequencies for the filter $h(t)$. This equation reveals that the spectral correlation at the output is completely specified by the spectral correlation at the input and the system function $G(t, f)$ of the linear periodic time-variant transformation. Most cyclic frequencies are related to bit rate, symbol rate, baud rate and carrier frequency, etc. (or multiples of these).

3.3 Applications of Cyclostationarity

There are many applications where spectral redundancy associated with the spectral correlation in cyclostationary signals can be exploited. These include:

- detecting the presence of signals buried in the noise and/or severely masked by interference,
- recognizing such corrupted signals according to modulation type,

- estimation of parameters such as time-difference-of arrival at two reception platforms and direction of arrival at a reception array on a signal platform,
- blind-adaptive spatial filtering of signals impinging on a reception array,
- reduction of signal corruption due to co-channel interference and/or channel fading for signal-receiver systems,
- linear periodically time-variant prediction, and
- identification of linear and non-linear systems from input and output measurements.

These application areas benefit from the spectral correlation formulas for AMPS derived in this research work. They are briefly described in the following section.

1) Detection and Classification

It is shown in [Gar87] that modulated signal can have similar spectra but different cyclic spectra. This property can be used for signal classification. Furthermore, signals that overlapped in frequency may not overlap in the cyclic frequency plane and this can be used for detecting co-channel signals.

2) Parameter Estimation

Once the signals have been detected and classified, their carrier frequencies and phases and the keying rate and phase of the signal can be estimated [GS93]. Furthermore, the SCD measurement is also useful, either directly or indirectly, for estimation of synchronization parameters required for the operation of synchronized receivers [Gar94].

3) Time-difference-of-arrival Estimation

Consider a received signal consisting of waveform $x(t)$ for one platform and multiple signals $w(t)$ with different gains and time delays from other platforms,

$$r(t) = x(t) + w(t) + n(t)$$

$$= x(t) + \sum_{l=1}^L a_l s_l(t-t_l) + n(t) \quad , \quad (3.36)$$

where t_l is the time delay and L is the number of multipath components. It can be shown that [Gar94]

$$S_{wx}^{\alpha}(f) = S_{s_l}^{\alpha}(f) a_l e^{-j2\pi\left(f + \frac{\alpha}{2}\right)t_l} \quad (3.37)$$

provided that $s_l(t)$ is the only signal with cyclic frequency α . A weighted least-squares fit with respect to α_l can then be used to estimate the time-delay for the desired signal [GC92].

4) Spatial Filtering

Continuing in the same vein, consider receiving the signals in noise with an antenna array. We can use the signal selectivity properties of cyclostationary signals to blindly adapt a linear combiner to perform spatial filtering. Specifically, by directing the linear combiner to enhance or restore spectral redundancy in its output for a particular cyclic frequency α , the combiner will adapt to null other signals if enough elements are available. No training sequence is required for this adaptation [Gar94].

5) Direction Finding

The results of spatial filtering can be used to obtain high resolution of direction of arrival. This is achieved by detecting the desired signal with a spatial filter and then adjusting the antenna weights to locate the source of the signal [SG93].

6) System Identification

The cyclostationary property of signals passing through a linear time-invariant system can be utilized in several ways to identify the system whose input signals are corrupted by

noise and interfering signals [Gar94].

7) Signal Extraction

Spectrally redundant signals that are corrupted by interfering signals can be more effectively extracted in some applications through the use of periodic or multiple-periodic linear time-varying filters, instead of the more common time-invariant filter. The frequency shifted spectrum is strongly correlated with the unshifted one and the time-dependent filter exploits this spectral redundancy to extract the desired signal. Generally, a time-invariant filter can only attenuate both the desired signal and the interference in the corrupted portion of the band, while a time-variant filter can replace the corrupted components of the signal of interest with spectral components from other parts of the band that are highly correlated with the desired components. For instance, if the main spectrum of the desired signal is corrupted by narrowband interference, the signal can be reconstructed by using the uncorrupted redundant frequency components. This is a very powerful technique for narrowband interference rejection for spread spectrum signals. Even if the full spectrum of desired signal is corrupted by interference, the desired signal can still be enhanced as long as the signal has a cyclic frequency that is distinct from that of the interfering signal. This property is exploited by the algorithm developed in this research.

Chapter 4. Cyclostationarity of AMPS Signals

4.1 AMPS Background

Early mobile radio systems pursued the objective of obtaining as large a coverage area as possible by using a single high powered transmitter with a tall antenna tower. In the early stages of development of mobile communications, the issue of coverage area was of prime concern. But as mobile radio became popular, demand increased and this led to new challenging problems like spectral congestion and interference limitations on user capacity. As the number of users increased, allocated frequency bands were often exhausted and new means were sought to accommodate the growing number of users. The cellular concept is a system level idea which calls for replacing a single high power base station with many low power base stations, each providing coverage only to a small portion of the service area. Each cellular base station is allocated a group of radio channels to be used within a small geographic area called a cell. Base stations in adjacent cells are assigned channel groups which contain completely different channels than those of the neighboring cells. A cluster is formed from a group of cells that cover the whole allocated frequency spectrum. The frequency band assignments for a particular cluster can be replicated for an adjacent cluster. A cell is typically represented by a hexagonal shaped area. A group of cells covering the whole radio band is called a cluster. The hexagonal cell shape map, as shown in Fig. 4.1, is a conceptual and a simplistic model of the coverage region for each base station. The actual radio coverage for a cell is also known as the “footprint”, and is determined from field measurements or propagation models. A cell must be designed to serve the weakest mobiles within the footprint, and these are typically located at the edge of the cell. For the current AMPS system [You79], the assigned frequency band is 824-849MHz for reverse channel and 869-894MHz for forward channel. Each cell has 57 channels with 30kHz separation and seven cells with 399 channels compose a cluster. These channels include both the voice links and the control links.

Fig. 4.1 illustrates some of the fundamental problems associated with frequency reuse technique. The frequency spectrum allocated in cluster C is reused in the adjacent cluster RC. Because the center frequencies for the two cells C1 and RC1 are the same, co-channel interference can occur. The distance between the cell and its co-channel cell depends on the local geography. For an acceptable voice signal in the AMPS system, the carrier to interference ratio must be kept above 18dB and this is obtained using a seven cell reuse pattern. Co-channel interference may become critical when the mobile unit is far away from its home base station, or the interfering signal is very strong. Co-channel interference cancellation is difficult since the spectra of the SOI and the SNOI are overlapped to a high degree.

One of the methods to circumvent the problem of co-channel interference is to use a fixed tone in the modulated voice signal. This supervisory auto tone (SAT) is used by a base station to identify the desired signal from an interfering one. For the current AMPS system, three frequencies are allocated for SAT signaling: 5970Hz, 6000Hz, and 6030Hz.

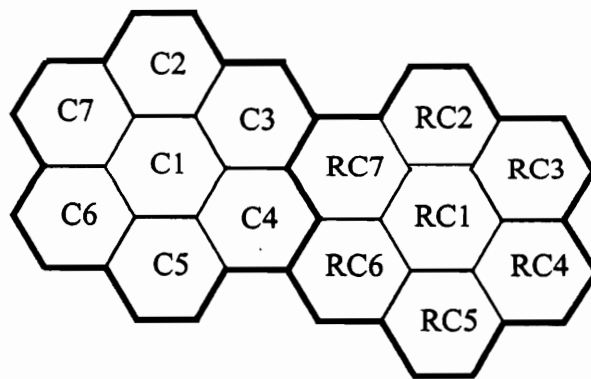


Fig. 4.1 Seven cell reuse concept

The cell site sends a SAT and receives a returned SAT from the mobile. If the SATs are the same, the cell site will complete the loop. Otherwise, the cell site interprets the incom-

ing RF power as being corrupted by interference for both the forward and the reverse channels. Each cluster has seven cells and each cluster is assigned one of these SAT frequencies. Thus the three-SAT scheme provides supervisory reliability by reducing the probability of misinterpreting interference as the desired signal.

4.2 Cyclostationarity of AMPS Signal

The cyclostationary behavior of a signal, as discussed in Chapter 3, is characterized by a periodic spectrum.

The SAT is a simple tone that is transmitted with the voice signals. The maximum FM deviation produced by the SAT is 2kHz, thus it is easily removed by the demodulator [You79].

The signal model of an AMPS signal containing a SAT can be expressed as

$$x(t) = \text{Real} \left\{ e^{j \left\{ \omega_c t + 2\pi\beta f_m \int_{-\infty}^t v(t) dt + k \sin(2\pi f_{sat} t) \right\}} \right\}, \quad (4.1)$$

or as

$$x(t) = \text{Real} \left\{ e^{j \left\{ \omega_c t + 2\pi\beta f_m \int_{-\infty}^t v(t) dt \right\}} e^{j \{ k \sin(2\pi f_{sat} t) \}} \right\}. \quad (4.2)$$

Parameters for the signal model are as follows:

- ω_c : carrier frequency.
- β : voice $v(t)$ modulation index which is 3 for AMPS.
- f_m : maximum voice frequency which is 4kHz (the amplitude of voice is normalized).
- k : modulation index for the SAT which is 1/3.
- f_{sat} : frequency of the SAT which is either 5970Hz, or 6000Hz, or 6030Hz.

This signal model can be used to determine the cyclic spectrum of the AMPS signal and the nature of this spectrum provides insight into the design of the time-dependent filter.

An AMPS signal without the SAT can be represented as

$$s(t) = e^{j\left\{\omega_c t + 2\pi\beta f_m \int_{-\infty}^t v(t) dt\right\}}. \quad (4.3)$$

The term $e^{j\{k\sin(2\pi f_{sat}t)\}}$ can be expanded using Bessel functions:

$$e^{j\{k\sin(2\pi f_{sat}t)\}} = \sum_{n=-\infty}^{+\infty} J_n(k) e^{jn2\pi f_{sat}t}, \quad (4.4)$$

where $J_n(k)$ are Bessel functions of order n and can be expressed as

$$J_n(k) = \frac{1}{2\pi} \int_{-\pi}^{+\pi} e^{jk\sin(2\pi f_{sat}t)} e^{-jn2\pi f_{sat}t} d(2\pi f_{sat}t). \quad (4.5)$$

Note that n is an integer and

$$J_n(k) = \begin{cases} J_{-n}(k) & n \text{ is even} \\ -J_{-n}(k) & n \text{ is odd} . \end{cases}$$

According to the definition in [Gar94], the cyclic autocorrelation is expressed as

$$R_{xx}^\alpha(\tau) = \lim_{T \rightarrow \infty} \int_{-\frac{T}{2}}^{\frac{T}{2}} x\left(t - \frac{\tau}{2}\right) x^*\left(t + \frac{\tau}{2}\right) e^{-j2\pi\alpha t} dt . \quad (4.6)$$

Substitute (4.2) and (4.4) into the definition of $R_{xx}^\alpha(\tau)$ in Eq. (4.6) [HR94],

$$R_{xx}^\alpha(\tau) = R_{ss}(\tau) \sum_{n=-\infty}^{+\infty} \sum_{m=-\infty}^{+\infty} J_n(k) J_m(k) e^{-j2\pi f_{sat} \frac{(n+m)}{2} \tau} \delta((n-m)f_{sat} - \alpha) \quad (4.7)$$

and the cyclic spectrum, which is the Fourier transform of $R_{xx}^\alpha(\tau)$ is

$$\begin{aligned} S_{xx}^\alpha(f) &= \int_{-\infty}^{+\infty} R_{xx}^\alpha(\tau) e^{-j2\pi f\tau} d\tau \\ &= \sum_{n=-\infty}^{+\infty} \sum_{m=-\infty}^{+\infty} J_n(k) J_m(k) S_{ss}\left(f + \frac{n+m}{2} f_{sat}\right) \delta((n-m)f_{sat} - \alpha) , \end{aligned} \quad (4.8)$$

where $R_{ss}^\alpha(\tau)$ is the autocorrelation of $s(t)$ in Eq. (4.3), and $S_{ss}(f)$ is the spectrum of the voice portion of the AMPS FM signal (SAT excluded). Only certain combinations of n and m that satisfy $\alpha = (n-m)f_{sat}$ will contribute to the summation in Eq. (4.7) and Eq. (4.8). The conventional spectrum consists of replicated versions of the original FM voice signal spectrum (excluding the SAT) scaled with different weights determined by products of

Bessel coefficients and is shown in Fig. 4.2. The spectrum correlation density function of this AMPS signal is shown in Fig. 4.3.

The generation of the AMPS FM signal incorporating the SAT is depicted in Fig. 4.4. The block begins with an A/D converter which samples the voice signal at 8192 Hz. The sampled signal is compressed at 2:1 ratio by a syllabic compressor. For every 2dB change in the input level, this 2:1 compressor changes the output level a nominal 1dB. The compressor serves two purposes: to confine the energy in the channel bandwidth and to generate a quieting effect during a speech pulse. The pre-emphasis must have a nominal +6dB per octave response between 300Hz and 3000Hz. The propagation channel is reflected by the inclusion of external factors such as AWGN, multipath, fading, and co-channel interference. For the demodulator, the expanding and de-emphasis are used to recover the original voice signal. Co-channel interference is generated the same way but has a different carrier frequency, fading, multipath delay and gain, and noise power.

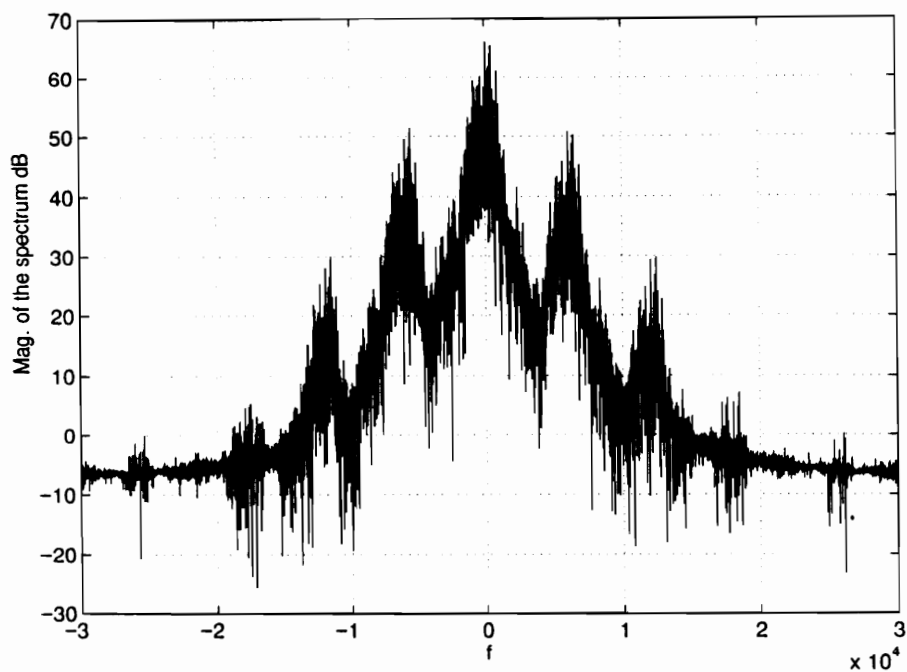


Fig. 4.2 Conventional spectrum of AMPS signal with SAT

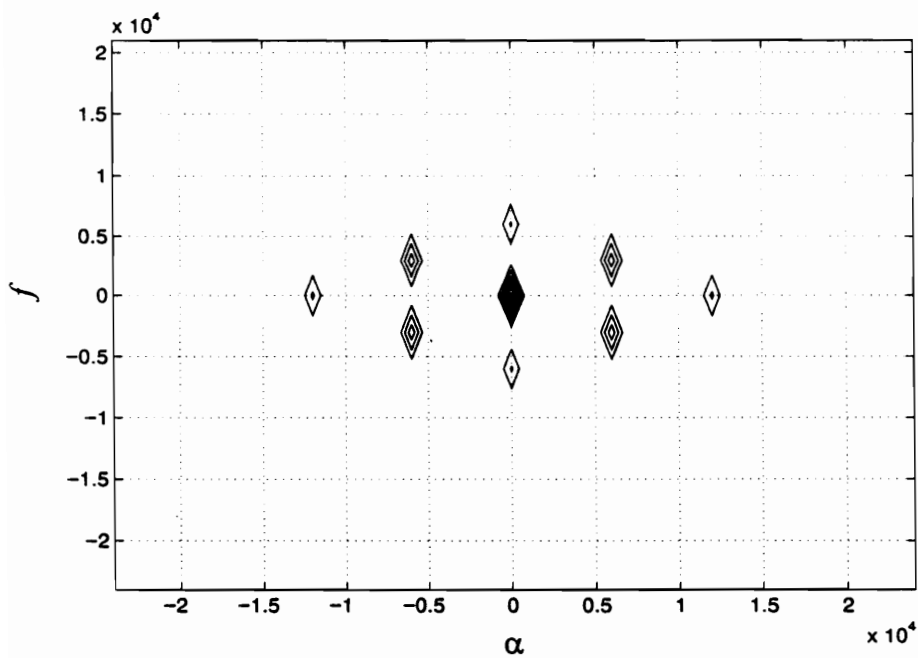


Fig. 4.3 Contour of spectrum correlation density function $S_x^\alpha(f)$ for AMPS signal with a SAT

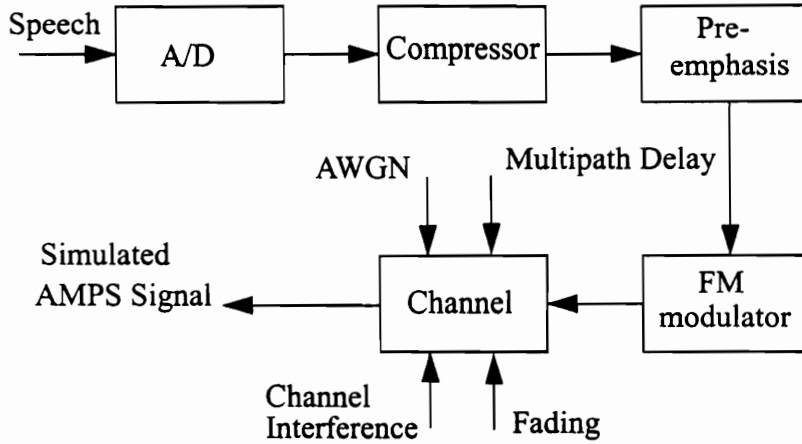


Fig. 4.4 AMPS signal generator

4.3 Cyclic Feature for AMPS Signals in Different Channels

The mobile environment distorts the signal in several ways and this distortion is dynamic. These distortions include:

- AWGN,
- interference,
- multipath, and
- fading.

The effects of these sources of distortion on the spectral correlation characteristics are described below.

A) AWGN Channel

If a zero-mean white Gaussian noise $n(t)$ is added to the SOI, the received signal is

$$\begin{aligned}
r(t) &= x(t) + n(t) \\
&= s(t)e^{j\{k\sin(2\pi f_{sat}t)\}} + n(t) \quad .
\end{aligned}
\tag{4.9}$$

The cyclic autocorrelation for $r(t)$ can be computed according to Eq. (4.6)

$$R_{rr}^{\alpha}(\tau) = R_{xx}^{\alpha}(\tau) + E\left[n\left(t - \frac{\tau}{2}\right)n^*\left(t + \frac{\tau}{2}\right)e^{-j2\pi\alpha t}\right] , \tag{4.10}$$

since the noise is a stationary random process, the second part will be zero for $\alpha \neq 0$ if a very large number of samples are used to perform the averaging, i. e.,

$$R_{rr}^{\alpha}(\tau) = R_{xx}^{\alpha}(\tau) . \tag{4.11}$$

In general, the cyclic spectrum of the received AMPS signal can be expressed as

$$R_{rr}^{\alpha}(\tau) = R_{ss}(\tau) \sum_{n=-\infty}^{+\infty} \sum_{m=-\infty}^{+\infty} J_n(k)J_m(k)e^{-j2\pi f_{sat}\frac{(n+m)}{2}\tau} \delta((n-m)f_{sat} - \alpha) + \sigma_n^2\delta(\alpha) , \tag{4.12}$$

where σ_n^2 is the power density of the noise. It can be seen from Eq. (4.12) that the conventional autocorrelation function ($\alpha = 0$) of the received signal consists of both the desired signal and the additive noise, while the cyclic autocorrelation function ($\alpha \neq 0$) only depends on the desired signal. The $R_{rr}^{\alpha}(\tau)$ is measured for an AMPS signal embedded in noise using 10^4 data points. The measured $R_{rr}^{\alpha}(\tau)$ is plotted in Fig. 4.5 as a function of carrier to noise ratio CNR and τ . It can be seen that the magnitude of $R_{rr}^{\alpha}(\tau)$ does not vary too much for different CNR s. For infinite data, it is an constant.

B) Co-channel Interference Corrupted Channel

A co-channel interfering signal (SAT excluded) can be expressed as

$$c(t) = ae^{j\left\{\omega_{cc}t + 2\pi\beta f_m \int_{-\infty}^t v_c(t)dt\right\}}, \quad (4.13)$$

where a is the amplitude of the interfering signal $c(t)$ and ω_{cc} is the carrier of the cochannel interference. Let f_{satc} represent the SAT frequency of the signal not of interest (SNOI) which is constrained to be different than that of the signal of interest (SOI). The combined signal is

$$r(t) = s(t)e^{j\{k\sin(2\pi f_{sat}t)\}} + c(t)e^{j\{k\sin(2\pi f_{satc}t)\}}. \quad (4.14)$$

Substituting Eq. (4.14) into the definition of the cyclic autocorrelation function in Eq. (4.6) results in

$$\begin{aligned} R_{rr}^\alpha(\tau) = & E\left[s\left(t-\frac{\tau}{2}\right)s^*\left(t+\frac{\tau}{2}\right) \sum_{n=-\infty}^{+\infty} \sum_{m=-\infty}^{+\infty} J_n(k)J_m(k)e^{j2\pi((n-m)f_{sat}-\alpha)t} e^{-j2\pi(n+m)f_{sat}\frac{\tau}{2}}\right] \\ & + E\left[c\left(t-\frac{\tau}{2}\right)c^*\left(t+\frac{\tau}{2}\right) \sum_{n=-\infty}^{+\infty} \sum_{m=-\infty}^{+\infty} J_n(k)J_m(k)e^{j2\pi((n-m)f_{satc}-\alpha)t} e^{-j2\pi(n+m)f_{satc}\frac{\tau}{2}}\right] \\ & + E\left[s\left(t-\frac{\tau}{2}\right)c^*\left(t+\frac{\tau}{2}\right) \sum_{n=-\infty}^{+\infty} \sum_{m=-\infty}^{+\infty} J_n(k)J_m(k)e^{j2\pi(nf_{sat}-mf_{satc}-\alpha)t} e^{-j2\pi(nf_{sat}+mf_{satc})\frac{\tau}{2}}\right] \\ & + E\left[c\left(t-\frac{\tau}{2}\right)s^*\left(t+\frac{\tau}{2}\right) \sum_{n=-\infty}^{+\infty} \sum_{m=-\infty}^{+\infty} J_n(k)J_m(k)e^{j2\pi((-nf_{sat}+m)f_{satc}-\alpha)t} e^{-j2\pi((-nf_{sat}-m)f_{satc})\frac{\tau}{2}}\right]. \end{aligned} \quad (4.15)$$

It is assumed that the two voice signals $v(t)$ and $v_c(t)$ are uncorrelated random processes.

Based on this assumption, the first expectation in Eq. (4.15) can be simplified as

$$R_{ss}^{\alpha}(\tau) \sum_{-\infty}^{+\infty} \sum_{-\infty}^{+\infty} J_n(k) J_m(k) e^{-j2\pi(n+m)f_{sat}\frac{\tau}{2}}, \quad (4.15.1)$$

which is equal to $R_{xx}^{\alpha}(\tau)$, the desired signal cyclic autocorrelation function. The third and fourth expectations in Eq. (4.15) are neglected because $v(t)$ and $v_c(t)$ are not correlated. In short, the cyclic autocorrelation of the co-channel interference corrupted received signal is the summation of the cyclic autocorrelation function of both the SOI and the SNOI. The parameter α which produces non zero $R_{rr}^{\alpha}(\tau)$, determines the filter periodicities of the optimal filter. If α is chosen to be the cyclic frequency corresponding to the desired signal and the SOI and the SNOI have different cyclic frequencies, then the contribution of the cyclic autocorrelation of the co-channel interference is zero and the cyclic autocorrelation of the received signal only depends on the desired signal. The cyclic autocorrelation function is measured for a desired AMPS signal (SOI) using 10^4 data points and its magnitude is shown in Fig. 4.6. The cyclic frequency is chosen to correspond to the SOI. It can be seen from Fig. 4.6 that the magnitude of $R_{rr}^{\alpha}(\tau)$ is still very high even for a low CIR.

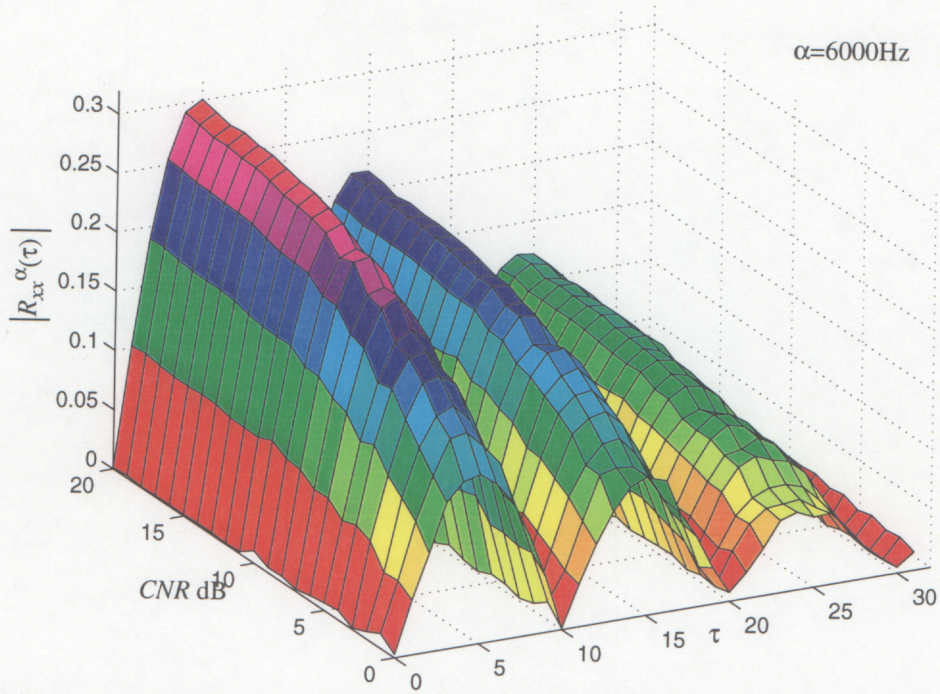


Fig. 4.5 Magnitude of the cyclic autocorrelation coefficients for AMPS signal with noise

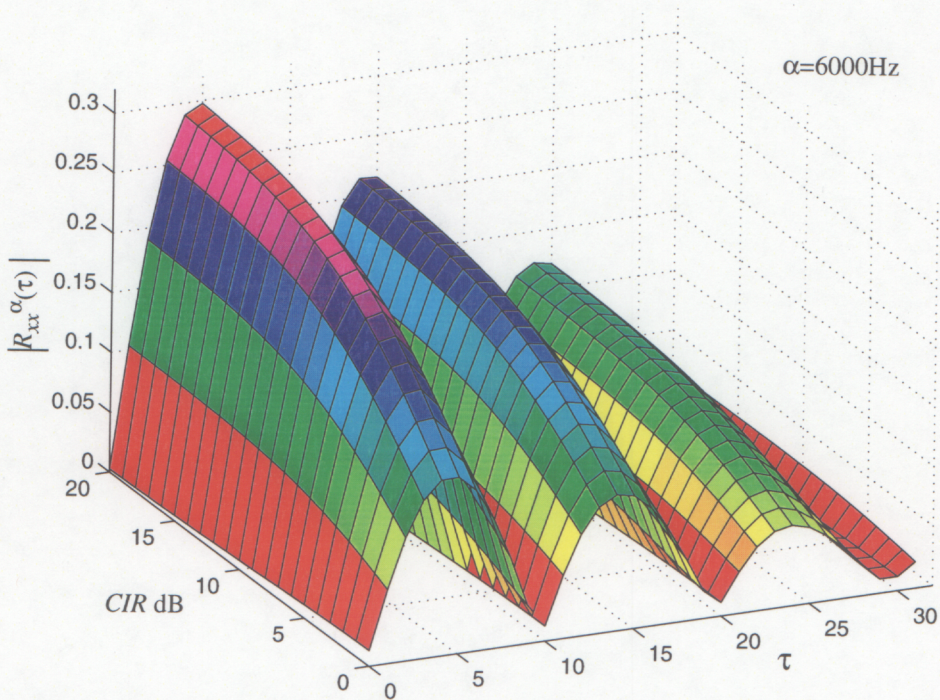


Fig. 4.6 Magnitude of the cyclic autocorrelation coefficients for SOI and SNOI ($\alpha=kf_{sat}$)

C) *Fading and Multipath Channel*

In mobile radio, fading and Doppler shifts arise as a result of motion of the receiver through a spatially-varying field. Multipath propagation arises from the fact that the transmitted signal is scattered by different sources, resulting in these reflected components combining with different amplitudes and time delays at the receiver. The effect of multipath propagation is to produce a received signal with an amplitude that changes substantially with location and time. If either the transmitter or receiver is in motion, each of the components of the received signal experiences a Doppler shift, the frequency shift being related the spatial angle α_n between the direction of arrival of that component and the direction of vehicle motion. For a vehicle moving at a constant speed v , the Doppler shift f_n of the n th plane-wave component is

$$f_n = \frac{v}{\lambda} \cos \alpha_n. \quad (4.16)$$

It can be seen that the waves approaching the vehicle in the front experience a positive Doppler frequency shift (maximum value $f_m = v/\lambda$) while those from behind experience a negative frequency shift. If we assume that the fraction of the incident power contained within a spatial angle between α and $-\alpha$ for an omnidirectional antenna is uniformly distributed in the angular range $(-\pi, \pi)$, the RF Doppler spectrum becomes [PG89]

$$S_E(f) = \frac{1.5}{\pi f_m} \left[1 - \left(\frac{f - f_c}{f_m} \right)^2 \right]^{\frac{1}{2}}, \quad (4.17)$$

where f_c is the RF carrier frequency. If there is a dominant component in the incoming signal, then this has a substantial influence on the signal spectrum. Such a component arriving at an angle α_0 gives rise to a spectral line at $f_c + f_m \cos \alpha_0$ in the RF spectrum, and two additional peaks at $f_m(1 \pm \cos \alpha_0)$ in the baseband spectrum.

Different multipath components combine to produce a resultant interference pattern consisting of a series of constructive and destructive interference sources. For time intervals dominated by constructive interference, the signal level is enhanced whereas in time intervals dominated by destructive interference, the signal strength is greatly diminished. As a mobile unit travels, the received signal varies accordingly. The received signal is said to undergo fading as it encounters a period of destructive interference. The fading envelope directly affects receiver performance. It is useful to consider the average rate at which the envelope crosses a given level and how long it remains below that level. The Rayleigh fading envelope only occasionally experiences very deep fades, for example, 30dB fades occur for only 0.1% of the time [Par89]. However, for cases of radio propagation through the ionosphere, the random nature of the channel can modify the cyclostationary properties of the received signal. If the time response of the channel impulse is $h(t, \tau)$, then the frequency response $H(t, f)$ can be expressed as

$$H(t, f) = \int_{-\infty}^{\infty} h(t, \tau) e^{-j2\pi f\tau} d\tau . \quad (4.18)$$

When a cyclostationary signal $x(t)$ passes through a fading channel with impulse response of $h(t, \tau)$, the output signal $x_f(t)$ can be expressed as:

$$x_f(t) = \int_{-\infty}^{\infty} h(t, \tau) x(t - \tau) d\tau , \quad (4.19)$$

where the baseband impulse response of a multipath channel can be expressed as [Rap96]:

$$h_b(t, \tau) = \sum_{i=0}^{N-1} a_i(t, \tau) e^{(j2\pi f_c \tau_i(t) + \phi_i(t, \tau))} \delta(\tau - \tau_i(t)) . \quad (4.20)$$

In Eq. (4.20), $a_i(t, \tau)$ and $\tau_i(t)$ are the real amplitudes and excess delays of i th multipath component at time t , and N is the total number of multipath components for the channel. The multipath effects cause the transmitted signal undergo different fading channels, and the cyclic feature of the transmitted signal will be modified accordingly. These modifications are discussed in the following sections.

1) Flat Fading Channel

In a mobile radio environment, the statistical time varying feature of the received signal envelope for flat fading is usually described by the Rayleigh distribution given in Eq. (4.21).

$$p(a) = \begin{cases} \frac{a}{\sigma^2} e^{-\frac{a^2}{2\sigma^2}} & 0 \leq a < \infty \\ 0 & a < 0 \end{cases} \quad (4.21)$$

Each individual multipath component can also be described by the Rayleigh distribution. To explain and model the statistical nature of the mobile channel, different multipath models have been developed. Among all these models, Clarke's model which is based on the scattering theory is widely used [Rap96]. The flat fading and two-ray Rayleigh fading channel are simulated using this model in our research.

Since the bandwidth of an AMPS signal is 30kHz, which is usually narrower than the radio channel bandwidth of several hundred kilohertz, flat fading is the principle fading distortion. In other words, the spectrum of the AMPS signal is preserved in a fading channel, but the signal power varies with time. This results in large amplitude fluctuations at the receiver due to the phase shifts of the many unresolved multipath components. Sometimes, flat fading is also called amplitude varying fading. The small scale fading can be described by [Rap96]:

$$h_b(t, \tau) = a(t)e^{j\phi(t)}\delta(\tau), \quad (4.22)$$

where $a(t)$ is Rayleigh distributed and $\phi(t)$ is uniformly distributed over $(-\pi, \pi]$. Thus, the received signal in Eq. (4.19) for the flat fading channel (free space) can be simplified as:

$$x_f(t) = a(t)x(t)e^{j\phi(t)}. \quad (4.23)$$

The procedure of generating a flat fading signal is shown in Fig. 4.7 [Rap96]. Two independent Gaussian random noise signals are filtered separately by a Doppler filter with magnitude equal to the Doppler spectrum in Eq. (4.17). The filtered signals are mixed with the carriers before they form a complex random signal, which has a Rayleigh-distributed envelope and a normally-distributed phase. An envelope detector is used to obtain the fading amplitude.

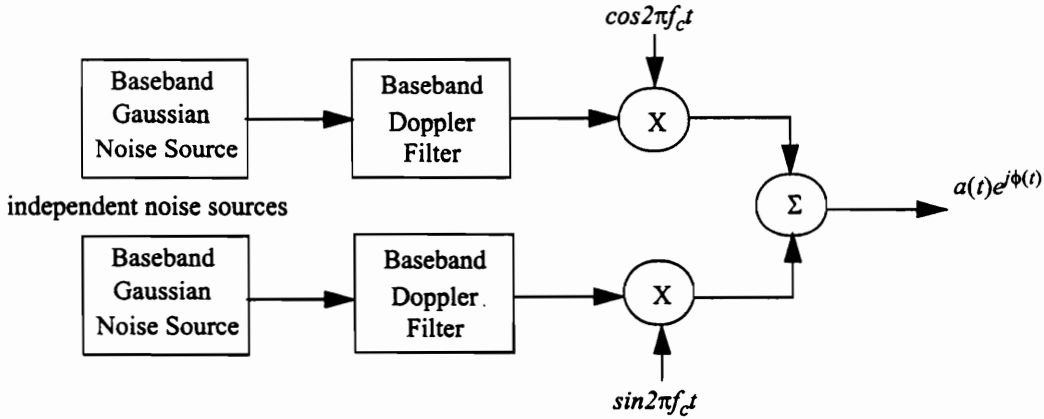


Fig. 4.7 Flat fading generation using baseband Doppler filter

The cyclic autocorrelation of the flat faded signal $x_f(t)$ can be computed using Eq. (4.6) and Eq.(4.23)

$$\begin{aligned}
 R_{x_f x_f}^\alpha(\tau) &= \lim_{T \rightarrow \infty} \int_{-\frac{T}{2}}^{\frac{T}{2}} x_f\left(t - \frac{\tau}{2}\right) x_f^*\left(t + \frac{\tau}{2}\right) e^{-j2\pi\alpha t} dt \\
 &= E \left[a\left(t - \frac{\tau}{2}\right) a^*\left(t + \frac{\tau}{2}\right) x\left(t - \frac{\tau}{2}\right) x^*\left(t + \frac{\tau}{2}\right) e^{-j2\pi\alpha t} e^{j\phi_1\left(t - \frac{\tau}{2}\right)} e^{-j\phi_2\left(t + \frac{\tau}{2}\right)} \right].
 \end{aligned}
 \tag{4.24}$$

If the transmitted signal and the Rayleigh distributed random signal are independent, the above equation can be simplified to:

$$R_{x_f x_f}^\alpha(\tau) = E \left[a\left(t - \frac{\tau}{2}\right) a^*\left(t + \frac{\tau}{2}\right) e^{j\phi_1\left(t - \frac{\tau}{2}\right)} e^{-j\phi_2\left(t + \frac{\tau}{2}\right)} \right] R_{xx}^\alpha(\tau),
 \tag{4.25}$$

assuming that the signal is a cyclo-ergodic process. To compute the autocorrelation of the electric field signal, we first need correlations and moments of the in-phase and quadrature components of the signal. Define

$$\begin{aligned}
 a(t) e^{j\phi(t)} &= T_c(t) + jT_s(t) \\
 E \left[T_c\left(t - \frac{\tau}{2}\right) T_c\left(t + \frac{\tau}{2}\right) \right] &= E \left[T_s\left(t - \frac{\tau}{2}\right) T_s\left(t + \frac{\tau}{2}\right) \right] = g(\tau) \\
 E \left[T_c\left(t - \frac{\tau}{2}\right) T_s\left(t + \frac{\tau}{2}\right) \right] &= -E \left[T_s\left(t - \frac{\tau}{2}\right) T_c\left(t + \frac{\tau}{2}\right) \right] = h(\tau)
 \end{aligned}
 \tag{4.26}$$

where [Jak74]

$$g(\tau) = \int_{f_c - f_m}^{f_c + f_m} S_i(f) \cos(2\pi(f - f_c)\tau) df,$$

$$h(\tau) = \int_{f_c - f_m}^{f_c + f_m} S_i(f) \sin(2\pi(f - f_c)\tau) df, \quad (4.27)$$

and $S_i(f)$ is the input spectrum defined in Eq. (4.17) (electric field) for $f_c - f_m < f < f_c + f_m$.

It can be shown that $h(\tau) = 0$ for all three field components which is a consequence of the symmetry of the spectra about f_c . Also for the electric field, we have [Jak74]

$$g(\tau) = b_0 J_0(2\pi f_m \tau), \text{ with } b_0 = \frac{3E_0^2}{4}, \quad (4.28)$$

where J_0 is the zero order first kind Bessel function. Defining the autocorrelation of the electric field signal as $\Gamma(\tau)$, it is not difficult to show that

$$\begin{aligned} \Gamma(\tau) &= E \left[a\left(t - \frac{\tau}{2}\right) a^*\left(t + \frac{\tau}{2}\right) e^{j\phi_1\left(t - \frac{\tau}{2}\right)} e^{-j\phi_2\left(t + \frac{\tau}{2}\right)} \right] \\ &= H_0^2 J_0(2\pi f_m \tau), \text{ where } H_0^2 = \frac{3E_0^2}{2}. \end{aligned} \quad (4.29)$$

The Bessel function of the first kind J_0 can be expanded using a infinite sequence summation as described below

$$J_0(x) = \sum_{m=0}^{\infty} (-1)^m \frac{x^{2m}}{2^{2m} m!^2}. \quad (4.30)$$

For a small value of x , Eq. (4.29) can be approximated as

$$\begin{aligned}\Gamma(\tau) &\approx H_0^2(1 - (\pi f_m \tau)^2) \\ &\approx H_0^2 e^{-\frac{\tau^2}{\tau_0^2}}, \text{ where } \tau_0 = \frac{1}{\pi f_m}.\end{aligned}\quad (4.31)$$

Eq. (4.29) and its approximation in Eq. (4.31) are plotted as a function of t in Fig. 4.8 and are represented by the solid line and the dash line, respectively. To validate Eq. (4.29), 12000 samples of simulated data using the fading generator described in Fig. 4.7 are used to numerically compute $\Gamma(\tau)$ and the results are plotted in Fig. 4.8 by the dash-dot line. From Fig. 4.8, it can be seen that the result using the simulated data is very close to the theoretical results. For small delay samples, such as $\tau < 300$ samples, the approximation in Eq. (4.31) fits both the theoretical and the simulated results well. In fact, large delays will not be considered in the filter design since the cyclic autocorrelation of $R_{xx}^2(\tau)$ diminishes dramatically after a delay of 300 samples.

Substituting Eq. (4.31) into Eq. (4.25), the cyclic autocorrelation function of a flat faded signal is

$$R_{x_f x_f}^\alpha(\tau) \approx |H_0|^2 e^{-\frac{\tau^2}{\tau_0^2}} R_{xx}^\alpha(\tau), \quad (4.32)$$

where τ_0 is the decorrelation time and is proportional to the fading rate. A large value of τ_0 corresponds to slow fading conditions or long fading durations. The power spectral density of the fading signal can be obtained by simply applying the Fourier transform to Eq. (4.29) and is given by

$$S_f(f) \approx |H_0|^2 \sqrt{\pi} \tau_0 e^{-\frac{f^2}{f_m^2}}, \quad (4.33)$$

where the approximation is from the Bessel function expansion in Eq. (4.30). The cyclic spectrum of the signal undergoing flat fading then can be calculated as follows:

$$S_{x_f x_f}^{\alpha}(f) = \int_{-\infty}^{\infty} S_f(v) S_{xx}^{\alpha}(f-v) dv ,$$

and its approximated value can be found by applying Eq. (4.33), which is

$$S_{x_f x_f}^{\alpha}(f) \approx |H_0|^2 \sqrt{\pi} \tau_0 \int_{-\infty}^{\infty} e^{-\frac{v^2}{f_m^2}} S_{xx}^{\alpha}(f-v) dv . \quad (4.34)$$

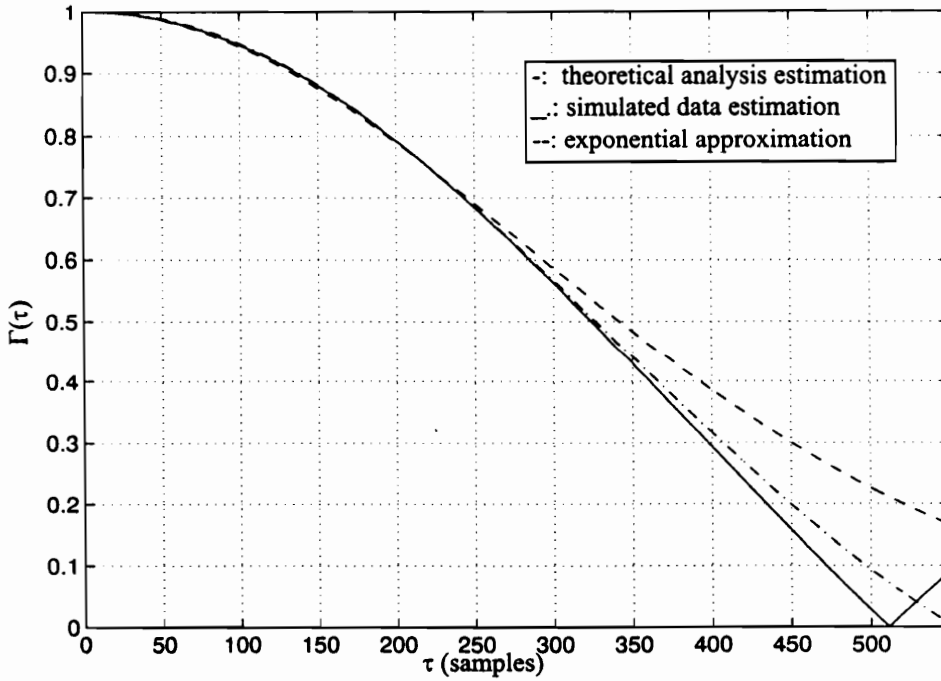


Fig. 4.8 Comparison of $\Gamma(\tau)$ using different measuring methods

Note that Eq. (4.32) and Eq. (4.34) hold only with the assumption that the incoming power

is uniformly distributed in angle. Also, the statistical characteristics of a faded signal are different than that of the envelope of a faded signal. Properties of the Rayleigh distributed envelope have been studied in many papers [Jak74][PG89]. These properties include mean, autocorrelation, autocovariance and power spectral density of the envelope. Here we compare the autocorrelation and the power spectral density of the envelope to that of the complex signal. The autocorrelation is given by [Jak74]

$$\Gamma_{env}(\tau) \approx \frac{3\pi E_0^2}{8} \left(1 + \frac{1}{4} J_0^2(2\pi f_m \tau) \right), \quad (4.35)$$

and the power spectral density function is

$$S_{bE}(f) = \frac{1}{8\pi f_m} K \left(\sqrt{1 - \left(\frac{f}{2f_m} \right)^2} \right), \quad (4.36)$$

where $K(\cdot)$ is the complete elliptical integral of the first kind and is defined in the following equation [Rap96]:

$$K(k) = \int_0^{\frac{\pi}{2}} \frac{1}{\sqrt{1 - k^2 \sin^2 \phi}} d\phi, \text{ for } k^2 < 1. \quad (4.37)$$

To evaluate it, we expand the integral in the form

$$(1 - k^2 \sin^2 \phi)^{-\frac{1}{2}} = 1 + \frac{k^2}{2} \sin^2 \phi + \frac{3k^2}{4} \sin^4 \phi + \dots \quad (4.38)$$

This series can be shown to be uniformly convergent for all k , and may, therefore be integrated term by term which results in $K(k)$ as [Gre85]:

$$K(k) = \frac{\pi}{2} \left[1 + \left(\frac{1}{2} \right) k^2 + \left(\frac{1.3}{2.4} \right)^2 k^4 + \left(\frac{1.35}{2.46} \right)^2 k^6 + \dots \right]. \quad (4.39)$$

The fourth and higher power terms can be eliminated since $k^2 \ll 1$. Then this formula can be approximated as

$$\begin{aligned} K(k) &\approx \frac{\pi}{2} \left[1 + \left(\frac{1}{2} \right) k^2 \right] \\ &\approx \frac{\pi}{2} e^{\frac{1}{2} k^2}. \end{aligned} \quad (4.40)$$

In this way, the baseband spectral density function in Eq. (4.36) can be simplified to:

$$S_{bE}(f) \approx \frac{\sqrt{e}}{16f_m} e^{\frac{f^2}{8f_m^2}}. \quad (4.41)$$

The theoretical autocorrelation function of the envelope in Eq. (4.35) is computed as a function of τ and is plotted in Fig. 4.9. To verify it, 12000 points of simulated Rayleigh fading envelope data are used to compute the autocorrelation and the result is represented by the dash-dot line in Fig. 4.9. The simulated results and the analytical results are very close. By comparing Fig. 4.8 and Fig. 4.9, it is not difficult to observe that the autocorrelation function of the faded complex signal declines faster than that of the envelope of the signal. For small delays, such as $\tau < 50$ samples, these two are very similar. However, when the delay increases, there is a significant difference between the two autocorrelation functions. Theoretically, the mean of the complex signals is zero due to the uniformly distributed phase of the arriving signal components, while the mean of the envelope of the signal is related to the electric field power ($E[r] = \frac{\pi}{2} b_0$). Also, it can be seen from Eq. (4.29) and Eq. (4.35) that the autocorrelation of the complex signal is a function of

$J_0(2\pi f_m \tau)$, while it is a function of $J_0^2(2\pi f_m \tau)$ for the signal envelope.

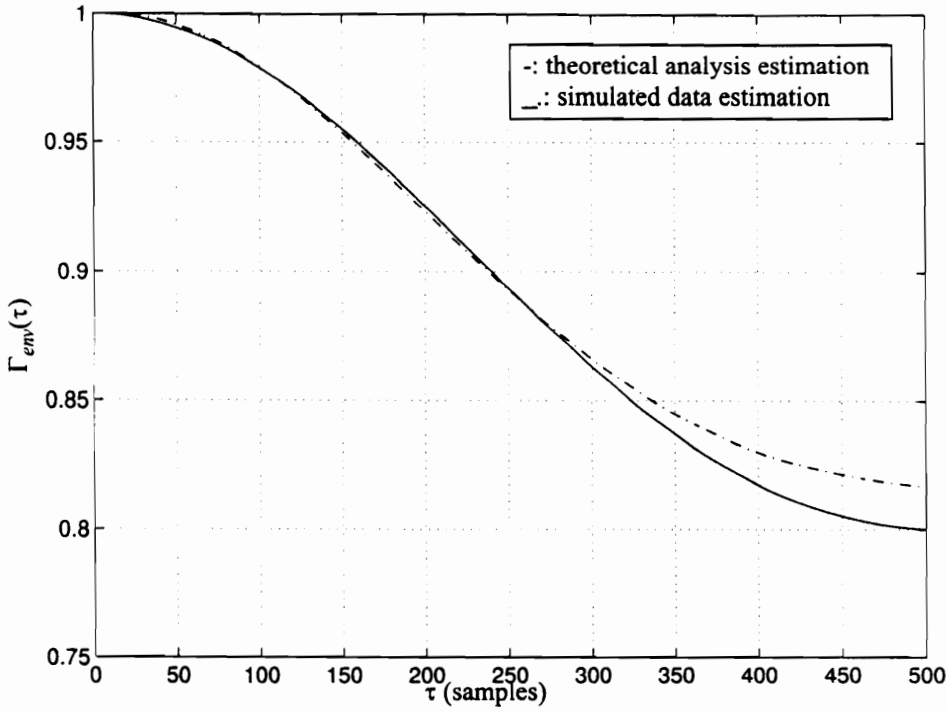


Fig. 4.9 Comparison of the envelop autocorrelation using theoretical results and simulated data

2) Frequency Selective Fading

For large scattering environments, the time varying channel impulse response of the fading channel is expressed in Eq.(4.20). When the multipath delays are significant compared to the reciprocal of the bandwidth for AMPS signals and the channel coherence bandwidth is smaller than the signal bandwidth, the signal undergoes frequency selective fading. The output signal $y(t)$ is simply a convolution between $x(t)$ and $h(t, \tau)$:

$$y(t) = \int h(t, \tau)x(t-\tau)d\tau. \quad (4.42)$$

Using the definition of the cyclic autocorrelation in Eq. (4.6), the cyclic autocorrelation of the frequency selective faded signal $y(t)$ is:

$$\begin{aligned}
 R_{yy}^{\alpha}(\tau) &= E\left[y\left(t-\frac{\tau}{2}\right)y^{*}\left(t+\frac{\tau}{2}\right)e^{-j2\pi\alpha t}\right] \\
 &= E\left[\int h\left(t+\frac{\tau}{2}, u\right)x\left(t+\frac{\tau}{2}-u\right)du \int h^{*}\left(t-\frac{\tau}{2}, v\right)x^{*}\left(t-\frac{\tau}{2}-v\right)dv e^{-j2\pi\alpha t}\right].
 \end{aligned}
 \tag{4.43}$$

If we assume that the transmitted signal $x(t)$ and the channel are independent, then

$$R_{yy}^{\alpha}(\tau) = \iint E\left[h\left(t+\frac{\tau}{2}, u\right)h^{*}\left(t-\frac{\tau}{2}, v\right)\right]R_{xx}^{\alpha}(\tau-(u-v))e^{-j2\pi\alpha\frac{(u+v)}{2}}dudv.
 \tag{4.44}$$

For a wide sense stationary channel, the autocorrelation of the channel impulse depends only on the time difference. Define the delay cross power $Q(t, \tau)$ as [BK94]

$$Q(t, \tau) = E\left[h\left(t+\frac{\tau}{2}, u\right)h^{*}\left(t-\frac{\tau}{2}, v\right)\right],
 \tag{4.45}$$

Eq. (4.44) can be simplified as:

$$\begin{aligned}
 R_{yy}^{\alpha}(\tau) &= \iint Q(\tau, u-v)\delta(u-v)R_{xx}^{\alpha}(\tau-(u-v))e^{-j2\pi\alpha\frac{(u+v)}{2}}dudv \\
 &= \int Q(\tau, u-v)R_{xx}^{\alpha}(\tau)e^{-j2\pi\alpha u}du \\
 &= \Gamma(\tau, \alpha)R_{xx}^{\alpha}(\tau),
 \end{aligned}
 \tag{4.46}$$

where $Q(t, \tau)$ is called the delay-cross power density [BK94], and $\Gamma(\tau, f_d)$ is the correlation function of the channel transfer function $H(t, f)$ valid for worst-case scintillation at HF, VHF, and UHF. For the strong scatter approximation, $\Gamma(\tau, f_d)$ is given by [BK94]

$$\Gamma(\tau, f_d) = E_t[H(t + \tau, f + f_d)H^*(t, f)]$$

$$= |H_0|^2 \exp \left\{ \frac{-\frac{\tau^2}{\tau_0^2}}{1 + j\frac{f_d}{f_0}} \right\} \frac{1}{1 + j\frac{f_d}{f_0}} \quad . \quad (4.47)$$

The coherence bandwidth f_0 is related to the *rms* of all the multipath delays σ_τ of the fading channel. If the coherence bandwidth is defined as the bandwidth over which the frequency correlation function is above 0.9, the coherence bandwidth is approximately [Rap96]:

$$f_0 \approx \frac{1}{50\sigma_\tau} \quad (4.48)$$

Fourier transformation gives the spectral correlation relationship

$$S_{yy}^\alpha(f) = \int_{-\infty}^{\infty} P(\nu, \alpha) S_{xx}^\alpha(f - \nu) d\nu \quad (4.49)$$

where

$$P(\nu, \alpha) = \int_{-\infty}^{\infty} \Gamma(u, \alpha) e^{-j2\pi\nu u} du \quad . \quad (4.50)$$

Clearly, the received signal still exhibits the cyclic feature which is related to the input signal $x(t)$. The spectral correlation function of the received signal is a spectrally blurred version of that of the transmitted signal and furthermore the spectral blurring function depends on the cycle frequency. Specifically, for $\Gamma(t, f_d)$ given in Eq. (4.47), Eq. (4.50) becomes

$$P(\nu, \alpha) = |H_0|^2 \tau_0 \sqrt{\frac{\pi}{1 + j \frac{\alpha}{f_0}}} e^{-\frac{(\pi \tau_0 \nu)^2}{1 + j \frac{\alpha}{f_0}}} \quad (4.51)$$

The area of this function is concentrated in the region $|\nu| < 1/\tau_0$ and $|\alpha| < f_0$. Therefore the spectral blurring width is on the order of the reciprocal channel decorrelation time and the spectral correlation function is attenuated for cycle frequencies greater than the channel coherence bandwidth. It can be seen that if the multipath delay time is zero, or the coherence bandwidth f_0 is infinite, Eq. (4.46) and Eq. (4.49) degenerate to the Eq. (4.32) and Eq. (4.34), which is the flat fading case.

Most of the fading experienced by AMPS signals is flat since the bandwidth of the signals (30kHz) is usually less than the channel coherence bandwidth (typically as 100kHz). The phase distortion of the received signal which is the summation of different multipath components can not be compensated for by using a conventional equalizer. This results in large amplitude fluctuation of the received signal. The amplitude is well known to be Rayleigh distributed. For flat fading, the channel coherence bandwidth is infinite. Since the cyclic frequencies in which the AMPS signal exhibits spectral correlation are within the channel coherence bandwidth, the cyclic feature of the AMPS signal is preserved. Analytical results show that the cyclic autocorrelation function of the received signal is the same as that of the signal that does not undergoes fading channel except it is multiplied by a scaling factor. For flat fading case, this scaling factor only depends on the fading rate. Fig. 4.10 depicts the autocorrelation of complex faded signals for a flat fading channel as a function of time delay τ for different fading rates, or Doppler frequencies. A large fading rate, or large Doppler spread results in greater attenuation than a smaller fading rate. It can be seen from Fig. 4.10 that for a short time delay within 10 samples, the scaling factor $\Gamma(\tau, \alpha)/|H_0|^2$ does not change much for different Doppler spreads. However, significant differences can be observed when the delay is large. If the velocity of the mobile is close to

zero, the scaling factor is unity for all delays, i. e., no fading is introduced. On the other hand, the scaling factor $\Gamma(\tau, \alpha)/|H_0|^2$ decreases dramatically for high Doppler spreads when the delay is large. The cyclic autocorrelation coefficient is reduced to 50% for Doppler frequency of 95Hz when the delay is greater than 160 samples. This trend can also be observed in Fig. 4.12 which plots the Fourier transform of $\Gamma(\tau, \alpha)/|H_0|^2$ as a function of frequency and the Doppler spread.

A simulated flat faded AMPS signal is used to measure the cyclic autocorrelation function and the result is shown in Fig. 4.14 as a function of time delay. It closely matches the theoretical cyclic feature in that the impact of fading for a short time delay is less than that for a long time delay. The cyclic frequency chosen here is 6000Hz and the Doppler frequency is 80Hz. For frequency selective fading, if the channel coherence bandwidth is less than the primary cyclic frequencies, the cyclic feature will be distorted severely since the signals are no longer correlated due to the channel effects. $\Gamma(\tau, \alpha)/|H_0|^2$ is also computed and plotted in Fig. 4.11 for a two-ray Rayleigh fading model with $\sigma_\tau = 5\mu\text{s}$. The channel coherence bandwidth is only 4kHz and within the cyclic frequencies of the desired signal¹. It can be seen that the cyclic feature is reduced to 50% even though the fading rate is very low. This is also reflected in Fig. 4.13 which shows the frequency response of the channel correlation for the frequency selective case. It is interesting to notice that the effect due to different Doppler frequencies on the scaling factor for the frequency selective fading is less than that for the flat fading case. It can be seen from Fig. 4.10 and Fig. 4.11 that $\Gamma(\tau, \alpha)/|H_0|^2$ drops 50% from a Doppler spread of 5Hz to 95Hz (at delay of 160 samples) for flat fading, while $\Gamma(\tau, \alpha)/|H_0|^2$ only drops 20% for frequency selective channel. This is because the multipath delay plays an important role in $\Gamma(\tau, \alpha)/|H_0|^2$ for the frequency selective fading. It is also interesting to notice that a long optimal filter length does not give better performance for the fading channel because the cyclic feature is diminished for

1. This coherence bandwidth may not be realistic for AMPS, but it does illustrate in general terms the impact of frequency selective on the cyclic feature of a modulated signal.

large lags. This provides insight in selecting the optimal filter length for fading channels. The limitation of using additional filter weights is validated in the next chapter.

From the above discussion, it can be seen that the cyclostationarity of the transmitted signal is preserved after passing through different realistic channels, although it is diminished because of fading. Nevertheless, the spectral correlation property still provides a means to separate the desired signal and the interference even in the presence of fading as shown in Chapter 5.

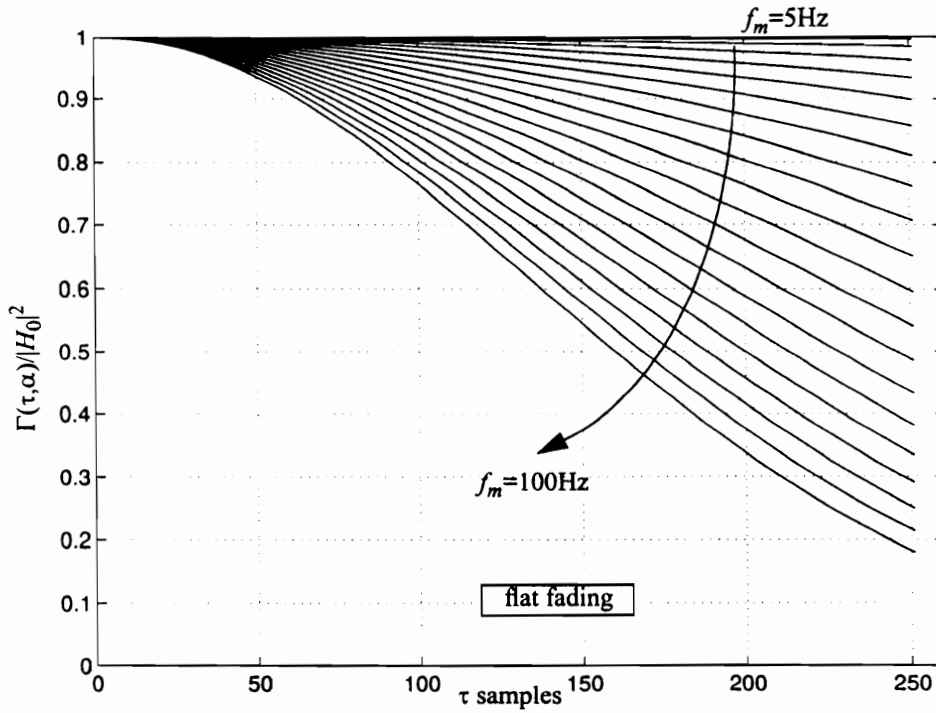


Fig. 4.10 Autocorrelation function of the faded complex signal for flat fading channel

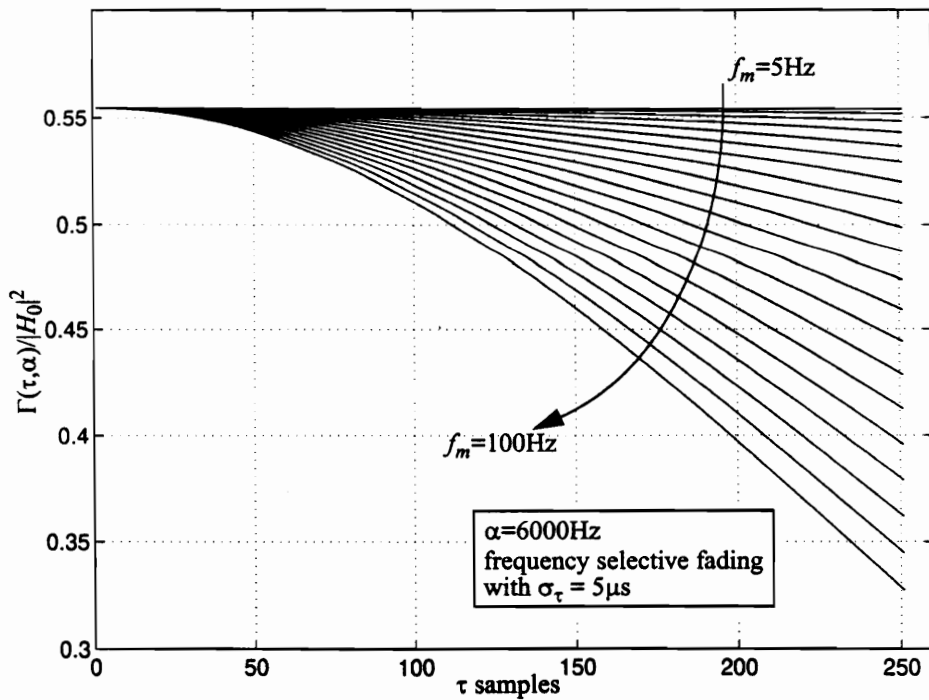


Fig. 4.11 Autocorrelation function of the faded complex signals for frequency selective fading channel

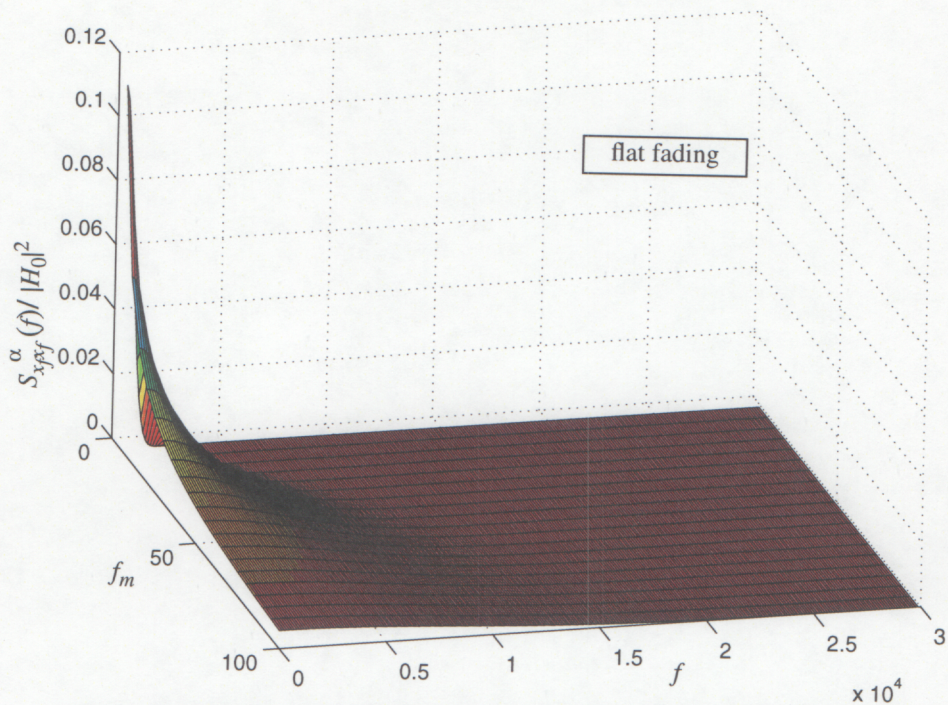


Fig. 4.12 Fourier transform of $\Gamma(\tau,\alpha)/|H_0|^2$ for flat fading channel

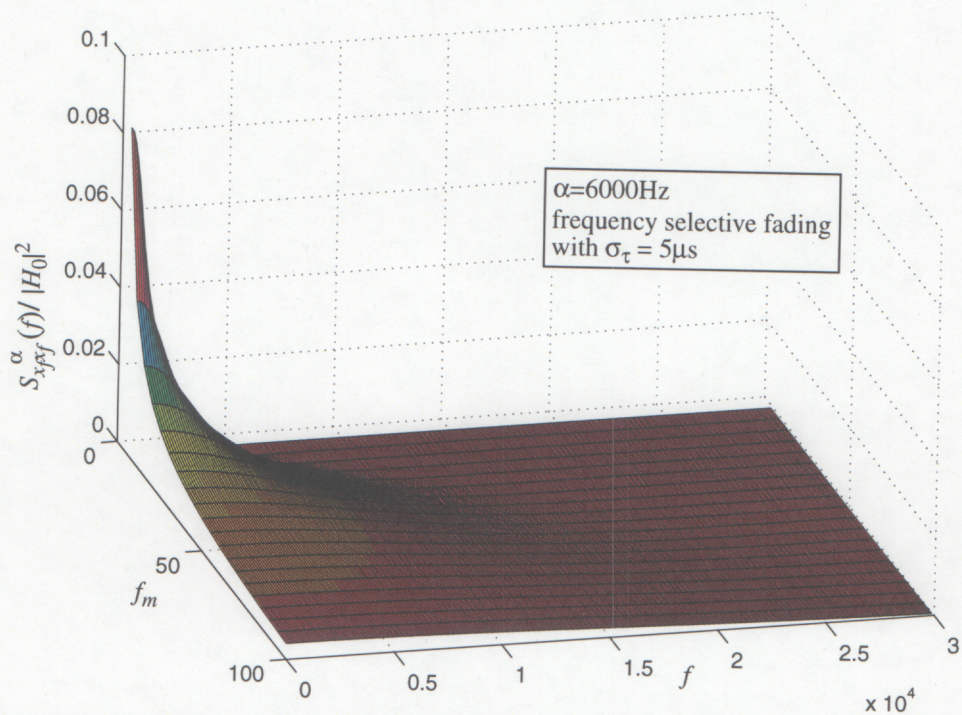


Fig. 4.13 Fourier transform of $\Gamma(\tau,\alpha)/|H_0|^2$ for frequency selective fading channel

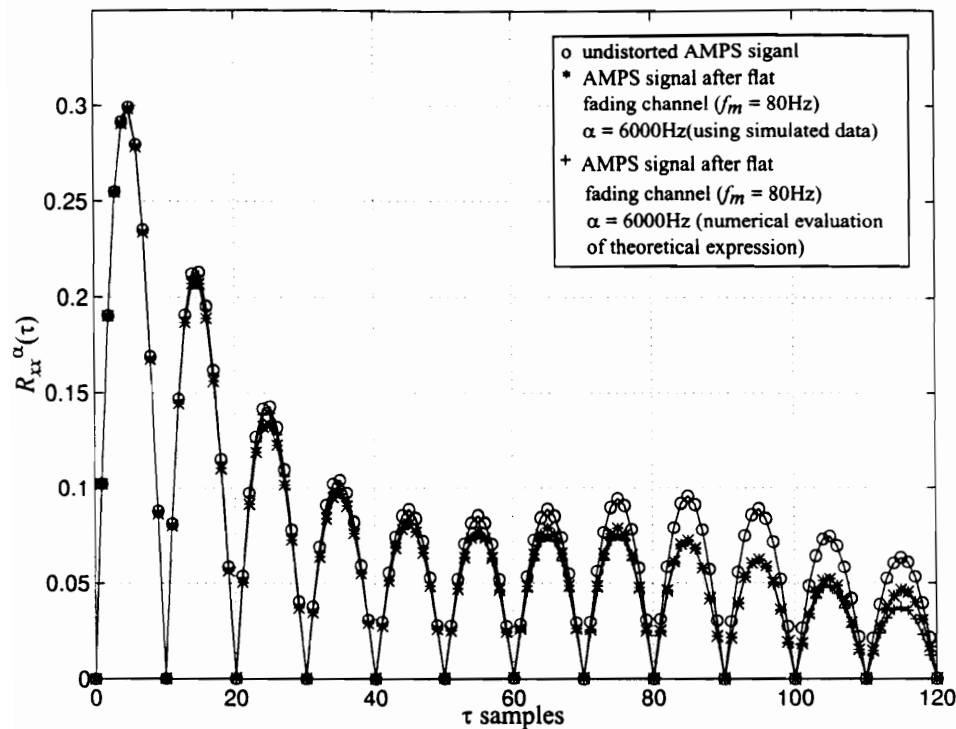


Fig. 4.14 Comparison of the cyclic autocorrelation function for undistorted and faded AMPS signals

Chapter 5. Optimal and Adaptive Time-Dependent Filtering

5.1 Introduction

As the study of adaptive filters has matured over the past 30 years, they have been shown to be useful in a wide variety of applications. Linear time invariant adaptive filters¹ with a finite duration impulse response have been used in such diverse fields as communications, controls, radar, sonar, etc. In this chapter, a time-dependent adaptive filter is introduced for processing cyclostationary signals. A time-dependent adaptive filter (TDAF) can enhance the desired signal by taking advantage of spectrally redundant information contained in the received signal. This filter can be implemented either in the time domain or in the frequency domain. A frequency shifted (FRESH) filter is a specific type of TDAF that involves jointly filtering frequency shifted versions of the signal.

The time-sequenced adaptive filter (TSAF) is a TDAF ideally suited for operating on a signal with periodic statistics [RQH88]. In Fig. 5.1, the TSAF utilizes a bank of M conventional LMS adaptive filters whose weights are denoted by the column vector $H_k(m)$ for $m=0,1,2,\dots,M-1$. Each adaptive filter is periodically updated and a filter output is chosen synchronously with the periodicity of the signal statistics. The filter output at time k is given by the inner product of the input vector and the H_k with the largest multiple of M in $[k]$,

$$y(k) = X_k^T H_k(k - [k]_M M) \quad . \quad (5.1)$$

The TSAF can be interpreted as an adaptive filter that converts the nonstationary signal into a set of jointly stationary processes using the time-series representation (TSR) for

1. Here we refer to time-invariant adaptive filter as an adaptive filter that changes in time to track a dynamic signal, but does not have a periodic impulse response.

adaptation and filtering [Fer85b]. In the literature, the TSAF is often referred to as the TSR TDAF. A frequency domain equivalent to the TSAF (FD TSAF) has been developed by Ferrara [Fer85b]. It can be easily derived by modeling the m -th filter's sampler in Fig. 5.1 as mathematically equivalent to multiplication of the filtered outputs by the discrete Fourier series representation of a periodic pulse train with a period of M samples. Using the Fourier series representation (FSR), it is shown in [RQH88] that an equivalent structure is the FRESH filter, shown in Fig. 5.2. The FRESH filter is more flexible because the filter periodicity α_m can be explicitly specified. However, the FRESH filter requires more computations. For the TSAF the periodicities are all harmonics of the switching rate.

Frequency domain adaptive filters are of interest because they have been shown in certain instances to converge faster and require fewer computations than the transversal LMS adaptive filter [RQH88]. A circular frequency domain adaptive filter can be generalized to process cyclostationary and nearly cyclostationary signals by exploiting the spectral correlation property as shown in Fig. 5.3. The circular FSR TDAF can be viewed as a multi-channel adaptive filter which estimates a frequency bin $Y_k(f_i)$ by using weighted bins $W_{k,m}(f_i)X_k(f_i - \alpha_m)$ separated by cycle frequencies α_m corresponding to the SOI or the SNOI. The cycle frequencies are constrained to lie within the possible FFT bins.

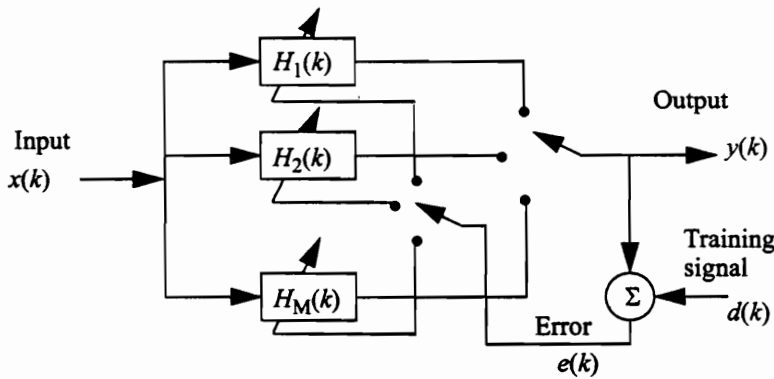


Fig. 5.1 The TSR TDAF

5.2 Optimal Time-Dependent Filtering

It is shown in Chapter 4 that the spectrum of an AMPS signal consists of the FM modulated voice (SAT excluded) replicated at the carrier and at the carrier plus and minus multiples of the SAT frequency. A TDAF can combine the replicated versions of the SOI FM voice signal (excluding the SAT) to enhance the SOI. Alternatively, the time-dependent optimal filter, periodic at multiples of the SNOI SAT frequency, estimates and cancels the replicated versions of the SNOI modulated voice, thus improving the quality of the SOI signal at the filter output.

Given this conceptual view of the optimal filter, the theory of the optimal filter is now presented. The impulse response $h(t, u)$ of an optimal time-dependent filter can be represented by

$$h(t, u) = \sum_m g_m(t - u) e^{j2\pi\alpha_m u}, \quad (5.2)$$

where $g_m(t)$ is the Fourier component for all time t and α_m represents the filter periodicities. The output, which is an estimate of the desired signal $d(t)$, is given by

$$\begin{aligned} d(t) &= \sum_m \int_{-\infty}^{+\infty} g_m(t - u) x(u) e^{j2\pi\alpha_m u} du \\ &= \sum_m g_m(t) \otimes x_m(t), \end{aligned} \quad (5.3)$$

where $x_m(t) = x(t) e^{j2\pi\alpha_m t}$ are frequency-shifted versions of the input signal.

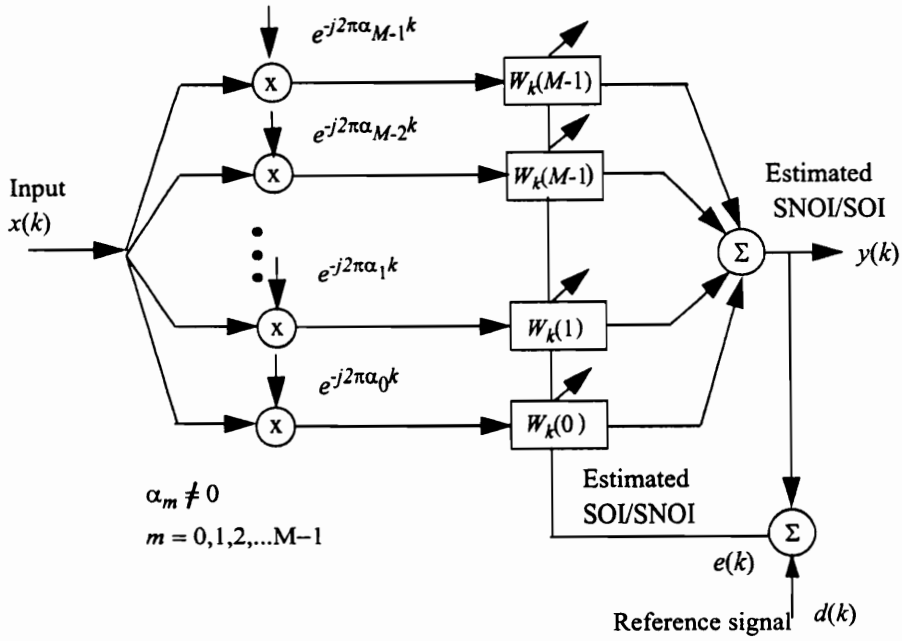


Fig. 5.2 The FRESH filter

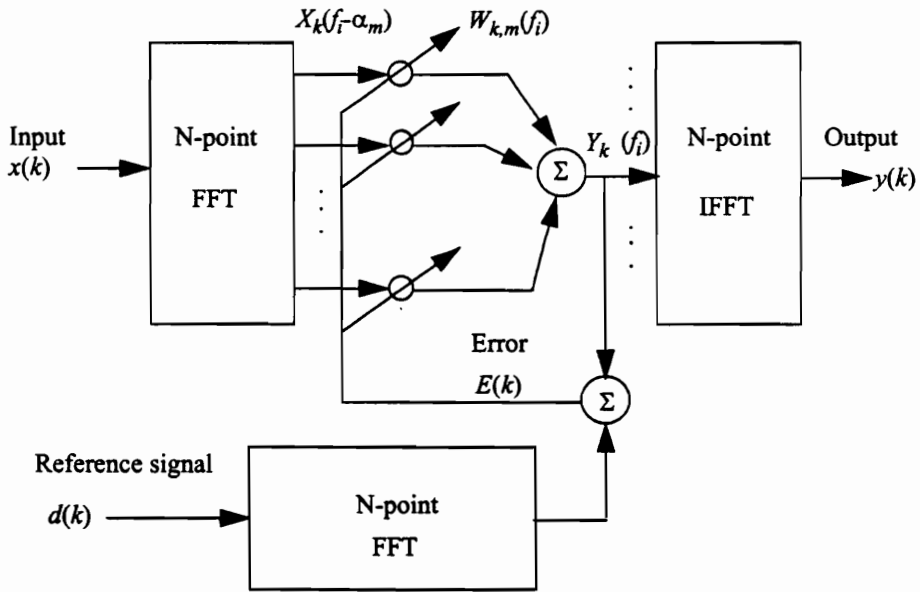


Fig. 5.3 The circular FSR TDAF

The optimal Wiener solution for this filter is given by [Gar94]

$$R_{dx}^{\beta_n}(u)e^{j\pi\beta_n u} = \sum_m g_m(u) \otimes (R_{xx}^{\beta_n - \alpha_m}(u)e^{j\pi(\beta_n + \alpha_m)u}) \quad , \quad (5.4)$$

where $R_{dx}^{\beta_n}(u)$ is the cyclic cross-correlation between the training signal $d(t)$ and the observed signal $x(t)$. The frequency domain equivalent representation is

$$S_{dx}^{\beta_n}\left(f - \frac{\beta_n}{2}\right) = \sum_m G_m(f) S_{xx}^{\beta_n - \alpha_m}\left(f - \frac{\beta_n + \alpha_m}{2}\right), \quad (5.5)$$

where β_n ranges over all the possible values of α_m .

Define the mean square error (*MSE*) as the expectation (in a time-average sense) of the difference between the desired signal spectrum $S_d(f)$ and the estimated signal spectrum $S_y(f)$,

$$MSE = \int_{-\infty}^{+\infty} |S_d(f) - S_y(f)| df. \quad (5.6)$$

The *MSE* can be calculated using the results contained in [RH90]

$$MSE = \int_{-\infty}^{+\infty} \left| S_d(f) - \sum_n G_n(f) S_{dx}^{\beta_n}\left(f - \frac{\beta_n}{2}\right)^* \right| df. \quad (5.7)$$

To estimate the analytical performance of the TDAF (no $\alpha=0$ Hz term) for AMPS signals, we consider that only two filter periodicities of ± 6 kHz are used for the TDAF shown in Fig. 5.3. The ± 12 kHz frequency shifted versions are usually distorted and attenuated by

the roll-off effect of the bandpass filters at transmitters and receivers and provide only marginal performance gain. To provide an intuitive understanding of the performance of the TDAF, we evaluate Eq. (5.5) using two periodicities α_0 and α_1 (+/- 6kHz),

$$\begin{cases} S_{dx}^{\alpha_0}\left(f - \frac{\alpha_0}{2}\right) = G_0(f)S_{xx}^0(f - \alpha_0) + G_1(f)S_{xx}^{\alpha_0 - \alpha_1}\left(f - \frac{\alpha_0 + \alpha_1}{2}\right) \\ S_{dx}^{\alpha_1}\left(f - \frac{\alpha_1}{2}\right) = G_0(f)S_{xx}^{\alpha_1 - \alpha_0}\left(f - \frac{\alpha_0 + \alpha_1}{2}\right) + G_1(f)S_{xx}^0(f - \alpha_1) \end{cases} \quad (5.9)$$

Solving the two linear equations, we have

$$G_0(f) = \frac{S_{dx}^{\alpha_0}\left(f - \frac{\alpha_0}{2}\right)S_{xx}^0(f - \alpha_1) - S_{dx}^{\alpha_1}\left(f - \frac{\alpha_1}{2}\right)S_{xx}^{\alpha_0 - \alpha_1}\left(f - \frac{\alpha_0 + \alpha_1}{2}\right)}{S_{xx}^0(f - \alpha_0)S_{xx}^0(f - \alpha_1) - S_{xx}^{\alpha_1 - \alpha_0}\left(f - \frac{\alpha_0 + \alpha_1}{2}\right)S_{xx}^{\alpha_0 - \alpha_1}\left(f - \frac{\alpha_0 + \alpha_1}{2}\right)} \quad (5.10a)$$

and

$$G_1(f) = \frac{S_{dx}^{\alpha_1}\left(f - \frac{\alpha_1}{2}\right)S_{xx}^0(f - \alpha_1) - S_{dx}^{\alpha_0}\left(f - \frac{\alpha_0}{2}\right)S_{xx}^{\alpha_1 - \alpha_0}\left(f - \frac{\alpha_0 + \alpha_1}{2}\right)}{S_{xx}^0(f - \alpha_1)S_{xx}^0(f - \alpha_0) - S_{xx}^{\alpha_0 - \alpha_1}\left(f - \frac{\alpha_0 + \alpha_1}{2}\right)S_{xx}^{\alpha_1 - \alpha_0}\left(f - \frac{\alpha_0 + \alpha_1}{2}\right)} \quad (5.10b)$$

If $\alpha_0 = -\alpha_1$, then the solution can be simplified to:

$$G_0(f) = \frac{S_{dx}^{\alpha_0}\left(f - \frac{\alpha_0}{2}\right)S_{xx}^0(f + \alpha_0) - S_{dx}^{-\alpha_0}\left(f + \frac{\alpha_0}{2}\right)S_{xx}^{2\alpha_0}(f - \alpha_0)}{S_{xx}^0(f - \alpha_0)S_{xx}^0(f + \alpha_0) - S_{xx}^{-2\alpha_0}(f)S_{xx}^{2\alpha_0}(f)} \quad (5.11a)$$

and

$$G_1(f) = \frac{S_{dx}^{-\alpha_0}\left(f + \frac{\alpha_0}{2}\right)S_{xx}^0(f - \alpha_0) - S_{dx}^{\alpha_0}\left(f - \frac{\alpha_0}{2}\right)S_{xx}^{-2\alpha_0}(f + \alpha_0)}{S_{xx}^0(f + \alpha_0)S_{xx}^0(f - \alpha_0) - S_{xx}^{2\alpha_0}(f)S_{xx}^{-2\alpha_0}(f)} . \quad (5.11b)$$

From the SCD values shown in Fig. 4.3, $S_{xx}^{2\alpha_0}(f \pm \alpha_0)$ is 30dB down from $S_{xx}^0(f \pm \alpha_0)$ and 20dB down from $S_{dx}^{\alpha_0}\left(f \pm \frac{\alpha_0}{2}\right)$ for $\alpha_0=6\text{kHz}$. Thus the solution of Eq. (5.11) can be approximated as:

$$G_0(f) \approx \frac{S_{dx}^{\alpha_0}\left(f - \frac{\alpha_0}{2}\right)}{S_{xx}^0(f - \alpha_0)} \quad (5.12a)$$

and

$$G_1(f) \approx \frac{S_{dx}^{-\alpha_0}\left(f + \frac{\alpha_0}{2}\right)}{S_{xx}^0(f + \alpha_0)} . \quad (5.12b)$$

From Eq. (5.12), the optimal solution of the time-dependent filter computes the ratio of the cross cyclic spectral correlation density between the desired signal and the input signal over the conventional spectral density of the input signal. Since the cyclic frequencies of the desired signal and the interference are different, the cyclic spectral correlation density between the reference signal $d(t)$ and the interfering signal $i(t)$ is zero if the periodicities of the filter are chosen to correspond to the desired signal. In other words, when a corrupted signal $x(t)$ passes through a filter with frequency response given by Eq. (5.12), the desired signal will be enhanced and the interference will be attenuated.

Using the optimal filter solution, the cyclic spectrum density of the estimated signal $y(t)$

is

$$S_{yy}^{\alpha}(f) = \sum_{n=0}^{L-1} \sum_{m=0}^{L-1} G_n\left(f + \frac{\alpha}{2}\right) G_m^*\left(f - \frac{\alpha}{2}\right) S_{xx}^{\alpha-\beta_n+\gamma_m}\left(f - \frac{\beta_n+\gamma_m}{2}\right). \quad (5.13)$$

The conventional spectrum density is given in the following equation by simply setting $\alpha=0$ in Eq. (5.13),

$$S_{yy}(f) = \sum_{n=0}^{L-1} \sum_{m=0}^{L-1} G_n(f) G_m^*(f) S_{xx}^{-\beta_n+\gamma_m}\left(f - \frac{\beta_n+\gamma_m}{2}\right). \quad (5.13a)$$

By substituting Eq. (5.13a) into Eq. (5.6), the *MSE* for this TDAF then can be formed as

$$\begin{aligned} MSE &= \int_{-\infty}^{\infty} |S_d(f) - S_y(f)| df \\ &= \int_{-\infty}^{\infty} \left| S_d(f) - \sum_{n=0}^{L-1} \sum_{m=0}^{L-1} G_n(f) G_m^*(f) S_{xx}^{-\beta_n+\gamma_m}\left(f - \frac{\beta_n+\gamma_m}{2}\right) \right| df. \end{aligned} \quad (5.14)$$

Another alternative to measure the performance of the TDAF is to calculate the output *CIR* and compare it to the input *CIR*. Since the TDAF is a linear system, the output *CIR* can be calculated by filtering the desired signal $s(t)$ and the interference separately using the converged filter response. From Eq. (5.9) and Eq. (5.14), the analytical *CIR* for the TDAF given in Fig. 5.2 is given by

$$\frac{C}{I} = \frac{\int_{-\infty}^{\infty} \left(G_0(f) S_{ds}^{\alpha_0}\left(f - \frac{\alpha_0}{2}\right)^* + G_1(f) S_{ds}^{-\alpha_0}\left(f + \frac{\alpha_0}{2}\right)^* \right) df}{\int_{-\infty}^{\infty} \left(G_0(f) S_{di}^{\alpha_0}\left(f - \frac{\alpha_0}{2}\right)^* + G_1(f) S_{di}^{-\alpha_0}\left(f + \frac{\alpha_0}{2}\right)^* \right) df}. \quad (5.15)$$

For the case of extracting and equalizing a distorted signal in co-channel interference and noise, the filter response, the *MSE* and the output *CIR* can be simplified to a form which provides a more intuitive interpretation of the filter performance. The received signal contains the desired signal $s(t)$, with the interference $i(t)$ and channel noise $n_x(t)$,

$$x(t) = h(t) \otimes s(t) + i(t) + n_x(t) , \quad (5.16)$$

and the cyclic spectrum of $x(t)$ is [Gar94]

$$S_{xx}^\alpha(f) = H\left(t + \tau, f + \frac{\alpha}{2}\right) H^*\left(t, f - \frac{\alpha}{2}\right) S_{ss}^\alpha(f) + S_{ii}^\alpha(f) + N_{xx}^\alpha(f) . \quad (5.17)$$

If the noise $n_x(t)$, the signal $s(t)$, and $i(t)$ are statistically independent, the cross cyclic spectrum of the desired signal and the input signal is

$$S_{dx}^\alpha(f) = H^*\left(f - \frac{\alpha}{2}\right) S_{ss}^\alpha(f) . \quad (5.18)$$

Substitute Eq. (5.17) and (5.18) into Eq. (5.12), the filter response of the TDAF is

$$G_0(f) \approx \frac{H^*(f - \alpha_0) S_{ss}^{\alpha_0}\left(f - \frac{\alpha_0}{2}\right)}{H(f - \alpha_0) H^*(f - \alpha_0) S_{ss}(f - \alpha_0) + S_{ii}(f - \alpha_0) + N_{xx}(f - \alpha_0)} , \quad (5.19a)$$

and

$$G_1(f) \approx \frac{H^*(f + \alpha_0) S_{ss}^{-\alpha_0}\left(f + \frac{\alpha_0}{2}\right)}{H(f + \alpha_0) H^*(f + \alpha_0) S_{ss}(f + \alpha_0) + S_{ii}(f + \alpha_0) + N_{xx}(f + \alpha_0)} . \quad (5.19b)$$

By substituting Eq.(5.17) into the Eq. (5.14), MSE can be evaluated using Eq. (5.6),

$$\begin{aligned}
 MSE = & \int_{-\infty}^{\infty} |S_d(f) - \sum_{n=0}^{L-1} \sum_{m=0}^{L-1} G_n(f) G_m^*(f) H(t+\tau, f-\beta_n) H^*(t, f-\gamma_m) S_{ss}^{-\beta_n+\gamma_m} \left(f - \frac{\beta_n+\gamma_m}{2}\right)| \\
 & - \sum_{n=0}^{L-1} \sum_{m=0}^{L-1} G_n(f) G_m^*(f) \left(S_{ii}^{-\beta_n+\gamma_m} \left(f - \frac{\beta_n+\gamma_m}{2}\right) + N_{xx}^{-\beta_n+\gamma_m} \left(f - \frac{\beta_n+\gamma_m}{2}\right) \right) df .
 \end{aligned} \tag{5.20}$$

The cyclic frequencies of the interference are different than those of the desired signal and the noise is assumed to be stationary with spectral density of $\frac{\eta}{2}$. Thus only when $-\beta_n + \gamma_m = 0$ are the correlation terms for the noise and the interference present in Eq. (5.20).

Usually the signal-not-of-interest includes background noise, channel interference, fading and multipath, etc. The performance of the TDAF under these conditions is analyzed in the following section based on the above example.

1) Noise-only Channel

In this case, the input signal is simply a sum of the desired signal $s(t)$ and noise $n(t)$

$$x(t) = s(t) + n(t) , \tag{5.21}$$

and the desired signal $d(t) = s(t)$. It can be seen that the only correlation between $x(t)$ and $d(t)$ is due to $s(t)$. Thus the cyclic spectrum of $x(t)$ is

$$S_{xx}^\alpha(f) = S_{ss}^\alpha(f) + \frac{\eta}{2} \tag{5.22}$$

and the cross cyclic spectrum is

$$S_{dx}^{\alpha}(f) = S_{ss}^{\alpha}(f). \quad (5.23)$$

Assuming $s(t)$ and $n(t)$ are statistically independent. The filter response from Eq. (5.19) is approximately

$$G_0(f) \approx \frac{S_{ss}^{\alpha_0}\left(f - \frac{\alpha_0}{2}\right)}{S_{ss}(f - \alpha_0) + \frac{\eta}{2}} \quad (5.24a)$$

and

$$G_1(f) \approx \frac{S_{ss}^{-\alpha_0}\left(f + \frac{\alpha_0}{2}\right)}{S_{ss}(f + \alpha_0) + \frac{\eta}{2}}. \quad (5.24b)$$

The filter response obtained from Eq. (5.24) is a generalized Wiener solution for an optimal time-dependent filter. For a time-invariant optimal filter, the filter response is the ratio of the spectrum of the desired signal to the spectrum of the noise corrupted signal. The degenerate filter response provided in Eq. (5.24) when $\alpha=0\text{Hz}$ is the time-invariant case. For a time-varying optimal filter, the numerator of the filter response is the cyclic spectrum of the desired signal, since a frequency shifted version of the received signal is applied as the input of the FIR filter. Also, a frequency shift occurs in the denominator of Eq. (5.24).

The MSE in Eq. (5.20) for this case is simplified as

$$MSE = \int_{-\infty}^{\infty} \left| S_d(f) - \sum_{n=0}^{L-1} \sum_{m=0}^{L-1} G_n(f) G_m^*(f) \left(S_{ss}^{-\beta_n + \gamma_m} \left(f - \frac{\beta_n + \gamma_m}{2} \right) + \frac{\eta}{2} \right) \right| df. \quad (5.25)$$

Referring to Eq.(5.15), the *CNR* of the TDAF processed AMPS signal can be computed from the following equation

$$\frac{C}{N} = \frac{\int_{-\infty}^{\infty} \left(G_0(f) S_{ds}^{\alpha_0} \left(f - \frac{\alpha_0}{2} \right)^* + G_1(f) S_{ds}^{-\alpha_0} \left(f + \frac{\alpha_0}{2} \right)^* \right) df}{\int_{-\infty}^{\infty} \left(G_0(f) S_{dn}^{\alpha_0} \left(f - \frac{\alpha_0}{2} \right)^* + G_1(f) S_{dn}^{-\alpha_0} \left(f + \frac{\alpha_0}{2} \right)^* \right) df} . \quad (5.26)$$

2) Co-channel Interference Channel

Rejecting co-channel interference is the main goal of this research. For this case, the received signal is simply a summation of the desired signal $s(t)$ and the co-channel interference $i(t)$

$$x(t) = s(t) + i(t) . \quad (5.27)$$

Assume that the desired signal is $d(t) = s(t)$. The only correlation between $x(t)$ and $d(t)$ is due to $s(t)$. The cyclic spectrum of $x(t)$ can be computed in the following equation:

$$S_{xx}^{\alpha}(f) = S_{ss}^{\alpha}(f) + S_{ii}^{\alpha}(f) , \quad (5.28)$$

and the cross cyclic spectrum is

$$S_{dx}^{\alpha}(f) = S_{ss}^{\alpha}(f) . \quad (5.29)$$

Assuming $s(t)$ and $i(t)$ are statistically independent. The filter response degenerates to:

$$G_0(f) \approx \frac{S_{ss}^{\alpha_0}\left(f - \frac{\alpha_0}{2}\right)}{S_{ss}(f - \alpha_0) + S_{ii}(f - \alpha_0)} \quad (5.30a)$$

and

$$G_1(f) \approx \frac{S_{ss}^{-\alpha_0}\left(f + \frac{\alpha_0}{2}\right)}{S_{ss}(f + \alpha_0) + S_{ii}(f + \alpha_0)} . \quad (5.30b)$$

From Eq. (5.30), it can be seen that the filter weights only depend on the ratio of the cyclic spectrum of the desired signal to the spectrum of the input signal. When $\alpha=0\text{Hz}$, Eq. (5.30) degenerates to the filter response for a time-invariant optimal filter. For other α values, which are the time-varying portions of the filter, the numerator is the cyclic spectrum of the desired signal instead of the conventional spectrum of the desired signal. Assume that the cyclic frequency for the SOI is 6kHz ($\alpha_0=6\text{kHz}$) and for the SNOI it is 6030Hz, and the carrier frequencies are equal. The filter responses in Eq. (5.30a) and Eq. (5.30b) for different interference powers are numerically calculated and plotted as a function of input *CIR* in Fig. 5.4a and 5.4b. It can be seen from Fig. 5.4a that there are two strong impulses in the filter response for $G_0(f)$, at $f = 0\text{Hz}$ and $f = 6000\text{Hz}$. These features are explained by Eq. (5.30). Since the cyclic spectrum of the desired signal at α_0 has maximum values at $f=\pm \alpha_0/2$, and the shifting of the cyclic spectrum by $\alpha_0/2$ results in maximum values at $f = 0\text{Hz}$ and $f = \alpha_0$ scaled by the reciprocal of the shifted version of the conventional spectrum of the input signal by α_0 . This is similar to $G_1(f)$ which has maximum values at $f = 0\text{Hz}$ and $f = -\alpha_0$.

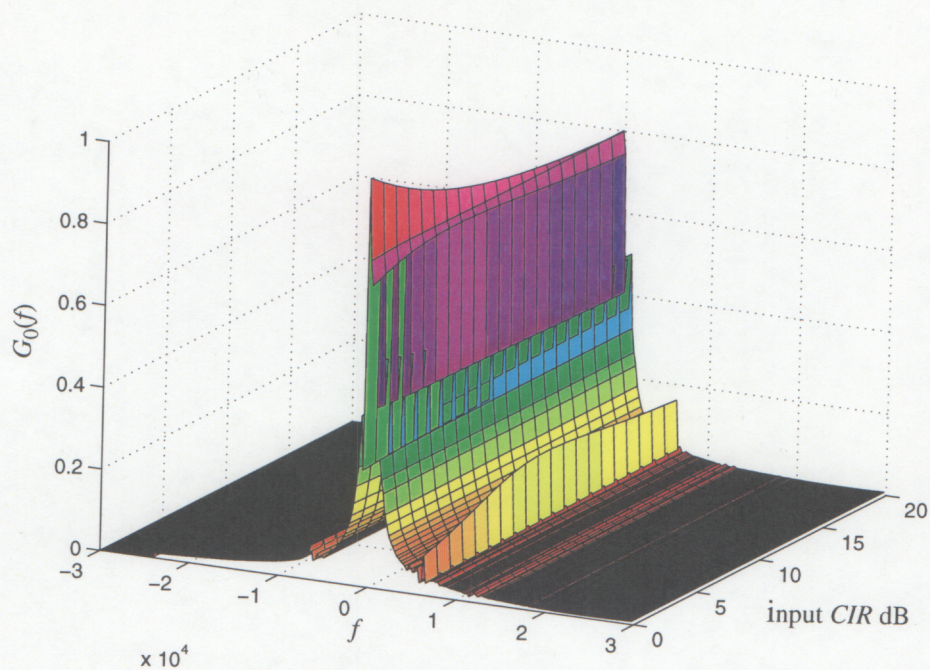


Fig. 5.4a Filter response $G_0(f)$ of optimal time-dependent filter

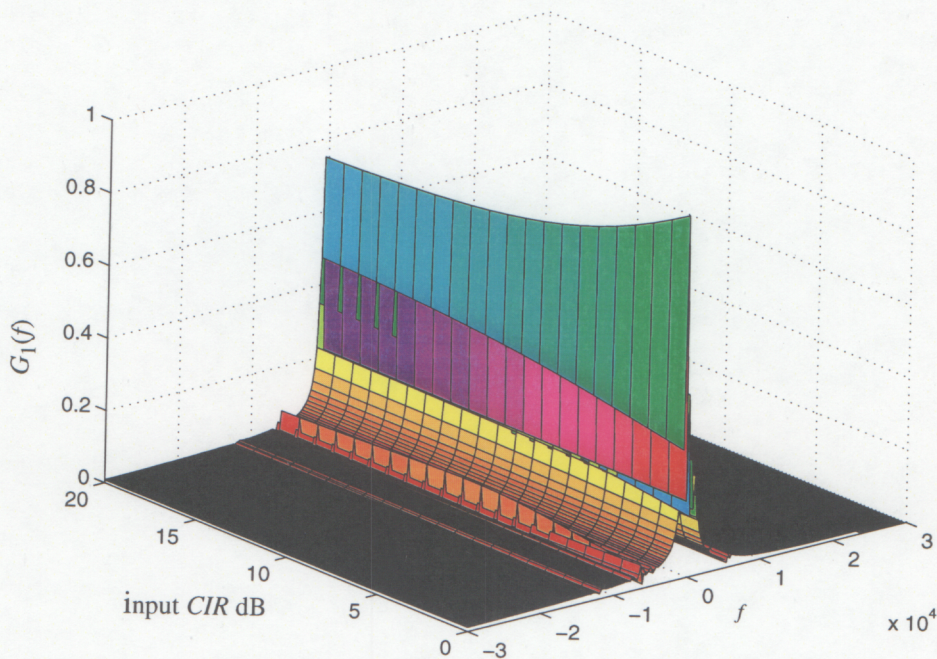


Fig. 5.4b Filter response $G_1(f)$ of optimal time-dependent filter

The *MSE* in Eq. (5.20) for this case can be simplified as

$$MSE = \int_{-\infty}^{\infty} \left| S_d(f) - \sum_{n=0}^{L-1} \sum_{m=0}^{L-1} G_n(f) G_m^*(f) \left(S_{ss}^{-\beta_n + \gamma_m} \left(f - \frac{\beta_n + \gamma_m}{2} \right) + S_{ii}^{-\beta_n + \gamma_m} \left(f - \frac{\beta_n + \gamma_m}{2} \right) \right) \right| df. \quad (5.31)$$

Because the periodicities of the filter are chosen to be the cyclic frequencies of the desired signal, the spectral correlation density for the interference will be zero except when $\beta_n = \gamma_m$. If L covers all the possible cyclic frequencies for the desired signal, the theoretical *MSE* for the TDAF can be simplified to

$$MSE = \int_{-\infty}^{\infty} \left(\sum_{n=0}^{L-1} G_n(f) G_n^*(f) S_{ii}(f - \beta_n) + N_y(f) \right) df. \quad (5.32)$$

Note that the *MSE* is a function of a distortion term for the filtered SOI $N_y(f)$ and the filtered interference. The optimal solution trades distortion for noise and interference rejection to produce a minimal *MSE*.

The output *CIR* is evaluated numerically using Eq. (5.15). To simplify the numerical computation involved in Eq. (5.15) and (5.30), we make the following assumptions:

- The spectral correlation of an AMPS signal at $\pm 2\alpha$ (twice the SAT frequency) is small enough to be neglected.
- The interference has a different SAT frequency than the SOI.
- Filter periodicities associated with the desired signal are used, excluding the time-invariant term.
- The desired signal and the interfering signal are statistically independent.
- The noise in the channel is statistically independent from the AMPS signals.

Fig. 5.5 shows the output *CIR* as a function of the input *CIR* using 10^4 data points. The

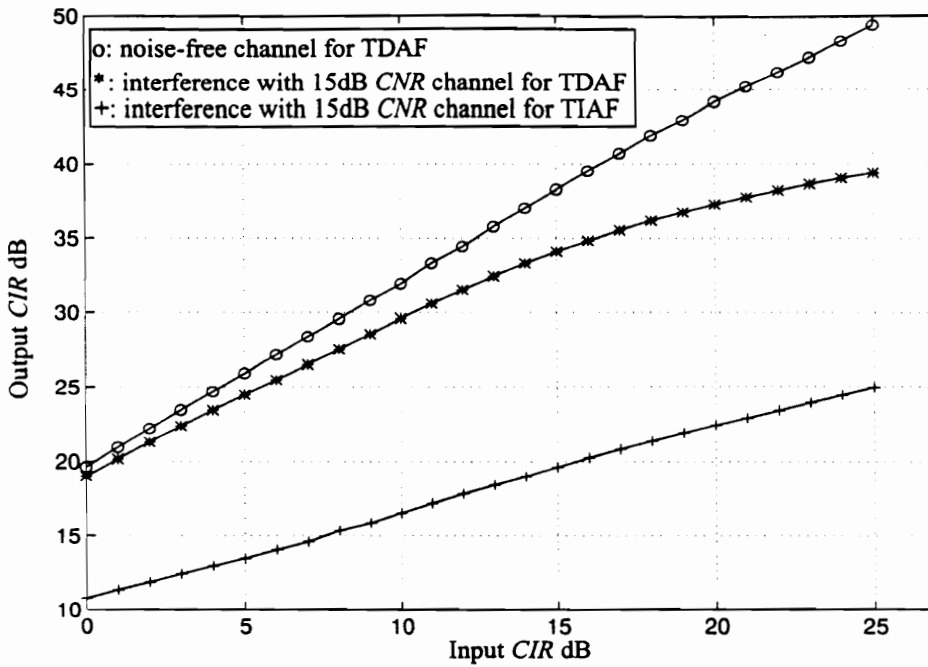


Fig. 5.5 Output *CIR* of the TDAF and TIAF processed signal for interference-only and noisy channels

received signal is formed by adding the SOI and the SNOI together. Both of them are complex baseband AMPS FM signals with SAT frequencies of 6000Hz and 6030Hz, respectively. In Fig. 5.5, it can be seen that the output *CIR* increases almost linearly with input *CIR* when noise is absent. When noise is present the overall gain provided by the TDAF is reduced and is no longer linear in the region for high input *CIR*. When the input *CIR* is high, the noise is a significant factor affecting the performance. For example, the analytical *CIR* of the output is 26dB for a noise free channel when the input *CIR* is 5dB, and it is 25dB for a noisy channel ($CNR=15$ dB) for the same input *CIR*. On the other hand, the analytical output *CIR* is 43dB for a noise-free channel when the input *CIR* is 20dB, while the *CIR* is 25dB for a noisy channel for the same input *CIR*. AWGN can be reduced by the TDAF but can not be totally removed. To compare the performance of a TDAF and a time-invariant filter (TIAF), the analytical output *CIR* of an AMPS signal after a TIAF is also evaluated using the same design equations, i.e., $\alpha=0$ Hz only. The results are plotted in Fig. 5.5. It can be seen that the improvement provided by the TIAF is

10-15dB less than that provided by the TDAF. The results prove that a TDAF is superior to a TIAF for interference rejection for a signal that exhibits statistical periodicity.

3) Fading Channel

The effects of different types of fading on the cyclic features have been analyzed in Chapter 4. Thus, the performance of the TDAF when the signal undergoes fading can also be computed. Let

$$E_{in}(f) = \sum_{n=0}^{L-1} G_n(f) G_n^*(f) S_{ii}(f - \beta_n) + \frac{\eta}{2}. \quad (5.33)$$

Substitute Eq. (4.34) and (5.33) into Eq. (5.20), the *MSE* for a flat fading channel is

$$MSE = \int_{-\infty}^{\infty} |S_d(f) - \sum_{n=0}^{L-1} \sum_{m=0}^{L-1} G_n(f) G_m^*(f) |H_0|^2 \sqrt{\pi\tau_0} \int_{-\infty}^{\infty} e^{\frac{v^2}{f_m^2} - \beta_n + \gamma_m} \left(f - \frac{\beta_n + \gamma_m}{2} - v\right) dv - E_{in}(f) | df. \quad (5.34)$$

The *MSE* for a frequency selective fading channel is obtained by substituting Eq. (4.42) into Eq. (5.20)

$$MSE = \int_{-\infty}^{\infty} |S_d(f) - \sum_{n=0}^{L-1} \sum_{m=0}^{L-1} G_n(f) G_m^*(f) |H_0|^2 \sqrt{\pi\tau_0} \int_{-\infty}^{\infty} \left(\frac{1}{1 + j \frac{-\beta_n + \gamma_m}{f_0}} \right) e^{\frac{(\pi\tau_0 v)^2}{1 + j \frac{-\beta_n + \gamma_m}{f_0}}} S_{ss}^{-\beta_n + \gamma_m} \left(f - \frac{\beta_n + \gamma_m}{2} - v\right) dv - E_{in}(f) | df. \quad (5.35)$$

The output *CIR* of the TDAF processed signal for the flat fading channel is

$$\frac{C}{I} = \frac{\int_{-\infty}^{\infty} \left| \sum_{n=0}^{L-1} \sum_{m=0}^{L-1} G_n(f) G_m^*(f) |H_0|^2 \sqrt{\pi} \tau_0 \int_{-\infty}^{\infty} e^{\frac{v^2}{f_m^2}} S_{ss}^{-\beta_n + \gamma_m} \left(f - \frac{\beta_n + \gamma_m}{2} - v \right) dv \right| df}{\int_{-\infty}^{\infty} \left| \sum_{n=0}^{L-1} \sum_{m=0}^{L-1} G_n(f) G_m^*(f) S_{ii}^{-\beta_n + \gamma_m} \left(f - \frac{\beta_n + \gamma_m}{2} \right) \right| df} , \quad (5.36)$$

and for frequency selective fading is

$$\frac{C}{I} = \frac{\int_{-\infty}^{\infty} \left| \sum_{n=0}^{L-1} \sum_{m=0}^{L-1} G_n(f) G_m^*(f) |H_0|^2 \sqrt{\pi} \tau_0 \int_{-\infty}^{\infty} \left(\frac{1}{1 + j \frac{-\beta_n + \gamma_m}{f_0}} \right) e^{\frac{(\pi \tau_0 v)^2}{1 + j \frac{-\beta_n + \gamma_m}{f_0}}} S_{ss}^{-\beta_n + \gamma_m} \left(f - \frac{\beta_n + \gamma_m}{2} - v \right) dv \right| df}{\int_{-\infty}^{\infty} \left| \sum_{n=0}^{L-1} \sum_{m=0}^{L-1} G_n(f) G_m^*(f) S_{ii}^{-\beta_n + \gamma_m} \left(f - \frac{\beta_n + \gamma_m}{2} \right) \right| df} . \quad (5.37)$$

Fig. 5.6 shows the output *CIR* assuming flat fading and various different Doppler frequencies. The output *CIR* for a non-fading channel is also plotted in the same figure for comparison. It can be seen from Fig. 5.7 that a 1-3dB degradation results from lower Doppler frequencies such as 30Hz, while 3-5dB degradation results from high Doppler frequencies such as 60Hz. Although the channel here is flat, the amplitude fluctuations result in smearing the cyclic autocorrelation function shown in Eq. (4.33). Consequently, the output *CIR* of the TDADF is affected by Doppler shift. For frequency selective fading, the degradation of the output *CIR* is caused by both the motion of the vehicle and multipath. A two-ray Rayleigh fading model can be used to demonstrate this point. Multipath is usually characterized by the *rms* of the multipath delay σ_τ , which is directly related to the channel coherence bandwidth f_0 directly. Fig. 5.7 shows the output *CIR* for different σ_τ when the Doppler frequency is 30Hz. For comparison, the *CIR* of the flat fading case is also plotted in the same figure. From Fig. 5.7, it can be seen that degradation caused by the multipath delay ($\sigma_\tau = 2.5\mu s$) is not significant if the channel coherence bandwidth f_0 is larger than

the cyclic frequencies of the desired signal. However, when the delay increases, the channel coherence bandwidth decreases. When f_0 is smaller than α , the degradation is significant. For example, given a Doppler frequency of 30Hz and $\sigma_\tau = 10\mu\text{s}$, the output CIR drops 5dB compared to the flat fading case. This example is repeated for a high Doppler frequency of 60Hz and the results are shown in Fig. 5.8. The performance of the filter declines in a similar way for different σ_τ as the low Doppler frequency case shown in Fig. 5.7. Clearly, the performance degradation is more severe than in the lower Doppler case since the motion of the vehicle results in a higher Doppler shift.

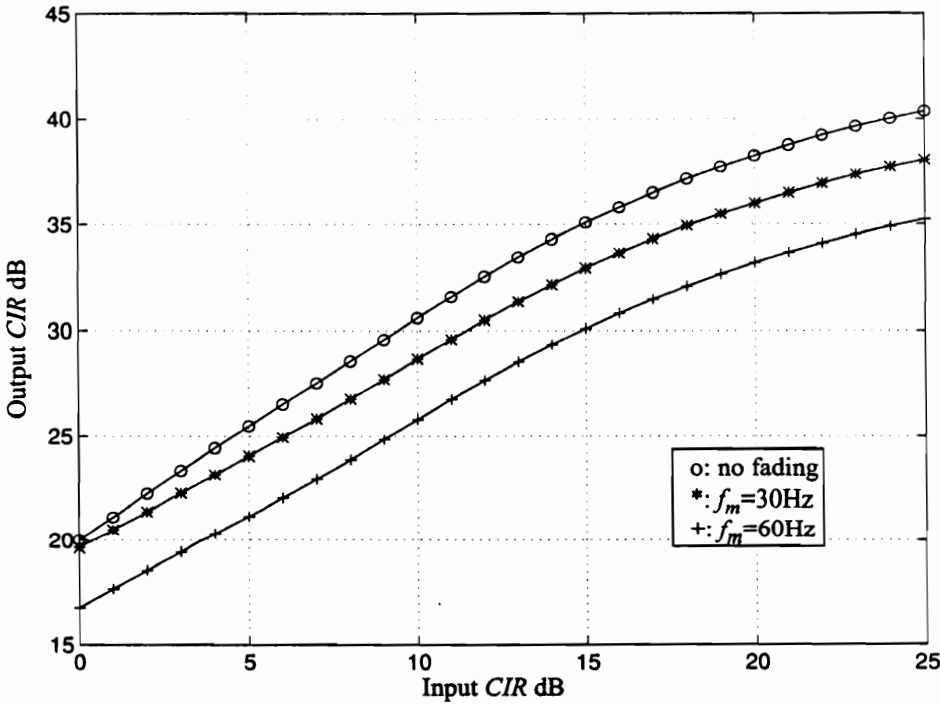


Fig. 5.6 Output CIR of the TDAF processed signal of flat fading case for different Doppler frequencies

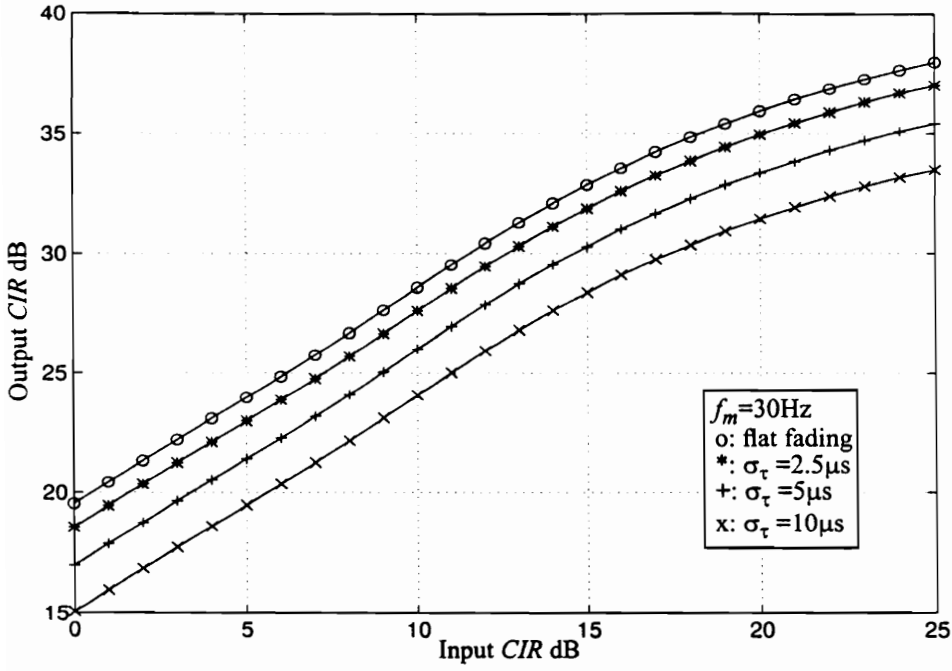


Fig. 5.7 Output *CIR* of the TDAF assuming frequency-selective fading and various channel delay spread, Doppler frequency is 30Hz

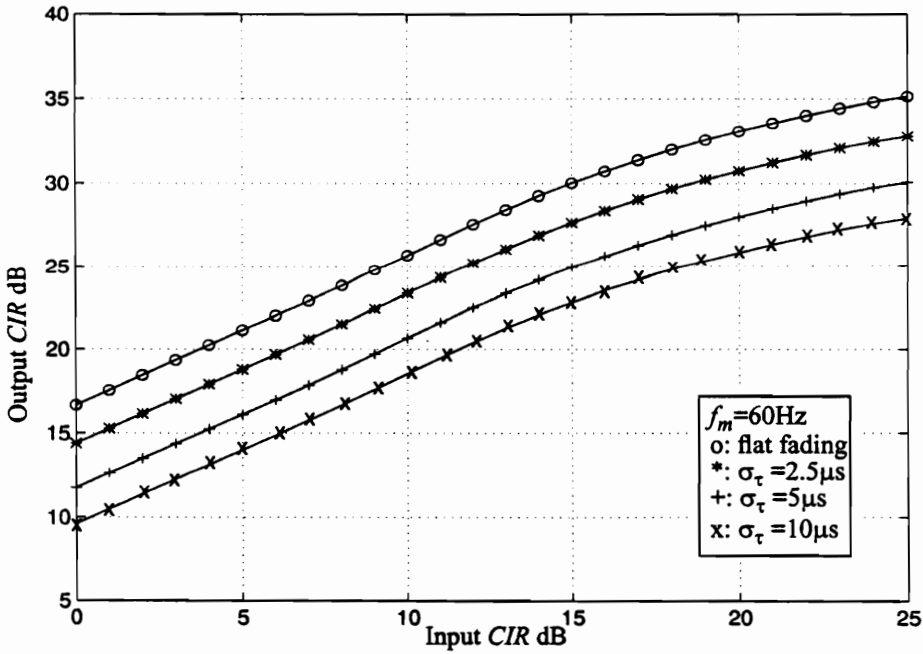


Fig. 5.8 Output *CIR* of the TDAF assuming frequency-selective fading and various channel delay spread, Doppler frequency is 60Hz

5.3 Configuring the Adaptive Time-Dependent Filtering for Enhancing AMPS Signals

As described in Section 5.1, a TDAF can be implemented either in the time domain or frequency domain. In this chapter, a time domain implementation of the TDAF, the FRESH filter, is used for AMPS co-channel interference rejection.

A reference signal is needed to train an adaptive filter. This reference signal can be correlated with either the desired signal or the interference depending on whether the filter enhances the SOI at the filter output or at the error output. For the AMPS signal, no direct training sequence is available. However, an optimal TDAF under ideal conditions, i.e., with a training sequence (clear SOI), can provide a theoretical upper bound on TDAF performance. The TDAF can be realized in the manner shown by Fig. 5.2. The input signal $x(k)$ is first frequency shifted by the cycle frequencies corresponding to the desired signal. M FIR filters are used to jointly filter the shifted versions of $x(k)$ to produce the output $y(k)$. The difference between the reference signal and the estimated signal $y(k)$ forms the error $e(k)$ which is used to update the weights of the FIR filters.

Although using an ideal training sequence is not practical for real situations, the SAT information can be used to train the filter. A blind adaptive implementation of the TDAF shown in Fig. 5.9 can exploit the spectral correlation due to the SAT to extract the signal of interest. A delayed version of the input serves as the training signal for the TDAF as long as the filter periodicities are constrained to not have the time-invariant term, i.e., $\alpha_m \neq 0$. The filter uses frequency shifted versions to estimate the incoming signal. Signals which exhibit spectral correlation for the chosen frequency shifts are passed by the filter, hence this filter can be viewed as a spectral correlation predictor (SCP). The filter periodicities α_m are multiples of the cycle frequency of either the SOI or SNOI. If the periodicities correspond to multiples of the SOI SAT frequency, then the output $y(k)$ of the filter is an estimate of the SOI and the error $e(k)$ contains an estimate of the SNOI. The recursive least

square (RLS) algorithm is used to adapt the filter. The update algorithm for the filter structure is provided by the procedure in Table 5.1.

A receiver composed of a two-stage TDAF, shown in Fig. 5.10 provides better performance than the single stage TDAF. The filter at the first stage is periodic at multiples of the SOI SAT frequency and is used to estimate the SOI. The output is fed to the second filter, whose periodicities correspond to the SNOI SAT frequency, and is used to estimate and remove the SNOI. The two-stage processing provides both signal enhancement and interference suppression. Our simulation experience has shown that two-stage processing tends to be more robust to fading than single-stage processing [HR95], and this is demonstrated in the following section.

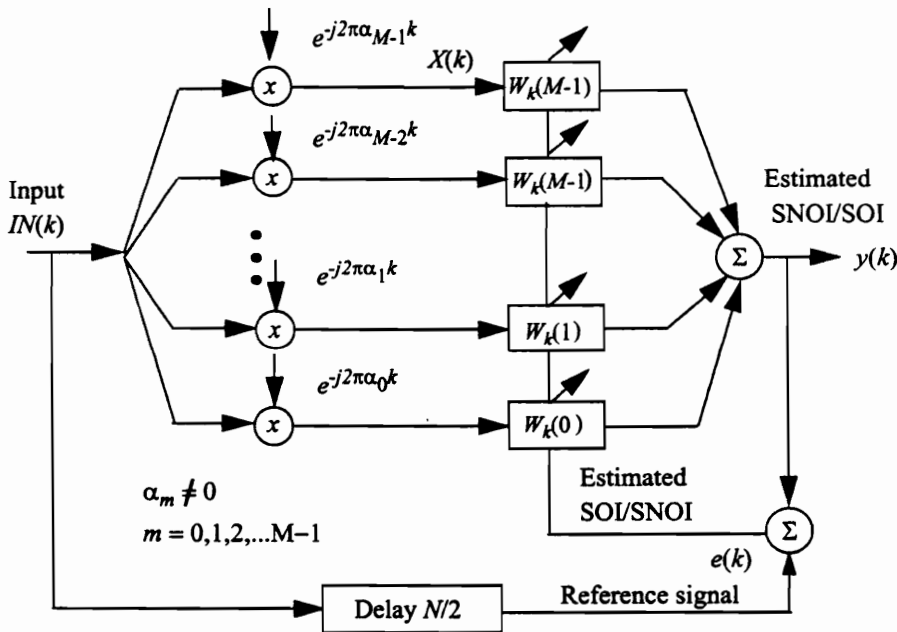


Fig. 5.9 Block diagram of the spectral correlation predictor (SCP)

Table 5.1 Circular RLS Algorithm [Hay91]

$P_0 = \delta^{-1}I$, δ is a very small positive number (NM, NM)
 (N is the filter length and M is the number of periodicities)
 $W_0 = 0$, initial weights ($NM, 1$)
 λ = positive forgetting factor ≤ 1
 T = sampling period
 α_m = cyclic periodicity
 for $k=1, 2, 3, \dots$
 $IN_k = kth$ input vector $[x(k) \ x(k-1) \ \dots \ x(k-N+1)]^T$
 $x_k(m) = IN_k e^{j2\pi\alpha_m kT}$, subvector for each α_m
 $X_k = [x_k(M-1) \ x_k(M-2) \ \dots \ x_k(0)]^T$, frequency shifted input vector ($NM, 1$)
 $P_k = X_k^H P_{k-1}$, intermediate result
 $s(k) = 1 + P_k X_k$
 $C_k = P_k^T / s(k)$, gain vector
 $y(k) = W_{k-1}^H X_k$, output
 $e(k) = x(k-N/2) - y(k)$, error
 $W_k = W_{k-1} + C_k e^*(k)$, weight update
 $P_k = 1 / (P_{k-1} - C_k P_k)$, inverse correlation matrix update

H: hermitian transpose

*: conjugate

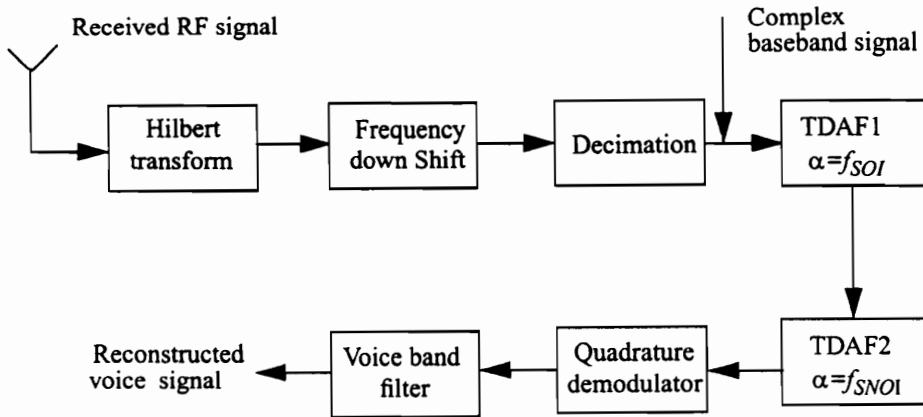


Fig. 5.10 Block diagram of a receiver using two-stage TDAF

5.4 Simulation Study

Here results are presented to show the potential of the TDAF for rejecting AMPS interference.

5.4.1 Assumptions

The simulation study is based on the following assumptions:

- Rayleigh fading is applied that assumes an 800MHz carrier and mobile unit velocities of 5mph and 65mph.
- Two ray propagation channels are applied to both the SOI and SNOI. Different channel parameters are used for SOI and SNOI.
- The SOI is a digitized signal with carrier frequency of 30kHz, sample rate of 120kHz and SAT frequency of 6kHz. The interference is another digitized signal with same carrier frequency and sample rate, but having a SAT frequency of 6030Hz. Both the SOI and the SNOI are frequency down converted to complex baseband signals.
- The filter periodicities are chosen to be the periodicities of the SOI.
- A commonly used quadrature demodulation structure shown in Fig. 5.11 performs the FM demodulation. The receiver performance depends on the type of demodulator as

well as the TDAF. This quadrature demodulator works well for relatively high levels of carrier-to-interference ratios (*CIRs*), but fails to produce a satisfactory output when the *CIR* drops below 9dB. This is especially true when the FM signal is corrupted by Gaussian noise. This demodulator provides the baseline performance for evaluating the new techniques.

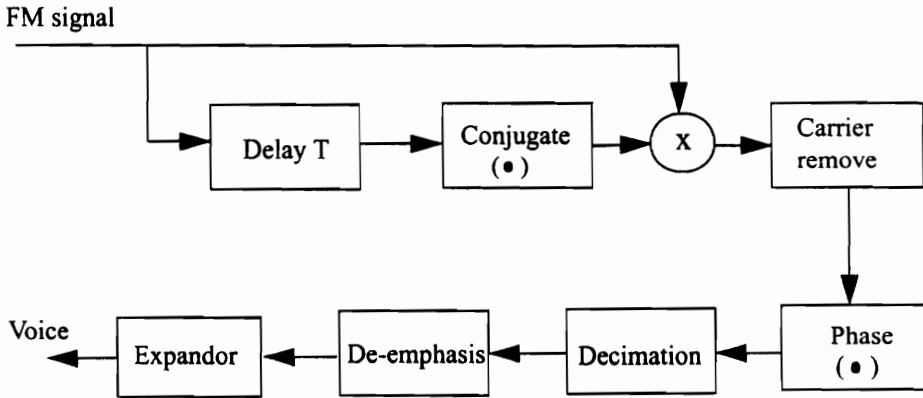


Fig. 5.11 Block diagram for AMPS quadrature demodulator

5.4.2 Experimental Procedure

Most of the simulation results presented are obtained using digitized AMPS signals. However, results based on simulated data are also presented to validate our analytic model and to show how non-ideal implementations degrade the performance.

Two digitized data files representing the SOI and SNOI are used here. The modulated signals are baseband signals which are sampled at 60kHz. The received signal is generated by adding the SOI to the SNOI with an appropriate level of noise and flat fading. The noise level for the digitized data itself is about 17dB.

Different cases using various carrier separations and fading characteristics are examined. A bandpass filter with passband from 300Hz to 3000Hz is used after the demodulator to extract the voice signal. We assume in our calculations that the digitized signals are noise

free and the corresponding demodulated voice signal is noise free. In other words, the distortion introduced by the quadrature demodulator is assumed to be negligible at this point. The output *CIRs* are calculated to measure the performance improvement provided by the SCP. The output *CIRs* can be measured by passing the SOI and the SNOI through the SCP separately after the filter has converged because of the linearity of the SCP. However, these measurements are not stable if the channel varies rapidly. One solution to overcome the fluctuations of the measurements is to measure the *CIR* each time the weights are updated.

Perhaps the best way to evaluate the SCP is by assessing the quality of the demodulated voice signals. The method that was used by the previous section for calculating *CIRs* is no longer suitable here since the quadrature demodulator is a non-linear process. Instead, the *MSE* can be used to calculate the processing gains. It is not a perfect indicator of voice perceptibility, but it does provide a general indication. *MSE* usually is calculated by two methods [GBGM80]. The first method computes *MSE* by averaging instantaneous *MSE* for 20-30msec time slots. The second method smooths the *MSE* by averaging the difference in FFT bin magnitudes over the band 300Hz to 3000Hz. In our simulations, the *MSE* for the voice signal is calculated via the former method.

Another good method for determining the performance gain is to measure the *MSE* of the SAT after the SCP. To measure the *MSE* of the SAT of the received or the processed AMPS signals, a very narrow bandpass filter centered at the desired SAT frequency, such as 6000Hz with bandwidth of 30Hz, is used before the voice bandpass filter to extract the SAT signals.

5.4.3 Results

The results using digitized data are presented in Table 5.2. Table 5.2 shows the output *CIR* provided by the TDAF for various input *CIRs* and carrier separations. Also shown is the *MSE* of the demodulated voice signal provided at the output of the demodulator. The *MSE*

of the SAT is also available in this table.

Fig. 5.12 shows the output *CIRs* for different carrier separations as a function of input *CIR* assuming no fading and a *CNR* of 25dB. It can be seen that the performance improvement increases slightly when the carrier separation of the two signals increases. For example, the output *CIR* is about 31dB for carrier separation of 400Hz at an input *CIR* of 15dB, while it is about 28dB for a carrier separation of 0Hz. This can be explained by the fact that the degree of overlap is reduced when the carrier frequencies of the two signals are separated further. Nevertheless, the difference is only 1-3dB. All the three curves show the similar the performance trend of the SCP, i.e., the output *CIRs* are almost linear functions of the input *CIRs*. This observation is consistent with the theoretical results which are shown in Fig. 5.5.

The corresponding *MSEs* of the demodulated voice signal and SAT are plotted in Fig. 5.13 and Fig. 5.14 for different carrier separations. The *MSEs* of the demodulated voice signal and SAT for the input signals are also plotted in the same figures for comparison. Generally for the voice signals, 20-25dB of *MSE* represents intelligible quality, 25-40dB of *MSE* provides adequate quality and 40-50dB of *MSE* gives superior quality. From Fig. 5.13, it can be seen that there is 15dB improvement for the voice signals provided by the SCP. The improvement is almost a linear function of input *CIR*. Fig. 5.13 also shows that the *MSEs* for different carrier separations do not differ much, although a larger carrier separation provides slightly better performance. The SAT *MSE* improvements are shown in Fig. 5.14. The *MSEs* do not vary linearly with the input *CIR*. There is an average 10-15dB improvement provided by the SCP for the SAT *MSE*. This improvement is more significant for lower input *CIRs* than the higher *CIRs*.

Table 5.2 CIR, MSE improvement of the voice signals and the SAT provided by a two-stage TDAF

Output CIR, MSE of voice signal, SAT in dB/ Carrier Separation	Input CIR									
	0dB	3dB	6dB	9dB	12dB	15dB	18dB	21dB	24dB	27dB
0Hz (25dB CNR)	15.2 (output CIR) -29.9 (MSE voice signal) -24.5 (MSE SAT power)	18.2 -34.1 -27.3	21.1 -37.4 -28.6	23.9 -40.4 -29.5	26.4 -42.9 -30.1	28.9 -45.7 -38.8	30.9 -47.9 -42.0	33.0 -50.3 -44.6	34.8 -52.4 -47.5	36.5 -54.9 -50.2
200Hz (25dB CNR)	16.1 -30.4 -25.6	19.1 -34.7 -28.4	22.1 -38.2 -30.2	24.9 -40.9 -31.0	27.5 -43.9 -31.6	30.1 -46.8 -31.7	32.3 -49.2 -31.9	34.6 -51.7 -31.9	36.6 -54.1 -32.0	38.0 -56.3 -32.0
400Hz (25dB CNR)	16.9 -31.8 -26.2	19.8 -35.6 -29.7	22.7 -38.8 -31.5	25.6 -41.7 -32.4	28.4 -44.7 -32.9	31.1 -47.5 -32.9	33.6 -50.2 -33.0	35.8 -52.4 -33.0	37.8 -54.9 -33.0	39.4 -57.1 -33.1

To verify the fading effects for the SCP as described in section 5.2, the output *CIRs* and the *MSEs* for the demodulated voice signals and the SAT are measured for different Doppler frequencies. Fig. 5.15 shows the output *CIRs* for Doppler frequencies of 30Hz and 60Hz, and for the non-fading case as well. Clearly, the performance is degraded by several dB when the velocity of the mobile increases. Since the amplitude fluctuates faster for the higher Doppler shift case, the tracking ability of the adaptive filter is affected. The simulation results are very close to the theoretical evaluation for the fading case shown in Fig. 5.6. Also, the *MSEs* of the demodulated voice signals and the SAT, plotted in Fig. 5.16 and Fig. 5.17, show a similar degradation caused by Doppler shifts. Notice that the degradation in the voice signals is worse than that in the FM signals. Based on our simulation experiences, a higher Doppler shift causes more phase discontinuities in the processed signal which results in more spikes in demodulated voice signal when the quadrature demodulator is used.

Table 5.2 and Figures 5.12 to 5.17 show that the *CIR*, voice signal *MSE* and the SAT *MSE* are generally improved when the carrier separation increases and fading is reduced. The lower the *CIR*, the more pronounced the improvement. For example, there is a 15dB *CIR* improvement for the case where the carrier separation is 200Hz and the input *CIR* is 0dB. However, there is only a 4dB improvement when the input *CIR* is 15dB. Also, the more the signals' carriers are separated, the more pronounced the improvement provided by the SCP.

Typically, there is 3-8dB degradation between the cases of lower Doppler frequency and higher Doppler frequency.

The observations are general trends, but not absolute rules. For instance, if two FM signals are very close in frequency, the demodulated voice signal tends to have significant distortion in the sub-audio band and in the super-audio band. This distortion can be filtered without affecting audio quality. However, if the distortion is in the audio band, it

cannot be removed by the bandpass filter and this produces more noticeable distortion.

Uncorrupted, corrupted and reconstructed voice signals are shown in Figures 5.20 and 5.21. In each case, the top subplot is the original voice signal, and the second one is the demodulated voice signal of the corrupted FM signal. The demodulated TDAF filtered signal is plotted at the bottom of these figures. The plots clearly show the effectiveness of the TDAF. The TDAF processed signals are much better than the corrupted signals.

The results for the simulated signals are very similar to those of the digitized signal. However, there is typically a 3-5dB degradation for the digitized data. Fig. 5.19 compares the results of the simulated and the digitized data for a carrier separation of 200Hz and with low Doppler frequency (5mph). The sources of this degradation could be:

- Practical filter roll-offs at the transmitter and the receiver cause a reduction in the second sidelobe energy of the digitized AMPS signals. This information is available and useful for enhancing the simulated signals.
- Imperfect sample rate conversion causes additional distortion of the real data.
- The SAT frequency of the digitized signal is slightly off its ideal frequency. This is the most likely source of degradation.

To confirm the performance of the blind TDAF and also to provide an theoretical bound on performance, output *CIRs* of the AMPS FM signals are measured for the filter trained using a known training sequence. The theoretical performance for the blind adaptive filter is numerically computed and shown in Fig. 5.19 as a function of input *CIR* along with the experimental results. The top curve is the theoretical *CIR* computed from Eq. (5.15). The second curve is the *CIR* for the TDAF with an ideal training sequence. The third curve shows the *CIR* of the blind TDAF, the SCP. It can be seen from the figure that the experimental results with the training sequence are very close to the theoretical values based on the assumption that the *CIRs* are measured after the filter converges. Note that the performance of the SCP is several dB lower than that of the TDAF with a training sequence.

Refinements of the blind adaptive algorithm could improve the performance of the SCP. The theoretical and experimental results discussed above do not include a time-invariant term in the filter. From our simulation experience, the theoretical performance of the optimal filter can be improved by including the time independent branch with the TDAF. This suggests that a modified filter algorithm containing the time-invariant term should be sought to obtain substantially higher output *CIR* levels.

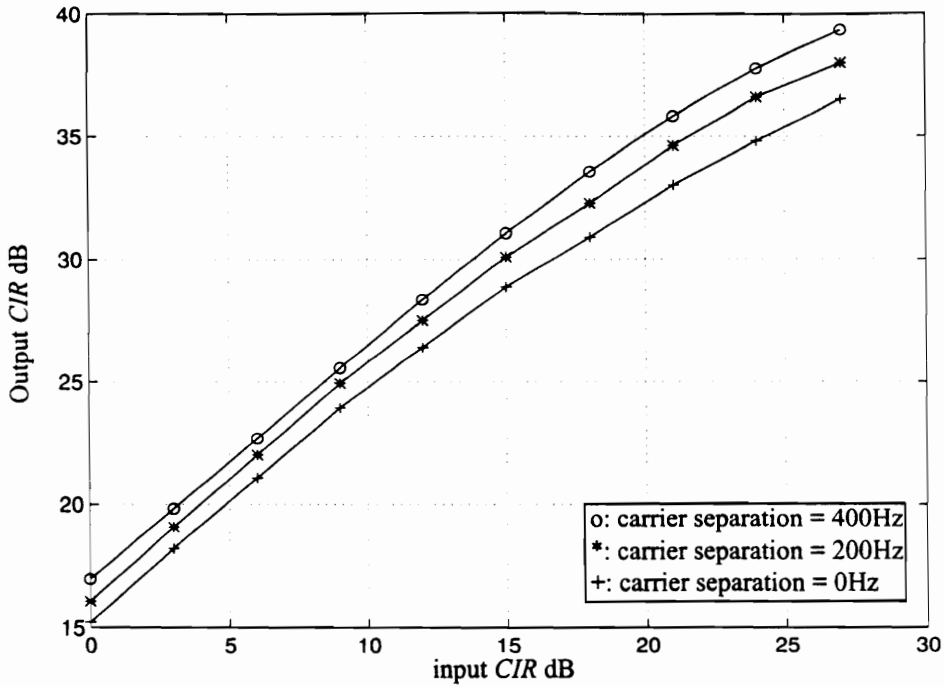


Fig. 5.12 Output *CIR*s after the SCP for different carrier separations, $CNR=25$ dB

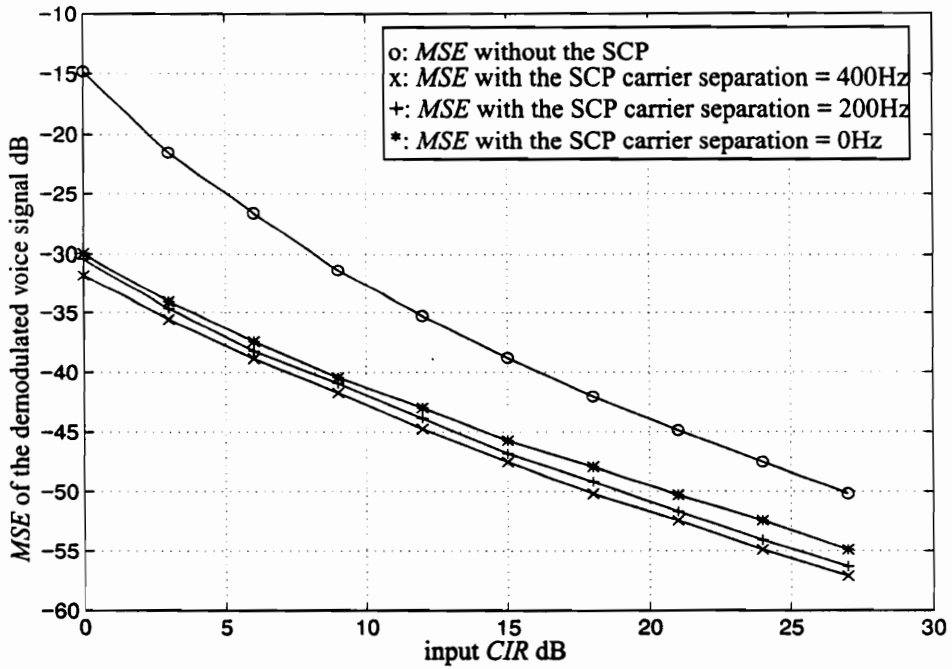


Fig. 5.13 *MSE* of the demodulated voice signals after the SCP for different carrier separations, $CNR=25$ dB

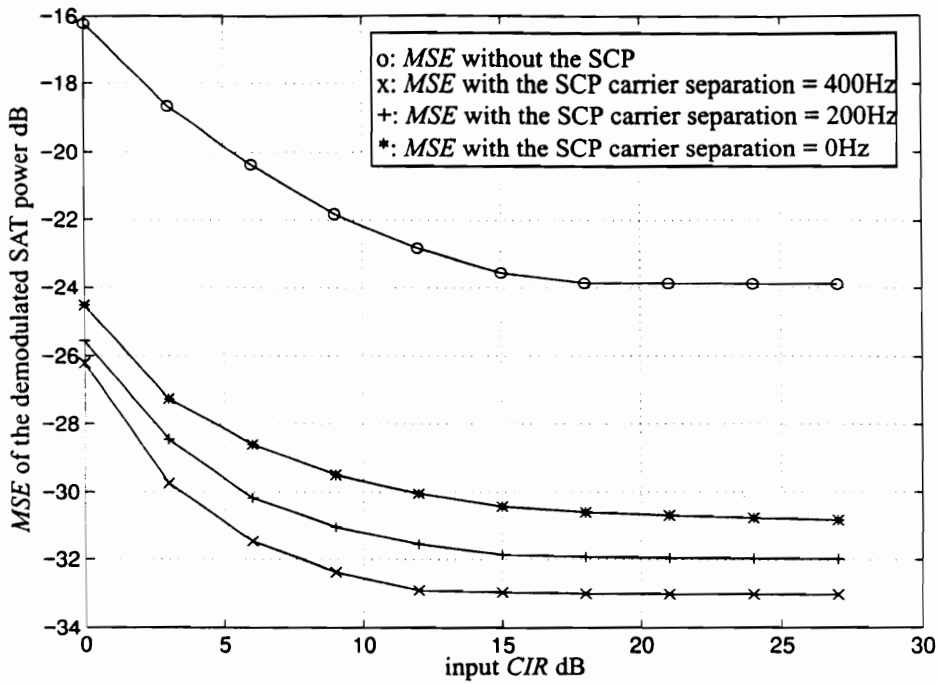


Fig. 5.14 MSE of the demodulated SAT after the SCP for different carrier separations, $CNR=25\text{dB}$

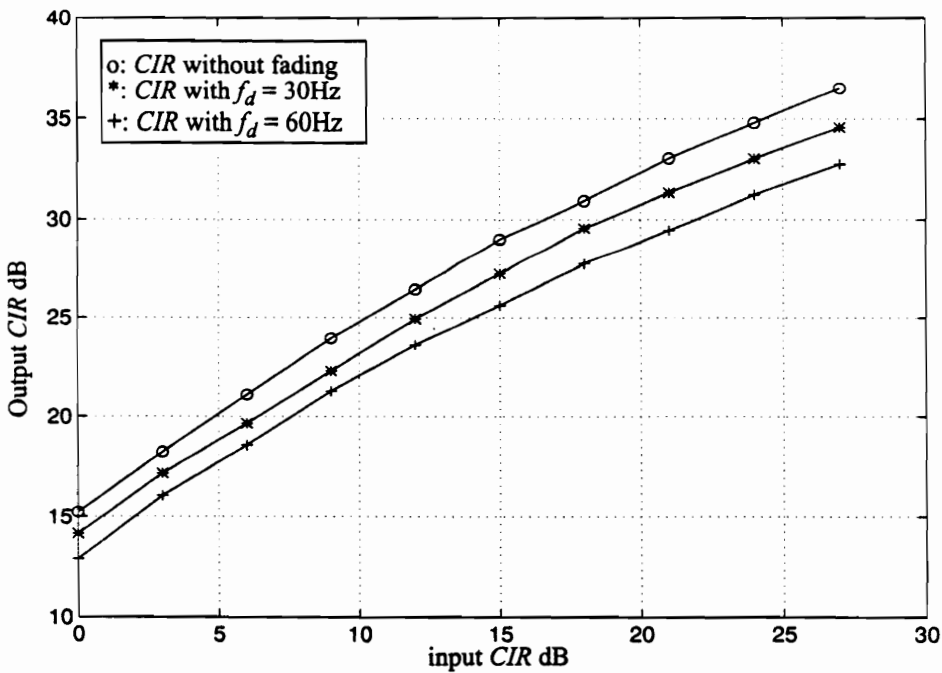


Fig. 5.15 Output CIRs after the SCP for different Doppler frequencies, $CNR=25\text{dB}$

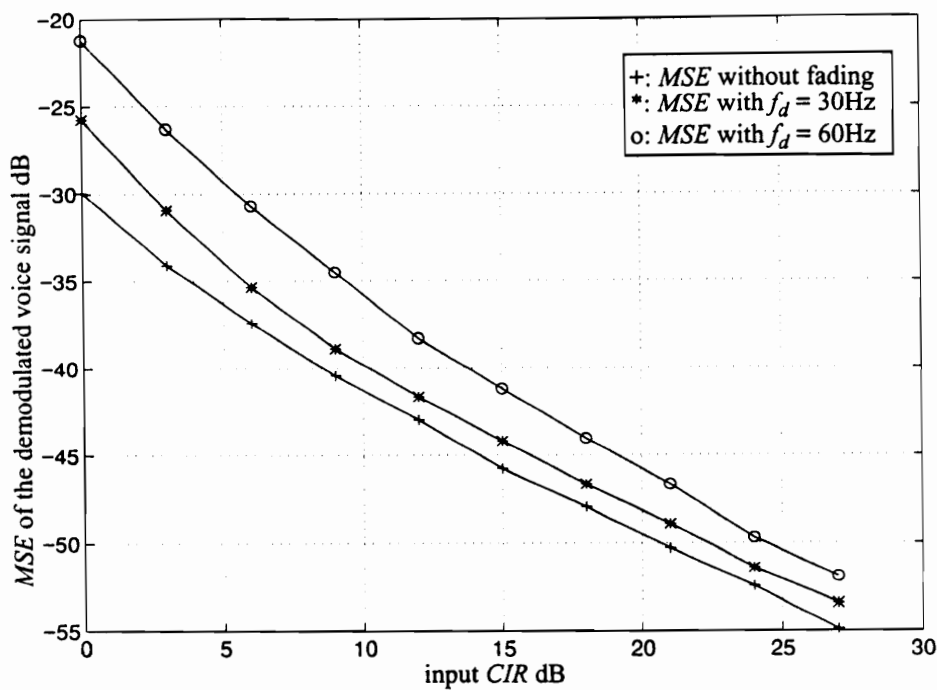


Fig. 5.16 MSE of the demodulated voice signals after the SCP for different Doppler frequencies, $CNR=25\text{dB}$

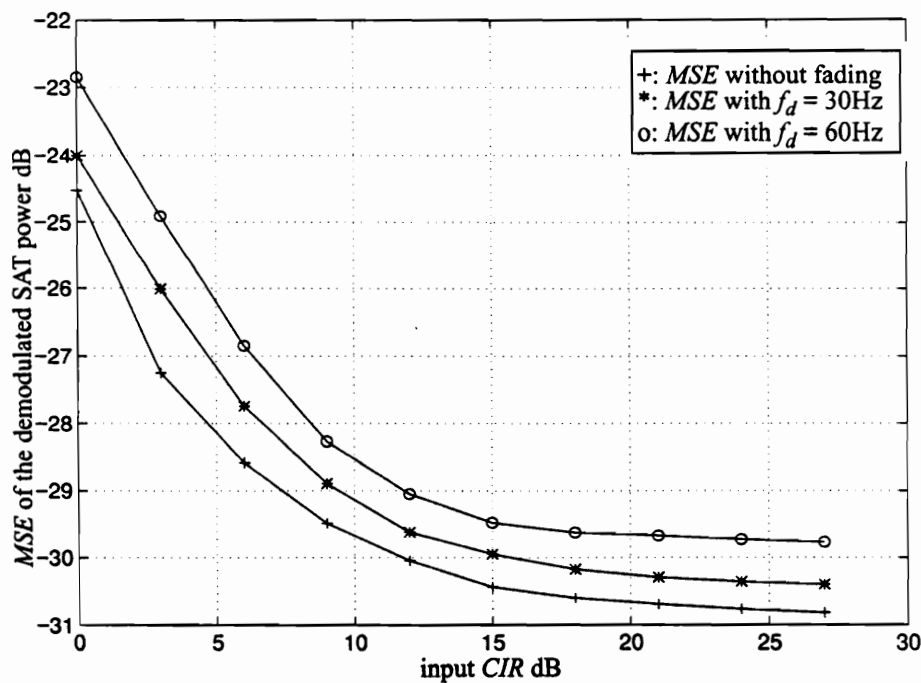


Fig. 5.17 MSE of the demodulated SAT after the SCP for different Doppler frequencies, $CNR=25\text{dB}$

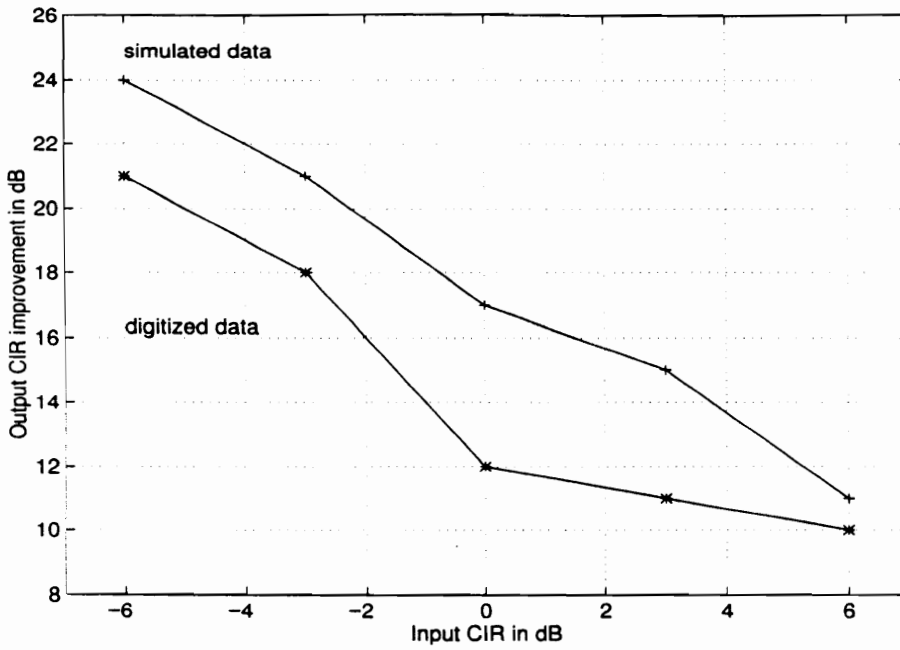


Fig. 5.18 Comparison of *CIR* improvement for simulated and digitized signal, $f_d=60\text{Hz}$, carrier separation is 0Hz and CNR is 25dB

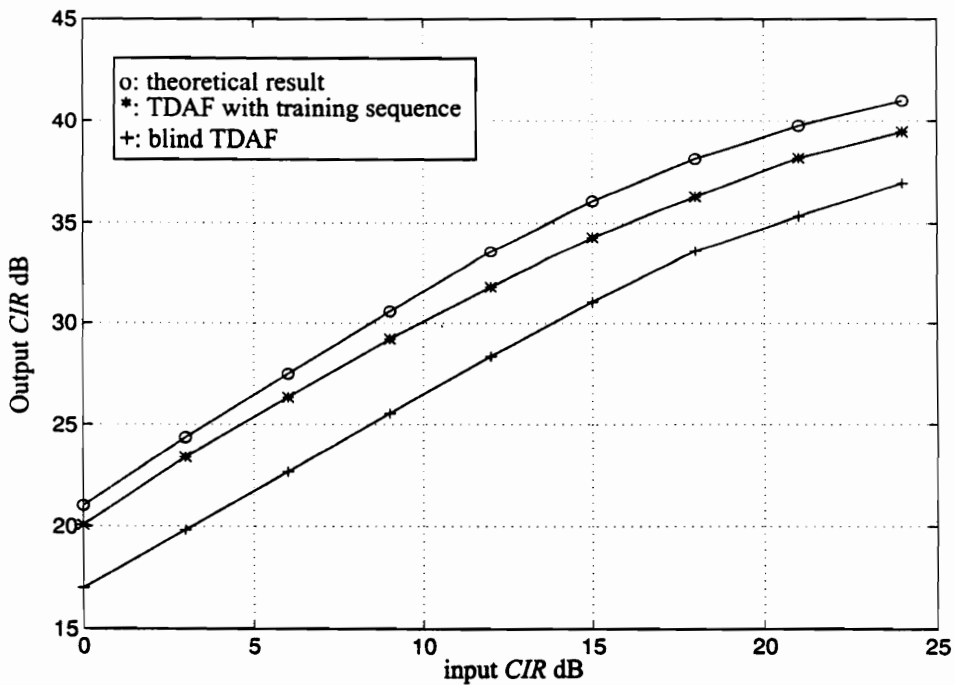


Fig. 5.19 *CIR* Comparison of the theoretical and blind TDAF for the AMPS FM signals, carrier separation= 400Hz , $\text{CNR}=25\text{dB}$

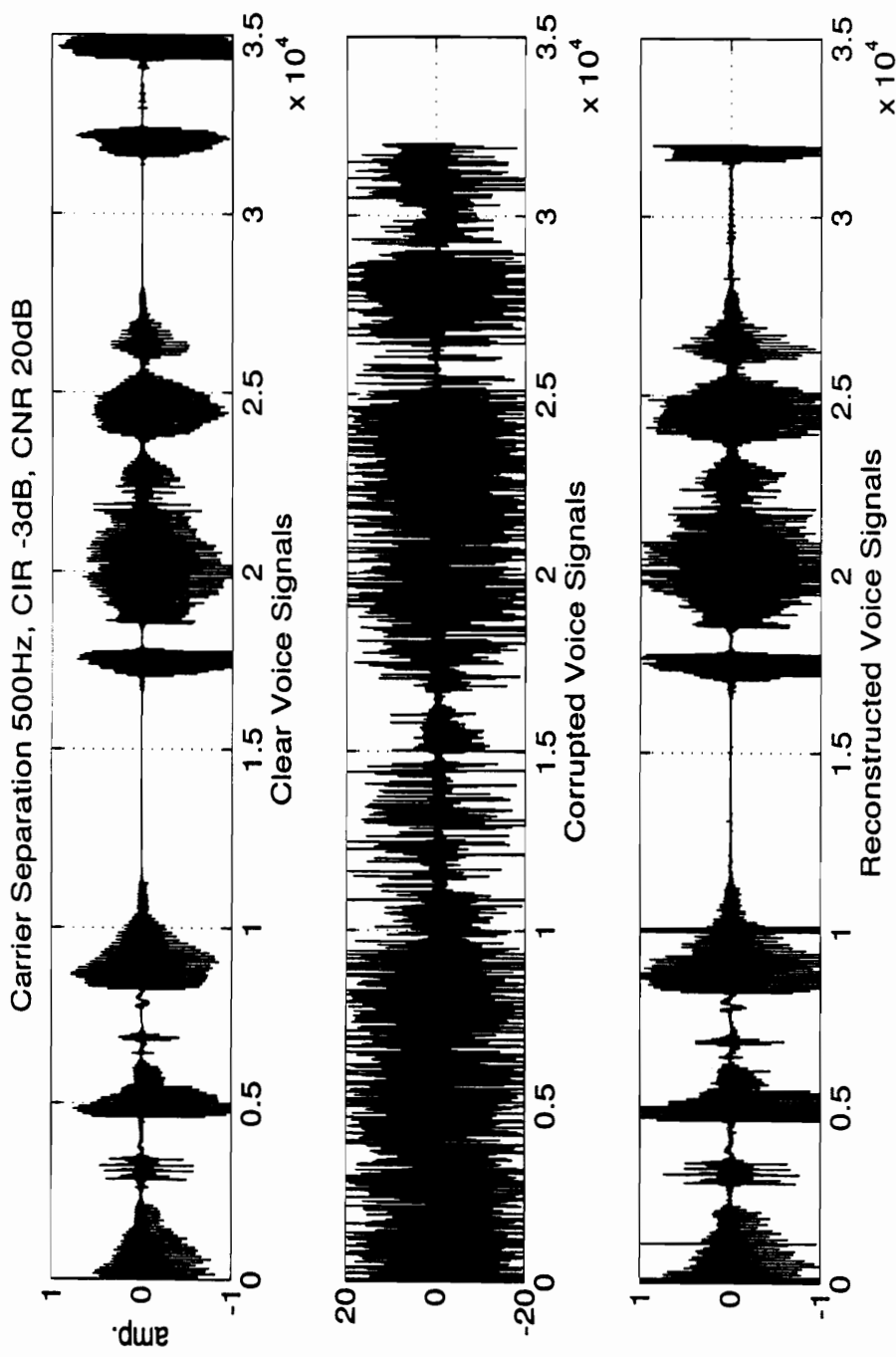


Fig. 5.20 Demodulated voice for $CIR=-3dB$ and $CNR=20dB$, no fading

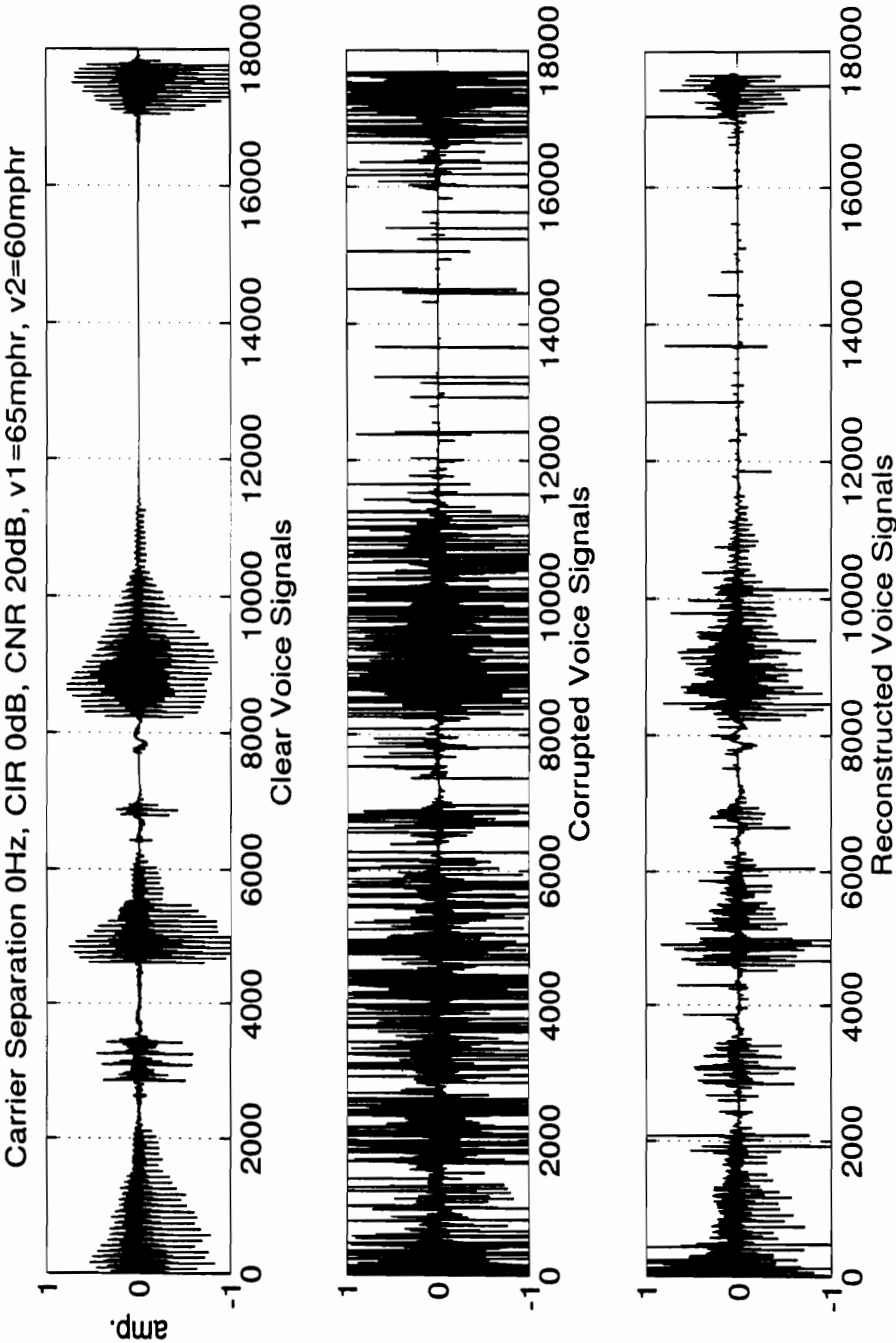


Fig. 5.21 Demodulated voice for $CIR=0dB$ and $CNR=20dB$, high Doppler Frequency

5.4.4 Convergence and Computational Complexity

All the results discussed in the previous section are based on one assumption that they are measured after the filter has converged. The filter convergence rate and computational complexity are also very important in an adaptive filter design. The most convenient method to measure convergence is a short-term average *MSE* as a function of time. There are different ways to compute the short-term average *MSE* (local *MSE*) using a sliding window. For example, a low pass filter with a very small cutoff frequency of 300Hz can be applied to obtain the short-term averaged *MSE*. The lowpass filtered *MSEs* are plotted in Fig. 5.22 as a function of time for different input *CIRs*. The carrier separation here is 0Hz and no fading is introduced. Fig. 5.22 shows that the adaptive filter converges after 0.3 seconds for different *CIRs* ranging from 0dB to 18dB. Fig. 5.23 shows the results for a Doppler frequency of 30Hz. Because of the amplitude fluctuation, the *MSE* is not as smooth as the non-fading case. However, the average *MSE* still converges after 0.3 seconds. When the Doppler frequency increases to 60Hz, the *MSE* converges slower than the previous cases. This is depicted in Fig. 5.24 for different input *CIRs*. It can be seen that the filter does not converge until after about 0.5 seconds. A higher Doppler frequency, which results in frequent amplitude fluctuations, reduces the filter convergence rate. To circumvent this problem, some refined algorithms can be applied and are discussed in the next section.

Besides the convergence rate, the computational complexity is also an important consideration, especially when the algorithms are implemented in real time systems. Generally, we use the number of arithmetic operations required to perform one iteration of the algorithm as a measure of computation complexity. Arithmetic operations include multiplications, divisions, and additions/subtractions. Table 5.3 presents the comparison of the computational complexities of the least mean square (LMS) and recursive least mean squares (RLS) algorithms [Hay91]. In each case, it is assumed that the input data are real-valued and that the order of the estimator equals N , i.e., there are $(N+1)$ coefficients to be estimated.

Table 5.3 Comparison of computational complexities of LMS and RLS algorithms

Algorithm	Number of operations per iteration		
	Multiplications	Divisions	Addition/subtraction
LMS	$2N+1$	0	$2N$
RLS	$2N^2+7N+5$	N^2+4N+3	$2N^2+6N+4$

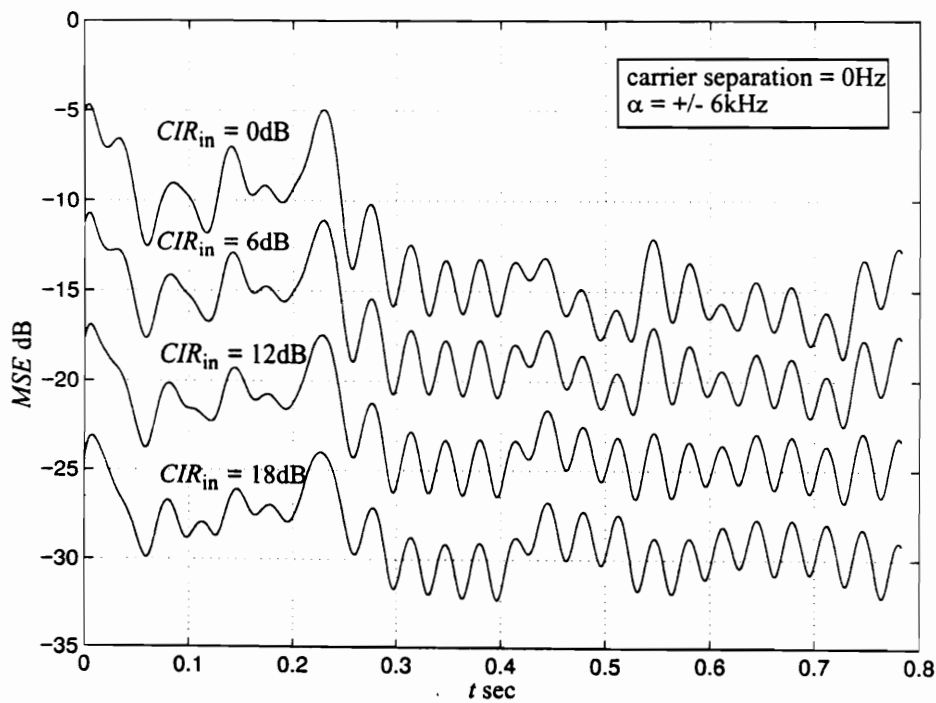


Fig. 5.22 Filtered *MSEs* of the TDAF processed signals for different input *CIRs*.
Carrier separation is 0Hz and *CNR* is 25dB

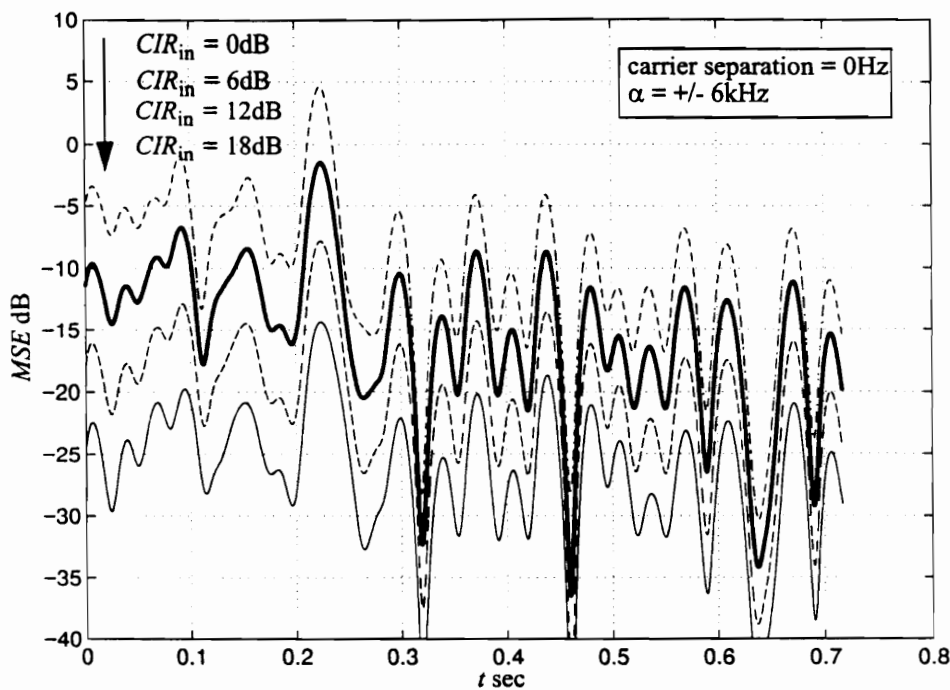


Fig. 5.23 Filtered *MSEs* of the TDAF processed signals for different input *CIRs*, $f_d=30\text{Hz}$. Carrier separation is 0Hz and *CNR* is 25dB

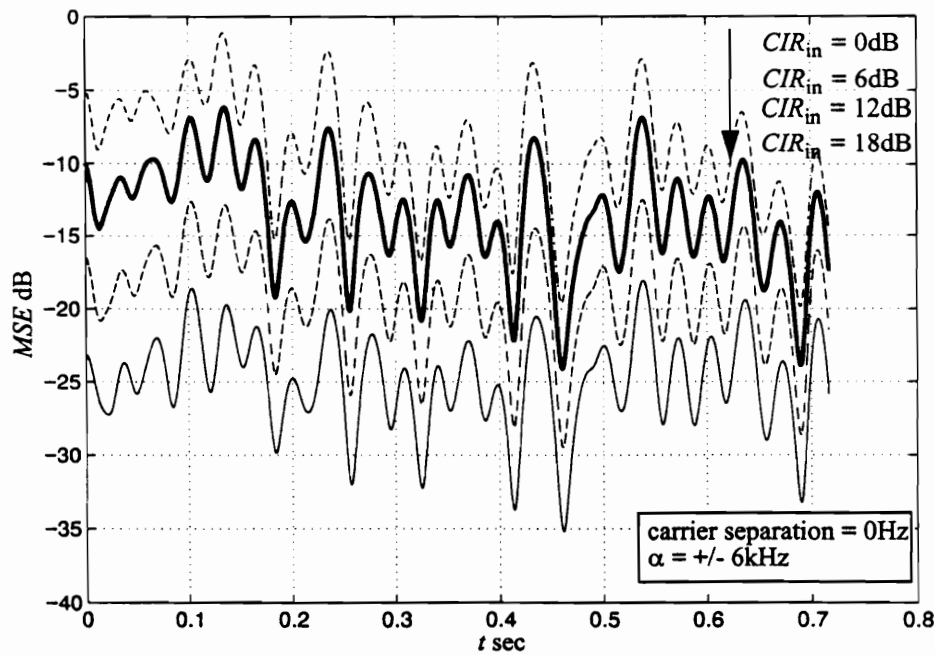


Fig. 5.24 Filtered *MSEs* of the TDAF processed signals for different input *CIRs*, $f_d=60\text{Hz}$. Carrier separation is 0Hz and *CNR* is 25dB

From Table 5.3, it can be seen that the LMS algorithm is much less computationally demanding than the RLS algorithm. On the other hand, the LMS algorithm is less attractive than the RLS algorithm due to its slow convergence, relative sensitivity to the eigenvalue spread and higher steady-state mean squared error [Hay91]. If we assume that the sampling rate is 60kHz, the FIR filter length is 20 and two frequency-shifted versions are used ($N=20$ and $M=2$), the total operations needed for the TDAF using the LMS algorithm are 10^7 per second. An AD21020 DSP processor with a 30nsec instruction cycle only needs 0.3 second to process one second of data. The filter operations are highly parallel. Vector multiplication could be implemented with an application specific integrated circuit (ASIC) and would probably be power efficient enough to be implemented at the mobile unit.

In general, a floating point division takes at least eight times as long as a floating point multiplication. Thus, the total operations needed using the RLS algorithm are about 10^9 per second. In other words, the AD21020 needs 30 seconds to process a one second of data. Clearly, the cost to implement the RLS algorithm is tremendously high. To make a TDAF feasible for a base station, and especially for a mobile station, a modified LMS algorithm with comparable performance to the RLS algorithm needs to be developed. Refinements of the LMS algorithms and structures are discussed in the following section to achieve this performance gain.

5.5 Refinements of TDAF Algorithms and Structures

Improvements can be made to the SCP so that it is more robust for harsh channels, has better overall performance and is less computationally complex. These improvements are described below.

5.5.1 Refinements of the Algorithms

Two adaptive algorithms, LMS and RLS algorithms, are applied to the FRESH filter struc-

ture in this research. Both algorithms use the received corrupted signal as a reference signal to update the weights of the adaptive filter. The LMS algorithm takes a longer time to converge and has less immunity to noise and fading than the RLS algorithm. However, the computational complexity is more intensive for the RLS algorithm than the LMS. Based on our experiments, even the RLS algorithm is sensitive to high levels of noise and fast fading. If the instantaneous power of the desired signal is low, then the algorithms have difficulty in tracking the desired signal, resulting in spikes in the demodulated voice signal.

To overcome the weakness of the TDAF, several algorithms are proposed below. Each has computational complexity similar to the LMS algorithm described previously.

Griffith's Algorithm

For most adaptive algorithms, the desired signal $d(k)$ must be available. However, no reference signal is provided in the AMPS case. The SCP we discussed in the previous sections uses the received signal itself as the reference signal. Although the filter exploits the spectral correlation characteristics of the signal, the absence of a good reference for the blind implementation implies that the minimum mean squared error will be greater than for the training sequence directed least mean square algorithm (LMS) algorithm. Griffith [TJL87] developed an algorithm which can be used in applications in which $d(k)$ is not available, but the correlation function between $d(k)$ and the data vector $X(k)$ is available. The *a priori* knowledge of the correlation function of an AMPS signal can be pre-computed or measured. The basic idea behind the approach is to substitute the expected average value of $d(k)X(k)$ for the vector itself in the adaptive algorithm and thus avoid the need for $d(k)$. Several tests have demonstrated the potential of this approach for fast fading signals. Results show that this new approach helps the filter to converge even if the input signal varies dramatically for a short time period. However, these results presented here do not assume strong multipath.

Here we describe a TDAF based on the Griffith's algorithm. The LMS can be used to update the weights for the FIR filters. In this LMS algorithm, assume that W_k is the current weight vector, W_{k+1} is the new weights, and μ is the adaptation size, the relationship of these parameters are expressed in the following formula:

$$\begin{aligned}
 W_{k+1} &= W_k + \mu e^*(k) X_k \\
 &= W_k + \mu (r^*(k) - y^*(k)) X_k \\
 &= W_k + \mu r^*(k) X_k - \mu y^*(k) X_k \\
 &= W_k + \mu P_k - \mu y^*(k) X_k \quad .
 \end{aligned}
 \tag{5.38}$$

Here X_k is the input of the FIR filters containing the frequency shifted received signals. From Eq. (5.38), it can be seen that an instantaneous reference signal $r(k)$ can be substituted by a cross-correlation vector P_k between the reference signal and the input signal to update the weights as shown below,

$$P_k = \frac{1}{L+1} \sum_{l=-\frac{L}{2}}^{\frac{L}{2}} r(l) X^*(l+k) \quad .
 \tag{5.39}$$

For this blind algorithm, a delayed version of the received signal is used as the reference signal. This reference signal contains the faded desired signal and interference; thus, the convergence speed is reduced and output quality of the filter is diminished. Ideally, only the desired signal component in the received signal and the frequency shifted data in the FIR filters for filter periodicities equal to the cyclic periodicities of the SOI (excluding the time-invariant term) are correlated. Therefore, Eq. (5.39) can be written as

$$P_k = \frac{1}{L+1} \sum_{l=-\frac{L}{2}}^{\frac{L}{2}} s(l)S^*(l+k) , \quad (5.40)$$

if we assume that no multipath is presented. Here $S(k)$ is the frequency-shifted version of the desired signal $s(k)$. Since this algorithm circumvents using a noisy training signal, it is less susceptible to fading and noise, thus improving the convergence rate. The Griffith's like LMS algorithm is described in Table 5.4.

Table 5.4 Griffith's like LMS algorithm for the TDAF

$IN_k = [IN(k-1) \ IN(k-2) \ ... \ IN(k-N+1)]$	<i>input vector TDAF</i>
$X_k = IN_k e^{j2\pi\alpha kT}$	<i>frequency shifted versions of the input</i>
$y(k) = W^H X_k$	<i>estimate of the desired signal</i>
$W_{k+1} = W_k + \mu P_k - \mu y^*(k) X_k$	<i>update weights</i>

where:

H : hermitian transpose

$*$: complex conjugate operation

P_k : pre-estimated correlation vector of the desired signal and its shifted versions

μ : LMS adaptive size

α : cyclic frequencies corresponding to the desired signal

N : FIR filter taps

CMA Constrained TDAF

The fact that an FM signal has constant envelope has motivated the development of a constant modulus algorithm (CMA) TDAF. A CMA constrained TDAF works to restore a constant envelope in a FM signal and unlike the SCP, allows for a time-invariant term.

Several interference rejection techniques using the hybrid CMA and time-dependent filtering have been developed in the past years [MRH89][MRHA91]. Basically, there are two types of algorithm in this category [MRHA91]: one is the CMA applied to a full time-dependent filter structure (CMA/TDAF) and the other one is the hybrid CMA and the TDAF, which uses the CMA to adapt the time-invariant portion and the TDAF to adapt the time varying portions of the filter structure. The first algorithm is shown in Fig. 5.25. The filter consists of a number of time-dependent branches which are frequency-shifted versions of the input signal IN_k and a time-independent branch of IN_k . The adaptive algorithm used is different than the RLS or the LMS algorithms that we used in our previous simulations. In general, there are four types of CMA algorithms with different cost functions. The cost function depends on variables p and q as described below [MRHA91]

$$\langle [A^p - |\hat{y}_k|^p]^q \rangle_M \quad (5.41)$$

where $\langle \cdot \rangle$ denotes time averaging over M samples. A represents the modulus of the signal. Given an arbitrary amplitude of A , the error formed for the four p - q algorithms are expressed as follows [MRHA91]:

$$\begin{aligned} p = q = 1: 1-1 & \quad e_k = \frac{\hat{y}_k}{|\hat{y}_k|} \text{sgn}(A - |\hat{y}_k|) \\ 2-1 & \quad e_k = 2\hat{y}_k \text{sgn}(A^2 - |\hat{y}_k|^2) \\ 1-2 & \quad e_k = \frac{2\hat{y}_k}{|\hat{y}_k|} \text{sgn}(A - |\hat{y}_k|) \end{aligned}$$

$$e_k = 4\hat{y}_k \text{sgn}(A^2 - |\hat{y}_k|^2). \quad (5.42)$$

The CMA/TDAF works to restore the envelope of the signal. When interference which also has a constant envelope is added with to the desired signal, this algorithm could capture the interference, thus enhance the interference instead of the SOI. The second type of CMA algorithm as shown in Fig. 5. 26 is a hybrid of the CMA and the Griffith's like algorithm and tends to be less susceptible to the capture problem. For this structure the time-dependent paths are adapted using the SCP while the time-invariant path is adapted by the CMA algorithm. They both share the same output \hat{y}_k . In this way, two properties of the desired signal are exploited simultaneously. The algorithm is summarized below

CMA portion:

$$W_{(CMA)k+1} = W_{(CMA)k} + \mu e_k I N_k$$

Griffith portion:

$$W_{(Griffith)k+1} = W_{(Griffith)k} + \mu P_k - \mu y^*(k) X_k \quad (5.43)$$

and the estimated signal is

$$\hat{y}_k = \hat{y}_{(CMA)k} + \hat{y}_{(Griffith)k} \quad (5.44)$$

To insure that the CMA and the Griffith's like algorithms will not conflict in determining the processing gain, it is necessary to know the true magnitude of the desired signal for the CMA algorithm. This can be done by computing the cyclic autocorrelation of the signal in a recursive way [MRHA91]. In our simulations, we assume perfect magnitude estimates and the absence of multipath.

5.5.2 Refinements of the Structures

Although the performance of a SCP using the RLS algorithm is good, the computation complexity is impractical for real time implementation in a handset with today's micro-

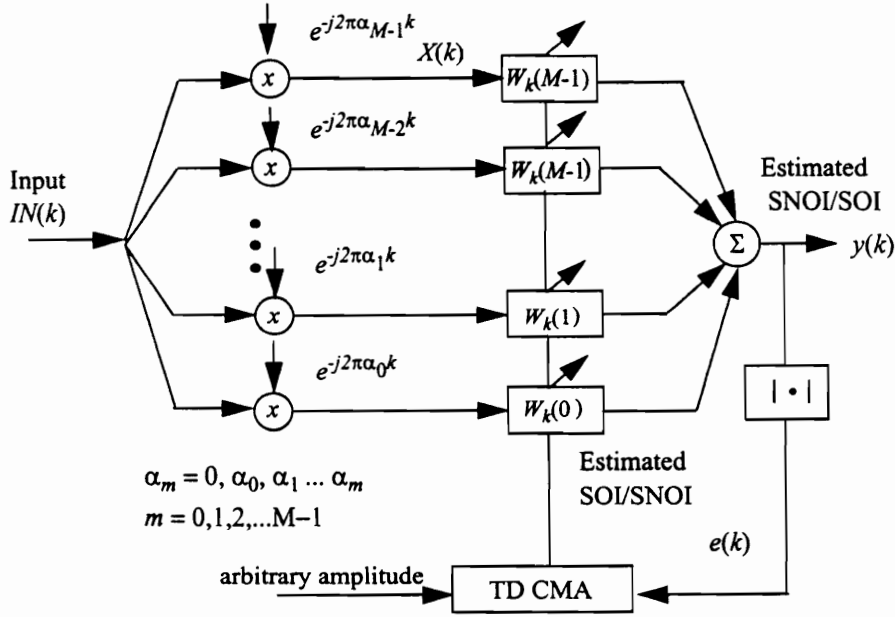


Fig. 5.25 The CMA/TDAF structure

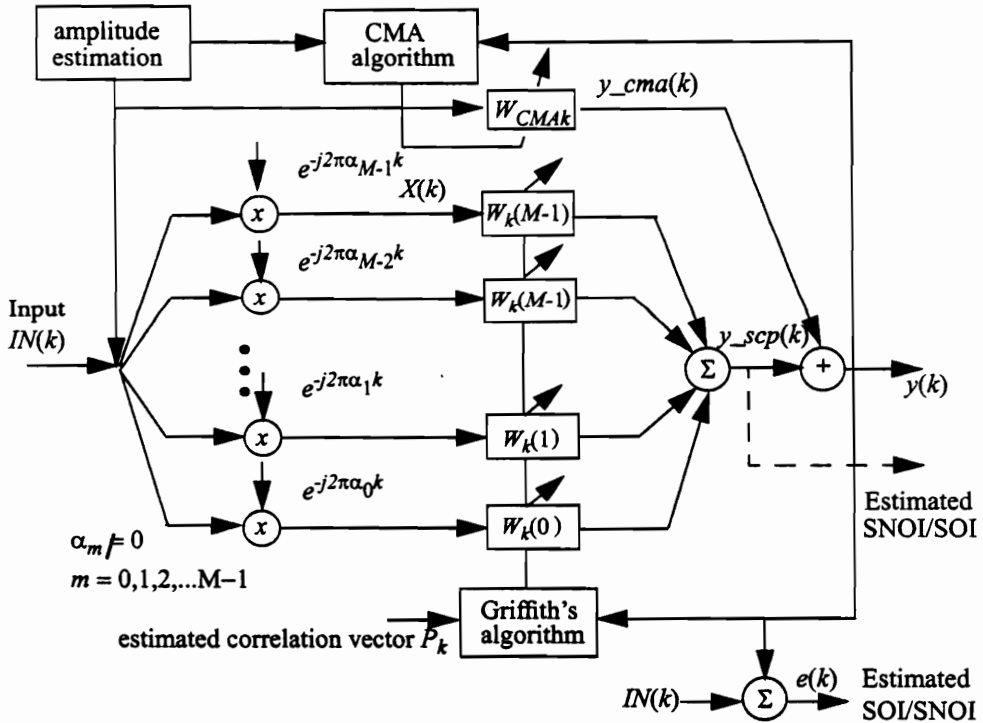


Fig. 5.26 Hybrid structure of CMA and Griffith's algorithm

processors. A simple adaptive filter structure with low computational complexity is needed. In this section, we will show that the combination of the CMA and a TDAF with the Griffith's algorithm, shown in Fig. 5.26, provides these requirements. This combination also dramatically increases the convergence rate of the adaptive filter.

Different cases using various carrier separations and fading characteristics are evaluated. The CNR is 25dB and the Doppler frequencies are 30Hz and 60Hz. From the simulation results, it is noted that most of the performance gain is due to the time-dependent portion. The CMA works to restore the constant envelope of the desired signal, but has less direct impact on the distorted phase. It can be seen from Fig. 5.27 that there is an average of 3-5dB improvement provided by the hybrid structure compared to the SCP except when the input CIR is 0dB. For a 0dB CIR , the CMA branch could capture the interference, resulting in worse performance than the SCP. To evaluate the contribution from the CMA branch and the time-varying branch, different branch outputs of the hybrid filter are demodulated and are plotted in Fig. 5.28. The CNR here is 25dB, the fading rate is 60Hz and the carrier separation is 0Hz. The top subplot shows the demodulated voice signal of the uncorrupted AMPS signal for comparison. The second subplot shows the demodulated voice signal of the combined output y_k . The third subplot shows the voice signal of the CMA processed signal $y_{(CMA)k}$ and the bottom subplot is for the voice signal of the Griffith's algorithm processed signal $y_{(Griffith)k}$. It can be seen that the performance contribution from the time-varying portion of the filter is much more significant than that from the time-invariant portion. However, combining the CMA and Griffith's algorithms does provide extra gains by restoring the constant envelope of the desired FM signal. The results for different channels are described below.

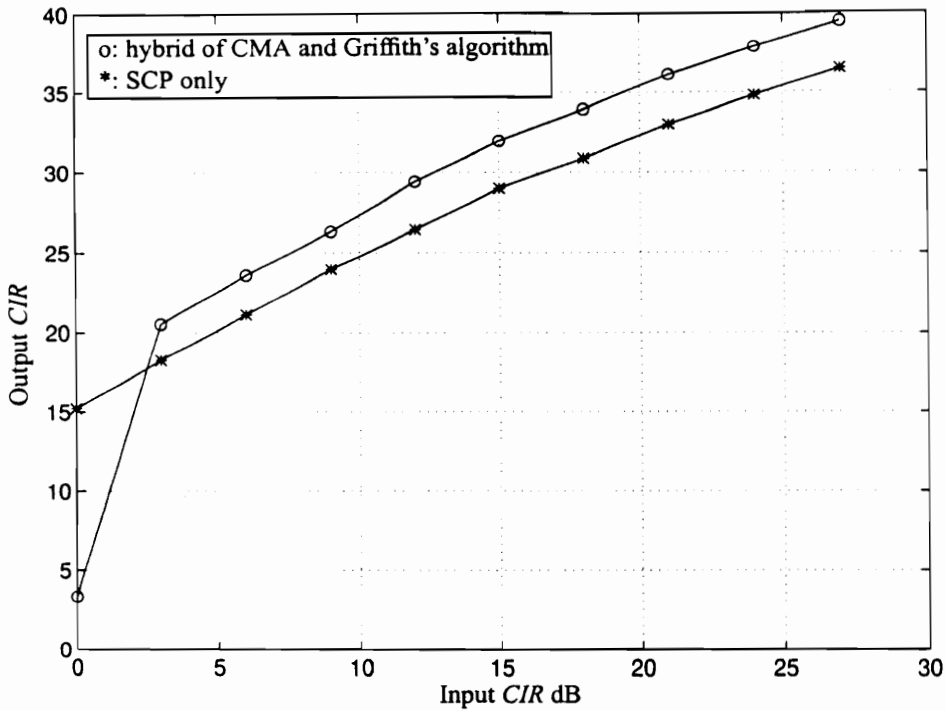


Fig. 5.27 Output *CIR*s of the SCP and the hybrid CMA and Griffith's algorithm, $CNR=25\text{dB}$

The most significant advantage of this structure is its improved convergence rate. From the *MSE* of the processed signals shown in Fig. 5.29, the filter converges after 0.025sec, which is only 1/6 the SCP convergence rate shown in Fig. 5.22. This improvement can also be seen from Fig. 5.30, which depicts the amplitude convergence rate for the hybrid CMA and Griffith's algorithm. The amplitude of the signal processed by the hybrid CMA and Griffith's algorithm converges to the desired level much quicker than that of the signal processed by the time-varying branch.

The performance of the hybrid CMA and Griffith's algorithm for a 30Hz Doppler shift is also measured. The output *CIR* and the *MSE* for the demodulated voice signals are plotted in Fig. 5.31 and Fig. 5.32, respectively. The results show the same pattern as the former non-fading case. Comparison of the demodulated voice waveforms is also plotted in Fig. 5.33.

The improvement in convergence is most noticeable for high Doppler frequencies. For a Doppler frequency of 60Hz, Fig. 5.34 and Fig. 5.35 show the output *CIR* and the *MSE* for the demodulated voice signals. Fig. 5.36 shows the comparison of the demodulated voice signals by the hybrid CMA and SCP using Griffith's algorithm. In the figure, the top left subplot is the original voice signal, and the top right subplot is the demodulated voice signal with *CIR* of 3dB. Both the desired signal and the interfering signal suffer severe fading with Doppler frequency of 60Hz. In the bottom left subplot of the figure, the demodulated voice signal from the SCP (using the general LMS algorithm) is presented. The bottom right subplot of the figure shows the demodulated voice signal for the hybrid CMA and Griffith's algorithm. Because of the severe fading, the instantaneous *CIR* can be very low even though the average *CIR* is 3dB. This low instantaneous *CIR* makes it difficult for the SCP to track the desired signal. It can be seen that the voice signal contains some spikes using the SCP although most of the desired signal is recovered. However, these spikes can be removed and the convergence rate is increased by incorporating the Griffith's algorithm with the CMA.

In this chapter, the theoretical performance of the time dependent filter in different radio channels is analyzed. The performance is also verified by extensive simulations. The adaptive algorithms and structures are refined to have less computational complexity and faster convergence. Results show that there is a significant improvement in the received signal quality. The new techniques can be incorporated with the current AMPS receiver for co-channel interference rejection at a low cost. These techniques also provide potential for increasing system capacity, which is discussed in Chapter 7.

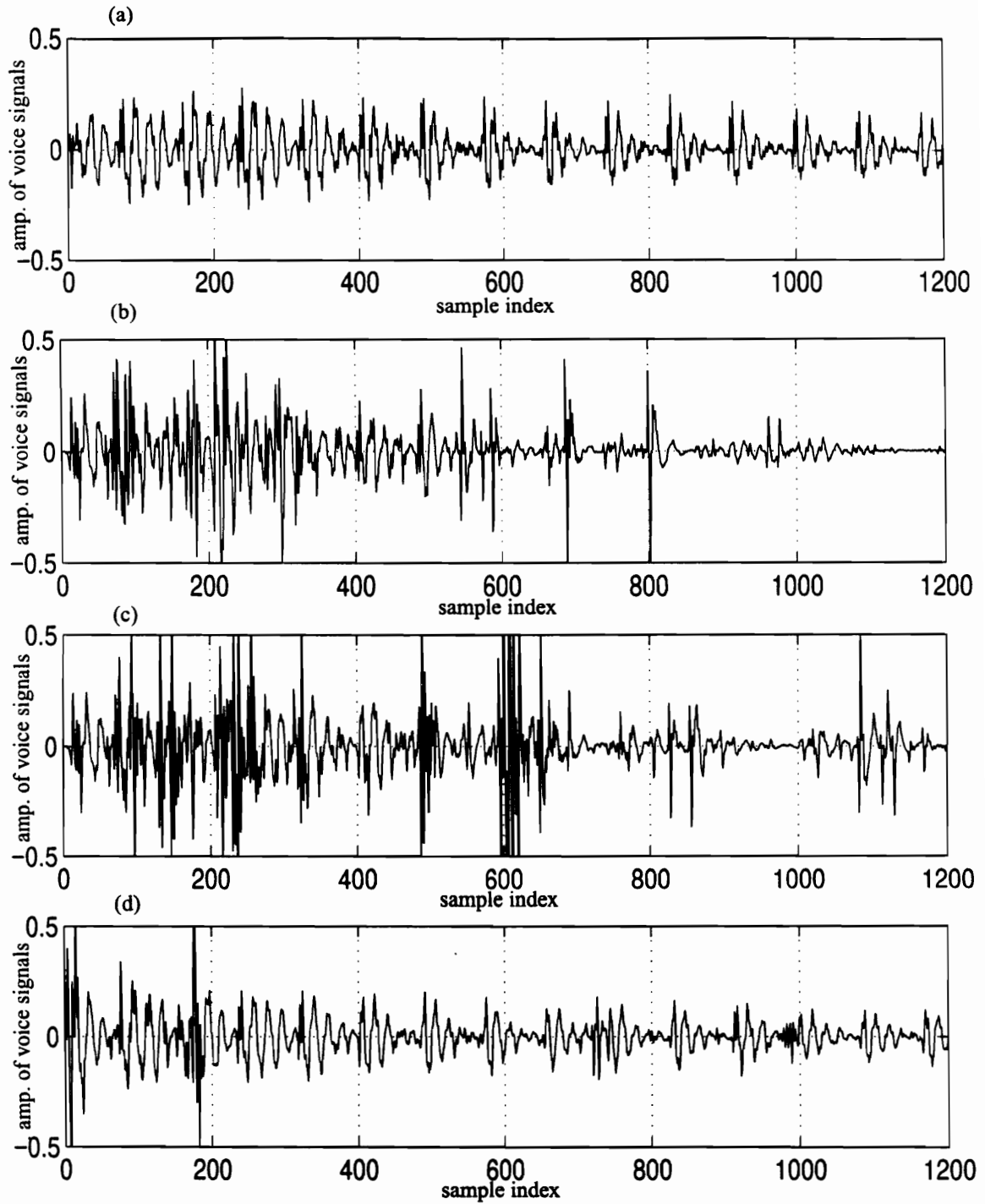


Fig. 5.28 Comparison of the demodulated voice signals for different output branches using hybrid CMA and Griffith's algorithm, (a) uncorrupted voice signal (b) output y_k (c) CMA branch, $y_{(CMA)k}$ (d) Griffith's branch, $y_{(Griffith)k}$

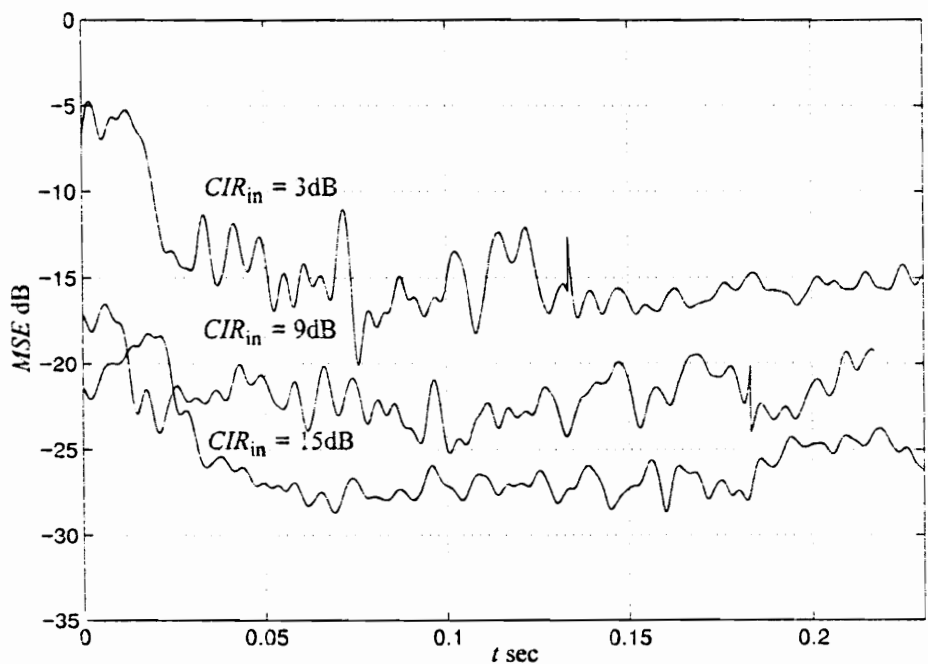


Fig. 5.29 Smoothed *MSEs* of the hybrid CMA and Griffith's algorithm processed signals for different input *CIRs*. Carrier separation is 0Hz and *CNR* is 25dB

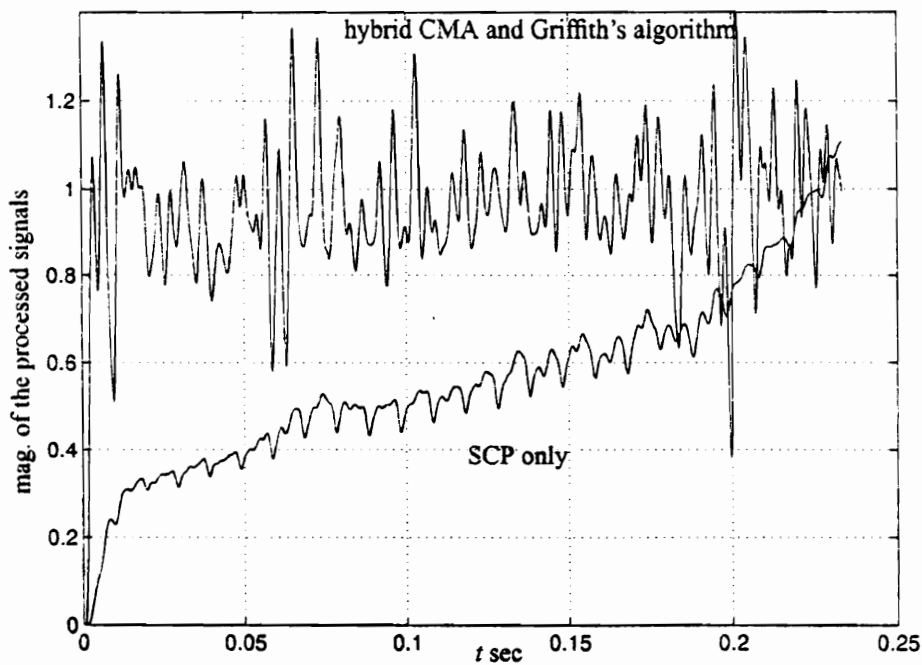


Fig. 5.30 Smoothed magnitude of the hybrid CMA and Griffith's algorithm processed signals, carrier separation is 0Hz and *CNR* is 25dB

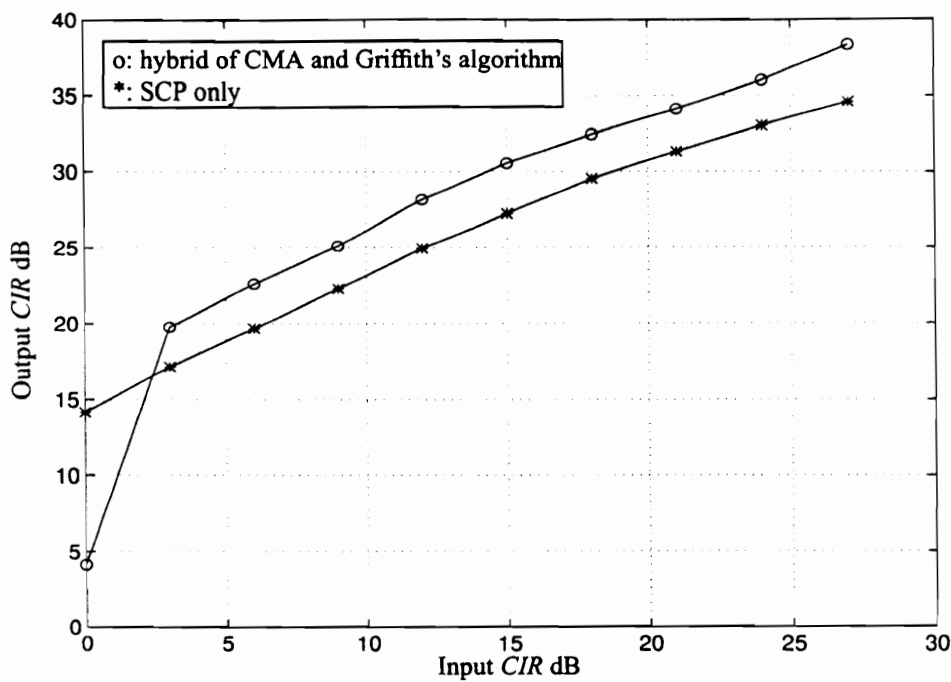


Fig. 5.31 Output *CIR*s of the SCP and the hybrid CMA and Griffith's algorithm, $f_d=30\text{Hz}$, $\text{CNR}=25\text{dB}$

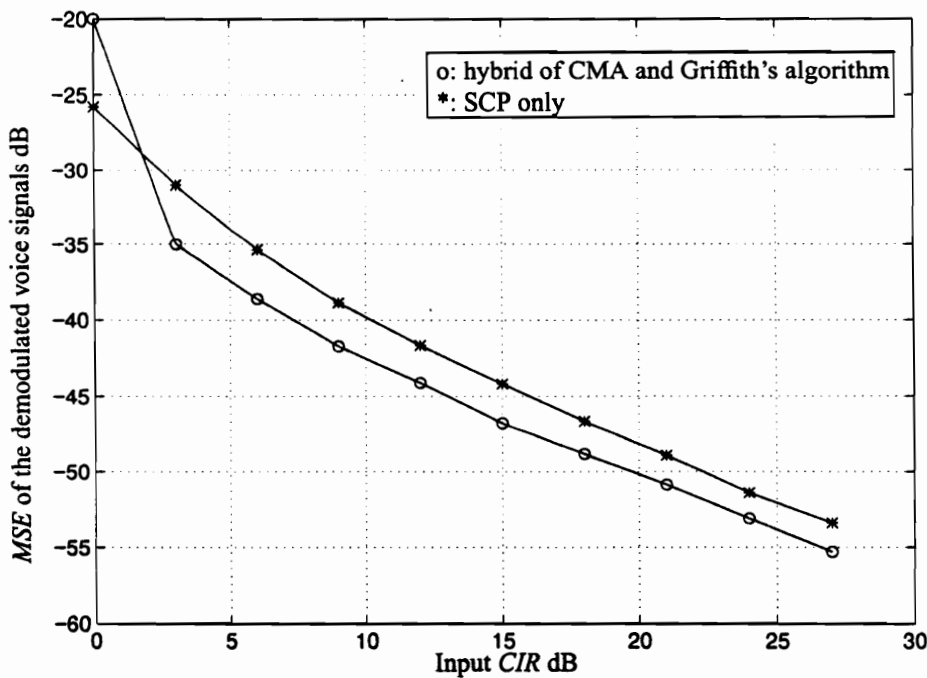


Fig. 5.32 *MSE* of the demodulated voice signals after the SCP and the hybrid CMA and Griffith's algorithm, $f_d=30\text{Hz}$, $\text{CNR}=25\text{dB}$

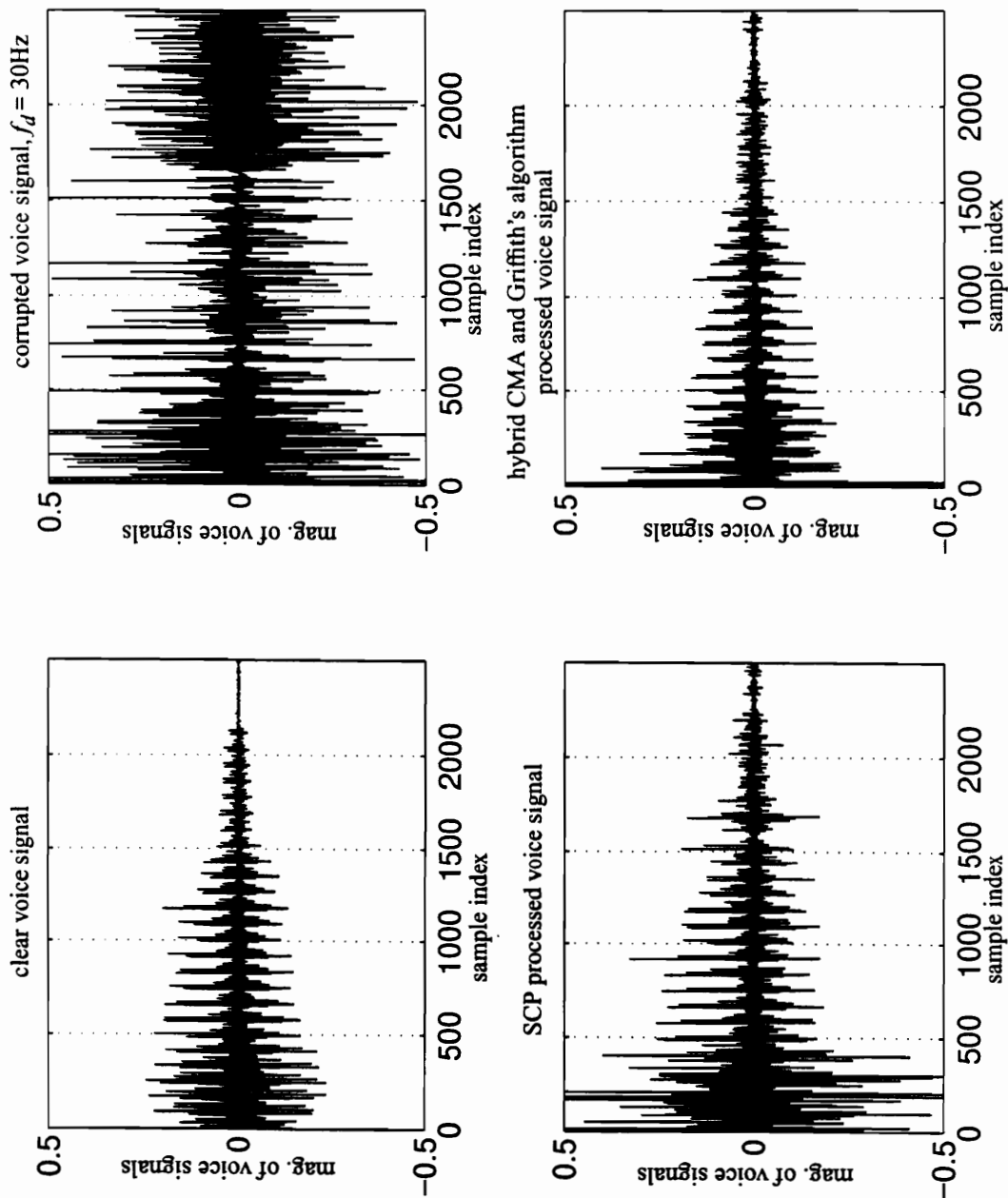


Fig. 5.33 Comparison of the demodulated voice signals using SCP and hybrid CMA and Griffith's algorithm

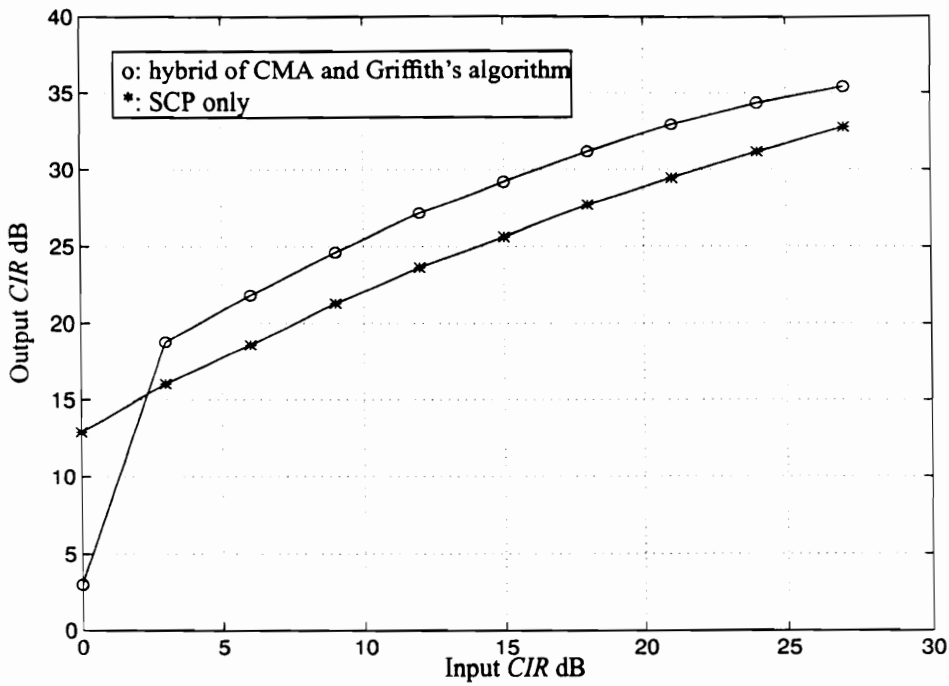


Fig. 5.34 Output *CIRs* of the SCP and the hybrid CMA and Griffith's algorithm, $f_d=60\text{Hz}$, $\text{CNR}=25\text{dB}$

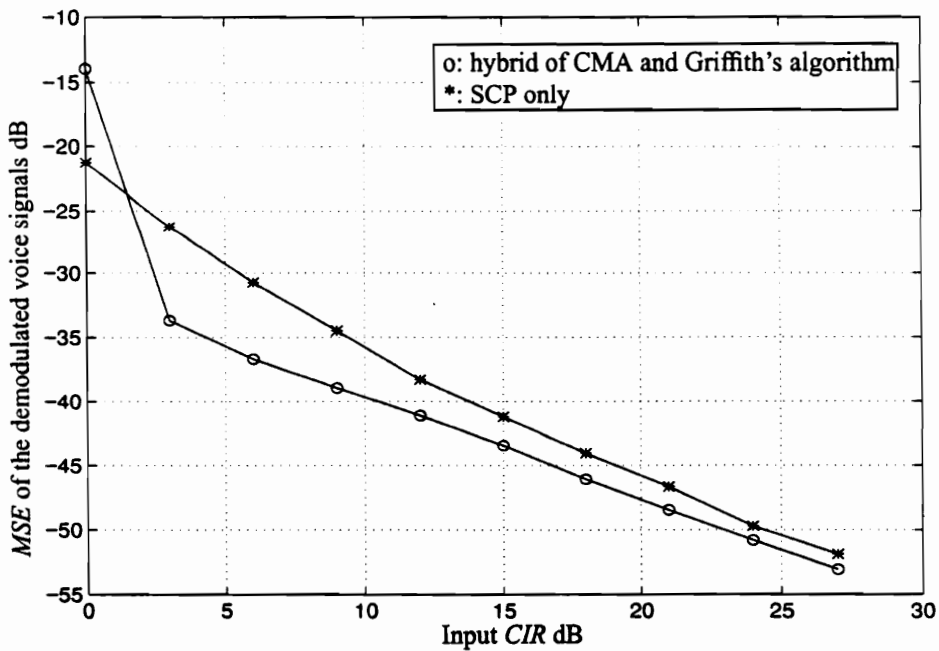


Fig. 5.35 *MSE* of the demodulated voice signals after the SCP and the hybrid CMA and Griffith's algorithm, $f_d=60\text{Hz}$, $\text{CNR}=25\text{dB}$

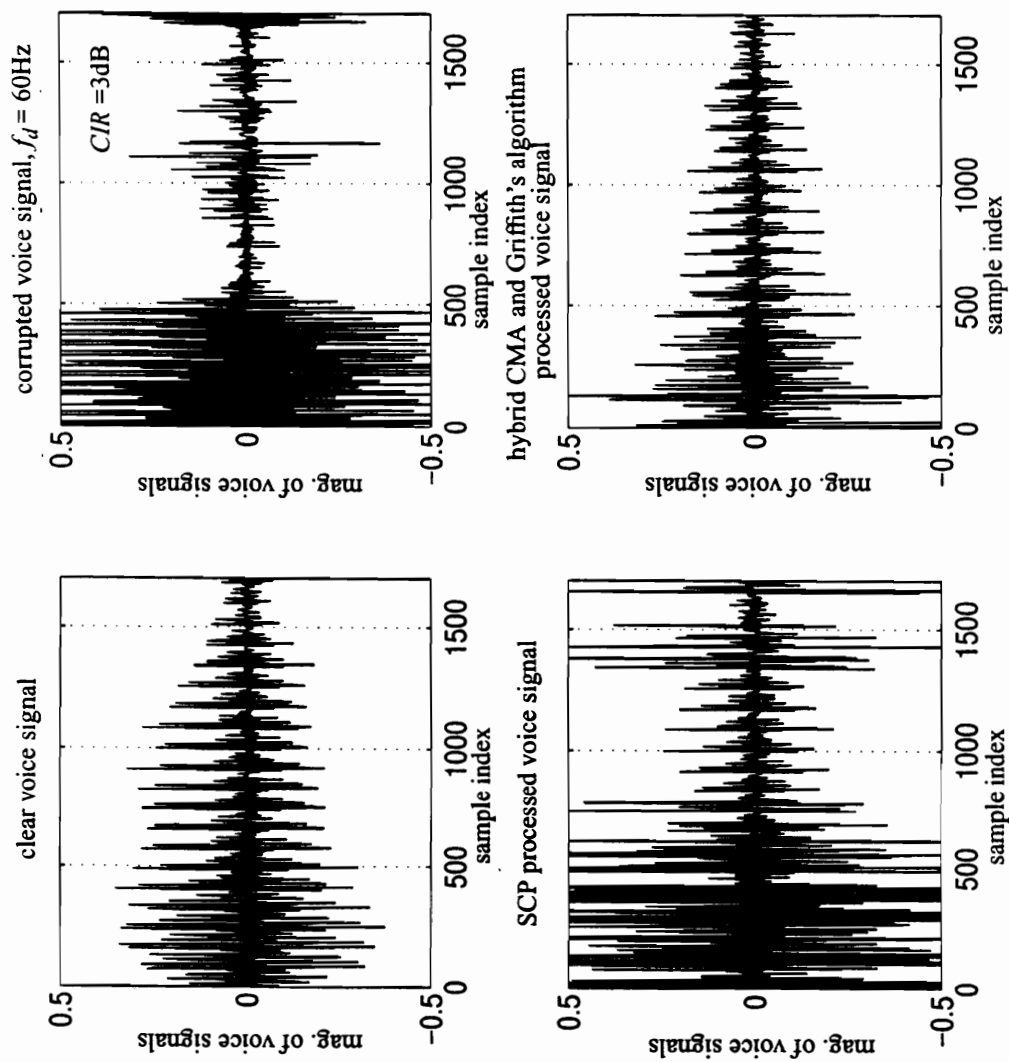


Fig. 5.36 Comparison of the demodulated voice signals using SCP and hybrid CMA and Griffith's algorithm

Chapter 6. Time-dependent Adaptive Filtering Techniques for NAMPS Co-channel Interference Rejection

6.1 Introduction

To improve the channel capacity of the current AMPS system, the Narrowband AMPS (NAMPS) system, which is a modified version of the AMPS system, was developed by Motorola several years ago. Instead of using 30kHz bandwidth, NAMPS uses a 10kHz channel bandwidth for the FM signal. This results in three NAMPS channels in place of a single AMPS channel. Another significant difference is that NAMPS uses a digital SAT (DSAT) instead of the analog tone used in AMPS. The DSAT is a set of seven distinct 24-bit Manchester coded sequences which are lowpass filtered and repeatedly transmitted at 200 bits per second, forming the control signal in the sub-audio band. This scheme provides supervisory control for the NAMPS system while ensuring the frequency components of the control signal are below the audio frequency band, and can be easily removed by the demodulator. In the AMPS system, one SAT frequency, either 5970Hz, 6000Hz or 6030 Hz, is allocated to a seven-cell cluster. For the NAMPS system, the DSAT allocation is different. Instead of one SAT per cluster, the NAMPS system assigns one DSAT per cell.

Like the AMPS signal, the NAMPS signal exhibits spectral correlation. Thus, a TDAF can be applied to reject co-channel interference. In this chapter, a brief mathematical analysis of the cyclostationary features of the NAMPS signal is provided. A time domain optimal time-dependent adaptive filter (TDAF) is derived that makes use of these features. Performance of the TDAF is examined using simulated NAMPS signals with realistic channel conditions. Results indicate a significant improvement in carrier-to-interference and noise ratio ($CINR$) can be achieved by applying the TDAF. Section 6.2 describes the spectral correlation characteristics of the NAMPS signal that results from the digital supervisory audio tone (DSAT). The optimal TDAF with a training sequence can exploit the spectral correlation to suppress co-channel interference and enhance the desired signal.

The filter structure is given in section 6.3. Simulation results are shown in section 6.4. Future work is discussed in section 6.5.

6.2 Cyclostationarity of NAMPS Signal

A NAMPS signal containing a DSAT can be expressed as

$$s(t) = e^{j \left(2\pi f_c t + 2\pi \beta f_m \int_{-\infty}^t v(t) dt + 2\pi k f_d \int_{-\infty}^t DSAT(t) dt \right)}, \quad (6.1)$$

where

- f_c : carrier frequency
- β : voice modulation index which is 1.25 here, $\beta f_m = 5000\text{Hz}$
- k : DSAT modulation index which is 3.5 here, $k f_d = 700\text{Hz}$
- $v(t)$: voice signal
- $DSAT(t)$: periodic 24 bits DSAT with a 200Hz bit rate.

For notational simplicity, define

$$s_v(t) = e^{j \left(2\pi f_c t + 2\pi \beta f_m \int_{-\infty}^t v(t) dt \right)}, \quad (6.2)$$

then the NAMPS signal with a DSAT can be written as

$$s(t) = s_v(t) e^{j \left(2\pi k f_d \int_{-\infty}^t DSAT(t) dt \right)}. \quad (6.3)$$

The DSAT signal, which is a digital sequence with a 200Hz bit rate and a 200/24 code

repeating rate, can be represented by a Fourier series expansion. Substituting the series expansion into Eq. (6.2), $s(t)$ becomes

$$s(t) = s_v(t) e^{j2\pi k f_d \int_{-\infty}^t \left(a_0 + \sum_{n=1}^{\infty} (a_n \cos \omega_n t + b_n \sin \omega_n t) \right) dt}, \quad (6.4)$$

where

$$a_0 = \frac{1}{T} \int_{-\frac{T}{2}}^{\frac{T}{2}} DSAT_T(t) dt = 0, \quad (6.5a)$$

$$a_n = \frac{1}{T} \int_{-\frac{T}{2}}^{\frac{T}{2}} DSAT_T(t) \cos \omega_n t dt, \quad (6.5b)$$

$$b_n = \frac{1}{T} \int_{-\frac{T}{2}}^{\frac{T}{2}} DSAT_T(t) \sin \omega_n t dt. \quad (6.5c)$$

The period T of the Fourier series is the same as the DSAT code period, which is 24/200sec, and $\omega_n = n\omega_0 = 2\pi n(200/24)$. Eq. (6.4) can be simplified to

$$s(t) = s_v(t) \prod_n e^{j2\pi k f_d \frac{a_n}{\omega_n} \cos \omega_n t - j2\pi k f_d \frac{b_n}{\omega_n} \sin \omega_n t}. \quad (6.6)$$

Let $c = 2\pi k f_d \frac{a_n}{\omega_n}$, the terms $e^{j2\pi k f_d \frac{a_n}{\omega_n} \cos \omega_n t}$ and $e^{-j2\pi k f_d \frac{a_n}{\omega_n} \sin \omega_n t}$ can be expanded using

Bessel functions as

$$e^{j2\pi k f_d \frac{a_n}{\omega_n} \cos \omega_n t} = \sum_{p=-\infty}^{+\infty} J_p(c) e^{jp\omega_n t} , \quad (6.7a)$$

and

$$e^{-j2\pi k f_d \frac{a_n}{\omega_n} \sin \omega_n t} = \sum_{q=-\infty}^{+\infty} J_q(-c) e^{jq\omega_n t} , \quad (6.7b)$$

where

$$J_n(c) = \frac{1}{2\pi} \int_{-\pi}^{+\pi} e^{jc \sin \omega_n t} e^{-jn\omega_n t} d(\omega_n t) . \quad (6.8)$$

Note that p and q are integer numbers and

$$J_{p,q}(c) = \begin{cases} J_{-p,q}(c) & p,q \text{ even} \\ -J_{-p,q}(c) & p,q \text{ odd} \end{cases} . \quad (6.9)$$

Finally, the NAMPS FM signal $s(t)$ can be interpreted as

$$\begin{aligned} s(t) &= s_v(t) \prod_n \sum_p \sum_q J_p(c) J_q(-c) e^{j(p+q)n\omega_0 t} \\ &= s_v(t) \prod_n \sum_p \sum_q J_p(c) J_q(-c) e^{jL\omega_0 t} , L \text{ is an integer number} . \end{aligned} \quad (6.10)$$

From Eq. (6.10), it can be seen that the spectrum of the modulated voice signal is replicated at multiples of the cyclic frequencies ω_0 . In other words, a NAMPS signal exhibits cyclostationarity with a fundamental periodicity of ω_0 .

6.3 Filter Implementation

A time-dependent adaptive filter can be very effective in estimating and enhancing a cyclostationary signal. A time-dependent adaptive filter combines the replicated versions of the desired signal and enhances each replicated image using other replicated images.

The impulse response $h(t, u)$ and the output $y(t)$ of an optimal time-dependent filter have been discussed in Chapter 5. The optimal Wiener solution of this filter and the MSE are also given in Chapter 5. The filter periodicities range over all the possible values of nf_0 within the bandwidth of the signal, where $f_0=200/24$ and n is an integer number.

For a NAMPS signal, a large number of cyclic frequencies can be exploited within the signal band. The time-domain FSR TDAF structure is not an efficient and realistic implementation for this application since it requires a huge number of parallel filters. For example, if the sample rate is 25kHz for a NAMPS FM signal, the FSR TDAF needs 3000 parallel filters to exploit all the cycle frequencies. The time-sequenced adaptive filter (TSAF) is a TDAF ideally suited for processing signals having a large number of statistical harmonics [ROH88]. As shown in Fig. 6.1, the TSAF utilizes a bank of M conventional adaptive filters whose weights are denoted by the column vector $H_k(m)$ for $m=0, 1, 2, \dots, M-1$. Each adaptive filter is periodically updated and a filter output is chosen in synchronous with the periodicity of the signal statistics. For the NAMPS signal, the periodicity of the filter bank is 200/24Hz. The filter output at time k is given by the inner product of the input vector and the H_k ,

$$y(k) = X_k^T H_k(k - [k]_M M) . \quad (6.11)$$

where $[k]_M$ is the largest multiple of M in k . The TSAF can be interpreted as an adaptive filter that converts the nonstationary signal into a set of jointly stationary processes using the time-series representation (TSR) for adaptation and filtering [Fer852]. In the literature, TSAF is often referred as a TSR TDAF.

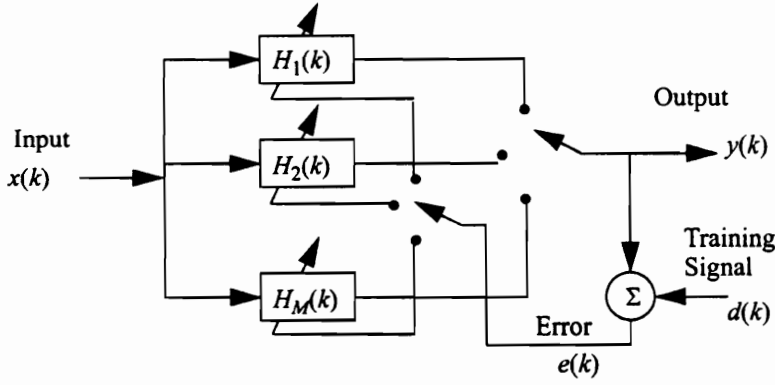


Fig. 6.1 The TSAF (or TSR TDAF)

6.4 Simulation Results

Here we examine the optimal TDAF, i.e., a TDAF adapted based on the *MSE* criterion outlined in Chapter 5 and using a training sequence. This case provides a performance bound for the TDAF. As an example, two NAMPS signals are generated individually using different voice files and DSATs. The carrier frequency separation for these two FM signals is 100Hz, which is a typical oscillator accuracy for 900MHz. Independent fading with a 20Hz Doppler frequency is applied to both the desired signal and the co-channel interference signal along with additive white Gaussian noise. The signal generator is shown in Fig. 6.2. The same quadrature demodulator used for the AMPS simulations is used to recover the voice signal.

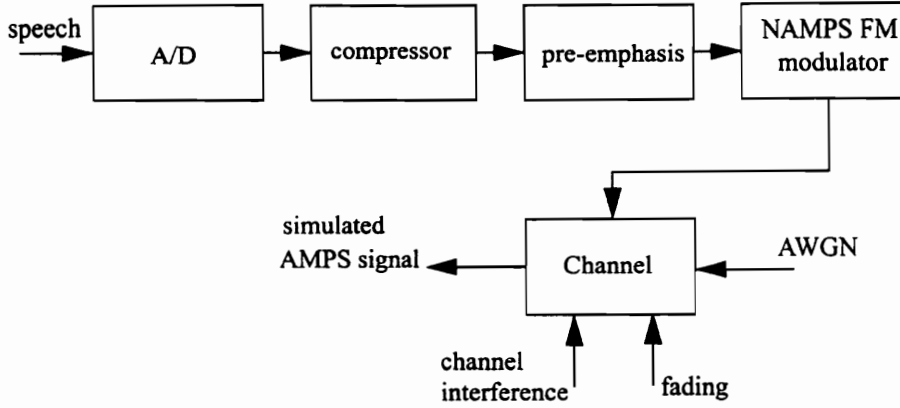


Fig. 6.2 NAMPS signal generator

The averaged *CINR* is defined as

$$CINR = \frac{\text{power of desired FM signal}}{\text{power of (FM interference + noise)}} \quad (6.12)$$

and it is measured over 10ms segments. The *CINR* as a function of segment number is plotted in Fig. 6.3 for a five seconds of data. From the top plot in Fig. 6.3, it can be seen that the averaged *CINR* is 12dB. The variation of the *CINR* is caused by the fading and noise fluctuations. The cumulative density function (*CDF*) for the received FM signal versus segmented *CINR* is plotted at the bottom at Fig. 6.3. The *CINR* after the optimal TDAF is plotted in Fig. 6.4 using the same methods. From the plot, it can be seen that the average *CINR* value is improved and now is above 18dB. Note, 45% of the segmented *CINR* measurements are below 10dB for the corrupted FM signal, while less than 15% are below 10dB for the TDAF filtered signal.

A significant drawback of the quadrature demodulator is its sensitivity to fading. Fig. 6.3 and Fig. 6.4 show the segmented *CINR* and its corresponding *CDF* for corrupted NAMPS signals and TDAF filtered signals for *CIR*=12dB. The demodulated voice signal shown in

Fig. 6.5 contains spikes due to the impact of fading on the quadrature demodulator. The spikes in the demodulated signal greatly deteriorate the voice quality. The corresponding segmented *SINR* and *CDF* are plotted on the same page. The demodulated voice waveform, segmented *SINR*, and corresponding *CDF* for the TDAF filtered signals are shown in Fig. 6.6. Based on experience, a -20dB *SINR* can cause a noticeable pop in the voice signal. From the *CDF* curve in Fig. 6.5, 15% of the segmented *SINRs* are below -20dB for the corrupted signal, however, only 2% of the segmented *SINRs* are below -20dB for the TDAF processed signal shown in Fig. 6.6. The demodulated voice signal shown in the graph on the top of Fig. 6.6 is much smoother than that shown in Fig. 6.5, which is consistent with the *CDF* results. For convenience in Fig. 6.7, a comparison of the *CDF* with and without the TDAF is made for both the FM and demodulated voice signals. In addition to the 12dB input *CIR* test condition, simulations were performed using an 18dB input *CIR* without a TDAF at the receiver. The resulting *CDF* is shown in Fig. 6.7. From this figure, the *CDF* corresponding to the TDAF processed signal (with input *CIR* of 12dB) is much better than the *CDFs* corresponding to the unprocessed signals (with input *CIR* of 12dB and 18dB). However, for the segmented *SINR*, corresponding to the demodulated voice signals, the performance improvement is less. The *CDF* for the TDAF demodulated voice signal with input *CIR* of 12dB is similar to the *CDF* for the unprocessed signal with input *CIR* of 18dB. In other words, a processed voice signal with an input *CIR* of 12dB sounds similar to a non-processed voice signal with *CIR* of 18dB. This is verified by our subjective evaluation of the audio signals.

Figures 6.8 through 6.12 depict the results for a test case similar to the previous one. For this test case, the input *CIR*=15dB instead of 12dB in the previous test. Results for this case show the demodulated voice signal using a TDAF has been improved to provide equivalent quality of a demodulated voice signal having *CIR*=20dB. A better demodulator, like the model based receiver, could be used to replace the quadrature receiver to obtain even better voice quality. Overall, the improvement provided by the TDAF is significant.

6.5 Summary and Future Work

The theoretical cyclostationarity properties of the NAMPS signal are analyzed. The analysis shows that spectral redundancy is introduced because of the DSAT. A time-dependent adaptive filter which takes advantage of the spectral correlation can be implemented for co-channel interference rejection. A TDAF that uses a training sequence has been simulated to obtain a performance bound for the algorithm. The performance of the TDAF has been evaluated using different fading conditions and different interference levels. The results show a substantial improvement in both the *CINR* level and the voice quality by using a TDAF.

The next step is to investigate blind adaptive techniques for training the TDAF. Different types of constraints could be used based on the knowledge of the cyclic spectra for NAMPS signals with different DSATs. These constraints may be applicable for creating a blind TDAF. CMA, linear constrained CMA, Griffith's like algorithm, or etc., are possible approaches for creating blind algorithms for NAMPS.

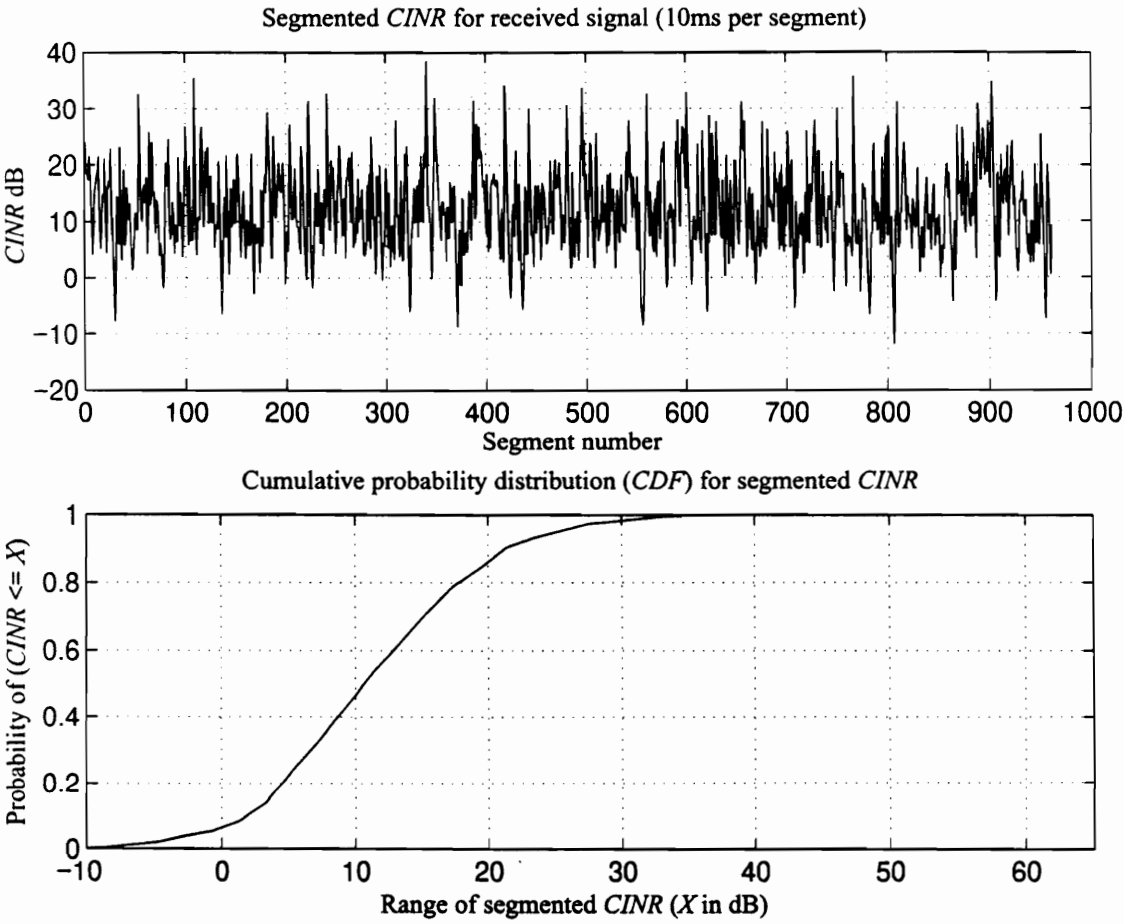


Fig. 6.3 $CINR$ and CDF of segmented $CINR$ for the corrupted NAMPS FM signal, $CIR=12\text{dB}$

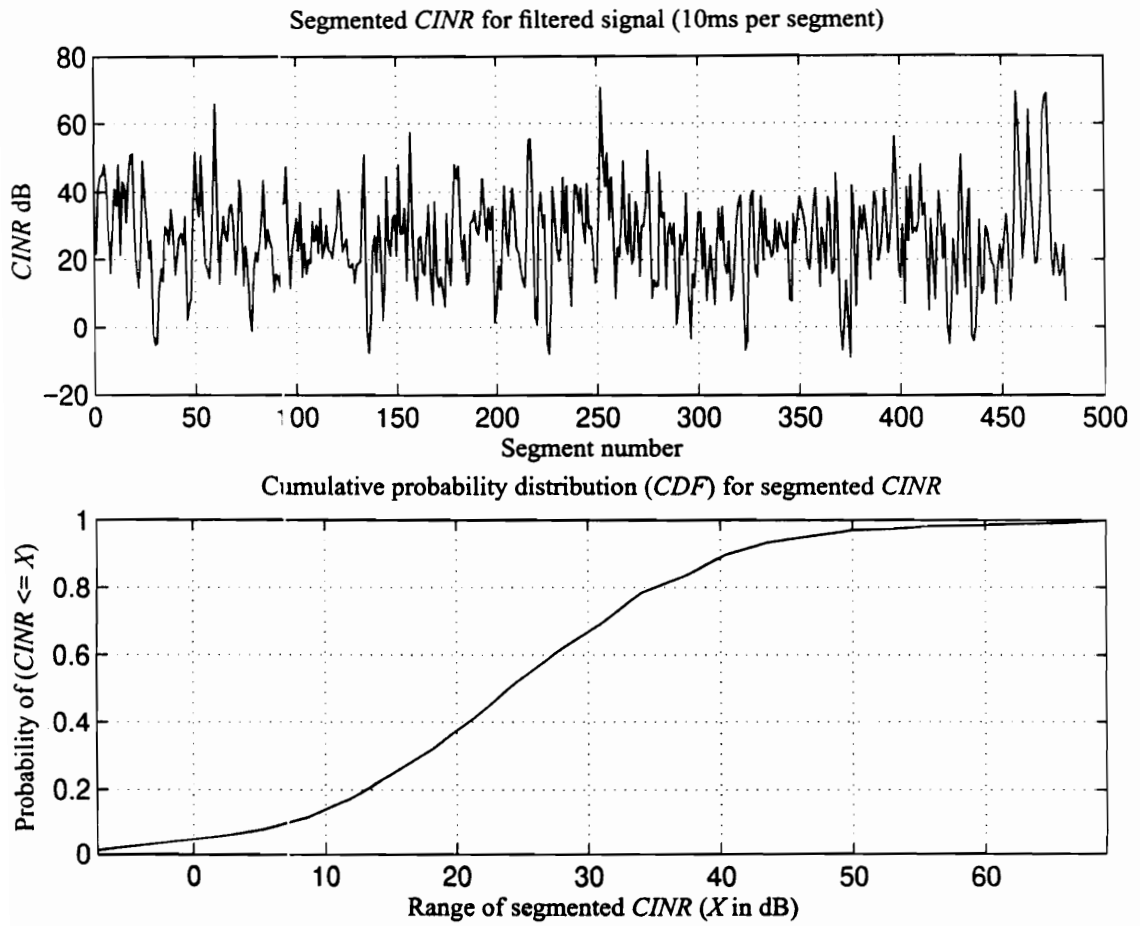


Fig. 6.4 $CINR$ and CDF of segmented $CINR$ for the TDAF filtered NAMPS FM signal, $CIR=12\text{dB}$

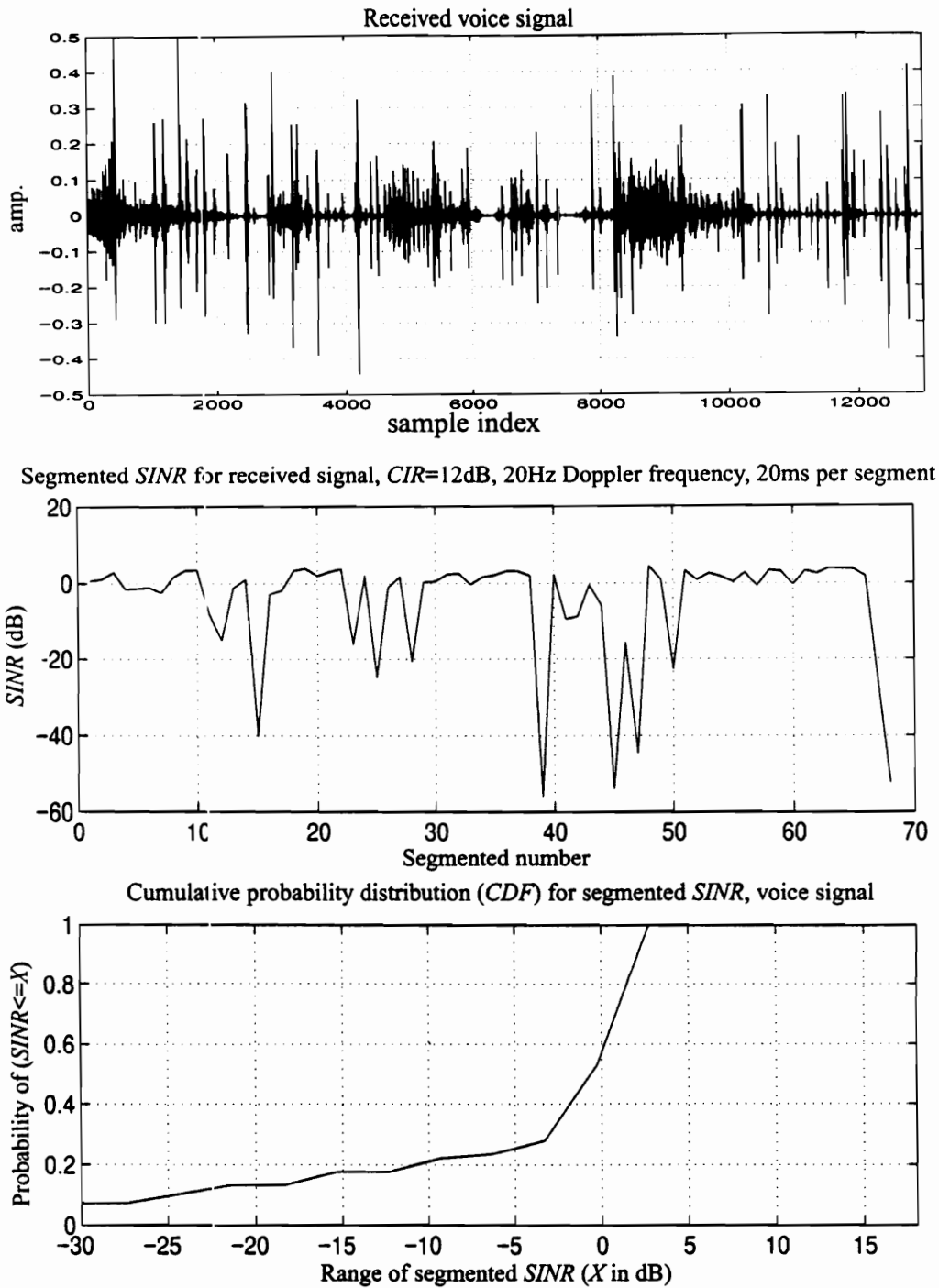


Fig. 6.5 Demodulated voice signal without using the TDAF, and the corresponding segmented SINR and CDF, CIR=12dB

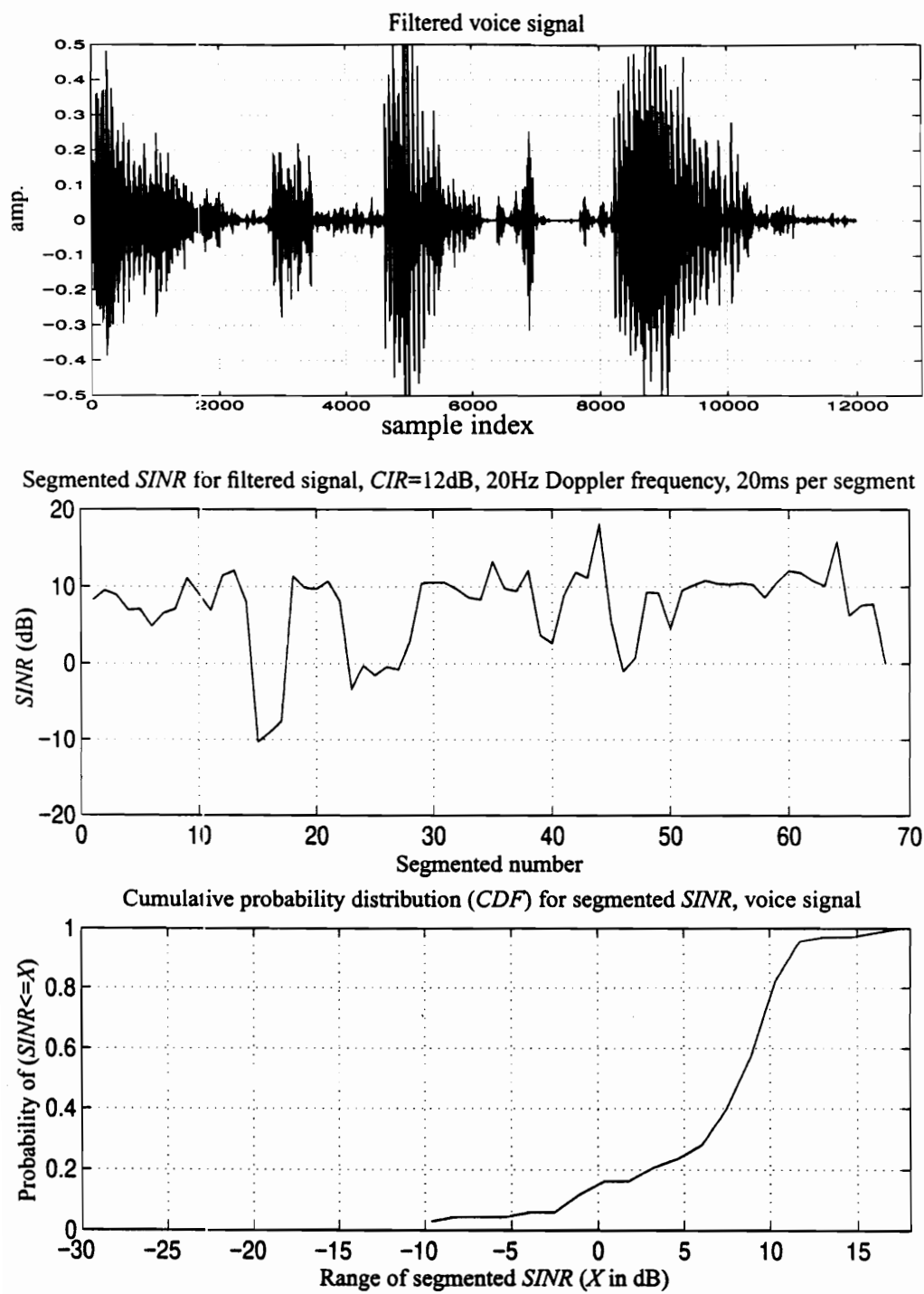


Fig. 6.6 Demodulated voice signal with the TDAF, and the corresponding segmented $SINR$ and CDF , $CIR=12\text{dB}$

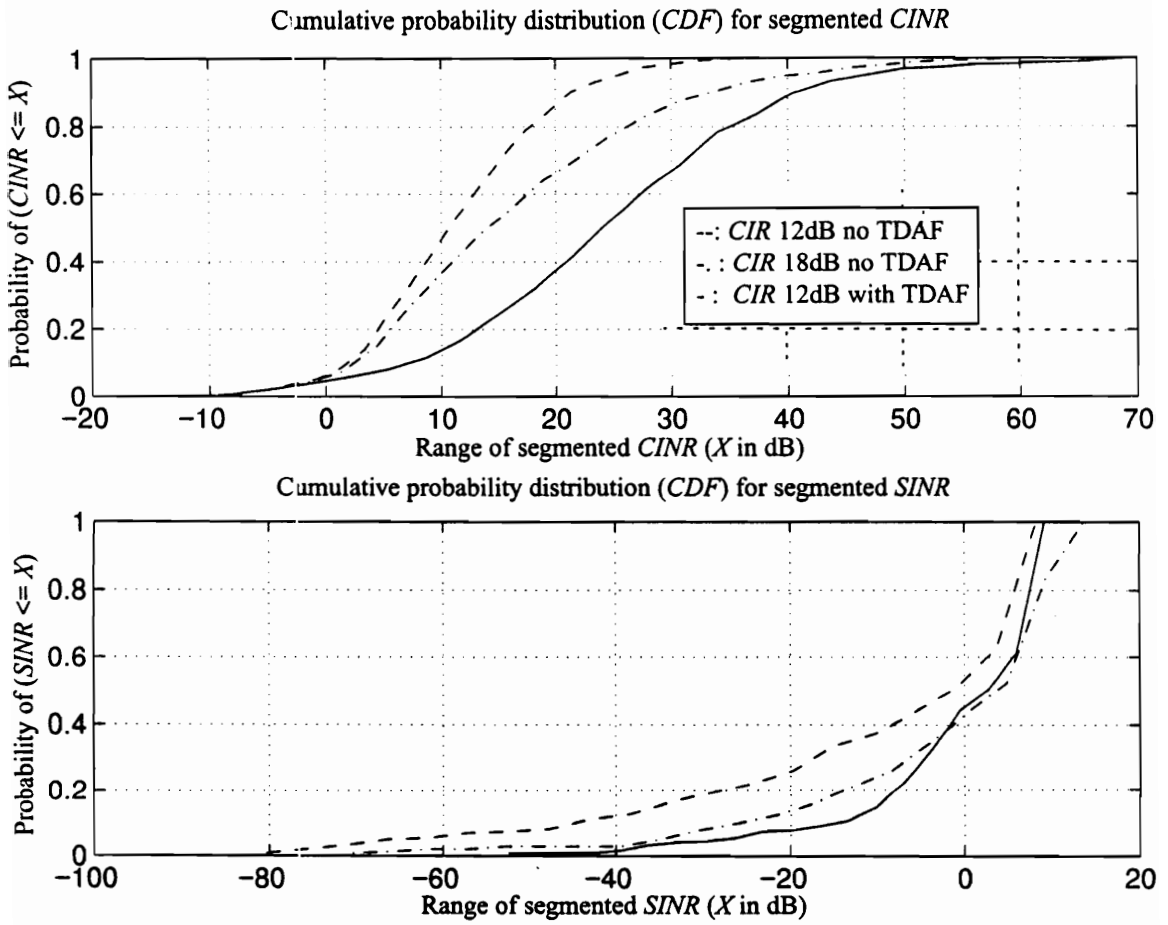


Fig. 6.7 CDF Comparison for segmented $CINR$ and $SINR$
with and without the TDAF, $CIR=12$ dB

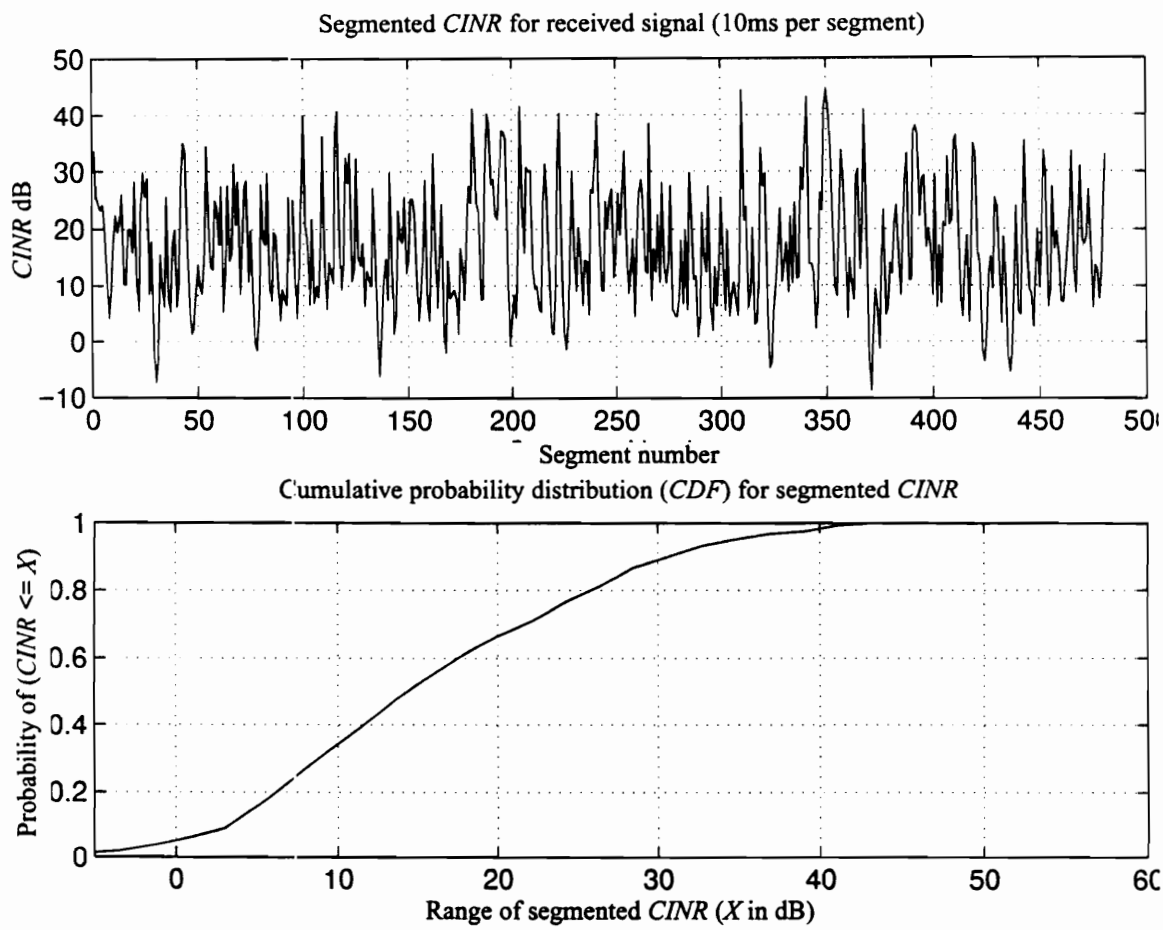


Fig. 6.8 $CINR$ and CDF of segmented $CINR$ for the corrupted NAMPS FM signal, $CIR=15\text{dB}$

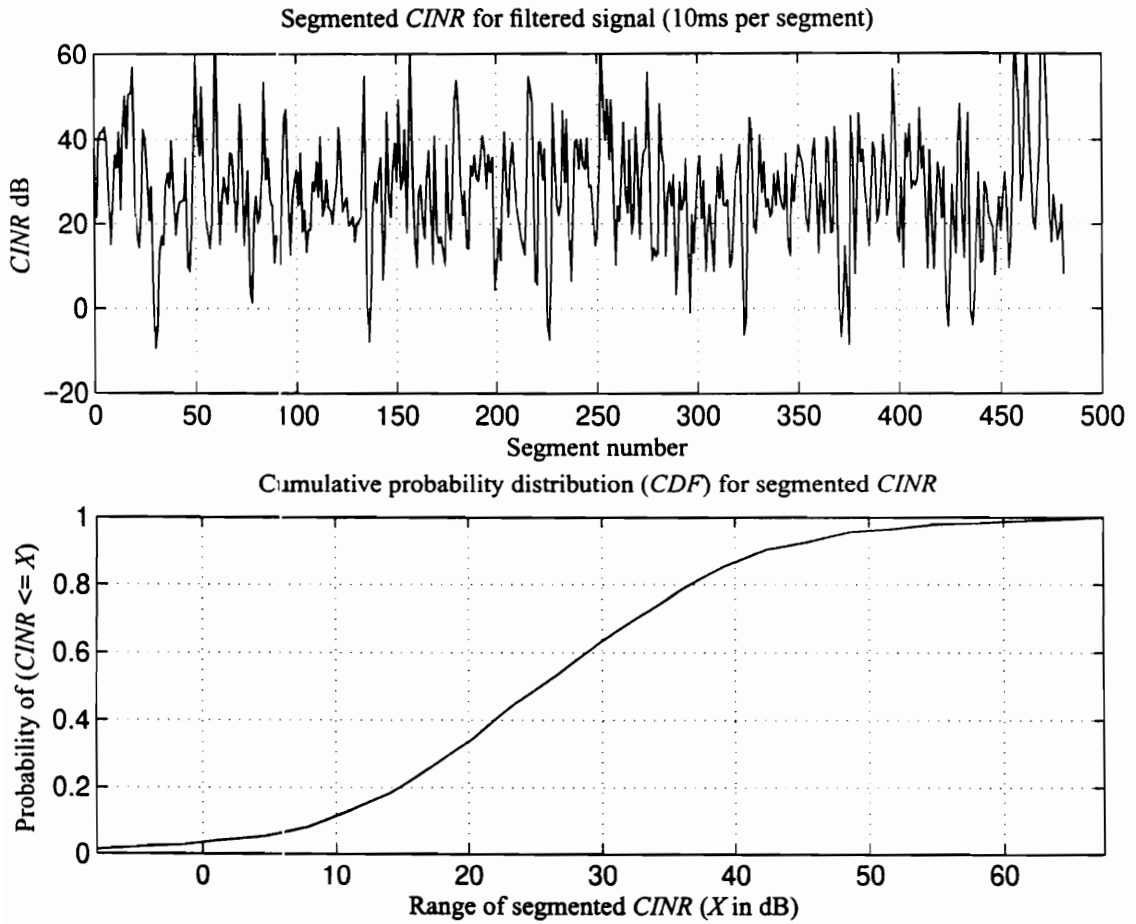


Fig. 6.9 $CINR$ and CDF of segmented $CINR$ for the TDAF filtered NAMPS FM signal, $CIR=15\text{dB}$

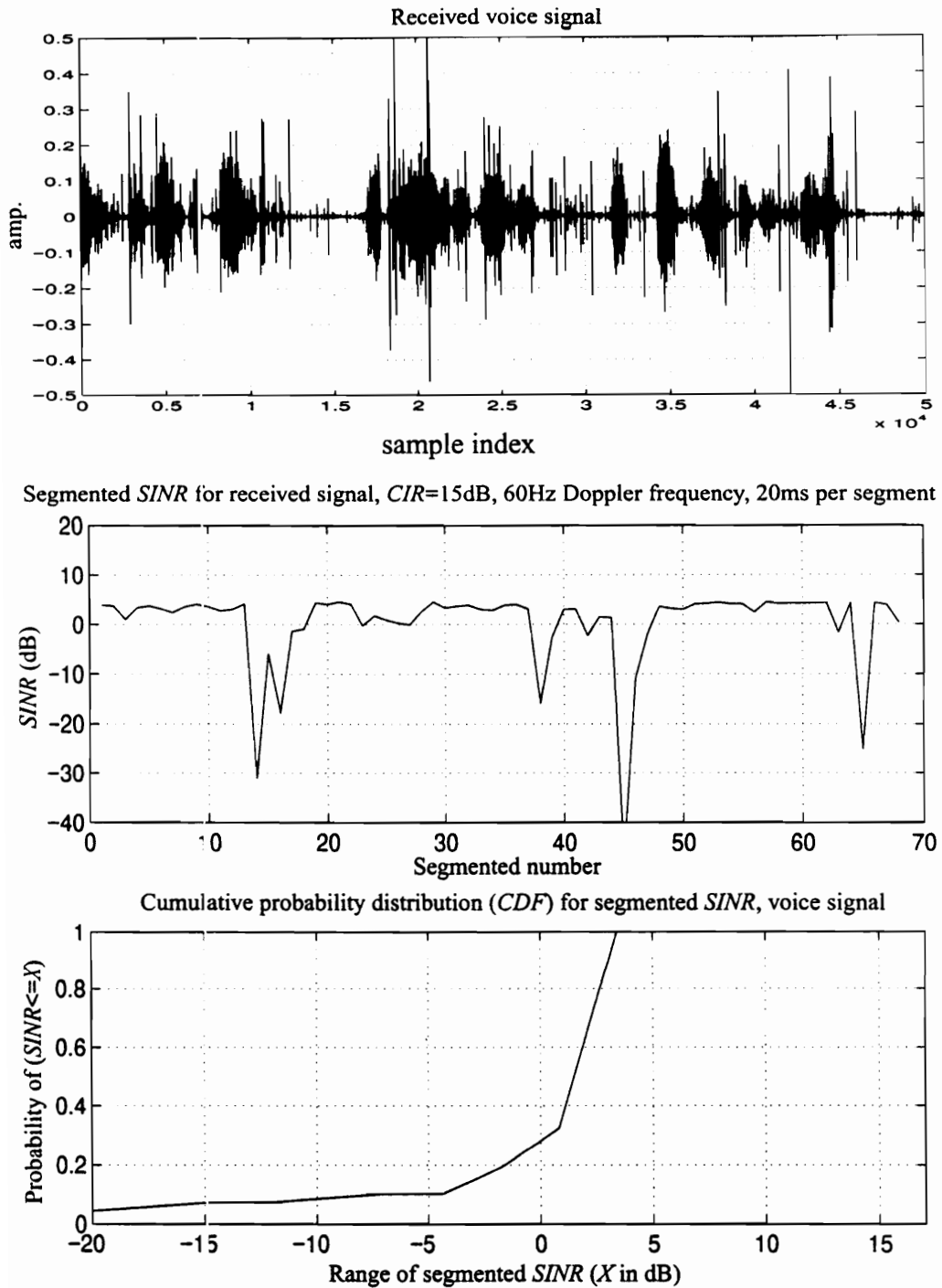


Fig. 6.10 Demodulated voice signal without the TDADF, and the corresponding $SINR$ and CDF , $CIR=15\text{dB}$

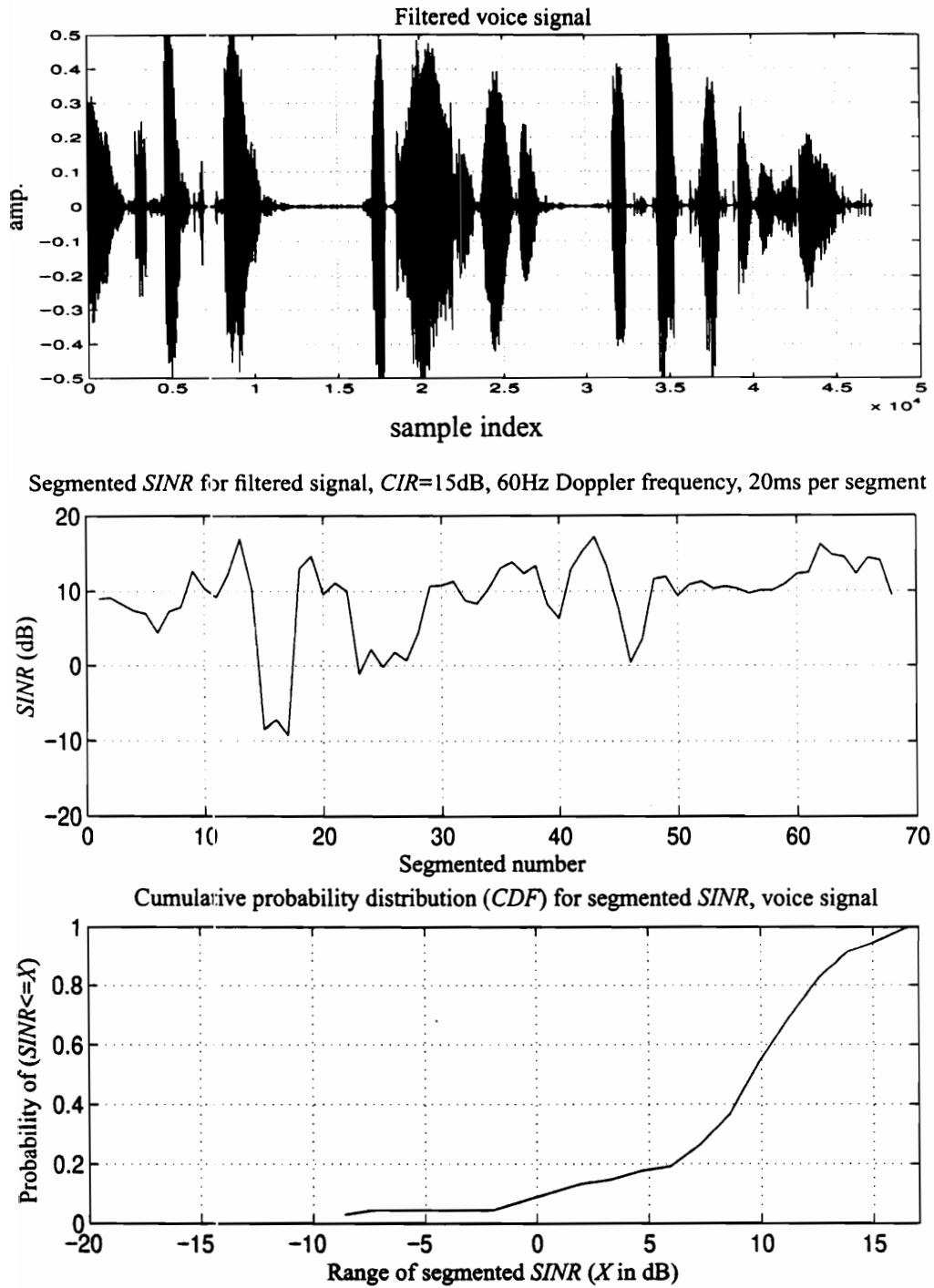


Fig. 6.11 Demodulated voice signal with the TDAF, and the corresponding segmented SINR and CDF, CIR=15dB

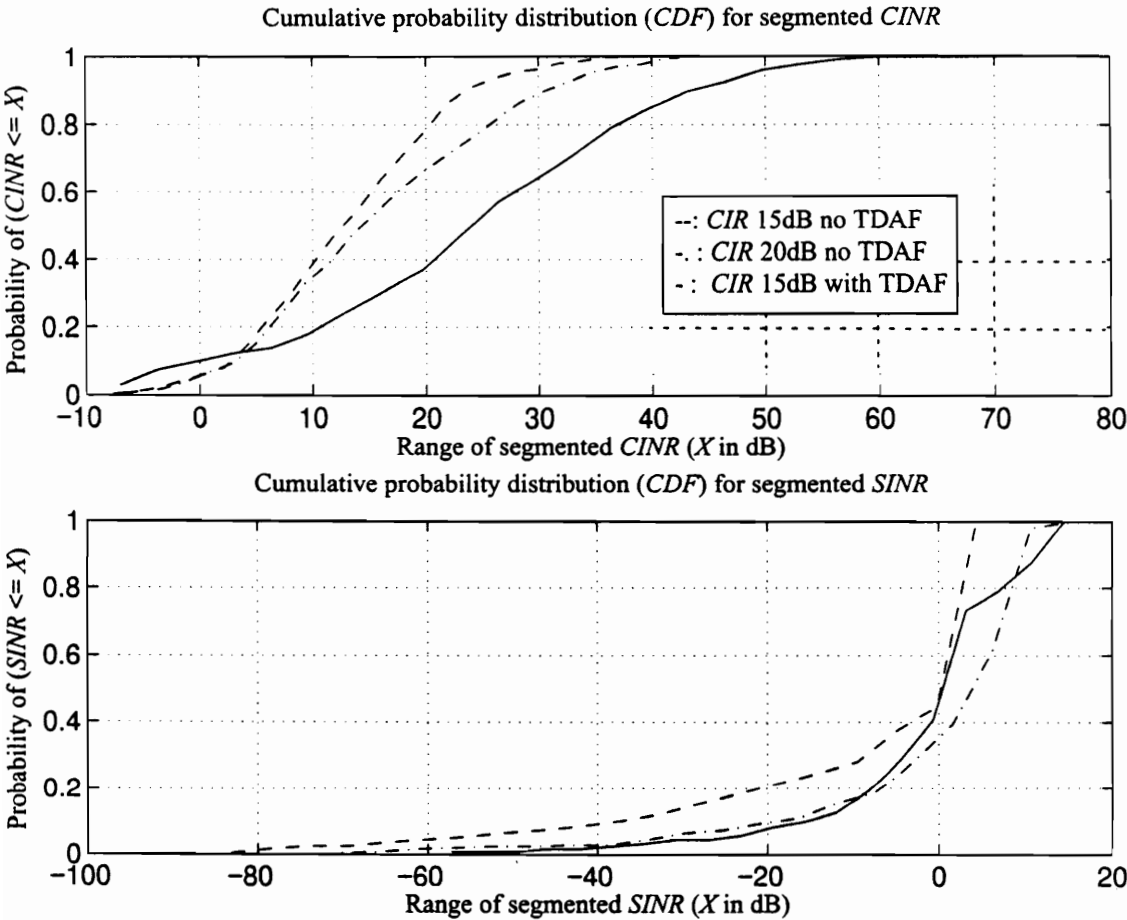


Fig. 6.12 CDF Comparison for segmented $CINR$ and segmented $SINR$ with and without the TDAF, $CIR=15\text{dB}$

Chapter 7. Statistical Analysis of Channel Interference and Capacity Improvement When Using Interference Rejection Techniques

Radio-frequency (RF) interference is one of the most important performance considerations in the design, operation, and maintenance of mobile communication systems. To satisfy the demand for more spectrum arising from the dramatic growth of these communication systems, it is necessary to minimize channel interference. Frequency reuse techniques are the usual solution. It is impossible, however, to provide an interference-free system.

There are two major interference problems in mobile radio systems: adjacent-channel interference and co-channel interference. Other types of interference are possible including intermodulation and intersymbol interference. Intermodulation interference is generated in a nonlinear circuit when the product of two or more signals results in another signal having a center frequency close to the desired signal. The interaction between the signals due to the power amplifier and the first frequency converter of the receiver typically produces this kind of interference. Intersymbol interference is intrinsic to digital networks and is a direct consequence of the limited bandwidth of the transmission medium. The transmitted symbols tend to spread in time and consequently overlap, which results in intersymbol interference. The main focus of this research is on co-channel interference and to a lesser extent, on adjacent channel interference. The following two sections will discuss each of these types of interference, especially co-channel interference. The average *CIR* coverage for both the base station and the mobile station is studied in Section 7.3. The effect of power control on the average *CIR* coverage is also evaluated in Section 7.4 along with the impact of new DSP techniques on average *CIR* coverage. Most important, the impact on system capacity using these DSP techniques is presented in Section 7.5.

7.1 Adjacent Channel Interference

Adjacent channel interference causes problems in mobile radio systems since channel spacing is minimized to obtain maximum spectral efficiency. Radio propagation characteristics and practical receiver limitations, such as frequency instability, filtering and random signal fluctuations, cause out of band energy thereby impacting adjacent channel interference.

There are two types of adjacent channel interference: intracell and intercell interference. Both types are described below.

Intracell Adjacent Channel Interference

A mobile unit which transmits from a short distance to the base station may interfere strongly with the signal of another mobile unit which transmits on an adjacent frequency channel from a long distance to the same base station. Fading can also cause a similar problem. This is known as *intracell adjacent channel interference*. Avoiding the use of adjacent channels within the same cell and applying power control to each user are possible solutions to this problem.

Intercell Adjacent Channel Interference

Consider two mobile units near a cell border, each transmitting to its own home base station on adjacent frequency channels. Due to the fact that signals experience uncorrelated fading, the received interfering signal may be larger than the desired signal at the base station. The base stations will receive the desired signal and a certain level of interference from the out-of-cell mobile. This is known as *intercell adjacent channel interference* or *adjacent-channel near use*.

Some statistical properties, such as the probability of occurrence, of both types of adjacent channel interference are investigated in this section. These properties are a function of the

propagation parameters and traffic distribution of the system. The study begins with the definition of the following parameters, assuming channel i is the channel of interest.

- p_1 : probability of occurrence of only one adjacent channel interferer, i.e., either $i+1$ channel or $i-1$ channel is active.
- p_2 : probability of occurrences of two adjacent channel interfering sources, i. e., both the $i+1$ and the $i-1$ channels are active.
- γ : proportion of mobiles with adequate ability to communicate with more than one base station, i.e., probability that a mobile can communicate through channels of two or more cells.
- δ : proportion of mobiles with adequate ability to communicate with more than two base stations, i.e., probability that a mobile can communicate through channels of three or more cells.
- μ' : probability of a mobile receiving a signal level below a given value.

Parameters p_1 and p_2 are dependent on both the channel assignment algorithm and the traffic load of the system. On the other hand, γ , δ and μ' depend on the mean signal strength. In a hexagonal cell array, as shown in Fig. 7.1a, δ is the probability that a mobile is in the vicinity of the border of three mutually adjacent cells (the joint corner of three adjacent cells). Therefore, $\delta/6$ is the probability that this mobile is at one out of the six possible "corners". The difference $\gamma-\delta$ gives the probability that a mobile is at the vicinity of a border between two adjacent cells as shown in Fig. 7.1b. Hence, $(\gamma-\delta)/6$ gives the probability that this mobile is at one out of the six possible joint borders.

Adjacent channel interference may occur at the mobile or at the base station. For the mobile case, the mobile using channel i may suffer interference from channel $i+1$ and (or) channel $i-1$ when the mobile is near the border of the two base stations. It can be shown that the probability of adjacent-channel interference at the mobile unit, p_M , for the forward link, is [Yac93]

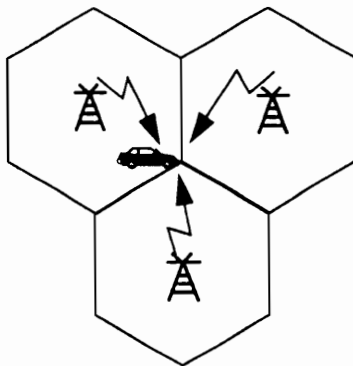


Fig. 7.1a Adjacent channel interference for a mobile at a joint corner

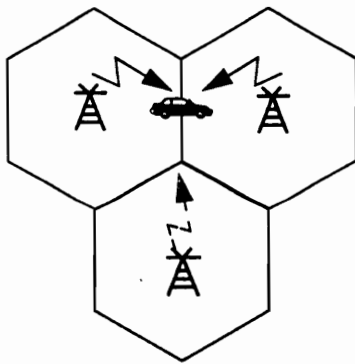


Fig. 7.1b Adjacent channel interference for a mobile at a joint border

$$p_M = \frac{\gamma + \delta}{3} I_A, \quad (7.1)$$

where I_A gives the incidence of adjacency, i. e., the proportion of occurrence of adjacent channel interference,

$$I_A = \frac{p_1 + 2p_2}{2}. \quad (7.2)$$

For the base station case, the base station using the i th channel may receive the desired signal and adjacent channel interference from another mobile which is near the border in an adjacent cell. The probability p_B of intercell adjacent-channel interference at the base station for the reverse link is [Yac93]

$$p_B = \frac{\gamma + \delta}{3} \mu' I_A. \quad (7.3)$$

In fact, γ and δ are not independent probabilities. It has been shown that δ is a function of γ and the relationship between them can be reasonably approximated by [Yac93]

$$\delta = \begin{cases} 1.25\gamma^2, & 0 \leq \gamma \leq 0.8 \\ \gamma, & 0.8 \leq \gamma \leq 1. \end{cases} \quad (7.4)$$

The probabilities of γ and δ are closely related with geographical location, and are also related with the probability of traffic density.

Assume $p(n)$ is the probability of n active adjacent channels ($n=0,1,2$). The state of the channels, in use or not in use, can be represented by the Bernouli distribution,

$$p(\omega) = p^\omega (1-p)^{1-\omega}, \quad \omega = 0, 1, \quad (7.5)$$

where p is the probability of the channel being active, $\omega=1$ indicates that the channel is in use, and $\omega=0$ indicates the channel is not in use. If all the cells have an equal capacity (i.e., the same number of channels per cell CN) and the traffic has an even distribution (i.e., the same blocking probability B in each cell), then $p=B^{1/CN}$ and [Yac93]

$$p(n) = \binom{2}{n} B^{\frac{n}{CN}} \left(1 - B^{\frac{1}{CN}}\right)^{2-n} . \quad (7.6)$$

Thus, p_1 and p_2 ($n=1$ and $n=2$) can be computed as follows,

$$p_1 = 2B^{\frac{1}{CN}} \left(1 - B^{\frac{1}{CN}}\right) , \quad (7.7)$$

$$p_2 = B^{\frac{2}{CN}} . \quad (7.8)$$

Figures 7.2 and 7.3 contain plots of p_1 and p_2 as a function of the blocking rate B for various values of CN , i.e., the number of channels per cell.

To suppress the intercell adjacent channel interference, the traditional method at the receiver (and the transmitter) is to bandpass filter each channel. This scheme does limit the adjacent channel interference to some extent. However, if the carrier frequencies drifts slowly and the power level fluctuates randomly, an adaptive solution is needed. Different types of adaptive filters, such as IIR, FIR, and a decision feedback filter, can be implemented by using different adaptive algorithms to address this problem.

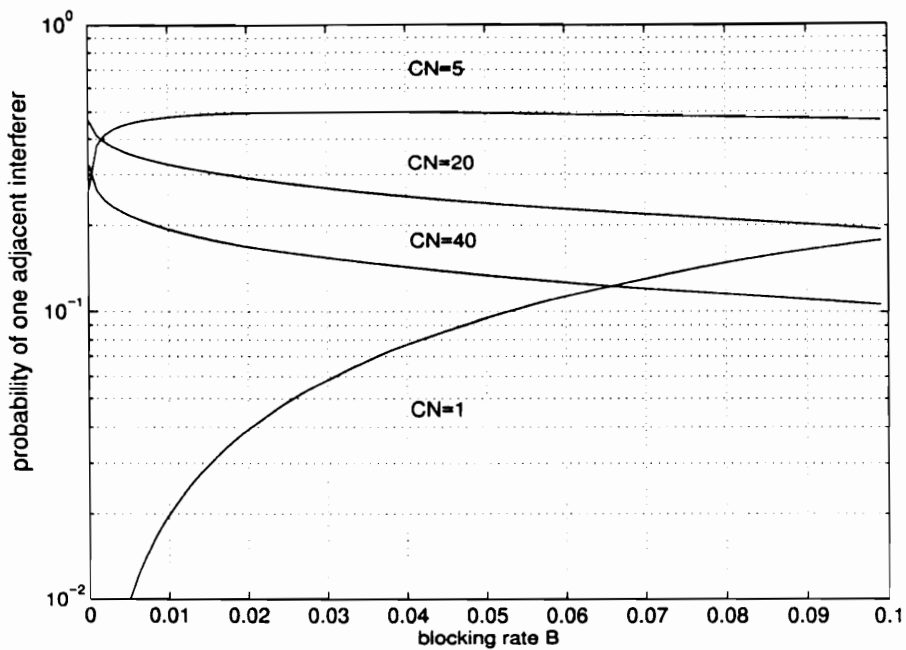


Fig. 7.2 Probability of one adjacent interferer

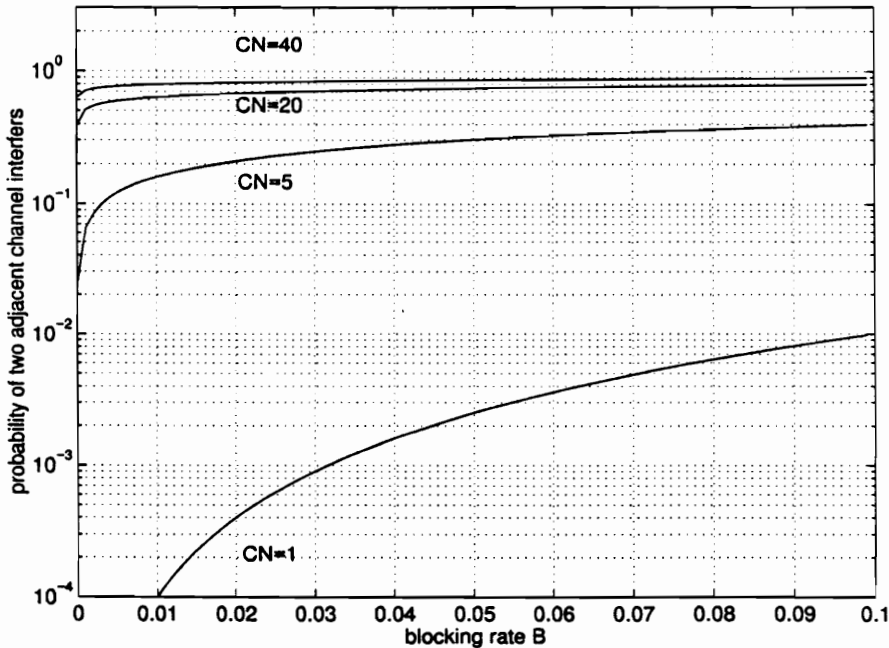


Fig. 7.3 Probability of two adjacent interferers

7.2 Co-channel Interference

Co-channel interference is the bottleneck for system capacity in the current mobile phone systems. Frequency reuse is typically applied to accommodate more users in the same area. For example, for the current analog AMPS system, 416 channels, including the control and voice channels, are allocated for the forward link operated in the frequency band of 869-890MHz. These 416 channels are assigned to 7 cells, yielding 57 voice channels for one cell. All of these RF channels can be simultaneously reused in the same region as long as the cell which reuses the same frequencies is far enough away to avoid co-channel interference. To reduce co-channel interference, we need to separate the co-channel cells by a minimum distance that will provide sufficient isolation. If the size of each cell in a cellular system is roughly the same, co-channel interference is independent of the transmitted power and becomes a function of the radius of the cell (R), and the distance to the center of the nearest co-channel cell (D). By increasing the ratio of D/R , the spatial separation between co-channel cells relative to the coverage distance of a cell is increased [Rap96].

Since an actual cell region is difficult to describe mathematically, a hexagon is often used to represent the cell. Given the fact that a hexagon has exactly six equidistant neighbors and that the lines joining the centers of the a given cell and each of its neighbors are separated by multiples of 60 degrees, there are only certain feasible cluster sizes and cell layouts which are possible to connect all the cells without gaps. The frequency reuse number N has to satisfy the equation [Rap96]

$$N = i^2 + ij + j^2, \quad (7.9)$$

where i and j are non-negative integers. Clearly, N can be 3, 4, 7, 12, 19, etc. for different combination of i and j . The nearest co-channel neighbors of a particular cell can be found by moving i cells along any chain of hexagons and then turning 60 degrees counter-clockwise and moving j cells. The co-channel reuse ratio Q is defined as [Rap96]

$$Q = \frac{D}{R} = \sqrt{3N}. \quad (7.10)$$

A smaller value of Q provides a larger capacity since the reuse factor N is small, but the signal quality is diminished. A larger value of Q improves the signal quality, due to the lower level of co-channel interference, but the system capacity becomes limited. A trade off must be made between these two objectives in actual cellular design.

Based on the propagation measurement in a mobile channel, the average received signal strength at any point decays as a power law of the distance of separation between a transmitter and receiver. The average received power P_r at a distance d from the transmitting antenna is approximated by [Rap96]

$$P = P_0 \left(\frac{d}{d_0} \right)^{-n}, \quad (7.11)$$

where P_0 is the power received at a close-in reference point in the far field region of the transmitting antenna at a distance of d_0 from itself, and n is the path loss exponent. The carrier to interference ratio for a receiver for a forward channel can be expressed as

$$\frac{C}{I} = \frac{C}{\sum_{m=1}^M I_m} = \frac{R^{-n}}{\sum_{m=1}^M D_m^{-n}}, \quad (7.12)$$

where C is the desired signal's power from the base station and I_m is the interference from the m th interfering co-channel cell base station. D_m is the center distance between the m th interfering cell and the desired cell. The actual CIR is a random variable, affected by random phenomena such as the location of a mobile and cell site, Rayleigh fading, lognormal shadowing, and antenna characteristics, etc. Assuming that the cell system is composed of

idealized hexagon cells and all the interfering cells are equidistant from the base station receiver, Eq. (7.12) can be written as

$$\frac{C}{I} = \frac{(\sqrt{3}N)^n}{M} . \quad (7.13)$$

Eq. (7.13) is optimistic since the assumptions used to derive it are rarely true. For the current analog system (AMPS), the total number of voice channels is 399. Each cell is assigned 57 channels for a seven-cell reuse pattern and 133 channels for a three-cell reuse pattern, and 99 channels for a four-cell reuse pattern. The required carrier to interference ratio determines the cell reuse factor. For the worst case when the mobile is at the cell boundary, the carrier to interference ratio is approximated as [Lee86][Rap96],

$$\frac{C}{I} = \frac{R^{-n}}{(D-R)^{-n} + \left(D - \frac{R}{2}\right)^{-n} + 2\left(D + \frac{R}{2}\right)^{-n} + (D+R)^{-n} + D^{-n}} . \quad (7.14)$$

Substituting $Q=D/R$ into the above equation, we have

$$\frac{C}{I} = \frac{1}{\frac{(Q+1)^n + (Q-1)^n}{(Q^2-1)^n} + \frac{(Q+0.5)^n + 2(Q-0.5)^n}{(Q^2-0.25)^n} + \frac{1}{Q^n}} . \quad (7.15)$$

For a seven-cell reuse pattern, $Q=4.583$, and thus the worst case C/I is evaluated to be 17.9681dB, which compares well with the exact value of 17.8483dB [Jac94]. Fig. 7.4 describes the CIR as a function of the pathloss exponent n for different frequency reuse patterns. The higher the n , the larger the average CIR will be. Obviously, the average CIR for a seven-cell reuse pattern is higher than for a three-cell reuse pattern since the distance between the desired cell and the co-channel cell is greater for the seven-cell reuse pattern.

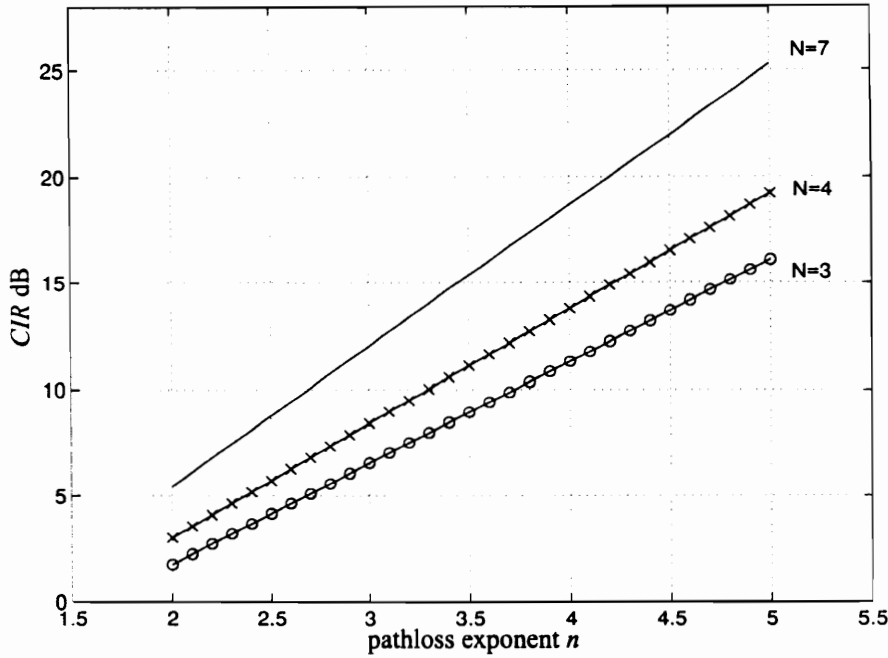


Fig. 7.4 Carrier to interference ratio for different frequency reuse patterns with equal interfering distances

The results shown above are based on the assumption that either the base station or the mobile unit receives all the first layer co-channel interfering sources at the same time. For practical systems, however, co-channel interference occurs with some probability related to the carrier to interference ratio and the traffic parameters.

A mobile radio in a given cell receives the desired signal power c from its base station, but it also receives interfering sources having powers i_j , $j=1,2,3,\dots, n_c$ (n_c is the number of active co-channel cells). For a hexagonal representation and omni-antenna, the maximum value of n_c is 6 if only the first tier interfering signals are considered. Co-channel interference will occur whenever the desired signal's power does not simultaneously exceed the minimum required signal level c_0 , and exceeds the total interfering signals by some protection ratio r . When the co-channel interference exceeds the protection ratio, interference has a significant effect on the desired signal. Given n_c interferers, the conditional outage

probability $p(CI|n_c)$ due to co-channel interference (CI) which is defined as the probability of failing to achieve adequate reception of desired signal is [Yac93]

$$p(CI|n_c) = 1 - \int_{c_0}^{\infty} p(s) \int_0^{\frac{c}{r}} p(i) di ds, \quad (7.16)$$

where $p(s)$ is the probability density function (*pdf*) for the desired signal's power, and $p(i)$ is the *pdf* of the total interfering signal's power. Clearly, the integral of $p(s)$ from c_0 to ∞ gives the probability of the desired signal exceeding the required level c_0 and simultaneously the integral of $p(i)$ from 0 to c/r gives the probability that all of the interferers are below the threshold c/r .

Generally, $p(i)$ is difficult to find due to the random statistics of the received signals. An alternative method is to consider each interfering signal i_j independently as in the following equation,

$$p(CI|n_c) = 1 - \int_{c_0}^{\infty} p(s) \int_0^{\frac{c}{r}} p(i_1) \int_0^{\left(\frac{c}{r} - i_1\right)} p(i_2) \dots \int_0^{\left(\frac{c}{r} - i_1 - \dots - i_{n_c-1}\right)} p(i_{n_c}) di_{n_c} \dots di_1 ds. \quad (7.17)$$

The total probability of co-channel interference can then be obtained by

$$p(CI) = \sum_{n_c} p(CI|n_c) p(n_c), \quad (7.18)$$

where $p(n_c)$ is the probability density function of the number of active interfering signals. To evaluate the conditional probability of $p(CI|n_c)$, the radio environment must be consid-

ered. Rayleigh and lognormal fading are usually assumed. The transmission strength between the base station and the mobile station is generally modeled by a rapidly changing Rayleigh distributed envelope gain $R(t)$ applied to a slowly varying mean signal strength $L(t)$. For a constant envelope modulated signal, the received signal can be expressed as

$$x(t) = R(t)L(t)e^{j(\Phi(t) + \Phi_r(t))}, \quad (7.19)$$

where $\Phi(t)$ is the phase of the desired signal including the carrier and $R(t)e^{j\Phi_r(t)}$ is a complex Gaussian random variable. The probability of occurrence of co-channel interference for a fading only channel and both a fading and a lognormal shadowing channel are discussed in the following sections.

7.2.1 Fading Only Environment

The probability density function of *CNR* for a received signal x in a Rayleigh environment for a fixed noise power is given by [Yac93]

$$p(x) = \frac{1}{\bar{x}} e^{-\frac{x}{\bar{x}}}, \quad (7.20)$$

where \bar{x} is the local signal-to noise ratio, i. e., $\bar{x} = E_0^2/NG$, with E_0 the average amplitude of the radio wave and NG the mean power of Gaussian noise. The *pdf* for the desired signal $p(s)$ and the interference $p(i_j)$ will be the same as expressed in Eq. (7.20).

For multiple interferers in a Rayleigh fading environment, the probability of occurrence of co-channel interference can be computed using Eq. (7.20) by following an analytical method using a recursive process given by Sowerby and Williamson to approximate Eq. (7.17) [Yac93]. Define the signal to the k th interference ratio as, $\Lambda_k = \bar{c} / \bar{i}_k$. For an ‘inter-

ference-only” environment, where the minimum signal requirement is ignored, i.e., $c_0=0$, and the desired signal is always present, it is shown that the outage probability $p(CI|n_c)$ is approximated by[Yac93]

$$p(CI|n_c) \approx \sum_{j=1}^{n_c} \prod_{k=1}^j \frac{\frac{\Lambda_{k-1}}{r}}{1 + \frac{\Lambda_k}{r}}, \text{ with } \Lambda_0 = 1. \quad (7.21)$$

If the power levels of the interfering signals are equal, then [Yac93]

$$p(CI|n_c) = 1 - \left(\frac{\frac{\Lambda}{r}}{1 + \frac{\Lambda}{r}} \right)^{n_c}. \quad (7.22)$$

To complete the evaluation of $p(CI)$, the probability of the number of active interfering signals, $p(n_c)$, must be determined. Again, it is described by the Bernouli distribution as given in Eq. (7.5). Assuming hexagonal representation and considering only the first tier of the co-channel interference, the probability $p(n_c)$ can be expressed as

$$p(n_c) = \binom{6}{n_c} p^{n_c} (1-p)^{6-n_c}, \quad (7.23)$$

where p is equal to $B^{1/CN}$, B is the blocking rate and CN is the total number of channels per cell. The probability $p(n_c)$ is shown in Fig. 7.5 as a function of p .

The total probability of $p(CI)$ in Eq. (7.18) can be evaluated as

$$p(CI) = \sum_{n_c} \binom{6}{n_c} p^{n_c} (1-p)^{6-n_c} \left(1 - \left(\frac{\frac{\Lambda}{r}}{1 + \frac{\Lambda}{r}} \right)^{n_c} \right),$$

(7.24)

where n_c varies from 0 to 6 assuming an omni-antenna.

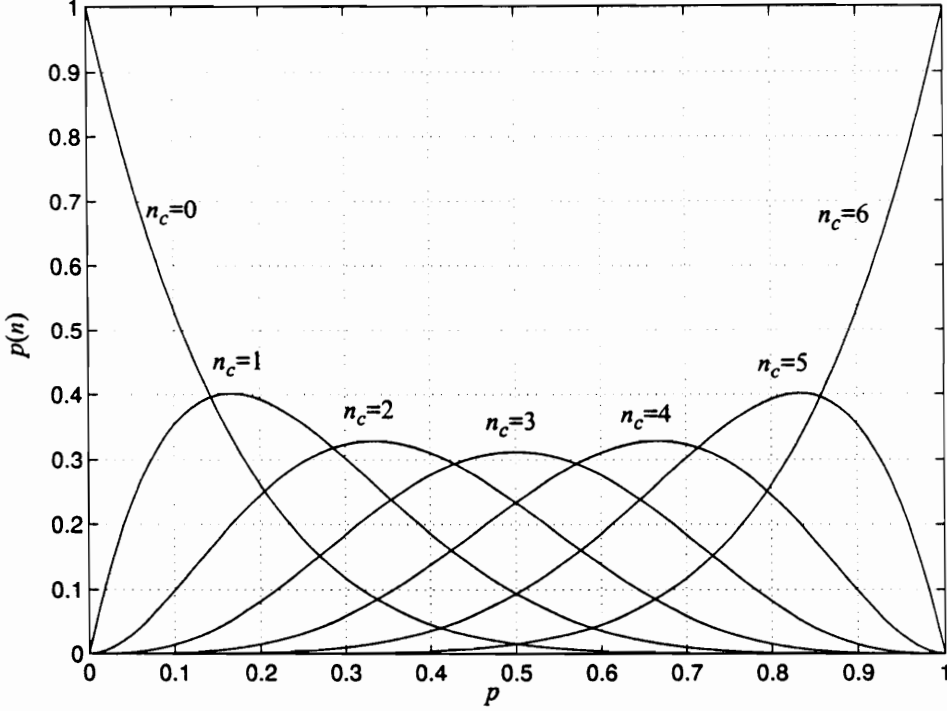


Fig. 7.5 Probability of n_c active interfering signals as a function of single channel blocking probability p

The three-dimensional plot in Fig. 7.6 shows the total probability in Eq. (7.24) as a function of both the CIR and the blocking rate. The protection ratio r is 8dB. A lower CIR causes a higher probability of occurrence of interference. From Fig. 7.6, it can be seen that the total probability of co-channel interference varies slightly for different blocking rates even though the probability of n_c active channels $p(n_c)$ is different for different blocking rates.

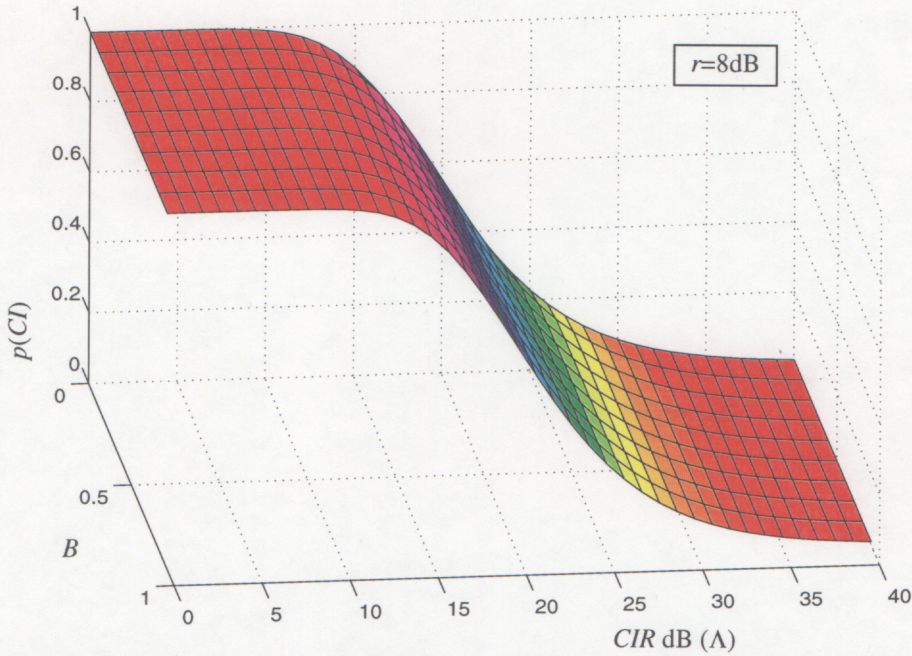


Fig. 7.6 Total probability of co-channel interference (Rayleigh only environment) of a seven-cell frequency reuse pattern as a function of blocking rate and CIR. Note there is little dependency on blocking rate

7.2.2 Fading and Lognormal Shadowing Environment

Here we estimate the probability of co-channel interference when the signal experiences both fading fluctuation and lognormal shadowing. The *pdf* of the received signal envelope can be derived and is given by[Mua82]

$$p(s) = \sqrt{\frac{\pi}{8\sigma^2}} \int_{-\infty}^{\infty} \frac{s}{10^{S_d/10}} e^{-\frac{\pi s^2}{4 \times 10^{S_d/10}}} e^{-\frac{(S_d - \bar{S}_d)^2}{2\sigma^2}} dS_d, (s > 0), \quad (7.25)$$

where S_d is the local mean in decibels, \bar{S}_d is the area mean in decibels and σ is the standard deviation in decibels (typically between 5dB to 12dB in urban locations). Eq. (7.25) also can be used to describe the *pdf* of each interfering signal. The difficulty in evaluating

Eq. (7.16) is the complexity of the joint *pdf* of all the interfering signals. However, it has been shown that the summation of such distributions can be approximated by a normal distribution [Mua82] for $\sigma=0\text{dB}$ and a lognormal distribution for $\sigma=6\text{dB}$ and 12dB . Therefore, the *pdf* of $i = \sum_{n_c} i_{n_c}$ is approximately another lognormal distribution assuming the signal envelope of all the interferers are independent and identically distributed, and it is given by [Mua82]

$$p(i) = \frac{20}{(\ln 10)\sqrt{2\pi i\sigma_i}} e^{-\frac{(20\log_{10} i - I_i)^2}{2\sigma_i}}, \text{ for } \sigma > 0, \quad (7.26)$$

where σ_i and I_i are, respectively, the variance and the mean value of the corresponding normal distribution i , both in decibels. These values are given by [Mua82]

$$\sigma_i^2 = \left(\frac{20}{\ln 10}\right)^2 \left\{ \ln \left(e^{\frac{\sigma^2 + (20/\ln 10)^2 \ln(4/\pi)}{(20/\ln 10)^2}} + n_c - 1 \right) - \ln n_c \right\},$$

$$I_i = \bar{I}_d - \frac{10}{\ln 10} \ln\left(\frac{4}{\pi}\right) + \frac{20}{\ln 10} \ln n_c + \frac{\sigma^2 + (20/\ln 10)^2 \ln(4/\pi) - \sigma_i^2}{40/\ln 10}, \quad (7.27)$$

where \bar{I}_d is the area mean of the interference. Thus, the conditional probability of co-channel interference in this case can be evaluated by substituting Eq. (7.25) and Eq. (7.26) into Eq. (7.16) while assuming $c_0=0$. This produces

$$p(CI|n_c) = \frac{10}{2\ln 10 \sigma \sigma_i} \int_{-\infty}^{\infty} dS_d \int_0^{\frac{c}{r}} di \int_0^{\frac{s}{i10^{S_d/10}}} \frac{s}{i10^{S_d/10}} e^{-\frac{\pi s^2}{4 \times 10^{S_d/10}}} e^{-\frac{(S_d - \bar{S}_d)^2}{2\sigma^2}} e^{-\frac{(20\log_{10} i - I_i)^2}{2\sigma_i}} ds di. \quad (7.28)$$

The total probability of co-channel interference, $p(CI)$, can be evaluated by substituting Eq. (7.23) and Eq. (7.28) into Eq. (7.18). The resulting expression is numerically evaluated and is plotted in Fig. 7.7 as a function of the average desired signal's power to the average interfering signal's power Λ , i.e., $\overline{S_d} - \overline{I_d}$. Again, the protection ratio r is 8dB. To compare the overall system performance, the probability of the co-channel interference for the Rayleigh only environment is also plotted in the same figure. It can be seen that for lower Λ , such as $\Lambda < 10\text{dB}$, the two probabilities do not differ much. However, the total probability of co-channel interference for a Rayleigh and lognormal shadowing environment is significantly higher than that for a Rayleigh only environment when Λ increases. For an example, the probability of co-channel interference is 80% for the former case when $\Lambda = 20\text{dB}$, while it is only 55% for the latter case. This can be explained by the fact that the signal power attenuates logarithmically as the transmitter-receiver (T-R) separation increases in addition to the Rayleigh fluctuations.

In a mature system where the number of channels per cell is relatively large, the impact of the blocking rate is not significant. For the AMPS system, 57 channels are allocated for one cell. This results in high probability of active channels for $n_c = 6$ as shown in Fig. 7.5. Consequently, the total probability of co-channel interference is very close to the conditional probability when $n_c = 6$, which apparently is not a function of the traffic load. It has been observed that for the Rayleigh and lognormal shadowing channel a similar result holds, i.e., the probability of co-channel interference is not greatly influenced by blocking rate.

7.3 Percentage of CIR Coverage at a Receiver

It is also useful to determine the percentage of useful CIR coverage at a receiver for both the mobile station and the base station. First of all, the percentage of useful CIR coverage where the carrier to interference ratio is above a certain level for a particular mobile loca-

tion is studied. The propagation model in Eq. (7.11) does not take into account the fact that the surrounding environmental clutter may lead to a deviation in the measured signal from the basic line-of-sight model given by Eq. (7.11). Measurements have shown that at any value of d , the received power $P(d)$ at a particular location is distributed log-normally (normal in dB) about the mean distance value d_0 , i.e.,

$$P(d) = P_0 - 10n \log_{10} \left(\frac{d}{d_0} \right) + X_\sigma \quad , \quad (7.29)$$

where X_σ is a zero-mean log-normally distributed random variable with standard deviation σ (in dB) [Rap96], and P_0 and d_0 are as defined in Eq. (7.11). This deviation reflects the different level of clutter on the propagation path within the same T-R separation. More generally, the logarithmic carrier to interference ratio for the case in Eq. (7.12) combined with Eq. (7.29) can be expressed as

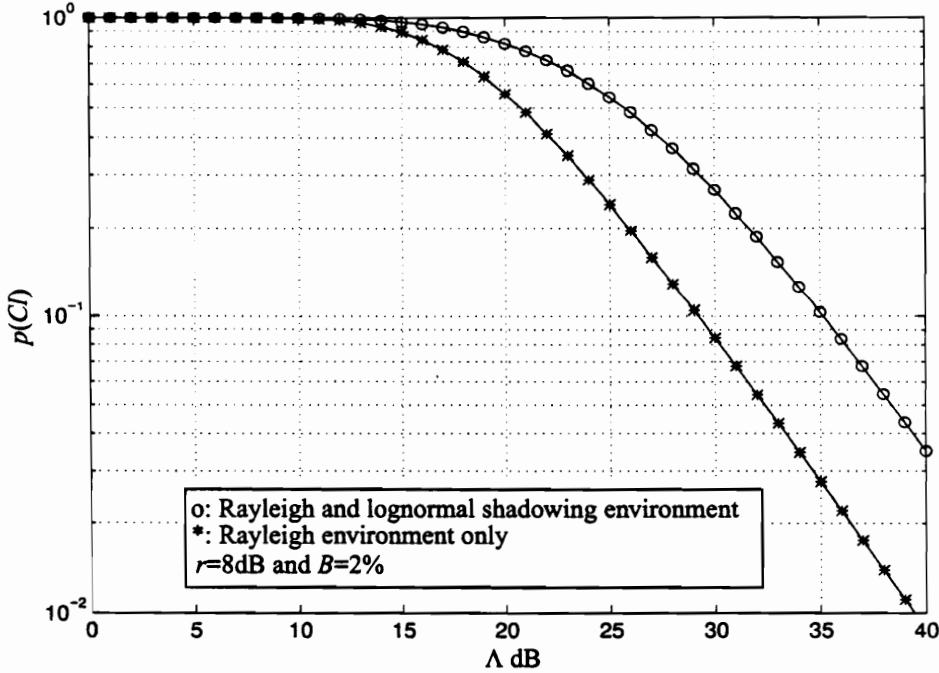


Fig. 7.7 Comparison of the total probability of co-channel interference as a function of CIR for the Rayleigh only environment and Rayleigh lognormal shadowing environment assuming a seven-cell frequency reuse pattern

$$\begin{aligned}
 10\log_{10}\frac{C}{I} &= K + P_0 - 10n\log_{10}\left(\frac{r_s}{d_0}\right) + S_{\sigma_s} - \left(P_0 - 10n\log_{10}\left(\frac{l}{d_0}\right) + I_{\sigma_l}\right) \\
 &= K - 10n\log_{10}\left(\frac{r_s}{l}\right) + S_{\sigma_s} - I_{\sigma_l} ,
 \end{aligned}
 \tag{7.30}$$

where $K = -10\log_{10}n_c$, which is a constant related to the number of interfering sources, r_s and l are the distance between the mobile unit to the desired base station and to the interfering base station, respectively, and S_{σ_s} and I_{σ_l} are random variables which are log-normally distributed with standard deviation of σ_s and σ_l . For Eq. (7.30), the same path loss exponent n is assumed for the desired signal and the interference, and all the interfering sources have the same power. Let $CIR = 10\log_{10}C/I$, where C is the local mean of the carrier to noise ratio for the desired signal and I is the local mean of the carrier to noise ratio for the interfering signal. Since both C and I are zero-mean log-normally distributed, the distribution of the CIR will also be log-normal, with mean μ and standard deviation σ given by

$$\begin{aligned}
 \mu &= \mu_s + \mu_l = 0 \\
 \sigma &= \sqrt{\sigma_s^2 + \sigma_l^2} .
 \end{aligned}
 \tag{7.31a}$$

The mean CIR in Eq. (7.30) is

$$\begin{aligned}
 \overline{P\left(\frac{r_s}{l}\right)} &= E\left[K - 10n\log_{10}\left(\frac{r_s}{l}\right) + S_{\sigma_s} - I_{\sigma_l}\right] \\
 &= K - 10n\log_{10}\left(\frac{r_s}{l}\right) + \mu_s + \mu_l \\
 &= K - 10n\log_{10}\left(\frac{r_s}{l}\right) .
 \end{aligned}
 \tag{7.31b}$$

Thus the percentage of CIR coverage for a particular mobile location can be calculated

from the cumulative density function as [Rap96]

$$\begin{aligned}
 p(CIR > CIR_0) &= Q\left(\frac{CIR_0 - \overline{P\left(\frac{r_s}{l}\right)}}{\sigma}\right) \\
 &= Q\left(\frac{CIR_0 - \left(K - 10n \log_{10}\left(\frac{r_s}{l}\right)\right)}{\sigma}\right),
 \end{aligned}
 \tag{7.32}$$

where the Q -function is defined as

$$Q(x) = \frac{1}{\sqrt{2\pi}} \int_x^{\infty} e^{-\frac{x^2}{2}} dx.
 \tag{7.33}$$

The outage probability is $p_{out} = 1 - p(CIR > CIR_0)$. For the worst case when the desired mobile station is located furthest from the base station and the interfering mobile at the co-channel cell is located at the closest possible location to the same base station, Eq. (7.32) simplifies to

$$p(CIR > CIR_0) = Q\left(\frac{CIR_0 - (K - 10n \log_{10}(\sqrt{3N} - 1)^{-1})}{\sigma}\right)
 \tag{7.34}$$

by using Eq. (7.10). Eq. (7.34) is evaluated for different cell reuse patterns with $K=0$ dB, i.e., a single co-channel interference source is considered. The results are plotted in Fig. 7.8. From the figure, it can be seen that the percentage of CIR coverage decreases significantly with a lower frequency reuse pattern. The worst case CIR coverage is 60% for a seven cell reuse pattern for a 18dB threshold, while it is only 20% for the three cell reuse

pattern. In the following sections, the percentage of average *CIR* coverage over a cell is discussed for both the mobile and base station.

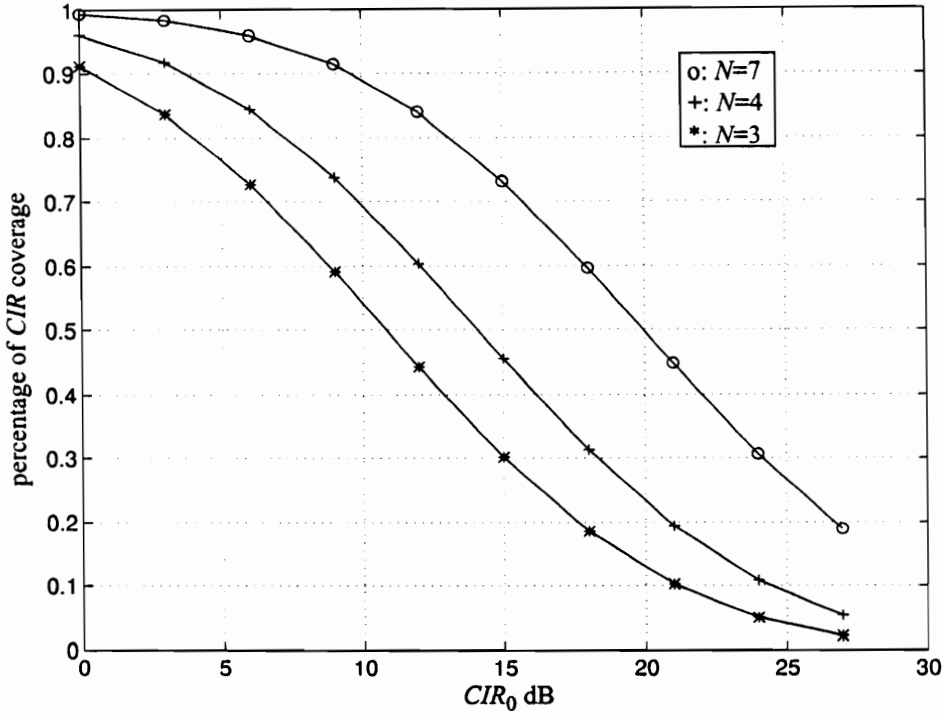


Fig. 7.8 Worst case $p(CIR > CIR_0)$ for different frequency reuse patterns, $n=3.6$ and $\sigma=8$ dB, assuming single interference source

7.3.1 Percentage of Average *CIR* Coverage at a Mobile Station

Fig. 7.9 illustrates how co-channel interference is introduced into a mobile station. When the mobile moves in its service cell B_1 , it receives the signal from the desired base station B_1 , but it also receives an interfering signal from its co-channel cell B_2 . Assuming the location of the mobile is at (r_s, θ) and the distance between the mobile and B_2 is l , the conditional probability of *CIR* coverage given r_s and l based on Eq. (7.32) is given as

$$p(CIR > CIR_0 | r_s, l) = Q \left(\frac{CIR_0 - \left(K - 10n \log_{10} \frac{r_s}{l} \right)}{\sigma} \right). \quad (7.35)$$

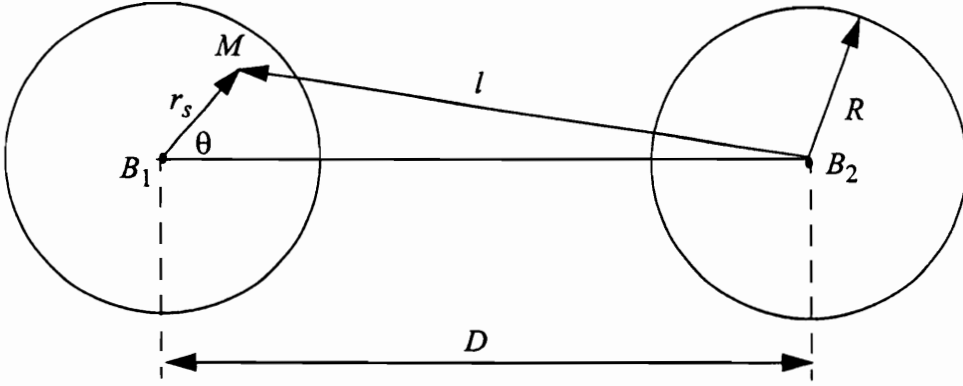


Fig. 7.9 Illustration of the co-channel interference for a mobile station

From Fig. 7.9, r_s/l can be expressed as a function of the location of the mobile (r_s, θ) and is given by

$$\frac{r_s}{l} = \frac{r_s}{\sqrt{D^2 + r_s^2 - 2Dr_s \cos \theta}}. \quad (7.36)$$

Assuming uniform usage in a cell, the *pdfs* of r_s and θ are independent with each other and are given by [Lib95]

$$\begin{aligned} p_{pdf}(\theta) &= \frac{1}{2\pi}, \quad (0 < \theta \leq 2\pi), \\ p_{pdf}(r_s) &= \frac{2r_s}{R^2}, \quad (0 < r_s \leq R). \end{aligned} \quad (7.37)$$

Thus, by combining Eq. (7.35) and Eq. (7.37), the joint pdf $p(CIR > CIR_0, r_s, \theta)$ is not difficult to compute as

$$\begin{aligned} p(CIR > CIR_0, r_s, \theta) &= p(CIR > CIR_0 | r_s, \theta) p_{pdf}(r_s, \theta) \\ &= p(CIR > CIR_0 | r_s, \theta) p_{pdf}(\theta) p_{pdf}(r_s). \end{aligned} \quad (7.38)$$

The average CIR coverage over the desired cell (base station B_1) for the mobile station, $p(CIR > CIR_0)_{MS}$, is

$$\begin{aligned} p(CIR > CIR_0)_{MS} &= \int_0^{2\pi} \int_0^R p(CIR > CIR_0, r_s, \theta) dr_s d\theta \\ &= \frac{1}{\pi R^2} \int_0^{2\pi} \int_0^R p(CIR > CIR_0 | r_s, \theta) r_s dr_s d\theta \\ &= \frac{1}{\pi R^2} \int_0^{2\pi} \int_0^R Q \left(\frac{CIR_0 - \left(K - 10n \log_{10} \frac{r_s}{\sqrt{D^2 + r_s^2 - 2Dr_s \cos \theta}} \right)}{\sigma} \right) r_s dr_s d\theta, \end{aligned} \quad (7.39a)$$

and using Eq. (7.10), it becomes

$$\begin{aligned} p(CIR > CIR_0)_{MS} &= \frac{1}{\pi R^2} \int_0^{2\pi} \int_0^R Q \left(\frac{CIR_0 - \left(K - 10n \log_{10} \frac{r_s}{\sqrt{3NR^2 + r_s^2 - 2\sqrt{3NR}r_s \cos \theta}} \right)}{\sigma} \right) r_s dr_s d\theta. \end{aligned} \quad (7.39b)$$

Eq. (7.39b) is numerically computed for different cell reuse patterns, $N=7$ and $N=3$ with

$K=0\text{dB}$, and the resulting graphs are shown as a function of the threshold CIR_0 in Fig. 7.10 and Fig. 7.11, respectively. The pathloss exponent n is 3.6 and log-normal shadowing power deviation σ is 8dB. These values correspond to a suburban area. Figures 7.10 and 7.11 also include the worst case CIR coverage, where it is assumed $r_s=R$ and $l=D-R$. From Fig. 7.10, the average CIR coverage for $CIR_0=18\text{dB}$ is 91% and for the worst case the coverage is only 60% for the same CIR_0 value. By comparing Fig. 7.10 and Fig. 7.11, it can be seen that the seven cell reuse pattern provides a mobile station higher CIR coverage than the three cell reuse pattern. As an example, when $CIR_0=18\text{dB}$, the average CIR coverage drops from 91% for the seven cell reuse pattern to 72% for the three cell reuse pattern. It is also noted that the CIR coverage for a three cell reuse pattern decreases faster for increasing CIR_0 than for the seven cell reuse pattern case.

7.3.2 Percentage of Average CIR Coverage at a Base Station

The co-channel interference introduced at a base station is defined differently than for the mobile station. As shown in Fig. 7.12, base station B_1 not only receives signals from its desired mobile M_1 , but also from M_2 which is in a co-channel cell B_2 . The distance from B_1 to M_1 is r_s and from B_1 to M_2 is l . The conditional pdf of CIR which exceeds a certain level CIR_0 given r_s and l is the same as in Eq. (7.35). However, the location of the interfering signal (r_i, θ_i) is statistically independent from the location of the desired mobile.

Unlike the interference for a mobile station, where the interfering signal strength depends on the location of the desired mobile, the interfering signal strength is independent of M_1 's position. The joint pdf of r_s and l therefore is

$$p_{pdf}(r_s, l) = p_{pdf}(r_s)p_{pdf}(l) . \quad (7.40)$$

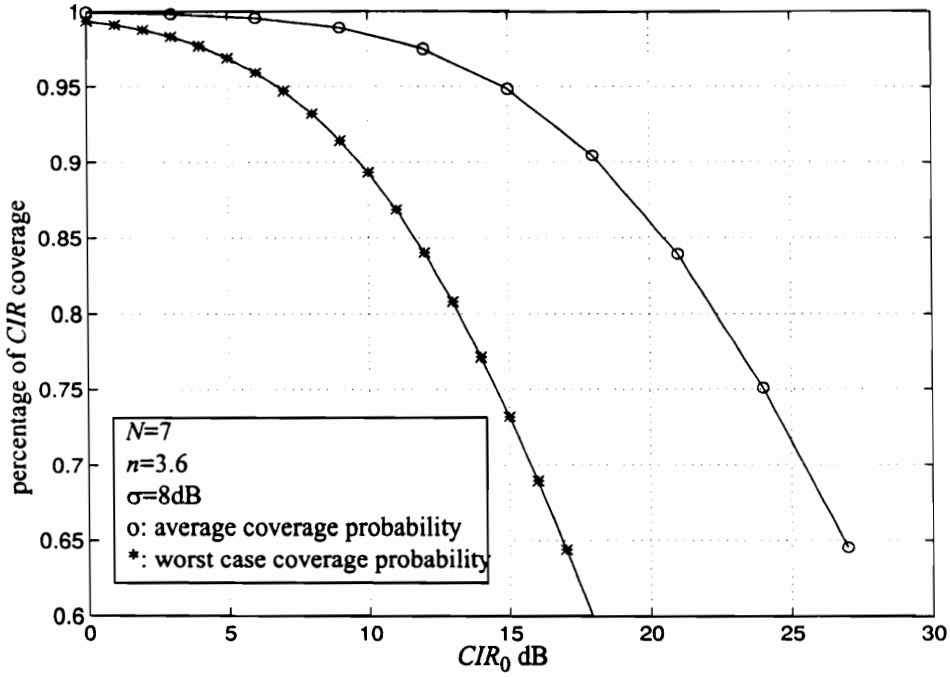


Fig. 7.10 CIR coverage comparison between a mobile station located at the worst location ($r_s=R$, and $l=D-R$) and the average value over the whole cell, $N=7$

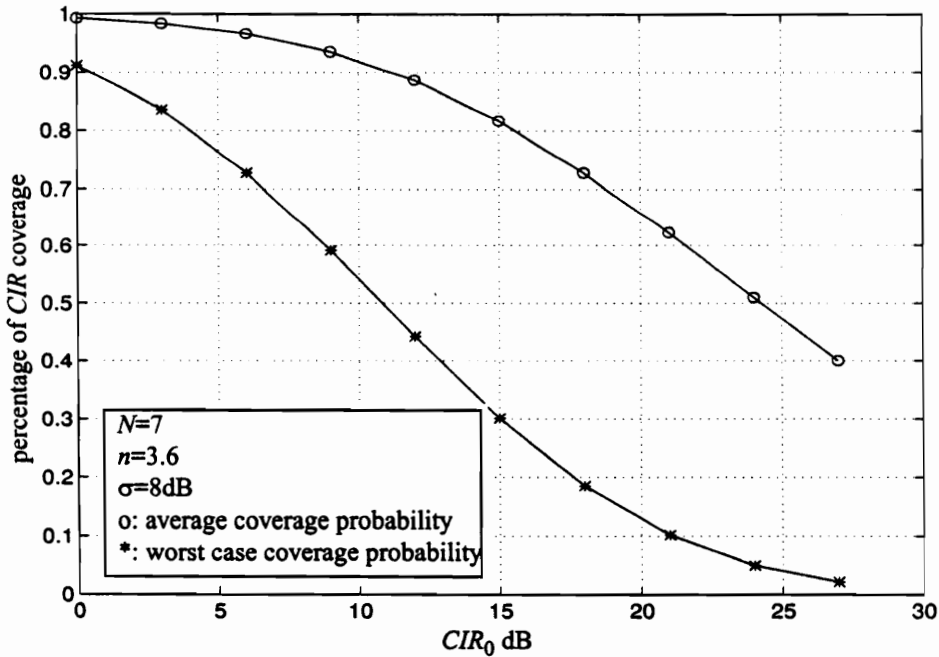


Fig. 7.11 CIR coverage comparison between a mobile station located at the worst location ($r_s=R$, and $l=D-R$) and the average value over the whole cell, $N=3$

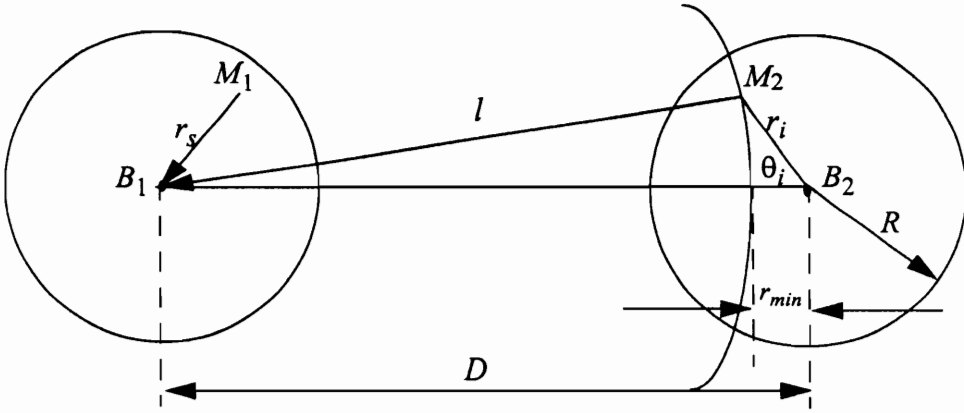


Fig. 7.12 Illustration of co-channel interference for a base station

The *pdf* of r_s is given in Eq. (7.37). To compute $p_{pdf}(l)$, the conditional *pdf* given r_i must be solved first. Their relationship is given in the following equation

$$\begin{aligned}
 p_{pdf}(l) &= \int_{r_i} p_{pdf}(l, r_i) dr_i \\
 &= \int_{r_i} p_{pdf}(l|r_i) p_{pdf}(r_i) dr_i.
 \end{aligned}
 \tag{7.41}$$

As shown in Fig. 7.12, the geometric relationship of l , r_i and θ_i is

$$l^2 = D^2 + r_i^2 - 2Dr_i \cos \theta_i.
 \tag{7.42}$$

The conditional *pdf* of l given r_i is related to $p(\theta_i)$ in the following equation

$$p_{pdf}(l|r_i) = \frac{p_{pdf}(\theta_i)}{\left| \frac{dl(\theta_i)}{d\theta_i} \right|} \bigg|_{\theta_i = f^{-1}(l(\theta_i))}.
 \tag{7.43}$$

Differentiating Eq. (7.42), we have

$$\frac{dl}{d\theta_i} = \frac{r_i D \sin \theta_i}{l}. \quad (7.44)$$

Also from Eq. (7.42),

$$\sin \theta_i = \pm \sqrt{1 - \left(\frac{D^2 + r_i^2 - l^2}{2Dr_i} \right)^2}. \quad (7.45)$$

Substituting Eq. (7.37), Eq. (7.44) and Eq. (7.45) into Eq. (7.43), the conditional *pdf* of l given r_i is

$$p_{pdf}(l|r_i) = \frac{1}{2\pi} \left| \frac{l}{\pm Dr_i \sqrt{1 - \left(\frac{D^2 + r_i^2 - l^2}{2Dr_i} \right)^2}} \right|. \quad (7.46)$$

From Fig. 7.12, it can be seen that the value of r_i is limited to a specific range for a given l .

The value of r_i varies from r_{min} to R , where $r_{min} = |D - l|$.

$p_{pdf}(l)$ can be solved by substituting Eq. (7.37) and Eq. (7.46) into Eq. (7.41), which produces

$$p_{pdf}(l) = \int_{r_i} \frac{1}{2\pi} \left| \frac{l}{\pm Dr_i \sqrt{1 - \left(\frac{D^2 + r_i^2 - l^2}{2Dr_i} \right)^2}} \right| \frac{2r_i}{R^2} dr_i$$

$$= \frac{1}{\pi R^2} \int_{r_{min}}^R \left| \frac{l}{\pm D \sqrt{1 - \left(\frac{D^2 + r_i^2 - l^2}{2Dr_i} \right)^2}} \right| dr_i . \quad (7.47)$$

Eq. (7.47) is numerically evaluated and is plotted in Fig. 7.13 as a function of l for a seven cell reuse pattern. To validate the result, $2 \cdot 10^4$ simulated data points of θ_i and r_i with uniform distribution and linear distribution, respectively, are used to represent l in Eq. (7.42). The histogram of the simulated values of l is also plotted on the same graph. As can be seen there is a good agreement between the analytical curve and the simulation results. Fig. 7.14 shows the case for three cell reuse pattern. Obviously, the range of the distance between the interfering mobile station and the desired base station l is from $D-R$ to $D+R$ which indicates the worst and the best locations of the interfering mobile station M_2 with respect to the desired base station B_1 . For both cases of $N=7$ and $N=3$, it can be seen that the probability density function of l has the maximum value at $l=D$.

Now, the percentage of average CIR coverage over the cell for basestation B_1 , $p(CIR > CIR_0)_{BS}$, is

$$p(CIR > CIR_0)_{BS} = \int_0^R \int_{D-R}^{D+R} p(CIR > CIR_0, r_s, l) dr_s dl$$

$$= \int_0^R \int_{D-R}^{D+R} \frac{2r_s}{\pi R^4} Q \left(\frac{CIR_0 - K + 10n \log_{10} \frac{r_s}{l}}{\sigma} \right) \left(\int_{r_{min}}^R \left| \frac{l}{\pm D \sqrt{1 - \left(\frac{D^2 + r_i^2 - l^2}{2Dr_i} \right)^2}} \right| dr_i \right) dr_s dl . \quad (7.48)$$

Eq. (7.48) is numerically computed for different cell reuse patterns $N=7$ and $N=3$ with

$K=0\text{dB}$. The results are depicted as functions of input CIR_0 in Fig. 7.15 and Fig. 7.16, respectively. The worst case CIR coverage where $r_s=R$ and $l=D-R$ is also computed and plotted in the corresponding figures. From Fig. 7.15, the average CIR coverage for $CIR_0=18\text{dB}$ is 89%, while for the worst case, it is only 60% for the same CIR_0 value. Comparing Fig. 7.15 and Fig. 7.16, it can be seen that the seven cell reuse pattern provides a base station higher CIR coverage than the three cell reuse pattern. For example, when $CIR_0=18\text{dB}$, the average CIR coverage drops from 89% for the seven cell reuse pattern to 70% for the three cell reuse pattern. It is also noticed that the CIR coverage for three cell reuse pattern decreases faster when CIR_0 increases than in the case of the seven cell reuse pattern. This result is the same as for the mobile station case in section 7.2.1.

To compare the percentage of CIR coverage for a base station and for a mobile station, both cases are plotted in Fig. 7.17 for $N=7$ and $N=3$. It is observed from the figure that the CIR coverage for a base station is slightly lower than that for a mobile station. The comparison is based on the assumption that both the base station and the mobile station receive single co-channel interference in addition to the desired signal. The average signal strength of the interfering signal only depends on the location of the desired mobile for a mobile station case, while the signal strength of the interfering signal is independent to the desired mobile location for the base station case. For the base station case, the interfering mobile has random locations when compared to the desired mobile, thus it introduces more interference on average. Consequently, the percentage of average CIR coverage for a base station is generally slightly lower than that for a mobile station.

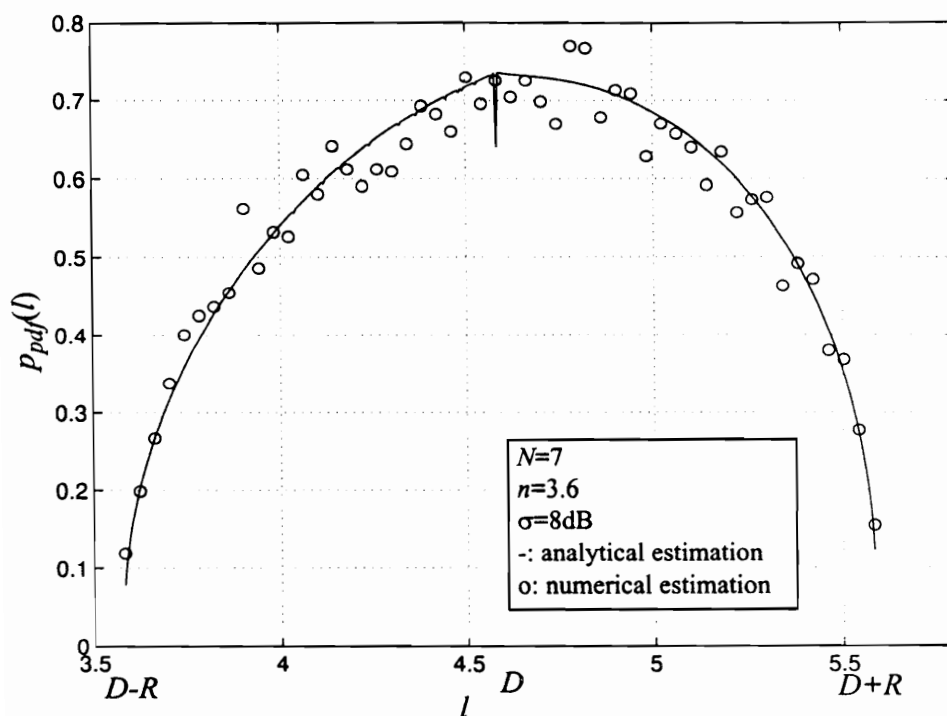


Fig. 7.13 Probability density function $p_{pdf}(l)$ for $N=7$

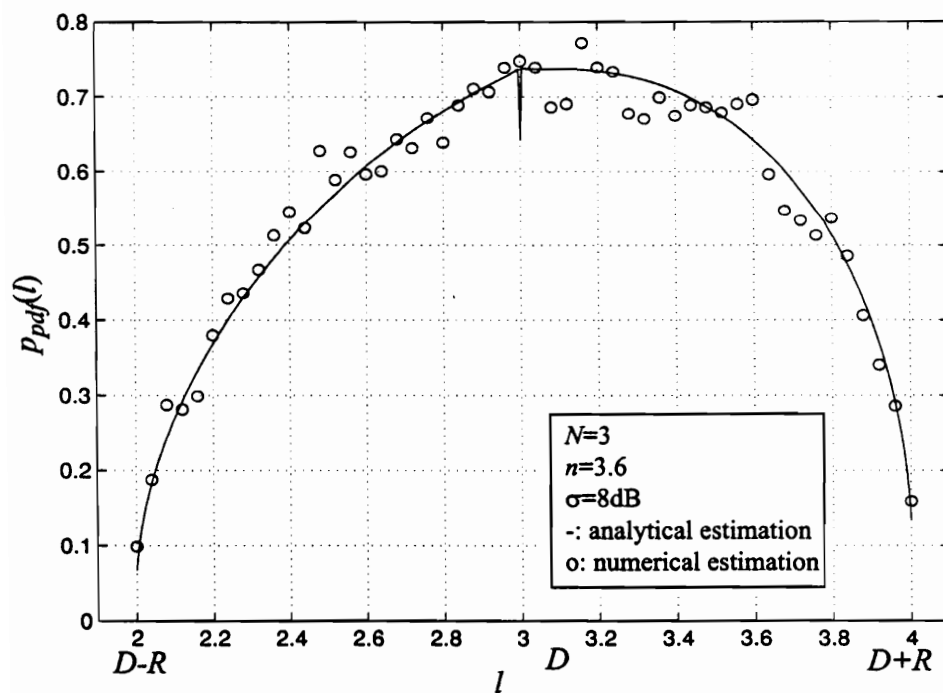


Fig. 7.14 Probability density function $p_{pdf}(l)$ for $N=3$

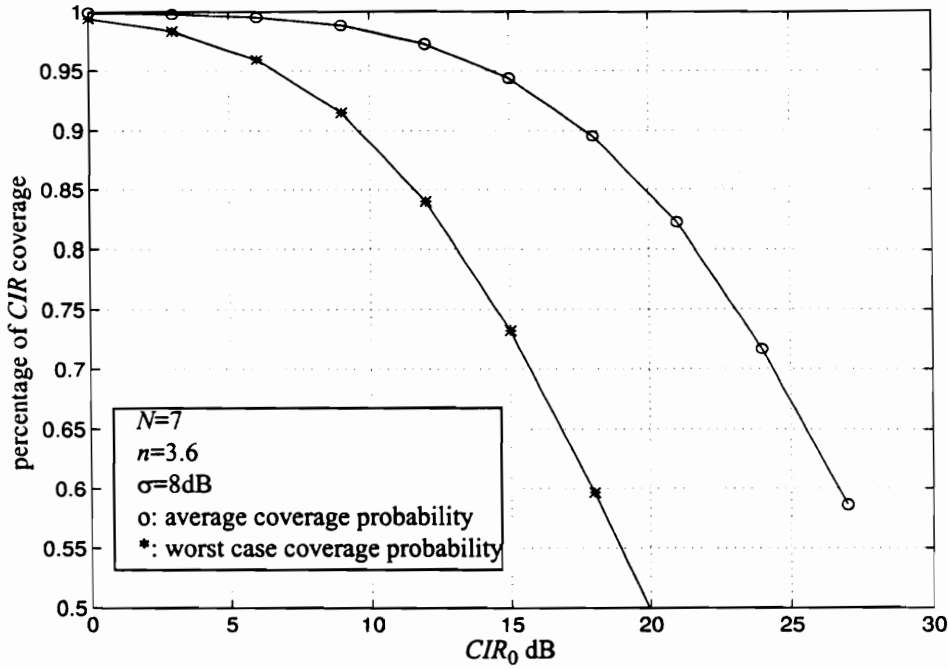


Fig. 7.15 CIR coverage comparison between a base station located at the worst location ($r_s=R$, and $l=D-R$) and the average value over the whole cell, $N=7$

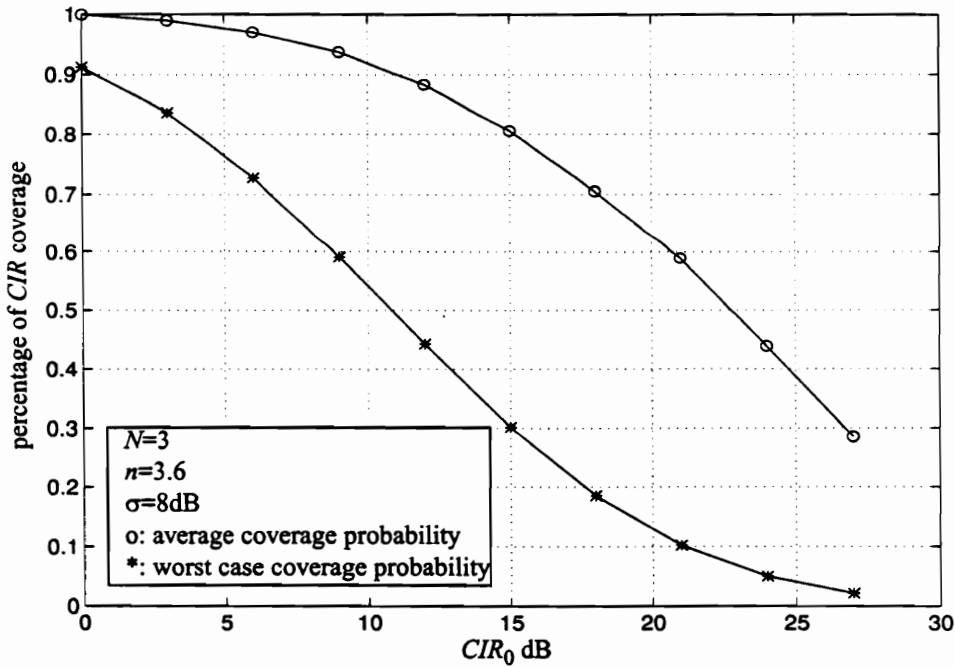


Fig. 7.16 CIR coverage comparison between a base station located at the worst location ($r_s=R$, and $l=D-R$) and the average value over the whole cell, $N=3$

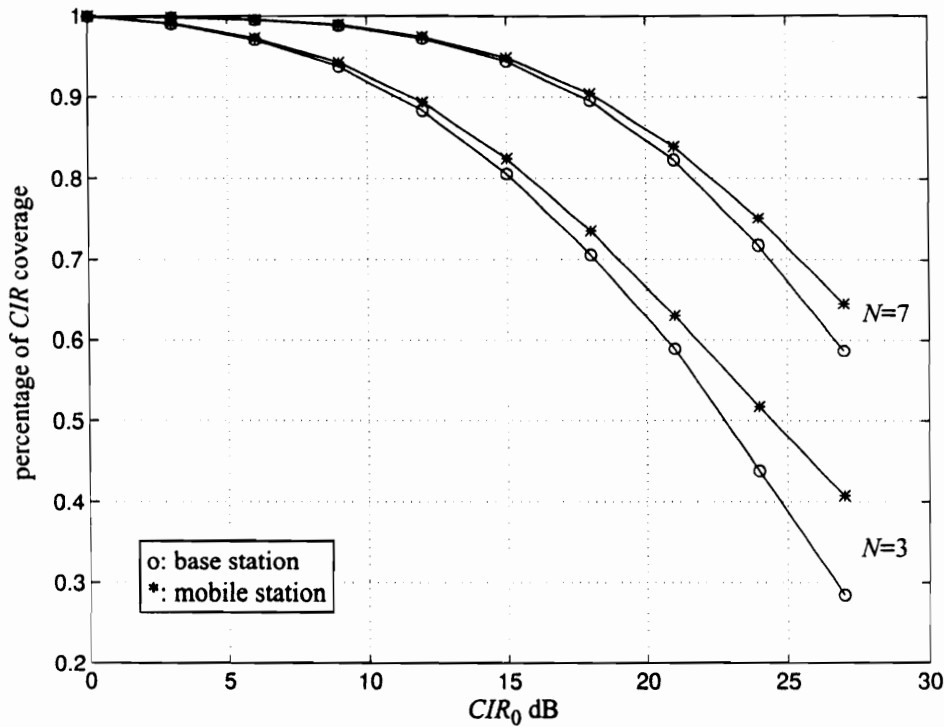


Fig. 7.17 Average *CIR* coverage comparison at a base station and at a mobile station for different frequency reuse patterns

7.4 Effect of Power Control on the Average *CIR* Coverage

All the calculations related to the average *CIR* coverage in the previous section are based on the assumption of constant transmit power. In real cellular systems, the power levels of the mobile unit and the base station are under constant control by the serving base stations. Power control ensures the smallest transmit power for both the forward link and the reverse link to maintain a good quality. Open-loop and close-loop power control techniques are especially important for CDMA systems to keep each subscriber at a nominal power since they share the same radio channel simultaneously. Power control not only prolongs the battery life of the subscriber, it also dramatically decreases the interference from other users. For the AMPS system, the power control is simple. All mobile station transmitters must be capable of reducing or increasing power on command from a base station specifying a power level numbered from 0 to 10 [EIA90]. The nominal effective

radiated power (ERP) for a mobile station is from -2dBW to -34dBW in an increments of -4dBW for each of the power levels (the first three power levels have the same nominal ERP) [IS5490]. To simplify the calculation, a log-linear model for the power control is assumed varying from -34dBW to -2dBW, when the distance r is varied from d_0 (normalized reference distance) to the cell boundary which is normalized to 1.

7.4.1 Effect of Power Control on the Average CIR Coverage at a Mobile Station

Fig. 7.18 illustrates how the co-channel interference is introduced into a mobile station when the serving base stations have power control. When the mobile moves in its service cell B_1 , it receives the signal from the desired base station B_1 , but it also receives an interfering signal from its co-channel cell B_2 . Unlike the case in Section 7.3.1 where the transmitted power levels from base stations B_1 and B_2 are constants, the power levels here from base stations B_1 and B_2 are functions of the mobile locations (r_s, r_i).

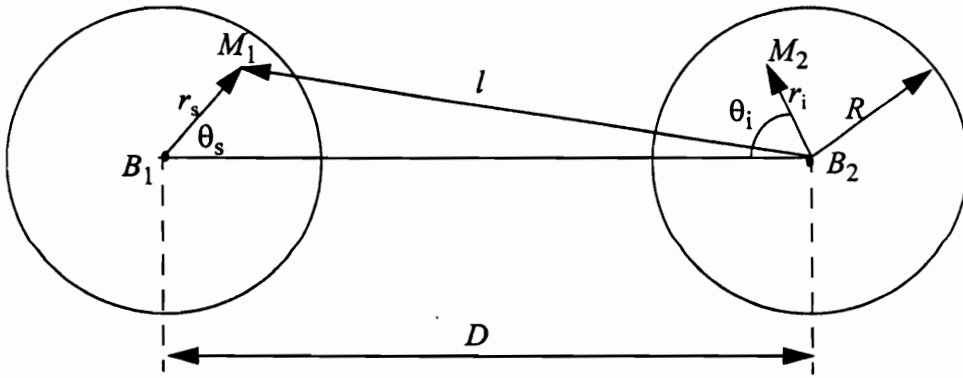


Fig. 7.18 Illustration of the co-channel interference for a mobile station with power control

Assume that the locations of the mobile M_1 and M_2 are (r_s, θ_s) and (r_i, θ_i) , respectively, and the distance between the mobile M_1 and B_2 is l , the received signal power C and the interference power I are (in dB)

$$C = PW_{B_1}(r_s) - 10n \log_{10} \frac{r_s}{d_0} + S_{\sigma_s} \quad (7.49a)$$

and

$$I = PW_{B_2}(r_i) - 10n \log_{10} \frac{l}{d_0} + X_{\sigma_i}, \quad (7.49b)$$

where $PW_B(r)$ is the power level transmitted by a serving base station as a function of the distance r to its intended mobile. The received CIR in dB then can be expressed in the following equation

$$\begin{aligned} 10 \log_{10} \frac{C}{I} &= K + PW_{B_1}(r_s) - 10n \log_{10} \left(\frac{r_s}{d_0} \right) + S_{\sigma_s} - \left(PW_{B_2}(r_i) - 10n \log_{10} \left(\frac{l}{d_0} \right) + I_{\sigma_i} \right) \\ &= K + PW_{B_1}(r_s) - PW_{B_2}(r_i) - 10n \log_{10} \left(\frac{r_s}{l} \right) + S_{\sigma_s} - I_{\sigma_i}, \end{aligned} \quad (7.50)$$

where K is a constant indicating the number of equal power interfering sources. Following the same development of Eq. (7.35), the conditional probability of CIR coverage for a power controlled base station given r_s , r_i and l is

$$p(CIR > CIR_0 | r_s, r_i, l) = Q \left(\frac{CIR_0 - \left(K + PW_{B_1}(r_s) - PW_{B_2}(r_i) - 10n \log_{10} \frac{r_s}{l} \right)}{\sigma} \right). \quad (7.51)$$

Since l is a function of r_s and θ_s and the $pdfs$ of r_s , r_i , θ_s and θ_i are independent of each other, the coverage probability can be written as

$$p(CIR > CIR_0, r_1, r_2, \theta_1, \theta_2) = p(CIR > CIR_0 | r_1, r_2, \theta_1, \theta_2) p_{pdf}(r_1, r_2, \theta_1, \theta_2)$$

$$= p(CIR > CIR_0 | r_1, r_2, \theta_1, \theta_2) p_{pdf}(r_1) p_{pdf}(r_2) p_{pdf}(\theta_1) p_{pdf}(\theta_2). \quad (7.52)$$

By substituting Eq. (7.36) and Eq. (7.37) into Eq. (7.52), the average CIR coverage over the cell with power-controlled base stations is

$$\begin{aligned} p_{pc}(CIR > CIR_0)_{MS} &= \int_0^{2\pi} \int_0^R \int_0^{2\pi} \int_0^R p(CIR > CIR_0, r_s, r_i, \theta_s, \theta_i) dr_s d\theta_s dr_i d\theta_i \\ &= \frac{1}{\pi^2 R^4} \int_0^{2\pi} \int_0^R \int_0^{2\pi} \int_0^R p(CIR > CIR_0 | r_s, r_i, \theta_s, \theta_i) r_s r_i dr_s d\theta_s dr_i d\theta_i \\ &= \frac{2}{\pi R^4} \int_0^{2\pi} \int_0^R \int_0^{2\pi} Q \left(\frac{CIR_0 - \left(K + PW_{B_1}(r_s) - PW_{B_2}(r_i) - 10n \log_{10} \frac{r_s}{\sqrt{D^2 + r_s^2 - 2Dr_s \cos \theta_s}} \right)}{\sigma} \right) r_s r_i dr_s d\theta_s dr_i d\theta_i. \end{aligned} \quad (7.53)$$

We assume that the power control is log-linear with a minimum value of -34dBW and a maximum value of -2dBW and that r is normalized from d_0 to 1. The power control model is created by assuming that the transmitted power for the mobile station at distance d_0 is -34dBW and that the transmitted power at the cell boundary $r=1$ is -2dBW. The transmitted power increases proportionally to $\log_{10} r$. Thus, $PW_B(r)$ can be expressed as

$$PW_B(r) = -2 - \frac{32}{\log_{10} d_0} \log_{10} r \text{ dBW}, \quad (7.54)$$

where d_0 is a normalized far-field reference distance. For example, a cell radius of 2km and far-field reference point of 200 meters leads to a normalized d_0 of 0.1, which we will use in the following analysis[Rap96][Lee93]. Referring to Eq. (7.10) and Eq. (7.54), Eq.

(7.53) can be represented by the frequency reuse pattern number and the mobiles locations as

$$p_{pc}(CIR > CIR_0)_{MS} = \frac{2}{\pi R^4} \int_0^{2\pi} \int_0^R \int_0^R \int_0^{2\pi} Q \left(\frac{CIR_0 - \left(K - \frac{32}{\log_{10} d_0} (\log_{10} r_s - \log_{10} r_i) - 10n \log_{10} \frac{r_s}{\sqrt{3NR^2 + r_s^2 - 2\sqrt{3}Nr_s \cos \theta_s}} \right)}{\sigma} \right) r_s r_i dr_s dr_i d\theta_s. \quad (7.55)$$

Eq. (7.55) is numerically computed for different cell reuse patterns $N=3$ and $N=7$ with $K=0$ dB. The results are shown as a function of the threshold CIR_0 in Fig. 7.19. The path loss exponent n is 3.6 and log-normal shadowing power deviation σ is 8dB which correspond to a suburban area. The CIR coverage for a mobile station without the power controlled base stations for both $N=3$ and $N=7$ are also plotted in the same figure. From Fig. 7.19, it can be seen that the average CIR coverage for a threshold $CIR_0=18$ dB is increased from 88% to 92% for a seven cell reuse pattern by using the power control in base stations. The improvement of the average CIR coverage for a three cell reuse pattern is very close to that of a seven cell reuse case. The average CIR coverage after applying the power control for both cases follows a the similar pattern as before when CIR_0 increases. Although the average CIR coverage is increased by applying power control at base stations for AMPS system, the improvement is not very significant. From our simulations, we note that the slope of the linear power control function does not affect the average CIR coverage dramatically.

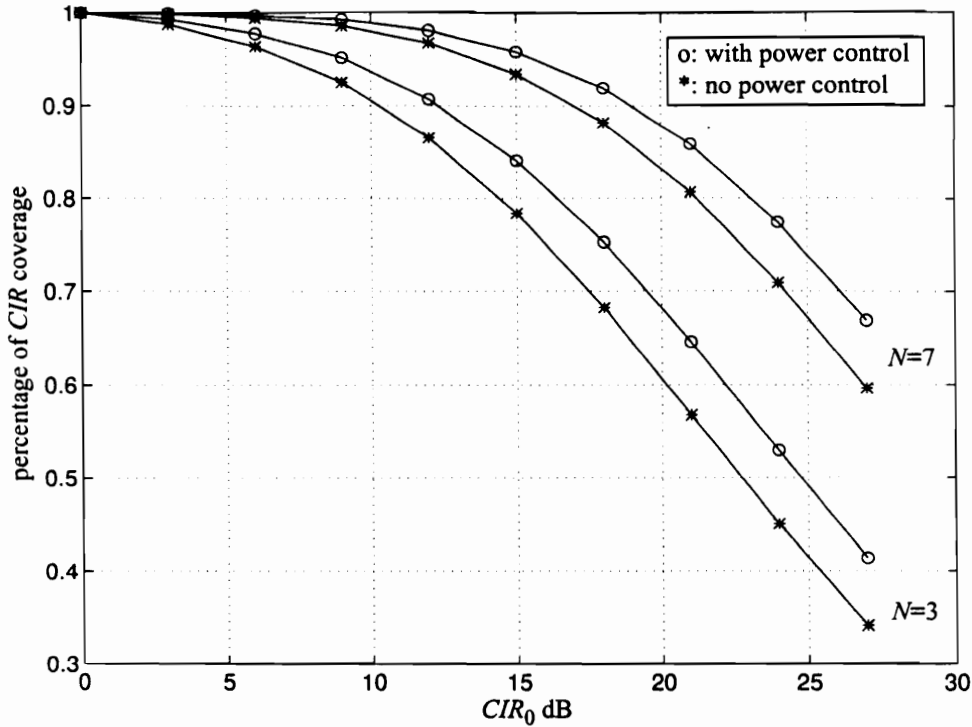


Fig. 7.19 Comparison of the CIR coverage for a mobile station with and without power-controlled base stations, $N=3, 7$

7.4.2 Effect of Power Control on the Average CIR Coverage at a Base Station

The effect of power control on the average CIR coverage at a base station is similar to that at a mobile station. As shown in Fig. 7.12, base station B_1 not only receives signals from its desired mobile M_1 , it also receives signals from M_2 which is in a co-channel cell B_2 . The difference from the case described in Section 7.3.2 is that the power levels from M_1 and M_2 are no longer constant. The power levels of all the mobiles can be increased or decreased depending on the command codes from their serving base stations. The further a mobile is from its serving base station, the greater its power needs to be to combat shadowing and fading. Again, the power control used in a mobile station can be represented as the same a linear function used in the base station CIR coverage evaluation.

The received signal power and interference power are the same as in Eq. (7.49). The conditional probability of *CIR* coverage given r_s , r_i and l is also the same as in Eq. (7.51). Substituting Eq. (7.37) and Eq. (7.47) into Eq. (7.51), the probability of the *CIR* coverage over a cell for a base station is

$$\begin{aligned}
 p_{pc}(CIR > CIR_0)_{BS} &= \int_{D-R}^{D+R} \int_0^R \int_{r_{min}}^R p(CIR > CIR_0, r_s, r_i, l) dr_i dr_s dl \\
 &= \frac{2}{\pi R^4} \int_{D-R}^{D+R} \int_0^R \int_{r_{min}}^R Q \left(\frac{CIR_0 - \left(K - \frac{32}{\log_{10} d_0} (\log_{10} r_s - \log_{10} r_i) - 10n \log_{10} \frac{r_s}{l} \right)}{\sigma} \right) \\
 &\quad \left| \frac{l}{\pm D \sqrt{1 - \left(\frac{D^2 + r_i^2 - l^2}{2Dr_i} \right)^2}} \right| r_i r_s dr_i dr_s dl.
 \end{aligned} \tag{7.56}$$

Eq. (7.56) is numerically computed for different cell reuse patterns with $K=0$ dB, and the results are shown as a function of the threshold CIR_0 in Fig. 7.20. The path loss exponent n is 3.6 and log-normal shadowing power deviation σ is 8dB which correspond to a suburban area. The *CIR* coverage for a base station without the power-controlled mobile stations for both $N=3$ and $N=7$ are also plotted in the same figure. From Fig. 7.20, it can be seen that the average *CIR* coverage for a threshold $CIR_0=18$ dB is increased from 90% to 94% for a seven cell reuse pattern by using the power control at the base stations. The improvement of the average *CIR* coverage for a three cell reuse pattern is very close to that for a seven cell reuse case. From the figure, it is obvious that the power control provides better improvement for a higher threshold than a lower one. For an example, the average *CIR* coverage is increased by 10% for $CIR_0=27$ dB after applying power control at the mobiles, while it is only increased by 4% for $CIR_0=18$ dB. Comparing Fig. 7.19 and Fig.

7.20, it is noted that the power control provides slightly greater improvement for a base station than for a mobile station. Although the average *CIR* coverage is increased by applying power control at mobile stations for the AMPS system, the improvement is still not very significant. These results suggest that power control is not as critical for an AMPS system as for a CDMA system. However, power control is necessary to maintain adequate transmitting power and longer battery life for a TDMA/AMPS dual mode phone [EIA90].

Power control helps to insure adequate power levels at a base station and a mobile station to combat the effects of fading and shadowing. The power level of the desired signal is decreased when the mobile is near its serving base station, and the power level is increased when the mobile is near the cell edge. For the IS-54 dual mode standard, the minimum power level is -34dBw and the maximum power level is -2dBw. When the radiated power is increased at a mobile station to provide good signal strength to its serving base station, it may introduce greater interference to the mobile in the co-channel cell. Thus, power control in this situation could have a negative effect and cell dragging is an example of this situation [Rap96]. The overall positive and negative effects of power control are reflected in Figures 7.19 and 7.20. To obtain large *CIR* improvement for the AMPS system, other approaches can be used, and they are discussed in the following section.

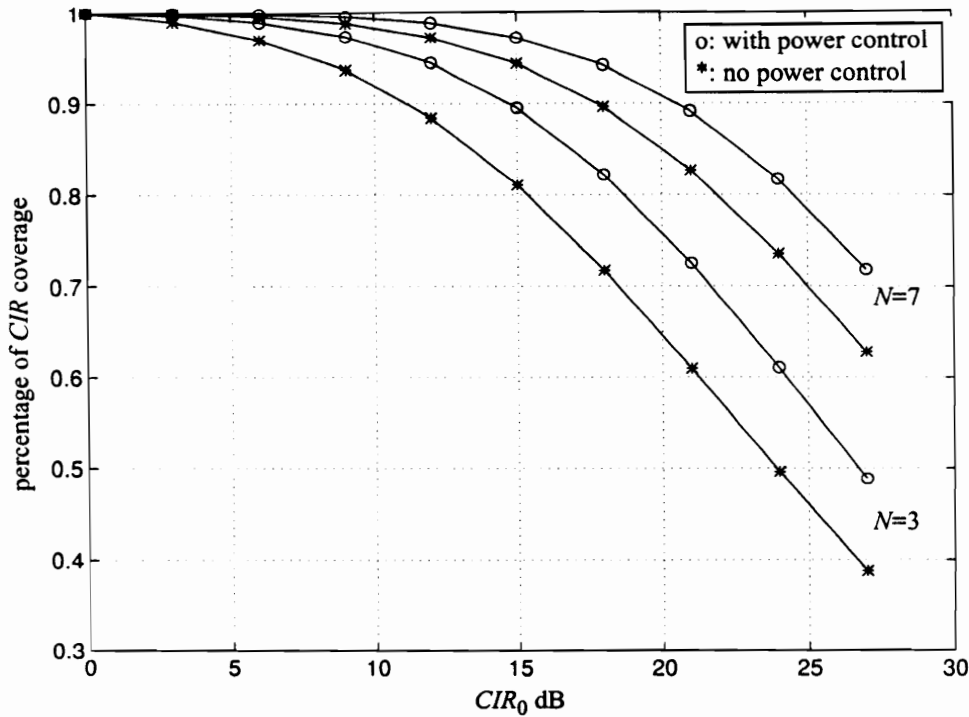


Fig. 7.20 Comparison of the CIR coverage for a base station with and without power controlled mobile stations, $N=3, 7$

7.5 System Capacity Improvement

System capacity has become the largest obstacle to the growth of the cellular industry. Different techniques are used to expand the capacity of cellular systems. They include *cell splitting*, *sectoring*, and *coverage zone approaches*. *Cell splitting* is the process of subdividing a congested cell into smaller cells, where each subdivided cell has a new base station and reduced transmit power. Generally, there are two kinds of splitting techniques: permanent splitting and dynamic splitting. Permanent splitting is easy to realize as long as the transition from large cells to small cells takes place for low traffic areas. Frequency reassignment should follow the rule based on the frequency-reuse distance ratio with the power adjusted [Lee93]. On the other hand, the dynamic splitting technique determines the orientation of the new set of seven cells, split dynamically according to the traffic demand. Idle small cell sites may be activated in order to increase the cell's traffic capac-

ity. Nevertheless, cell splitting can affect the neighboring cells and cause an imbalance in the distribution of power and frequency-reuse distance. Furthermore, it is a costly operation.

The *sectoring* approach replaces a single omni-directional antenna at the base station with several directional antennas, with each antenna radiating within a specified sector. By using this arrangement of antennas, a given cell will interfere only with a fraction of the co-channel cells. The factor by which the co-channel interference is reduced depends on the amount of sectoring used. The penalty paid for improved C/I , or in other words, for increased capacity, is an increase in the number of antennas at each base station and a decrease in trunking efficiency due to the channel sectoring at the base station [Rap96].

In the *coverage zone* approach, the concept of the microcell zone is introduced to avoid the increased number of hand-offs required in sectoring [Rap96]. In this model, a cell is divided into three or more zones, and each of these zones is connected to a single base station and shares the same radio equipment. As a mobile moves within the cell, it is served by the strongest signal. Any channel can be assigned to any zone by the base station. In addition, the mobile will remain on the same channel when it travels from one zone to another within the cell. The base station simply switches the channel to a different antenna or zone site. This technique is particularly useful along highways or along urban traffic corridors.

Besides these system layout improvements for increasing system capacity, new digital signal processing techniques, like the TDAF can be applied at the receiver. This technique provides an inexpensive and effective method of suppressing the co-channel interference and accommodating more users in the same region.

As mentioned earlier, the commonly employed frequency reuse patterns are three-cell, four-cell and seven-cell reuse. Among these patterns, the three-cell reuse pattern enjoys

the advantages of having the highest number of channels. However, from Fig. 7.4, for a path loss exponent of $n=4$, the mean *CIR* for three-cell reuse is around 12dB, which is not sufficient to provide acceptable toll quality. For the same n , the mean *CIR* level for a seven-cell reuse pattern is approximately 18dB. Thus, from the *CIR* point of view, a seven-cell reuse pattern is superior to the three-cell reuse pattern.

The TDAF can improve the *CIR* of the three-cell reuse system. From the theoretical results in Chapter 5, Section 5.2, the *CIR* improvement ranges from 14 to 30dB for an input *CIR* of 11dB depending on the carrier separation of the SOI and the SNOI, the type of fading, and the level of the noise. This performance is indicative of the theoretical performance of the blind TDAF (SCP). To compare the probability of *CIR* coverage before and after applying the time-dependent filter, the analytical probability $p(CIR > CIR_0)_{MS}$ in Eq. (7.39) is plotted as a function of CIR_0 for seven-cell reuse pattern in Fig. 7.21 and for three-cell reuse pattern in Fig. 7.22. Doppler frequencies of 30Hz and 60Hz are assumed for the flat fading channels. Assuming the *CIR* gains provided by the time-dependent filter shown in Chapter 5, Section 5.2, the probabilities of average *CIR* coverage for $N=7$ and $N=3$ are also plotted in Fig. 7.21 and Fig. 7.22, respectively. The figures show that the probability of the average *CIR* coverage is greatly increased by utilizing the time-dependent filter. The receiver which incorporates the time-dependent filter can provide 97% *CIR* coverage for *CIR* below 15dB. For example, the probability of average *CIR* coverage is 70% before applying the time-dependent filter and is increased to 98% after applying the time-dependent filter.

Since there is a slight degradation for the filter performance caused by high Doppler frequencies, the *CIR* coverage is also affected, especially for a high threshold CIR_0 . It can be seen from Fig. 7.21 that the probability of the average *CIR* coverage is almost the same when CIR_0 is below 18dB for both $f_m=30\text{Hz}$ and 60Hz, while there is a 15% difference when CIR_0 is 30dB. The same pattern holds for the three cell reuse case. It is also noted that the probability of the average *CIR* coverage for the three cell reuse pattern drops faster

than that for the seven cell reuse pattern.

To compare the probability of the average *CIR* coverage at a base station before and after applying the time-dependent filter, the analytical probability of the average *CIR* coverage $p(CIR > CIR_0)_{BS}$ based on Eq. (7.48) is plotted in Fig. 7.23 and Fig. 7.24 for $N=3$ and $N=7$, respectively. The probability of the average *CIR* coverage with a time-dependent filter, again assuming *CIR* improvements provided in Chapter 5, Section 5.2, is also plotted in the corresponding figures for different two-ray frequency selective fading channels. From these two figures, it can be seen that the larger the multipath delay, the lower the probability of the average *CIR* coverage, especially for a high threshold CIR_0 . However, the improvement is still significant compared to the conventional receiver, even when a lower frequency reuse pattern is assumed.

In short, by implementing a TDAF at the receiver, the channel reuse number can be reduced without significantly affecting the received voice quality. As a result, the system capacity can be increased significantly. The complexity of the implementation is comparable to that of an equalizer. The cost of the implementation is much lower than the system re-configuration methods. The improvement in co-channel interference reduction provided by the time-dependent filter is more significant than that provided by the power control technique. The time-dependent filtering technique allows a lower frequency reuse factor, a lower probability of co-channel interference, and a higher probability of average *CIR* coverage.

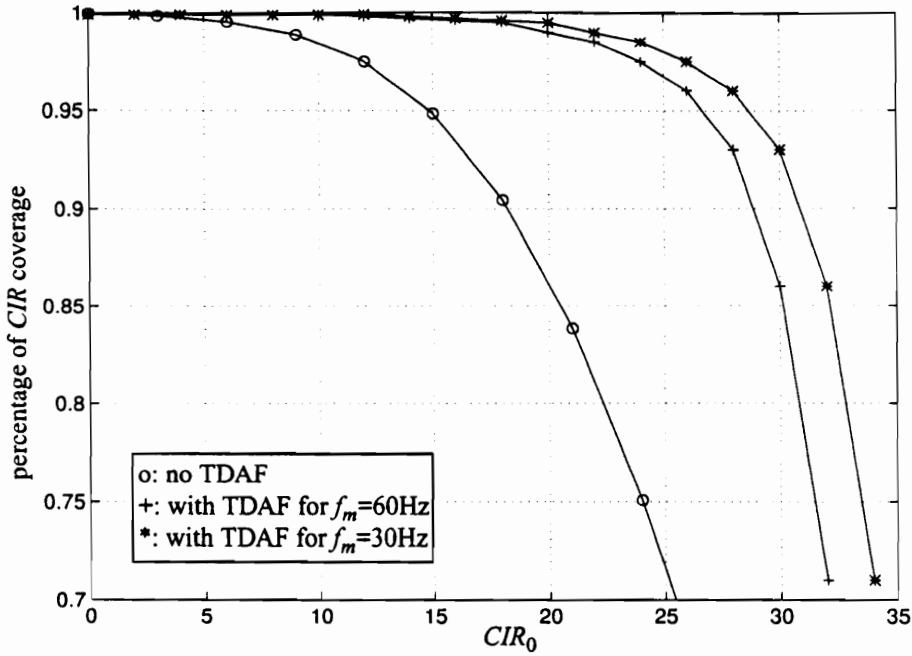


Fig. 7.21 Analytical CIR coverage at a mobile station by using the conventional receiver and the receiver incorporating a time-dependent filter. Flat fading channel models from Chapter 5, Section 5.2 are assumed, $N=7$

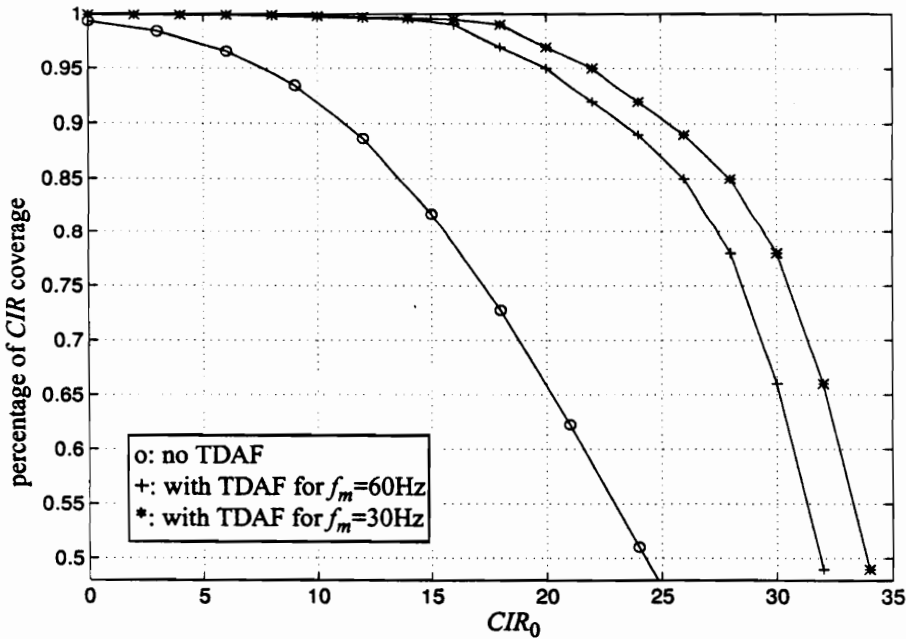


Fig. 7.22 Analytical CIR coverage at a mobile station by using the conventional receiver and the receiver incorporating a time-dependent filter. Flat fading channel models from Chapter 5, Section 5.2 are assumed, $N=3$

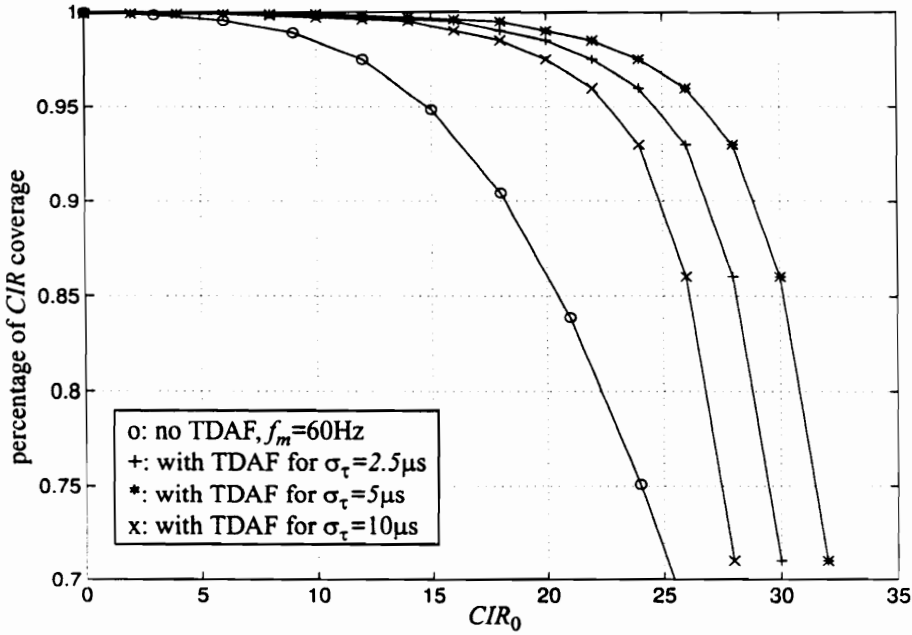


Fig. 7.23 Analytical CIR coverage at a base station by using the conventional receiver and the receiver incorporating a time-dependent filter. Frequency selective fading channel models from Chapter 5, Section 5.2 are assumed, $N=7$

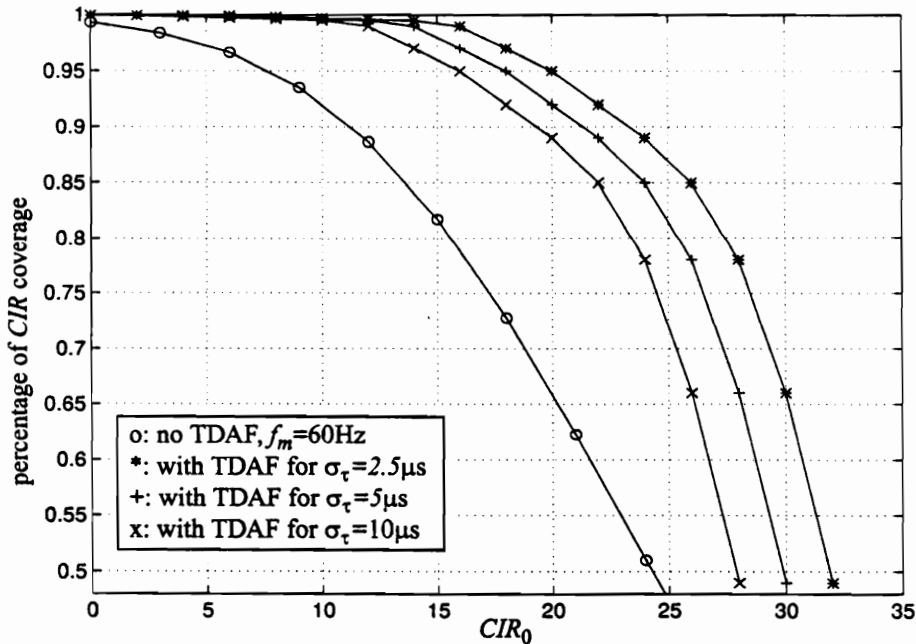


Fig. 7.24 Analytical CIR coverage at a base station by using the conventional receiver and the receiver incorporating a time-dependent filter. Frequency selective fading channel models from Chapter 5, Section 5.2 are assumed, $N=3$

Chapter 8. Future Work

In this chapter, a number of future research directions are proposed based on extending the theory and simulation results presented in this dissertation.

8.1 Performance of a TDAF with Multiple Co-channel Interfering Sources

In this dissertation, we have shown that the TDAF produces a significant improvement of *CIR* for an AMPS signal corrupted by a single co-channel interfering source. In a practical AMPS system, multiple co-channel interfering signals could come from different co-channel cell sites. The performance of the TDAF when two co-channel interfering signals are present needs to be examined.

8.2 Analysis of the Sensitivity to the SAT Frequency Bias

Another useful area of future work is to measure the sensitivity of the TDAF to the SAT frequency bias. In this dissertation, the filter periodicities are assumed to be exactly the same as the cyclic frequencies of the desired signal. Although the ideal SAT frequency of the desired signal is known, the actual SAT frequency in the AMPS signal may drift from the true value. The filter performance will be affected by the error in the received signal's SAT frequency. The maximum SAT frequency drift the filter can tolerate is an interesting and important topic.

8.3 Co-channel Interference Mitigation Using Spectral Correlation Detection Techniques and Switched Diversity

In smart antenna applications, detecting the existence of co-channel interference is important since a signal from the antenna which has the best signal quality is chosen for demodulation (switched diversity). For the AMPS system, this is achieved by detecting the SAT power of the incoming signal. In some cases, this measure is not very good because of the

rapidly varying channel. DSP detection techniques using spectral correlations provide a more robust means to detect interference in dynamic channels than a simple SAT power measurement. Thus, it may possible to develop a more robust switched diversity technique for interference rejection.

8.4 Adjacent Channel Interference Rejection Using DSP Techniques

Although co-channel interference in the AMPS system is one of the key factors affecting received signal quality, adjacent channel interference also plays an important role in signal quality. In practical systems, a steep roll-off bandpass filter is often used both at the transmitter and the receiver to filter the out-of-band interference and noise. However, leakage across channels often occurs since the channel is dynamic and interference levels can be high. Better adjacent channel interference rejection using a TDAF can allow more flexible channel assignments, potentially increasing system capacity and voice quality.

8.5 DSP Hardware for Real Time Implementation of the TDAF

For a real time filter implementation, complexity is a very critical issue. This necessitates designing computationally efficient techniques with low memory requirements for real time implementation of the TDAF. A proto-type real time TDAF would provide a means of testing the algorithms in real cellular systems and would significantly enhance our research efforts.

8.6 Extended Analysis of System Capacity to Sectorized Antennas

The capacity gains computed so far assume omni-directional antennas. In capacity-limited areas, sectorized antennas are being deployed. Thus, it would be beneficial to analytically determine capacity gains a TDAF can provide to these systems.

Chapter 9. Conclusions and Summary

This dissertation presents new techniques for achieving AMPS co-channel interference mitigation and achieving their impact on system capacity. Also included is a literature review of single channel interference cancellation techniques applicable to AMPS signals. The principles behind these techniques are described along with their advantages and disadvantages.

To describe the new techniques invented in this research, background material on second order cyclostationarity of communication signals is presented. A mathematical analysis of the cyclostationary, or equivalently the spectral correlation characteristics, produced by the supervisory audio tone (SAT) in an AMPS signal is derived and verified by numerical methods. The impact of different channel conditions, such as AWGN, co-channel interference, fading and multipath, on the spectral correlation characteristics of AMPS is also analyzed and numerically verified. These results show that although the spectral correlation may be diminished in these environments, it still provides a means for significant interference rejection.

A time-dependent filter is ideally suited for exploiting the cyclostationary properties. An AMPS receiver incorporating this new filter can reject co-channel interference and enhance the desired signal. The theory of this type of optimal filter is presented. Its performance is analyzed and measured under different channel conditions, such as the AWGN, co-channel interference, fading and multipath.

A blind spectral correlation predictor (SCP) is realized by using an adaptive FRESH filter structure to implement the time-dependent optimal filter. This blind algorithm uses the received signal as the training sequence to adapt the filter. Performance of this blind adaptive filter using simulated and digitized data is measured. Results show that there is a significant improvement in the carrier to interference-and-noise ratio of the filtered signal.

Both the adaptive algorithms and the structures are refined to obtain better performance and lower computational complexity.

These interference rejection techniques are also applied to the NAMPS signal since a NAMPS signal has signal structure similar to the AMPS signal. The TDAF is implemented using time sequence switching structure for the NAMPS signal instead of the FRESH structure used for the AMPS signal. Initial results show that these techniques are promising.

To determine the impact of the techniques on system capacity, the statistical relationship between interference and capacity is studied in this dissertation. This study includes the impact of both adjacent channel interference and co-channel interference on system capacity. Probability of the average *CIR* coverage is derived and numerically evaluated for both the base station and the mobile station using different cell reuse patterns. The probability of the average *CIR* coverage for time-dependent filtered signals and non-filtered signals is compared. Results show that by applying a time-dependent filter, the outage probability is significantly reduced for both the mobile station and the base station. These results imply that by using time-dependent processing, the system capacity could be increased by using a lower frequency reuse scheme than the current seven cell reuse scheme.

The research that has been presented in this dissertation provides new directions for reducing co-channel interference of AMPS signals and for increasing system capacity. These techniques can be used with a single antenna, or with smart antennas to improve the quality of received signals.

References

- [ASW90] B. G. Agee, S. V. Schell and W. A. Gardner, "Spectral self-coherence restoration: a new approach to blind adaptive signal extraction using antenna arrays," *Proceedings of IEEE*, vol. 78, no. 4, pp. 753-767, Apr. 1990.
- [Bar88] Y. Bar-Ness, "Co-channel interference suppression and signal separation method," *IEEE Military Conf.*, pp. 1077-1081, 1988.
- [Bar89] Y. Bar-Ness, "Adaptive co-channel interference cancelation and signal separation method," *IEEE Military Conf.*, pp. 825-830, 1989.
- [BCD84] Y. Bar-Ness, F. A. Cassara and R. Difazio, "Cross-coupled phase-locked loop with closed loop amplitude control," *IEEE Transactions on Commun.*, vol. 32, no. 2, pp. 195-199, Feb. 1984.
- [BK94] W. A. Brown and D. L. Knepp, "The effect of multipath propagation on cyclostationary signals," *The Second Workshop on Cyclostationary Signals*, pp. 9.1-9.4, Monterey, CA. 1994.
- [BL93] W. A. Brown and H. H. Loomis Jr., "Digital implementations of spectral correlation analyzers," *IEEE Transactions on Signal Processing*, vol. 41, no. 2, pp. 703-719, Feb. 1993.
- [Bra92] J. N. Bradley, "Suppression of adjacent channel and co-channel FM interference via extended Kalman filtering," *IEEE International Conference on Acoustics, Speech and Signal Processing*, pp. IV 693-696, Sep. 1992.
- [Bro87] W. A. Brown, *On the Theory of Cyclostationary Signals*, Ph.D. Dissertation.

- tion in Electrical Engineering Department, Univ. California at Davis, 1987.
- [Che89] C. K. Chen, "Spectral correlation characterization of modulated signals with application to signal detection and source location," Ph.D. Dissertation in Electrical Engineering Department, Univ. California at Davis, 1989.
- [CM92] S. Chen and B. Mulgrew, "Overcoming co-channel interference using an adaptive radial basis function equalizer," *Signal Processing*, vol. 28, pp. 71-107, 1992.
- [CSS80] F. A. Cassara, H. Schachter and G. H. Simowitz, "Acquisition behavior of the cross-coupled phase-locked loop FM demodulator," *IEEE Transactions on Commun.* vol. 28, no. 6, pp. 897-904, Jun. 1980.
- [Dav84] R. A. David, "A parallel structure for adaptive line enhancement," Invited paper, *American Control Conference of 1984*, Jun. 1984.
- [DSE83] R. A. David, S. D. Stearns and G. R. Elliott, "IIR algorithms for adaptive line enhancement," *IEEE Proc. Int. Conf. on Acoustics, Speech, and Signal Processing*, Apr. 1983.
- [ELA90] IS-54 Cellular system dual-mode mobile station - base station compatibility standard, *EIA/TIA Interim Standard*, May 1990.
- [Fer85a] E. R. Ferrara, Jr., "A method for cancelling interference from a constant envelop signal," *IEEE Transactions on Acoustics Speech and Signal Processing*, vol. 33, no. 2, pp. 316-319, Feb. 1985.
- [Fer85b] E. R. Ferrara, Jr., "Frequency domain implementations of periodically

- time-varying adaptive filters" *IEEE Transactions on Acoustics Speech and Signal Processing*, vol. 33, no. 8, pp. 883-892, Aug. 1985.
- [Gar86] W. A. Gardner, "Measurement of spectral correlation," *IEEE Transactions on Acoustics, Speech, and Signal Processing*, vol. 34, no. 5, pp. 1111-1123, Oct. 1986.
- [Gar87] W. A. Gardner, *Statistic Spectral Analysis: A Nonprobabilistic Theory*, Prentice-Hall, Inc., Englewood Cliffs, NJ, 1987.
- [Gar91] W. A. Gardner, "Exploitation of spectral redundancy in cyclostationary signals." *IEEE Communication Magazine*, pp. 14-35, Apr. 1991.
- [Gar93] W. A. Gardner, "Cyclic Wiener filtering: theory and method," *IEEE Transactions on communications*, vol. 41, no. 1, pp. 151-163. Jan. 1993.
- [Gar94] W. A. Gardner, *Cyclostationarity in Communications and Signal Processing*, The Institute of Electrical and Electronics Engineers, Inc., New York, 1994.
- [GBGM80] R. M. Gray, A. Buzo, A. H. Gray Jr. and Y. Matsuyama, "Distortion measures for speech processing," *IEEE Transactions on Acoustics, Speech, and Signal Processing*, vol. 28, no. 4, pp. 367-375, Aug. 1980.
- [GC92] W. A. Gardner and C. K. Chen, "Signal-selective time-different-of-arrival estimation for passive location of manmade signal sources in highly corruptive environments. Part I: Theory and Method," *IEEE Transactions on Signal Processing*, vol. 40, pp. 1168-1184, 1992.

- [GD89] R. P. Gooch and B. Daellenbach, "Prevention of interference capture in a blind (CMA based) adaptive receive filter," *Twenty-third Asilomar Conference on Signals System and Computers*, vol. 2, pp. 898-902, Nov. 1989.
- [GP92] W. A. Gardner and L. Paura, "Identification of polyperiodic nonlinear systems," *Technical Report*, Department of Electrical and Computer Engineering, Univ. of California at Davis, 1992.
- [Gre85] B. S. Grewal, *Higher Engineering Mathematics*, published by Romesh Chander Khanna, India, 1985.
- [GS93] W. A. Gardner and C. M. Spooner, "Detection and source location of weak cyclostationary signals: Simplifications of the maximum-likelihood receiver," *IEEE Transactions on Commun.*, vol. 41, 1993
- [Hay91] S. Haykin, *Adaptive Filter Theory*, Prentice-Hall, New Jersey, 1991.
- [HKH82] M. Hata, K. Kinoshita and K. Hirade, "Radio link design of cellular land mobile communication systems," *IEEE Transactions on Vehicular Technology*, vol. 31, no. 1, pp. 25-30, Feb. 1982.
- [HN91] D. Hatzinakos and C. L. Nikias, "Blind equalization using a tricepstrum-based algorithm," *IEEE Transactions on Commun.*, vol. 39, no. 5, pp. 669-681, May 1991.
- [HR94] R. He and J. H. Reed, "Spectral correlation of AMPS signals and its application to interference rejection," *IEEE MILCOM Conf.*, Oct, 1994.
- [HR95] R. He and J. H. Reed, "AMPS interference rejection by exploiting the SAT information," published in *IEEE Personal Indoor Mobile Radio Conf.*, Sep.

1995.

- [HR961] R. He and J. H. Reed, "A robust co-channel interference rejection technique for current mobile phone system," published in *IEEE Vehicular Technology Conference*, April 1996
- [HR962] R. He and J. H. Reed, "Interference rejection of AMPS using spectral correlation," submitted to *IEEE Transactions on Vehicular Technology*, 1996.
- [HRVH93] I. Howitt, J. H. Reed, V. Vemuri and T. C. Hsia, "Recent development in applying neural nets to equalization and interference rejection," *Virginia Tech's Third Symposium on Wireless Personal Communications, Proceedings*, Jun. 1993.
- [Jac94] J. Jacobsmeyer, "Improving throughput and availability of cellular digital packer data (CDPD)," *Virginia Tech 4th Symposium on Wireless Personal Commun.*, Jun 1994.
- [Jak74] W. Jakes, *Microwave Mobile Communications*, Wiley-Interscience, 1974.
- [Kha96] M. K. Khan, "Application of neural network to interference rejection for AMPS and GMSK signals," Master Thesis in the Bradley Department of Electrical Engineering, Virginia Polytechnic and State University, Jun. 1996.
- [KM89] T. Kwan and K. Martin, "Adaptive detection and enhancement of multiple sinusoids using a cascade IIR filter," *IEEE Transactions on Circuits and Systems*, vol. 36, no. 7, pp. 937-946, Jul. 1989.
- [KUL92] O. W. Kwon, C. K. Un and J. C. Lee, "Performance of constant modulus

adaptive digital filters for interference cancellation," *IEEE Transactions on Signal Processing*, vol. 26, no. 2, pp. 185-196, Feb. 1992.

- [Lee86] W. C. Y. Lee, "Elements of cellular mobile radio systems," *IEEE Transactions on Vehicular Technology*, vol. 35, no. 2, pp. 48-56, May 1986.
- [Lee93] W. C. Y. Lee, *Mobile Communications Design Fundamentals*, John Wiley & Sons, Inc., New York, 1993.
- [Lib95] J. C. Liberty Jr., *Analysis of CDMA Cellular Radio Systems Employing Adaptive Antennas*, Ph. D. dissertation submitted to the Bradley Department of Electrical Engineering, Virginia Polytechnic Institute and State University, Sep. 1995.
- [LR94] J. D. Laster and J. H. Reed, "A survey of adaptive signal channel interference rejection techniques for wireless communications," *Virginia Tech's Fourth Symposium on Wireless Personal Communications*, pp. 2.1-2.25, Blacksburg, 1994.
- [Mar84] S. C. Martin, "Some results of experiments in co-channel signal separation," *IEEE Military Commun.*, pp. 530-533, 1984.
- [MP93] K. W. Martin and M. Padmanabhan, "Using an IIR adaptive filter band to analyze short data segments of noisy sinusoids," *IEEE Transactions on Signal Processing*, vol. 41, no. 8, pp. 2583-2590, Aug. 1993.
- [MRH89] R. Mendoza, J. H. Reed, T. C. Hsia, "Interference rejection using a hybrid of a constant modulus algorithm and the spectral correlation discriminator," *IEEE MILCOM Conf.*, pp. 0491-0497, 1989.

- [MRHA91] R. Mendoza, J. H. Reed, T. C. Hsia and B. G. Agee, "Interference rejection using the time-dependent constant modulus algorithm and the Hybrid CMA/spectral correlation discriminator," *IEEE Transactions on Signal Processing*, vol. 39, no. 9, pp. 2108-2111, Sep. 1991.
- [MS94] T. Mizuno and O. Shimbo, "Response of an FM discriminator in the presence of noise and a co-channel interference," *IEEE Transactions on Commun.*, vol. 42, no. 11, pp. 3003-3009, Nov. 1994.
- [Mua82] R. Muammar and S. C. Gupta, "Channel interference in high capacity mobile radio system," *IEEE Transactions on Communications*, vol. 30, no. 8, pp. 1973-1978, Aug. 1982.
- [PG89] J. D. Parsons and J. G. Gardner, *Mobile Communication Systems*, published by John Wiley & Sons, Inc., New Jersey, 1989.
- [Rap96] T. S. Rappaport, *Wireless Communications: Principles and Practices*, published by Prentice Hall, 1996.
- [RBC94] D. A. Rich, S. Bo and F. A. Cassara, "Co-channel FM interference suppression using adaptive notch filters," *IEEE Transactions on Commun.*, vol. 42, no. 7, pp. 2384-2389, Jul. 1994.
- [RBL91] R. S. Roberts, W. A. Brown and H. H. Loomis Jr., "Computationally efficient algorithms for cyclic spectral analysis," *IEEE Signal Processing Magazine*, pp. 38-49, Apr. 1991.
- [RH90] J.H. Reed and T. C. Hsia, "The performance of time-dependent adaptive filters for interference rejection," *IEEE Transactions on Acoustics, Speech,*

and *Signal Processing*, vol. 38, no. 8, pp. 1373-1385, Aug. 1990.

- [RQH88] J. R. Reed, A. A. Quilici and T. C. Hsia, "A frequency domain time-dependent adaptive filter for interference rejection," *IEEE Military Commun. Conf.*, pp. 0391-0397, Oct. 1988.
- [SA88] S. V. Shell and B. G. Agee, "Application of the SCORE algorithm and SCORE extensions to sorting in the rank-L spectral self-coherence environment," *Conference Record, Twenty-second Asilomar Conf. on Signals Systems and Computers*, vol. 1, pp. 274-278, Oct. 1988.
- [SCS77] T. S. Sundresh, F. A. Cassara and H. Schachter, "Maximum a posteriori estimator for suppression of interchannel interference in FM receivers," *IEEE Transactions on Commun.*, vol. 25, no. 12, pp. 1480-1485, Dec. 1977.
- [SDS81] Z. D. Stojanovic, M. L. Dilic and I. S. Stojanovic, "A new demodulation methods improving FM system interference immunity," *IEEE Transactions on Commun.*, vol. 29, no. 7, pp. 1001-1010, Jul. 1981.
- [SG93] S. V. Shell and W. A. Gardner, "High resolution direction finding," Chapter in *Handbook of Statistics*, N. K. Bose and C. R. Rau, Amsterdam: Elsevier, 1993.
- [SN94] D. C. Shin and C. L. Nikias, "Adaptive interference canceler for narrow-band and wideband interferences using higher order statistics," *IEEE Transactions on Signal Processing*, vol. 42, no. 10, pp. 2715-2728, Oct. 1994.

- [Sto82] A. C. Stocker, "Co-channel Interference and its Avoidance in close Spaced Systems," *IEEE Transactions on Vehicular Technology*, vol. 31, no. 3, pp. 145-150, Aug. 1982.
- [SW88] K. W. Sowerby and A. G. Williamson, "Outage probability calculations for multiple cochannel interferers in cellular mobile radio systems," *IEE Proceedings*, vol. 135, no. 3, pp. 208-215, Jun. 1988.
- [TA83] J. R. Treichler and B. G. Agee, "A new approach to multipath correction of constant modulus signals," *IEEE Transactions on Acoustics, Speech, and Signal Processing*, vol. 31, no. 2, pp. 459-471. Apr. 1983.
- [TH93] P. Tichavsky and P. Handel, "Efficient tracking of multiple sinusoids with slowly varying parameters," *IEEE Int. Conf. on Acoustics, Speech, and Signal Processing*, pp. III 368-371, 1993.
- [TJL87] J. R. Treichler, C. R. Johnson Jr. and M. G. Larimore, *Theory and Design of Adaptive Filters*, published by John Wiley & sons. Inc., 1987.
- [XB92] Z. Xiang and G. Bi, "Fractionally spaced decision feedback multilayer perceptron for adaptive MQAM digital mobile radio reception," *SUPER-COMM/ICC'92. Discovering a New World of Communications*, vol. 3, pp. 1262-1266, Jun. 1993.
- [Yac93] M. D. Yacoub, *Foundations of Mobile Radio Engineering*, CRC Press, Inc., Florida, 1993.
- [You79] W. R. Young, "Advanced mobile phone service: Introduction, Background and Objectives," *The Bell System Technical Journal*, vol. 58, Jan. 1979.

- [YS84] Y. Yeh and S. Schwartz, "Outage probability in Mobile Telephony Due to Multipath Log-Normal Interferes," *IEEE Transactions on Communications*, vol. 32, no. 4, pp. 380-387, Apr. 1984.

Vita

Rong He was born on October 18, 1968 in Hangzhou, China. She received her Bachelor of Science Degree in the Electrical Engineering Department, with a specialty in microwave and electromagnetic theory, in July 1990 from Shanghai University, Shanghai, China. A year later, she went to the United States to pursue her advanced studies. In December 1992, she received her Master of Science degree from the Electrical Engineering Department, New Mexico State University, Las Cruces, New Mexico. Her master research focused on DSP and communications. She joined the Electrical Engineering Department of Virginia Polytechnic Institute and State University in Spring 1993 to pursue her Ph.D. In the summer of 1993, she began her research with Dr. Jeffrey H. Reed at the Mobile and Portable Radio Research Group in the area of interference cancellation and capacity enhancement of mobile phone systems. From August 1995 to December 1995, she worked with Northern Telecom in Richardson, Texas, where she was a software engineer designing an Operational Measurements (OM) System used in the cellular air traffic system for PCS1900. Her research interest includes modeling and simulation of radio communication systems, DSP implementation of mobile communication systems, interference rejection, and cellular system capacity analysis.

